Assessing the taphonomy of microbial biosignatures in hydrothermal sulfides – a geobiological approach

Dissertation

der Mathematisch-Naturwissenschaftlichen Fakultät

der Eberhard Karls Universität Tübingen

zur Erlangung des Grades eines

Doktors der Naturwissenschaften

(Dr. rer. nat.)

vorgelegt von

M.Sc. Eric Alexander Runge

aus Berlin

Tübingen

2024

Gedruckt mit Genehmigung der Mathematisch-Naturwissenschaftlichen Fakultät der Eberhard Karls Universität Tübingen.

Tag der mündlichen Qualifikation: 07.02.2025

Dekan: Prof. Dr. Thilo Stehle

1. Berichterstatter: Prof. Dr. Jan-Peter Duda

2. Berichterstatter: Prof. Dr. Andreas Kappler

3. Berichterstatterin: Prof. Julie Cosmidis, PhD

“Alles is overal, maar het milieu selecteert.”

– L.G.M. Baas Becking (1895-1963)

PREFACE

This thesis is a product of the research project “Reaching for life in the distant past – deciphering the geobiology of modern and ancient hydrothermal sulfides“ within the Emmy Noether Program of the Deutsche Forschungsgemeinschaft (DFG, Grant DU 1450/7-1 to Jan-Peter Duda). It received support from the SPP1833 “Building a habitable Earth” (DFG, Grant DU 1450/3-2 to Jan-Peter Duda). The work focuses on the taphonomy of biosignatures for microbial iron and sulfur cycling in hydrothermal sulfide systems. Laboratory experiments were conducted in Andreas Kappler’s Geomicrobiology lab (University of Tübingen, Germany). Scanning electron microscopy (SEM) was performed at the Tübingen Structural Microscopy Core Facility (University of Tübingen), funded by the Excellence Strategy of the German Federal and State Governments (EXC2124, 390838134). Stable sulfur and iron isotope analyses by secondary ion mass spectrometry (SIMS) were conducted in collaboration with Prof. Johanna Marin-Carbonne at the SwissSIMS center (University of Lausanne, Switzerland). The thesis is presented in English, organized as a cumulative dissertation, and submitted to the Faculty of Science (University of Tübingen). The introduction consists of a literature review on the broader scientific background (*Chapter 1*, Runge et al. 2023, *Geobiology*) and the ‘Objectives and Structure’ of the thesis (*Chapter 2*). The main section consists of three scientific manuscripts with first authorship (*Chapters 3 to 5,* Runge et al. 2023, *Earth and Planetary Science Letters*; Runge et al. 2024, *Communications Earth & Environment*; Runge et al., in revision for *Chemical Geology*). ‘Conclusions and Perspectives’ (*Chapter 6)* synthesizes key results, broader implications, and open questions, and suggests future work.

STATEMENT OF PERSONAL CONTRIBUTION

Prof. Jan-Peter Duda designed the conceptual background for this project. Prof. Duda was the main supervisor of my Ph.D. project, and Prof. Kappler was the second supervisor. I designed the experiments with Prof. Duda, Prof. Kappler, and Dr. Muammar Mansor and conducted them myself. The analysis and interpretation of the results and writing of all manuscripts were completed with Prof. Duda, Prof. Kappler, and Dr. Mansor. The contributions of people other than myself, Prof. Duda, Prof. Kappler, or Dr. Mansor were:

Chapter 2: Dr. Timm Bayer and Alex Chiu contributed to magnetite synthesis. Dr. Yali Liu and Prof. Dominique Lunter helped with Raman spectroscopy. Dr. Jeremiah Shuster and Dr. Stefan Shuster supported SEM analysis.

Chapter 3: Lars Grimm provided the initial culture of *Geobacter sulfurreducens*. Alex Chiu contributed to biogenic magnetite production. Carolin Dreher and Alex Chiu performed the μXRD analysis. Dr. Jeremiah Shuster supported SEM analysis. Dr. Stefan Fischer prepared samples for FIB-SEM and conducted the analyses. Eva Voggenreiter and Johann Holdt measured the total and dissolved organic carbon content in the incubation experiments.

Chapter 4: Dr. Thomas Bovay helped with sample preparation. Dr. Virgil Pasquier performed SIMS analysis and performed the initial data reduction. Dr. Jeremiah Shuster helped with SEM analysis. Prof. Johanna Marin-Carbonne wrote parts of the Method section.

I have not plagiarized or copied any of the text. *Chapters 1, 3, and 4* were published in different scientific journals so that they may appear in a different format elsewhere. However, no changes to their content have been made for this thesis. *Chapter 5* is currently in revision for *Chemical Geology*, so it may be published in a modified version. All co-authors listed in the individual chapters contributed to revising the manuscripts.

ACKNOWLEDGEMENTS

First, I want to express my sincerest gratitude to my advisor and mentor, Jan-Peter Duda, who gave me the opportunity and trust to work as his first doctoral student. It has been a pleasure working with you. I am glad I witnessed this young research group flourish despite starting from scratch during a pandemic and relocating mid-project. These past few years have been challenging in many ways, and I couldn't have wished for a more compassionate, supportive, and inspiring *Doktorvater*. Please never lose your curiosity and enthusiasm; they are contagious to everyone around you.

This study was also made possible by Andreas Kappler and Muammar Mansor. Andreas, you generously gave me every opportunity to learn and work in your lab. Your drive and passion have been constant sources of motivation. Muammar, your tireless efforts to open my eyes to the nanoscopic world of iron-sulfur biogeochemistry have forever changed how I view geology.

Many more friends and colleagues made this time an incredibly enriching experience. I'm indebted to you for various reasons: Carolin Dreher, Julius Havsteen, and Markus Gogouvitis turned Tübingen from a place to work into a temporary home for me. Alex Chiu and Hrvoje Višić were my constant companions in and outside the lab. Yu Pei never failed to cheer me up with her infectious energy. Johann Holdt mastered the chaos of my move to Tübingen and kindly arranged a new home in Göttingen. Katrin Wunsch, Marie Mollenkopf, and Hanna Grimm made our office a fun workplace. Stefan Fischer and Jeremiah Shuster guided me in sample preparation and shared fun SEM days. Eva Voggenreiter, Lars Grimm, and Timm Bayer patiently guided me from an absolute lab novice to my first dataset. Johanna Marin-Carbonne, Thomas Bovay, and Virgil Pasquier invited me to Lausanne and repeatedly took time for meetings on our data. All your personal and scientific support made this time much easier and infinitely more enjoyable. Thank you all so much.

These past few years have been the preliminary pinnacle of a journey that started much earlier. Joachim Reitner made me find my way into geobiology and encouraged

me to work on the most fascinating rocks I have ever laid my hands on. Margot Böse, Robert Hebenstreit, Kai Hartmann, and Jacob Hardt were inspiring teachers who drew me into the physical Earth sciences as an undergraduate through their example and guidance. Yan Dada and Bernd Wünnemann warmheartedly welcomed me for my first steps in research in Nanjing. All of you played a huge role in motivating me to pursue science. Danke & 谢谢!

Finally, I would like to thank my parents, Dodo and Thimo Runge, for always encouraging and supporting me on my way and my partner, Sara Vulpius, for walking this way with me. I take comfort in knowing I can always count on you. Vielen Dank, ich liebe euch.

LIST OF PUBLICATIONS

Included in this thesis

Runge, E.A.†, Mansor, M., Kappler, A., Duda, J.-P. (2023) Microbial biosignatures in ancient hydrothermal sulfides. *Geobiology* 21, 355–377 **(Chapter 1).**

Runge, E.A.†, Mansor, M., Shuster, J., Fischer, S., Liu, Y., Lunter, D.J., Kappler, A., Duda, J.-P.† (2023) Sulfidation of nano-magnetite to pyrite: Implications for interpreting paleoenvironmental proxies and biosignature records in hydrothermal sulfide deposits. *Earth and Planetary Science Letters* 617, 118261 **(Chapter 3).**

Runge, E.†, Mansor, M., Chiu, T.-H., Shuster, J., Fischer, S., Kappler, A., Duda, J.-P.† (2024) Hydrothermal sulfidation of biogenic magnetite produces framboid-like pyrite. *Communications Earth & Environment* 5, 252 **(Chapter 4).**

Runge, E.†, Mansor, M., Pasquier, V., Bovay, T., Marin-Carbonne, J., Fichtner, V., Kappler, A., Duda, J.-P., Stable isotope fingerprints of microbial iron and sulfur cycling preserved in ancient metamorphic hydrothermal sulfide deposits. In revision for *Chemical Geology* **(Chapter 5).**

Additional, not included in this thesis

Bronner, R., Thompson, K., Dreher, C., **Runge, E.**, Voggenreiter, E., Shuster, J., Wan, B., Joshi, P., Fischer, S., Duda, J.-P., Kappler, A., Mansor, M.† (2023) Co-reduction of Fe(III) and S0 drives Fe-S biomineral formation and phosphate mobilisation. *Geochemical Perspectives Letters* 24, 27–32.

Domingos, J.M., **Runge, E.**, Dreher, C., Chiu, T.-H., Shuster, J., Fischer, S., Kappler, A., Duda, J.-P., Xu, J., Mansor, M.† (2023) Inferred pyrite growth via the particle attachment pathway in the presence of trace metals. *Geochemical Perspectives Letters* 26, 14–19.

†corresponding authors

TABLE OF CONTENTS

ABSTRACT

Hydrothermal systems played a pivotal role in life's emergence and early evolution. To better understand this role, examining fundamental interactions between hydrothermal processes, minerals, and microbial life in deep time is paramount. Microbial biosignatures are the only available tool to investigate these interactions directly on the rock record. *Chapter 1* of this thesis reviews the Precambrian record of microbial biosignatures in deep-sea hydrothermal sulfides. The literature survey reveals that this record is scarce, and an insufficient understanding of taphonomic processes under sulfidic hydrothermal conditions limits its exploration. Aiming to tackle this problem, we integrate experimental and analytical techniques from mineralogy, geochemistry, and microbiology (e.g., reflected light microscopy, Raman spectroscopy, secondary ion mass spectrometry, and microbial culturing). This geobiological approach, detailed in *Chapter 2*, contributes to a more robust reconstruction of the deep-time evolution of life in hydrothermal systems.

Chapter 3 reports experiments simulating the sulfidic diagenesis of magnetite nanoparticles under hydrothermal conditions. Magnetite rapidly dissolved across all experimental setups and transformed to pyrite at pH ~7 and 80°C. The results highlight that magnetite sulfidation to pyrite is a critical taphonomic process in these environments. *Chapter 4* experimentally demonstrates that the hydrothermal sulfidation of abiogenic and biogenic magnetite yields pyrite with various distinct morphologies, including framboid-like spheroids. Notably, framboid-like pyrite, commonly considered a potential fingerprint of microbial sulfur cycling, was exclusively produced from the hydrothermal sulfidation of biogenic (i.e., organic matter-associated) magnetite. Thus, framboid-like pyrite is also a taphonomic fingerprint of biogenic iron minerals, providing a target for reconstructing the evolution of microbial iron cycling in deep time. *Chapter 5* presents textural and in-situ sulfur and iron isotope analyses of euhedral and framboidal pyrite from the ~390 Ma metamorphic Rammelsberg massive sulfide deposit. Combined $\delta^{34}S$, $\Delta^{33}S$, and $\delta^{56}Fe$ analyses record evidence of microbial sulfur and iron cycling despite extensive

alteration of the precursor sediment by sulfidic and iron-rich fluids and later greenschist metamorphism. Thus, coupled textural and in-situ stable isotope analysis could trace microbial sulfur and iron cycling in some of Earth's oldest rocks, including greenschist facies hydrothermal sulfides from the Pilbara Craton and Barberton Greenstone Belt.

Chapter 6 synthesizes how the results of this thesis substantially improve our understanding of the taphonomy of microbial biosignatures in hydrothermal sulfides. Combined textural and in-situ sulfur and iron isotope analyses of pyrite emerge as a promising approach for detecting microbial biosignatures throughout the geological record. This, in turn, is fundamental for understanding life's emergence and evolution in hydrothermal systems and other environments on early Earth.

ZUSAMMENFASSUNG

Hydrothermale Systeme spielten eine Schlüsselrolle bei der Entstehung und frühen Evolution des Lebens. Um diese Rolle besser zu verstehen, ist die Untersuchung grundlegender Wechselwirkungen zwischen hydrothermalen Prozessen, Mineralen und mikrobiellem Leben auf der frühen Erde von größter Bedeutung. Mikrobielle Biosignaturen sind das einzige verfügbare Werkzeug, um diese Wechselwirkungen direkt am Gesteinsbericht zu untersuchen. *Kapitel 1* dieser Arbeit gibt einen Überblick über den präkambrischen Bericht mikrobieller Biosignaturen in hydrothermalen Sulfiden der Tiefsee. Der Literaturüberblick zeigt, dass dieser Bericht nur spärlich bekannt ist, und ein unzureichendes Verständnis taphonomischer Prozesse unter sulfidisch-hydrothermalen Bedingungen seine Erforschung erschwert. Um diesem Problem entgegenzutreten, integriert diese Arbeit verschiedene experimentelle und analytische Techniken der Mineralogie, Geochemie und Mikrobiologie (z. B. Auflichtmikroskopie, Raman-Spektroskopie, Sekundärionen Massenspektrometrie, und mikrobielle Kultivierung). Dieser geobiologische Ansatz, der in *Kapitel 2* näher erläutert wird, trägt zu einer robusteren Rekonstruktion der Entwicklung des Lebens in hydrothermalen Systemen über geologische Zeiträume bei.

Kapitel 3 berichtet über Experimente zur Simulation der sulfidischen Diagenese von Magnetit-Nanopartikeln unter hydrothermalen Bedingungen. Magnetit löste sich in allen Versuchsanordnungen schnell auf und wandelte sich bei pH 7 und 80 °C in Pyrit um. Die Ergebnisse zeigen, dass die Sulfidisierung von Magnetit zu Pyrit ein kritischer taphonomischer Prozess in hydrothermalen Systemen ist. In *Kapitel 4* wird experimentell nachgewiesen, dass bei der hydrothermalen Sulfidisierung von abiogenem und biogenem Magnetit Pyrit mit unterschiedlichen Morphologien entsteht, einschließlich framboidähnlicher Sphäroide. Framboidähnlicher Pyrit, der gemeinhin als potenzieller Fingerabdruck des mikrobiellen Schwefelkreislaufs angesehen wird, entstand ausschließlich durch die hydrothermale Sulfidisierung von biogenem (d. h. mit organischem Material assoziiertem) Magnetit. Framboidähnlicher

Pyrit ist somit auch ein taphonomischer Fingerabdruck biogener Eisenminerale, und stellt somit ein Ziel für die Rekonstruktion der Entwicklung des mikrobiellen Eisenzyklus über geologische Zeiträume dar. *Kapitel 5* präsentiert Analysen der Mineraltexturen und in situ Schwefel- und Eisen-Isotopien von idiomorphem und framboidalem Pyrit aus der metamorphen Rammelsberg Massivsulfid-Lagerstätte (~390 Ma). Kombinierte $\delta^{34}S$, $\Delta^{33}S$ und $\delta^{56}Fe$ Analysen belegen mikrobielle Schwefel- und Eisenzyklen trotz intensiver Alteration des ursprünglichen Sediments durch sulfidische und eisenhaltige Fluide und späterer Grünschiefermetamorphose. Somit könnten gekoppelte Textur und in situ Isotopenanalysen den mikrobiellen Schwefel- und Eisen-Zyklus in einigen der ältesten Gesteine der Erde nachweisen, einschließlich grünschieferfazieller hydrothermaler Sulfide aus dem Pilbara Kraton und dem Barberton Grünschiefergürtel.

Kapitel 6 synthetisiert, wie die Ergebnisse dieser Arbeit das Verständnis der Taphonomie von mikrobiellen Biosignaturen in hydrothermalen Sulfiden erheblich verbessert haben. Die Kombination von Texturanalysen mit in situ Eisen- und Schwefel-Isotopensignaturen in Pyrit zeigt sich als vielversprechender Ansatz für den Nachweis von mikrobiellen Biosignaturen über geologische Zeiträume. Dies ist von grundlegender Bedeutung für das Verständnis der Entstehung und Entwicklung des Lebens in hydrothermalen Systemen und anderen Umgebungen auf der frühen Erde.

CHAPTER 1 – INTRODUCTION

Microbial biosignatures in ancient deep-sea hydrothermal sulfides

Eric Alexander Runge[1,†], Muammar Mansor[2], Andreas Kappler[2,3] & Jan-Peter Duda[4,1]

[1]Sedimentology and Organic Geochemistry, Department of Geosciences, Tübingen University, Tübingen, Germany,
[2]Geomicrobiology, Department of Geosciences, Tübingen University, Tübingen, Germany
[3]Cluster of Excellence EXC 2124, Controlling Microbes to Fight Infection, Tübingen, Germany
[4]Geobiology, Geoscience Center, Göttingen University, Göttingen, Germany

†corresponding author

Published in: *Geobiology*, 21(3), 355-377 (2023)

1.1 Abstract

Deep-sea hydrothermal systems provide ideal conditions for prebiotic reactions and ancient metabolic pathways and, therefore, might have played a pivotal role in the emergence of life. To understand this role better, it is paramount to examine fundamental interactions between hydrothermal processes, non-living matter, and microbial life in deep time. However, the distribution and diversity of microbial communities in ancient deep-sea hydrothermal systems are still poorly constrained, so evolutionary and ecological relationships remain unclear. One important reason is an insufficient understanding of the formation of diagnostic microbial biosignatures in such settings and their preservation through geological time. This contribution centers around microbial biosignatures in Precambrian deep-sea hydrothermal sulfide deposits. Intending to provide a valuable resource for scientists from across the natural sciences whose research is concerned with the origins of life, we first introduce different types of biosignatures that can be preserved over geological timescales (rock fabrics and textures, microfossils, mineral precipitates, carbonaceous matter, trace metal and isotope geochemical signatures). We then review selected reports of biosignatures from Precambrian deep-sea hydrothermal sulfide deposits and discuss their geobiological significance. Our survey highlights that Precambrian hydrothermal sulfide deposits potentially encode valuable information on environmental conditions, the presence and nature of microbial life, and the complex interactions between fluids, microorganisms, and minerals. It further emphasizes that the geobiological interpretation of these records is challenging and requires the concerted application of analytical and experimental methods from various fields, including geology, mineralogy, geochemistry, and microbiology. Well-orchestrated multidisciplinary studies allow us to understand the formation and preservation of microbial biosignatures in deep-sea hydrothermal sulfide systems and thus help unravel the fundamental geobiology of ancient settings. This, in turn, is critical for reconstructing life's emergence and early evolution on Earth and the search for life elsewhere in the universe.

1.2 INTRODUCTION

**see the glossary at the end of Chapter 1 for explanation of specific terms*

Deep-sea hydrothermal systems provide unique insights into life thriving under extreme conditions by any human standards. Driven by energy from Earth's interior, hot fluids circulate in the ocean crust and locally emanate into cool marine environments. Even in the absence of sunlight, these springs can fuel diverse ecosystems, from chemoautotrophs (i.e., microorganisms that fix inorganic carbon species such as CO_2) at the base to heterotrophic organisms such as tubeworms and bivalves at higher trophic levels. Metabolically diverse communities of chemosynthetic microorganisms utilize redox-active gases (e.g., H_2S, CH_4, H_2) and metals (e.g., Fe, Ni, Cu) delivered by hydrothermal fluids (Kelley *et al.*, 2002). Microorganisms are also ecologically diverse and adapted to highly different temperatures, ranging from psychrophiles and mesophiles that thrive at ambient seawater temperature (ca. 4–45°C) to hyperthermophiles that can tolerate temperatures up to 121°C (Kashefi & Lovley, 2003). The high metabolic and ecologic diversity in these systems is a consequence of steep spatial gradients and temporal variations in various environmental parameters, such as temperature, pH, availability and composition of minerals and organic substrates, and fluid chemistry (e.g., concentrations of metals), resulting in distinct ecological niches (Von Damm, 1995; O'Brien *et al.*, 2015). Therefore, geobiological studies on hydrothermal systems require a combination of geological, geochemical, and microbiological approaches.

Geobiological studies on hydrothermal systems are vital for understanding the emergence and early evolution of life on our planet. Hydrothermal vents were likely much more widespread on the early Earth due to a much higher heat flow from the mantle (Russell *et al.*, 2010; Johnson *et al.*, 2014). Some of these environments provided ideal conditions for the abiotic synthesis of organic molecules via Fischer-Tropsch-type (FTT) reactions linked to the serpentinization* of ultramafic* rocks. More specifically, these processes involve the hydrothermal reaction between minerals (olivine, pyroxene) and H_2O, resulting in the formation of H_2, which then may react with CO_2 from various sources to CH_4 and more complex hydrocarbons

(McCollom *et al.*, 1999; Holm & Charlou, 2001; Rushdi & Simoneit, 2001; McCollom & Seewald, 2007; Proskurowski *et al.*, 2008; McCollom, 2013; Konn *et al.*, 2015; Mißbach *et al.*, 2018). Metal sulfide minerals such as pyrite (FeS_2), sphalerite (ZnS), and chalcopyrite ($CuFeS_2$) are essential constituents of hydrothermal deposits, and their redox activity and reactive surfaces may have catalyzed the abiotic synthesis of organic matter under hydrothermal conditions (Wächtershäuser, 1990; Russell *et al.*, 1994, 2010; Huber & Wächtershäuser, 1997). Phylogenetic studies suggest that deep-branching (hyper)thermophilic microorganisms similar to those found around modern hydrothermal vents appear to be the closest living relatives of LUCA* (Weiss *et al.*, 2016). Similarly, the Asgard archaea – a group of microorganisms proposed as the 'missing evolutionary bridge' between prokaryotes and eukaryotes – were discovered in hydrothermal systems (Spang *et al.*, 2015; MacLeod *et al.*, 2019). Notably, hydrothermal systems may also exist in oceans of icy moons such as Enceladus, fueling the idea that life may also have emerged beyond Earth (Deamer & Damer, 2017).

To understand the significance of deep-sea hydrothermal systems in the emergence and early evolution of life, it is critical to examine their geobiology in deep time. One important reason is that models of potential prebiotic chemical evolution in hydrothermal environments must be consistent with conditions and processes in such systems on early Earth. Also, understanding fluid–microbe–mineral interactions in ancient hydrothermal settings is crucial to identifying metabolic pathways that might have played a vital role in the emergence of the earliest lifeforms. The only direct information on these interactions in our planet's past can be gleaned from the geological record.

The most important ancient equivalents of deep-sea hydrothermal systems are (i) volcanogenic massive sulfide deposits (VMS) and (ii) sedimentary exhalative massive sulfide ores (SEDEX). These deposits form in diverse deep-sea environments (i.e., below the photic zone), ranging from volcanic mid-ocean ridge, ocean-island, and (back-)arc settings to sediment-rich shelves, which accounts for profoundly different facies* (e.g., sulfidic chimney walls vs. sulfide-mineralized shales). Geological

evidence for such systems on Earth extends back to more than 3.2 billion years ago (Ga) (Vearncombe *et al.*, 1995; Rasmussen, 2000; Hofmann, 2011). Still, little is known about microbial life in ancient hydrothermal sulfide systems, which is due to (i) the low preservation potential of deep-sea deposits covering oceanic crust, (ii) the decreasing abundance of preserved rocks with increasing geological time, (iii) the obliteration of potential biosignatures by destructive processes in the environment and during later stages in history, and (iv) the difficulty in distinguishing biogenic from abiotic features (Westall, 2005; Javaux, 2019; Lepot, 2020; Georgieva *et al.*, 2021). Indeed, compared to other sedimentary settings, hydrothermal environments are characterized by strong chemical disequilibria, which commonly result in the syn-depositional alteration of biogenic features and self-assembly of mineral textures* that can resemble biological fingerprints (Fowler & L'Heureux, 1996; Southam & Saunders, 2005; Rouillard *et al.*, 2018). Therefore, a robust understanding of the formation and preservation of microbial biosignatures in deep-sea hydrothermal environments over geological timescales is vital to studies concerned with life's emergence and early evolution.

This paper on microbial biosignatures in Precambrian VMS- and SEDEX-type deposits aims to provide a resource for scientists from across the natural sciences whose research is concerned with life's emergence and early evolution. First, we introduce a range of candidate biosignatures for these environments and discuss their preservation potential under sulfidic hydrothermal conditions and over geological time scales. We then highlight examples of Precambrian deep-sea hydrothermal sulfide deposits for which biosignatures have been reported. Our review stresses the need to understand better the formation and preservation of microbial biosignatures in hydrothermal environments, which is of paramount importance for the search for the earliest life on Earth and, perhaps, beyond.

1.3 Microbial biosignatures – Concept & definitions

The Precambrian comprises the first 4 billion years in Earth's history, and most of this time, life was exclusively microbial (Knoll *et al.*, 2016). Problematically, microorganisms do not possess hard parts such as bones, shells, or wood. Therefore,

reconstructing the earliest evolution of life on Earth cannot rely on such "classic" fossils. However, rocks can preserve various other types of evidence that indicate the presence of microorganisms in ancient environments. These include rock fabrics* and textures, microbial microfossils, as well as minerals and organic matter with specific characteristics that are diagnostic for biologic activity (e.g., morphology, trace element signatures, stable isotope compositions) (Fig. 1.1). These features can be understood as *microbial biosignatures*, that is, signatures preserved in sediments and rocks that potentially testify to the presence of microbial life during their formation deposition.

The identification and interpretation of microbial biosignatures in the geological record are challenging. For one, this is because Earth's oldest rocks may preserve primary features that resemble diagnostic biosignatures but have an abiotic origin (i.e., pseudo-biosignatures) (e.g., Lowe, 1994; Brasier *et al.*, 2002; McCollom & Seewald, 2007; McLoughlin *et al.*, 2008; McMahon, 2019; Zawaski *et al.*, 2020). Discussing an abiotic explanation for observed features is relevant in rocks of any age but most critical for studies investigating periods in Earth's history for which the presence of life is not well constrained (i.e., before the Paleoarchean). Furthermore, biosignatures tend to get obscured over geological time scales by various processes. Alteration and destruction of biosignatures commence in the paleoenvironment and continue throughout diagenesis* and perhaps later stages (e.g., metamorphism*, metasomatism*, surface exposure) (Westall, 2005; Pinti *et al.*, 2009; Manning-Berg *et al.*, 2019). Primary signatures preserved in rocks might also be obscured by the formation of secondary minerals or the intrusion of organic matter during much later stages (e.g., van Zuilen *et al.*, 2002; Westall & Folk, 2003; Rasmussen *et al.*, 2008; Summons *et al.*, 2021). For these reasons, a robust knowledge of biosignature formation and preservation (i.e., taphonomy*) is critical to studies concerned with Precambrian geobiology and astrobiology, and the geological context of target records must always be considered.

1.4 Microbial biosignatues relevant to Precambrian deep-sea hydrothermal sulfide systems

Geobiological studies on Earth's oldest rocks ideally start at the outcrop scale and then progressively zoom in, perhaps down to the micron- or even nanoscale. Accordingly, this survey begins with morphological features ('rock fabrics and textures' and 'microbial microfossils': Figs. 1.1A, B), continues with mineralogical and organic components ('mineral precipitates' and 'carbonaceous matter': Figs. 1.1C, D), and concludes with chemical and isotopic fingerprints in rocks ('(bio)geochemical signatures': Fig. 1.1E). All the potential biosignatures discussed here may occur independently; that is, macroscopic life-like structures in rocks are not necessarily associated with mineralogical and chemical fingerprints of life and *vice versa*. However, this integrative multi-scale strategy is essential to critically assess the integrity and validity of potential microbial biosignatures in Earth's most ancient rocks and, simultaneously, helps avoid analytical and interpretative pitfalls.

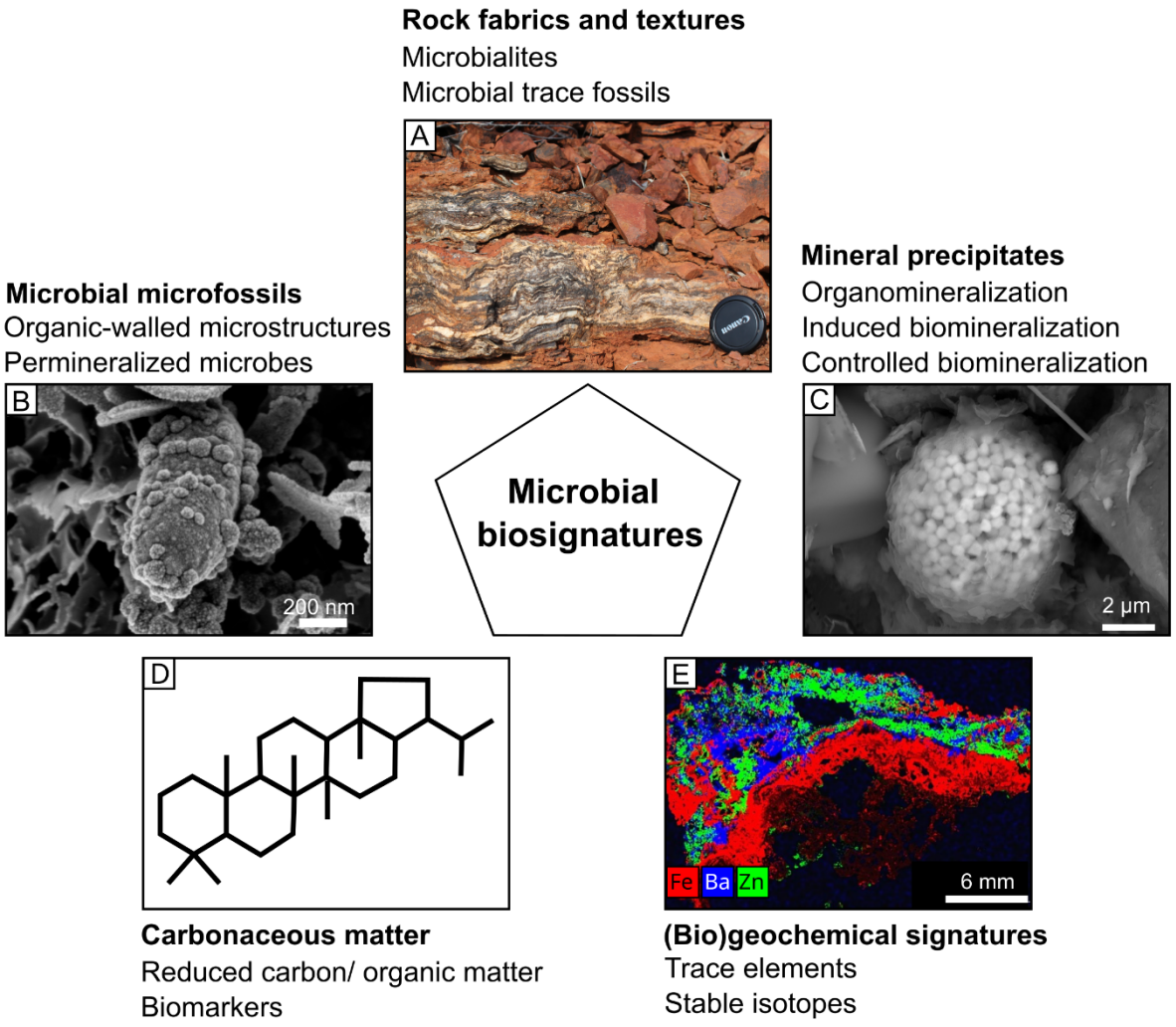

Figure 1.1: Examples of microbial biosignatures comparable to those that might form and preserve in deep-sea hydrothermal sulfide deposits; A: microbial rock fabrics and textures (here: originally sulfidized stromatolite in the ca. 3.48 Ga Dresser Formation, Pilbara Craton); B: microbial microfossils (here: a Fe(II)-oxidizing bacterium encrusted by Fe-(oxyhydr)oxides that formed through microbially-induced precipitation); C: microbial mineral precipitates (here: recent framboidal pyrite in sediments from the Norsminde Fjord, Denmark); D: (bio)geochemical signatures (here: µXRF scan showing chemical zoning in the exterior part of a recent black smoker chimney from the Manus Basin, Western Pacific Ocean); E: carbonaceous matter (here: structural formula of a C_{30} hopane, a geologically stable organic molecule that is diagnostic for commonly used bacterial biomarker).

1.4.1 Rock fabrics and textures

Microbialites

Benthic microbial communities organized as mats or biofilms can directly influence sedimentation by trapping and binding allochthonous* particles (Black, 1933; Reid *et al.*, 2003; Suarez-Gonzalez *et al.*, 2019) or, perhaps more importantly, by facilitating authigenic mineral formation (Labrenz *et al.*, 2000; Riding, 2000; Arp *et al.*, 2001;

Reitner *et al.*, 2005; Dupraz *et al.*, 2009; Reitner, 2011). These processes are commonly linked to organic extracellular polymeric substances (EPS) produced by microorganisms. They often result in specific fabrics and textures that may be preserved in rocks over geological time scales (e.g., domal or columnar shapes and layered or clotted macro- and microfabrics) (Arp *et al.*, 2003; Riding, 2011; Suarez-Gonzalez *et al.*, 2019; Grey & Awramik, 2020). Lithified sediments formed by benthic microbial communities such as biofilms or microbial mats are termed microbialites (Burne & Moore, 1987; Riding, 2000) (Fig. 1.1A). Perhaps the most famous type of microbialite are stromatolites, that is, organosedimentary growth structures that are characterized by distinct layering and/or lamination (Kalkowsky, 1908; Semikhatov *et al.*, 1979).

Biofilms, microbial mats, as well as microbialite-like rock fabrics formed by benthic microbial communities are present in today's deep-sea hydrothermal systems (Van Dover, 2000, 2019; Reysenbach & Cady, 2001; Blumenberg *et al.*, 2007; Moeller *et al.*, 2014; Flemming & Wuertz, 2019; Baumgartner *et al.*, 2022). Moreover, numerous Fe sulfide-bearing microbialites in the Precambrian hydrothermal deposits demonstrate their preservation potential over billion-year timescales (McGoldrick, 1999; Van Kranendonk *et al.*, 2008; Duda *et al.*, 2016; Baumgartner *et al.*, 2019, 2020a, 2020b; Mißbach *et al.*, 2021) (Fig. 1.1A). For these reasons, microbialites are a prime target for geobiological studies on ancient deep-sea hydrothermal systems.

The formation of microbialites in deep-sea hydrothermal sulfide systems results from a complex interplay of abiotic and biological processes. It may be fostered by biologically induced precipitation and/or encrustation of organic templates of biofilms and microbial mats in Fe and S minerals (see the section on Mineral precipitates). These structures may serve as precursors for the secondary sulfidation of Fe minerals and organic matter driven by reduced sulfur species from volcanic exhalation or microbial sulfur cycling (Russell, 1996; Little *et al.*, 1998; Kelley *et al.*, 2002; Campbell, 2006; Baumgartner *et al.*, 2022). The fabric, texture, and mineralogy of microbialites in deep-sea hydrothermal systems will likely depend on temperature, pH, and fluid chemistry. For instance, these parameters' steep gradients and

substantial temporal variations might result in distinct ecological niches occupied by different (stratified) microbial communities and characterized by specific microbe-mineral interactions (Toner *et al.*, 2013; O'Brien *et al.*, 2015). Furthermore, the (trans)formation of various metal sulfides in hydrothermal environments is influenced by metal concentrations (Ehrlich *et al.*, 2021; Park & Faivre, 2022) and gradients in fluid temperature, pH, and redox state (e.g., from hot to cooler: pyrrhotite ± magnetite > chalcopyrite to pyrite > sphalerite ± galena: Hannington, 2014) (Fig. 1.1D). These gradients may also control the identity of minerals precipitated in microbial mats and biofilms, potentially resulting in mineralogically and/or geochemically zoned microbialites in ancient hydrothermal deposits.

Abiotic processes, such as chemical precipitation or tectonic deformation of laminated rocks, can form rock fabrics resembling microbialites (Buick *et al.*, 1981; Grotzinger & Rothman, 1996; McLoughlin *et al.*, 2008; Allwood *et al.*, 2018; Zawaski *et al.*, 2020). This is particularly critical in hydrothermal settings, where physicochemical disequilibria may drive abiotic precipitation of colloform, botryoidal, and domal textures (Revan *et al.*, 2014; Maslennikov *et al.*, 2017). These precipitates mostly exhibit uniform, concentric, or laterally continuous banding (Foley *et al.*, 2001; Pirajno, 2010; Gao *et al.*, 2016). Further complicating, stromatolite-like fabrics, including wrinkly laminae (Buick *et al.*, 1981; Riding, 2000, 2011; Allwood *et al.*, 2009; Van Kranendonk, 2011), have also been replicated in abiotic laboratory experiments (McLoughlin *et al.*, 2008). Although the experimental conditions differed from those prevailing in deep-sea hydrothermal vent environments, this report cautions that features commonly associated with microbialites can also derive from abiotic processes.

Microbial trace fossils

Microbial trace fossils (not to be mistaken with microfossils, see next section) are µm-scale morphological or textural features formed by rock-inhabiting (i.e., endolithic) microorganisms. These organisms may actively create channels, voids, or cavities within rocks or minerals (Golubic *et al.*, 1981; Marlow *et al.*, 2015; Ivarsson *et al.*, 2021). For instance, oxidative dissolution of Fe sulfides by Fe(II)-oxidizing bacteria

can result in distinct cell-sized (i.e., µm-scale) etch-marks or pits on mineral surfaces (Andrews, 1988; Thorseth *et al.*, 2001; Rojas-Chapana & Tributsch, 2004). Such features and associated Fe (oxyhydr)oxides resulting from oxidative dissolution were reported on surfaces of sulfide minerals in modern seafloor hydrothermal deposits (Liu *et al.*, 2020). To the best of our knowledge, there are no reports of microbial trace fossils in Precambrian hydrothermal sulfides. However, etch marks and channels associated with Fe oxides and carbonaceous matter in detrital pyrite in the ca. 3.4 Ga Strelley Pool Formation were interpreted as evidence for microbially induced pyrite oxidation (Wacey *et al.*, 2011b). This suggests that microbial trace fossils may be preserved in ancient hydrothermal sulfides.

A common challenge in studying ancient microbial trace fossils is ensuring their endogeneity* and syngenicity* to the host rock. Endolithic microorganisms can inhabit a rock any time after its formation, even billions of years after deposition (Westall & Folk, 2003; McLoughlin *et al.*, 2007; Hoshino *et al.*, 2014). Moreover, it has been shown for other rock types (e.g., pillow basalts, seafloor volcanic glasses, and chert) that microbial trace fossils can be confused with abiotic post-depositional features such as ambient inclusion trails or metamorphic titanite microtubes (e.g., Knoll & Barghoorn, 1974; Lepot *et al.*, 2011; Grosch & McLoughlin, 2014; McCollom & Donaldson, 2019). The degree to which abiotic processes can mimic sulfide bio-alteration features is currently unknown. Moreover, experimental exposure of bio-alteration features to high temperatures is necessary to illuminate their preservation potential in hydrothermal systems.

Microbial microfossils

Microbial microfossils are organic remains or permineralized* microstructures of microorganisms preserved within rocks (Fig. 1.1B). In Precambrian cherts, microfossils typically range between 10 - 100 µm in size and exhibit spheroidal or filamentous shapes (Golubic & Hofmann, 1976; Knoll & Barghoorn, 1977; Rasmussen, 2000; Duck *et al.*, 2007; Sugitani *et al.*, 2007; Glikson *et al.*, 2008; Javaux & Lepot, 2018). The morphological preservation of such delicate structures may be aided by sulfide- and silica-bearing fluids causing mineral-coating or

permineralization in sulfide minerals and/or chert (Peter & Scott, 1988; Rasmussen, 2000; Konhauser *et al.*, 2004; Alleon *et al.*, 2016a, 2016b; Duda *et al.*, 2016; Delarue *et al.*, 2017; Manning-Berg & Kah, 2017; Georgieva *et al.*, 2018; Manning-Berg *et al.*, 2019; Reinhardt *et al.*, 2019; Gong *et al.*, 2020). Chert formation typically occurs in the lower temperature zones of deep-sea hydrothermal systems and is often associated with (microbial) Fe oxide formation, resulting in a characteristic jasper facies (Hannington *et al.*, 1998). These rocks could provide promising targets for studying ancient microbial microfossils; indeed, various reported microbial Fe oxide filaments were found in such jasper (Little *et al.*, 2004, 2021; Dodd *et al.*, 2017; Papineau *et al.*, 2022).

Despite this potential, recognizing microbial microfossils in the rock record remains difficult. One important reason is their small size and simple morphology (Buick, 1990; Brasier *et al.*, 2002). Furthermore, abiotic processes, such as self-assembly during syn-depositional or diagenetic mineral (trans)formations, can produce structures that morphologically resemble microbial microfossils (i.e., 'biomorphs': García-Ruiz *et al.*, 2003; Cosmidis & Templeton, 2016; Rouillard *et al.*, 2018; McMahon, 2019; Criouet *et al.*, 2021; Nims *et al.*, 2021). Abiotic biomorphs may also be present in hydrothermal sulfide systems. Experimental studies demonstrated the auto-assembly of mackinawite and elemental sulfur into filamentous structures in the presence of organic matter (Cosmidis & Templeton, 2016; Picard *et al.*, 2021). Significantly, these minerals are essential precursors to pyrite in lower temperature (<121°C) inhabited niches of hydrothermal environments (Kotopoulou *et al.*, 2022). Moreover, the organic compounds contributing to this auto-assembly may derive from the degradation of primary organic matter that does not testify to a biogenic origin of associated minerals (Simoneit, 1993; Brasier *et al.*, 2002; Simoneit *et al.*, 2004). Pyritization of such abiotic filaments may yield features resembling previously reported pyritized microfossils in hydrothermal sulfides (Rasmussen, 2000; Baumgartner *et al.*, 2022). The morphological preservation of abiotic biomorphs needs to be tested for hydrothermal conditions, but, likely, such features can easily be confused with microbial microfossils in ancient rocks.

Microfossil-like structures (“mimics”) may also form during later stages in the history of a rock, for instance, through the reorganization of carbonaceous matter during silica recrystallization or its migration into pre-existing voids or gas bubbles (Brasier *et al.*, 2002, 2005; Jones & Renaut, 2007; Wacey *et al.*, 2018b, 2018a; Rasmussen *et al.*, 2021). Given the complexity of such alteration processes, it may not be surprising that many purported microfossils from early Archean hydrothermal deposits have been re-interpreted as younger contaminants or abiotic mimics (Schopf & Packer, 1987; Brasier *et al.*, 2002, 2005, 2006; Wacey *et al.*, 2016). Because of these limitations and potential pitfalls, studying microbial microfossils requires careful and detailed microscopic observation. Critical morphological criteria include population-scale morphometric characteristics, cell-like ultrastructure, and taphonomic features such as cell-like deformation behavior (Javaux *et al.*, 2003; Grey & Sugitani, 2009; Rouillard *et al.*, 2019). Additional geochemical evidence (e.g., $\delta^{13}C^*$ signatures in carbonaceous matter, thermal maturity consistent with the metamorphic grade of the host rock) can help establish the syngenicity and biogenicity of organic microstructures (Javaux *et al.*, 2010; Lepot *et al.*, 2013; Sforna *et al.*, 2014).

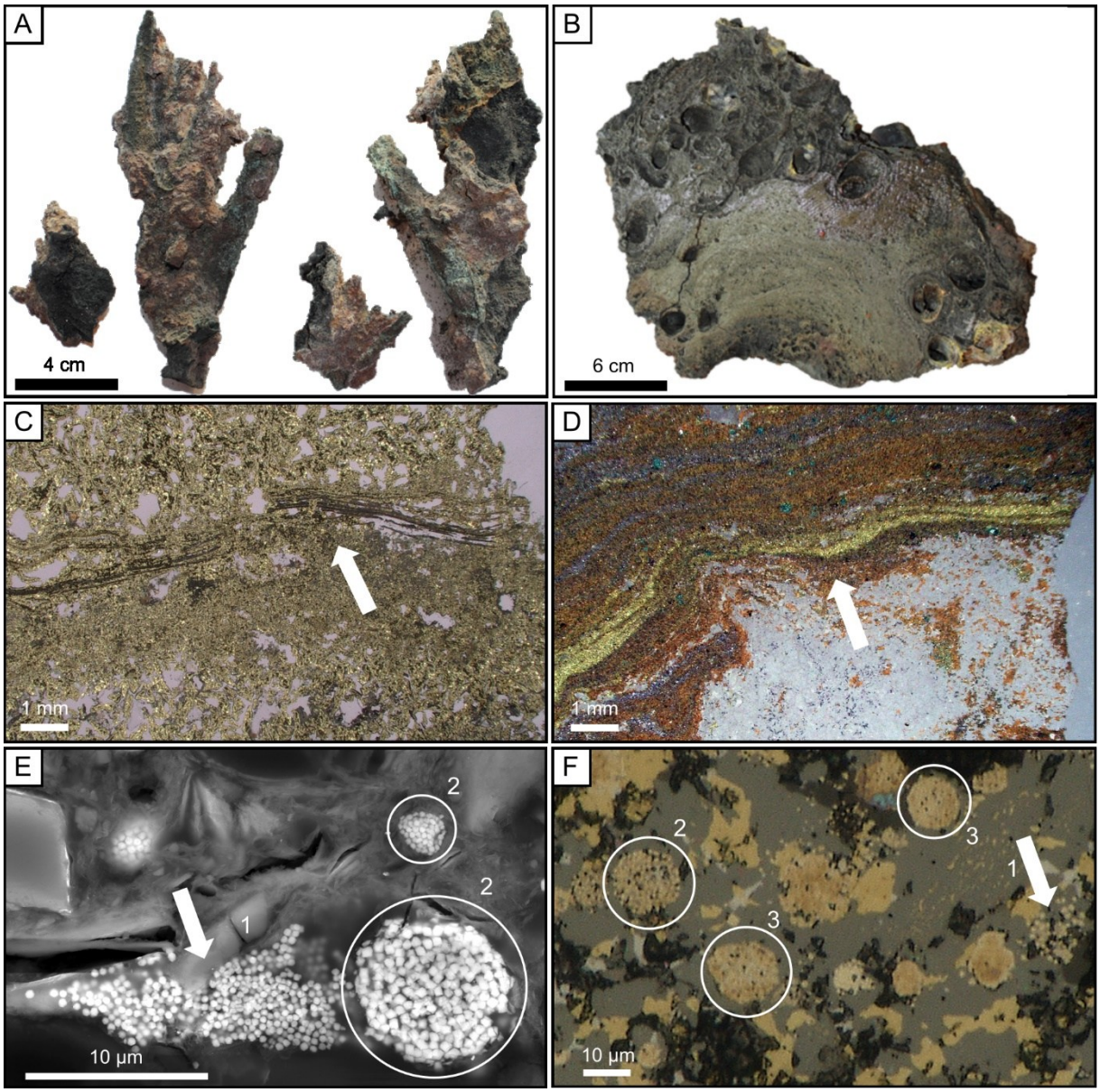

Figure 1.2: Comparison of modern and ancient hydrothermal sulfide deposits and microbial sulfide precipitates. A: modern black smoker chimney (Manus Basin), B: modern massive hydrothermal sulfide (Indian Ocean), C: pyritized biofilm (white arrow) in modern hydrothermal sulfide deposit (Indian Ocean), D: potential pyritized biofilm laminated sulfides in the ca. 390 Ma Rammelsberg SEDEX deposit (Harz mountains, Germany) (white arrow), strongly resembling recent pyritized biofilm structure in (C), E: loose aggregates of sub-µm scale pyrite crystals (white arrow; 1) and pyrite framboids (2) associated with organic matter in modern marine sediments from the Norsminde Fjord (Denmark), F: loose aggregate of sub-µm scale pyrite crystals (1), pyrite framboids (2), and infilled framboids (3) in the ca. 390 Ma Rammelsberg SEDEX deposit.

1.4.2 Mineral precipitates

Organomineralization and induced biomineralization

Microorganisms can facilitate extracellular mineral formation in various ways. One pathway is the nucleation of crystal growth on organic templates, such as cell wall surfaces or within EPS (i.e., "organomineralization": Addadi & Weiner, 1985; Reitner, 1993; Trichet & Défarge, 1995; or "biologically influenced mineralization": Cosmidis & Benzerara, 2022). In this case, the structural and chemical properties of the organic template facilitate mineral precipitation. Another possible pathway is the modification of the physicochemical microenvironment in microbial communities through their metabolic activity (i.e., "induced biomineralization": Lowenstam, 1981; Beveridge, 1989; or "biologically induced mineralization": Cosmidis & Benzerara, 2022). Organomineralization and induced biomineralization are not mutually exclusive and may co-occur. However, organomineralization is not necessarily linked to metabolic processes or limited to living organic matter and, therefore, can proceed during an organisms' lifetime and/or after its death (i.e., as a taphonomic process). Induced biomineralization, in contrast, requires metabolic activity and, thus, living organisms.

Fe and S minerals are the most promising minerals of potential biogenic origin in hydrothermal sulfide systems because their formation in most sedimentary environments dominantly results from microbial Fe and S cycling (Picard *et al.*, 2016; Kappler *et al.*, 2021). Important examples are Fe (oxyhydr)oxides such as ferrihydrite (Widdel *et al.*, 1993; Kappler *et al.*, 2005) and magnetite (Lovley *et al.*, 1987; Chaudhuri *et al.*, 2001; Köhler *et al.*, 2013). These minerals commonly exhibit nm-scale particle size and association with organic matter (Miot *et al.*, 2009; Han *et al.*, 2021). The reaction of Fe minerals and dissolved metals (e.g., Fe^{2+}, Zn^{2+}) with aqueous sulfide in anoxic to low-oxic settings drives sedimentary sulfide mineral formation (Berner, 1970, 1984; Rickard, 1975; Labrenz *et al.*, 2000; Schieber, 2002; Popa *et al.*, 2004). Notably, sulfate-reducing bacteria can influence the nucleation, particle size, and morphology of sulfide minerals via templating on cell walls and EPS, as well as through sulfur redox cycling (Ferris *et al.*, 1987; Donald & Southam, 1999; Xu *et al.*,

2016; Picard *et al.*, 2018; Mansor *et al.*, 2019; Thiel *et al.*, 2019; Park & Faivre, 2022) (Fig. 1.1C). Pyrite framboids are prominent examples that are often interpreted to result from biological mediation of sulfide mineral (trans)formation (Wilkin & Barnes, 1997; Popa *et al.*, 2004; Duda *et al.*, 2016), although the mechanisms leading to framboid assembly in microbial systems remain enigmatic (Ohfuji & Rickard, 2005). Similarly, the formation of metastable elemental sulfur can be induced by microbial oxidation of reduced sulfur species and facilitated by organic templates, which may also aid in the stabilization and preservation of elemental sulfur (Breier *et al.*, 2012; Cosmidis *et al.*, 2019; Cron *et al.*, 2019).

Identifying the products of induced biomineralization or organomineralization in ancient hydrothermal deposits is challenging. One important reason for this problem is that biological and abiotic precipitates might be texturally and compositionally similar. For instance, magnetite can form during diagenesis or low-grade metamorphism via thermochemical reduction of primary Fe oxyhydroxides such as ferrihydrite and lepidocrocite with sedimentary organic matter (Köhler *et al.*, 2013; Posth *et al.*, 2013, 2014; Halama *et al.*, 2016). Also, sulfides that abiotically precipitate from supersaturated fluids may exhibit colloform or framboid-like features (Fowler & L'Heureux, 1996; Wilkin & Barnes, 1997; Foley *et al.*, 2001; Ohfuji & Rickard, 2005), which resemble microbial textures from modern analog settings (Nozaki *et al.*, 2020) (Figs. 1.2E-F). Furthermore, primary biogenic minerals might be overprinted or replaced by abiotic precipitates resulting from intense fluid circulation in hydrothermal systems (Kesler *et al.*, 1989; Southam & Saunders, 2005). Consequently, biogenic and abiotic precipitates might co-exist in hydrothermal sulfide deposits and are potentially not or only barely distinguishable.

Despite these limitations, potential biogenic sulfide minerals have been reported from numerous ancient hydrothermal environments, ranging from the Phanerozoic (<541 million years, Ma) back to the early Archean (>3.2 Ga) (Rasmussen, 2000; Fallick *et al.*, 2001; Wilson *et al.*, 2003; Kucha *et al.*, 2005; Schroll & Rantitsch, 2005; Tornos *et al.*, 2014; Wacey *et al.*, 2015; Duda *et al.*, 2016; Georgieva *et al.*, 2018; Baumgartner *et al.*, 2019). While the biogenicity of precipitates has not been unequivocally

demonstrated in all of these cases, the combination of petrographic analyses with various mineralogical and geochemical approaches has helped reach a higher degree of confidence.

Controlled biomineralization

Some microorganisms can directly control the nucleation and growth of specific minerals within their cells (Weiner & Dove, 2003; Mansor & Xu, 2020). For instance, some S-oxidizing bacteria, such as *Allochromatium, Beggiatoa*, or *Thiothrix*, form intracellular deposits of amorphous S^0 (Prange *et al.*, 2002; Nims *et al.*, 2019; Dahl, 2020). Notably, the bacterium *Achromatium* occurs in modern deep-sea hydrothermal systems and precipitates both S^0 and $CaCO_3$ intracellularly (Benzerara *et al.*, 2020; Ionescu *et al.*, 2020). Perhaps most prominently, magnetotactic bacteria (MTB) precipitate nanocrystals of ferromagnetic minerals (magnetite [Fe_3O_4] or greigite [Fe_3S_4]) within membrane-bound organelles ('magnetosomes') (Amor *et al.*, 2020). Understanding the preservation potential of these precipitates could open new possibilities for detecting biominerals in the rock record.

Magnetite crystals in MTB have characteristic features that differ from their abiotic counterparts, making them a potential biosignature in sedimentary rocks (i.e., 'magnetofossils': Kirschvink & Chang, 1984). These features include narrow size/shape distributions, diagnostic crystal morphologies (e.g., bullet-shaped, elongated prismatic), an arrangement of crystals in chains, crystallographic perfection, major and trace element chemical purity, high Fe(II)/Fe(III) ratios, and isotopic fingerprints (e.g., Thomas-Keprta *et al.*, 2000; Lam *et al.*, 2010; Amor *et al.*, 2015, 2016). Greigite magnetosomes show distinctly different magnetic properties than abiotic greigite (Bai *et al.*, 2022). Still, greigite magnetosomes exhibit more crystallographic defects and chemical impurities than magnetite magnetosomes, making their identification more difficult (Kopp & Kirschvink, 2008).

MTB occur in suboxic to anoxic environments in freshwater and marine settings (Amor *et al.*, 2020). Magnetite-producing MTB are generally more abundant near the oxic-anoxic transition zone, while greigite-producing MTB more widely occur in

sulfidic environments (Reitner *et al.*, 2005; Amor *et al.*, 2020). The MTB strain *Magnetobacterium bavaricum* was found to inhabit recent deep-sea hydrothermal vent chimneys, supporting the potential presence of magnetofossils in ancient deposits from such settings (Suzuki *et al.*, 2004). Indeed, magnetite magnetofossils are widespread in modern deep-sea sediments (Chang & Kirschvink, 1989). Putative magnetofossils preserved in the ca. 1.9 Ga Gunflint Chert (Chang *et al.*, 1989) and the ca. 2.7 Ga Tumbiana Stromatolite (Akai *et al.*, 1997) suggest that MTB may be traced back to late Archean to early Paleoproterozoic times. This is supported by molecular clock studies suggesting an origin of controlled Fe biomineralization at ca. 3.2–3.4 Ga (Lin *et al.*, 2017). Taken together, magnetofossils seem to be promising candidate biosignatures for geobiological studies on ancient hydrothermal deposits.

The preservation potential of magnetofossils for microbial habitats in hydrothermal sulfide systems needs to be better understood. Sulfidation reactions may promote the reductive dissolution of magnetite and/or its transformation to Fe sulfide minerals (Canfield & Berner, 1987; Poulton *et al.*, 2004; Qian *et al.*, 2010, 2013; Bendt *et al.*, 2019). More experimental work is required to identify whether the transformation products of such reactions preserve biogenic characteristics. Moreover, high-temperature metamorphic reactions may produce magnetite crystals in the size range of MTB magnetite. Indeed, putative magnetofossils in the Martian meteorite ALH84001 are now widely considered abiotic products of high-temperature reactions (e.g., Brearley, 2003; Treiman, 2003; Bell, 2007; but see McKay *et al.*, 1996; Thomas-Keprta *et al.*, 2000). Therefore, the unambiguous identification of magnetofossils in ancient hydrothermal deposits requires distinct criteria that collectively differentiate them from abiotic precipitates (for a detailed review, see Kopp & Kirschvink, 2008).

1.4.3 Carbonaceous matter

All known life is based on reduced carbon, and organisms are the primary source of organic matter in sediments and rocks on Earth (Peters *et al.*, 2005a, 2005b; van Zuilen, 2019). Particularly interesting are organic molecules with specific biological sources (e.g., lipids, pigments) and their hydrocarbon derivates that are stable over geological timescales and retain source diagnostic structural characteristics. These

compounds are commonly termed “molecular fossils” or “biomarkers” (Eglinton *et al.*, 1964; Peters *et al.*, 2005a, 2005b) (Fig. 1.1E). Organic matter in modern and ancient deposits can be chemically and compositionally complex. It is operationally divided into proportions that are extractable and non-extractable with organic solvents (i.e., bitumen and kerogen, respectively) (Durand, 1980) (Fig. 1.3). Bitumen comprises mixtures of organic compounds that were directly preserved as free molecules or released through the thermal degradation of macromolecular fractions such as kerogen (Vandenbroucke & Largeau, 2007) (Fig. 1.3). The kerogen is particularly important since it usually comprises the bulk of the total organic matter in sediments and sedimentary rocks (typically >90% w/w: e.g., Peters *et al.*, 2005a, 2005b). Kerogen formation is complex but essentially involves the degradation, polymerization, and condensation of biomolecules (Durand, 1980; Farrimond *et al.*, 2003; Vandenbroucke & Largeau, 2007). Given that a post-depositional emplacement can be excluded, most of the bitumen preserved in ancient samples is derived from the thermal degradation of the corresponding kerogen during burial.

During burial, the degradation of organic matter is mainly driven by increasing temperatures, resulting in a progressive loss of N, S, O, and H. At ca. 200 – 300°C, extensive thermal cracking and aromatization of organic matter result in recalcitrant, high molecular-weight residues (Rouzaud *et al.*, 2015). Under metamorphic conditions, carbonization and crystallization processes transform organic matter within rocks into pure residual carbon or crystalline graphite, respectively (Bernard & Papineau, 2014; Rouzaud *et al.*, 2015) (Fig. 1.3). Despite their high maturity, pure residual carbon and graphite may still bear morphological or stable C isotopic characteristics related to biogenic precursor materials, thus serving as biosignatures (Mojzsis *et al.*, 1996; Schidlowski, 2001; Hayes & Waldbauer, 2006; Schiffbauer *et al.*, 2007; Bell *et al.*, 2015; for discussion on C isotopes, see also section on Stable isotopes). However, as detailed above (see the section on Microbial microfossils), life-like morphologies may result from secondary reorganization and hydrothermal overprint of the precursor materials, which can, in turn, be abiotic or biogenic in origin (Brasier *et al.*, 2005; Rouillard *et al.*, 2018).

The fate of organic matter in deep-sea hydrothermal vent systems is poorly understood. One important reason is that organic matter might be exposed to elevated temperatures at any stage, which is very different from conventional sedimentary environments where, in the absence of magmatic activity, thermal maturation is a function of burial depth (Logan *et al.*, 2001; McCollom & Seewald, 2007; Greenwood *et al.*, 2013) (Fig. 1.3). For instance, immature kerogen in hydrothermal surface environments might be thermally altered by percolating fluids, leading to the formation of "hydrothermal petroleum" and the degradation of hydrocarbons before deposition and burial (Simoneit, 1993; Simoneit *et al.*, 2004). Further complicating, hydrothermal fluid circulation can cause in-situ mixing of organic matter from various sources and environments, resulting in time- and space-averaged signals (Blumenberg *et al.*, 2007, 2012; Konn *et al.*, 2009; Duda *et al.*, 2018). On the other hand, early encapsulation of organic matter into hydrothermal sulfide minerals may promote its preservation (Greenwood *et al.*, 2013; Holman *et al.*, 2014b; Picard *et al.*, 2019, 2021). The removal of organic matter from hot zones and subsequent sequestration in minerals can also facilitate its preservation, as proposed for hydrocarbons that may have formed abiotically via FTT reactions linked to serpentinization (Delacour *et al.*, 2008).

Organic matter is widespread in modern deep-sea hydrothermal systems and potentially provides valuable insights into geomicrobiological key processes (Simoneit, 1993; Logan *et al.*, 2001; Simoneit *et al.*, 2004; McCollom & Seewald, 2007; Konn *et al.*, 2009; Holman *et al.*, 2014b; Reeves *et al.*, 2014). For instance, massive sulfide deposits from the Mid-Atlantic ridge, as well as sediments and chimneys of the arctic Loki's castle hydrothermal vent, were shown to contain bacterial fatty acids and archaeal isoprenoid lipids (Blumenberg *et al.*, 2007, 2012; Jaeschke *et al.*, 2014). Organic matter and source-diagnostic hydrocarbons were also reported from ancient hydrothermal sulfide ores (Mycke *et al.*, 1988; Logan *et al.*, 2001; Blumenberg *et al.*, 2007, 2012; Greenwood *et al.*, 2013). Genuine molecular records from the very ancient Earth are scarce. However, several early Archean hydrothermal deposits contain indigenous organic compounds that are demonstrably syngenetic to the host

rock and, in some cases, assuredly of biological origin (Marshall *et al.*, 2007; Duda *et al.*, 2018; Mißbach *et al.*, 2021). These studies demonstrate that molecular information on microbial life can be preserved under hydrothermal conditions.

Organic matter in hydrothermal systems may also derive from abiotic processes, such as FTT synthesis linked to serpentinization (McCollom *et al.*, 1999; Holm & Charlou, 2001; Rushdi & Simoneit, 2001; McCollom & Seewald, 2007; Delacour *et al.*, 2008; Proskurowski *et al.*, 2008; McCollom, 2013; Konn *et al.*, 2015; Milesi *et al.*, 2016; Mißbach *et al.*, 2018; Ménez *et al.*, 2018; Sforna *et al.*, 2018). However, the involved processes are complex, and the abiotic synthesis of organic matter is by no means an inevitable consequence of serpentinization. Furthermore, it has not been demonstrated that FTT-derived compounds would evolve into kerogens (Mißbach *et al.*, 2018), a crucial prerequisite for preserving over geological time scales. These fundamental uncertainties may result from the facts that FTT products show no distinct characteristics that would allow their discrimination from biotic compounds (McCollom & Seewald, 2006; Mißbach *et al.*, 2018) and that the presence of potential abiotic organics in Earth's history could have been masked by organic matter from biological sources. Hence, the quantitative significance of organic matter deriving from FTT synthesis under hydrothermal conditions remains unknown for any time in Earth's history.

Hydrothermal deposits may also contain secondary carbonaceous matter formed during metamorphic reactions (i.e., temperatures >200 °C; Fig. 1.3), such as the thermal decomposition of siderite [$FeCO_3$] (Lepland *et al.*, 2002; van Zuilen *et al.*, 2002, 2003; McCollom, 2003; Köhler *et al.*, 2013; Posth *et al.*, 2013; Milesi *et al.*, 2015; Halama *et al.*, 2016). Notably, such secondary abiotic graphite can exhibit $\delta^{13}C$ signatures consistent with a biogenic origin (e.g., -30‰: van Zuilen *et al.*, 2002). Graphite may also precipitate from reactions of abiotic CO_2 and CH_4 dissolved in hydrothermal fluids (Rumble & Hoering, 1986; Ortega *et al.*, 2010; Luque *et al.*, 2012). Thus, graphite in ancient metamorphic rocks may originate from the mixing of fluids containing carbon from either abiotic or biogenic sources and may be emplaced both syngenetically or from exogenous sources during younger metamorphic events

(Heijlen *et al.*, 2006; Papineau *et al.*, 2010a, 2010b, 2011; Lepland *et al.*, 2011). These potential sources of carbonaceous further complicate the identification of primarily biogenic materials in the rock record.

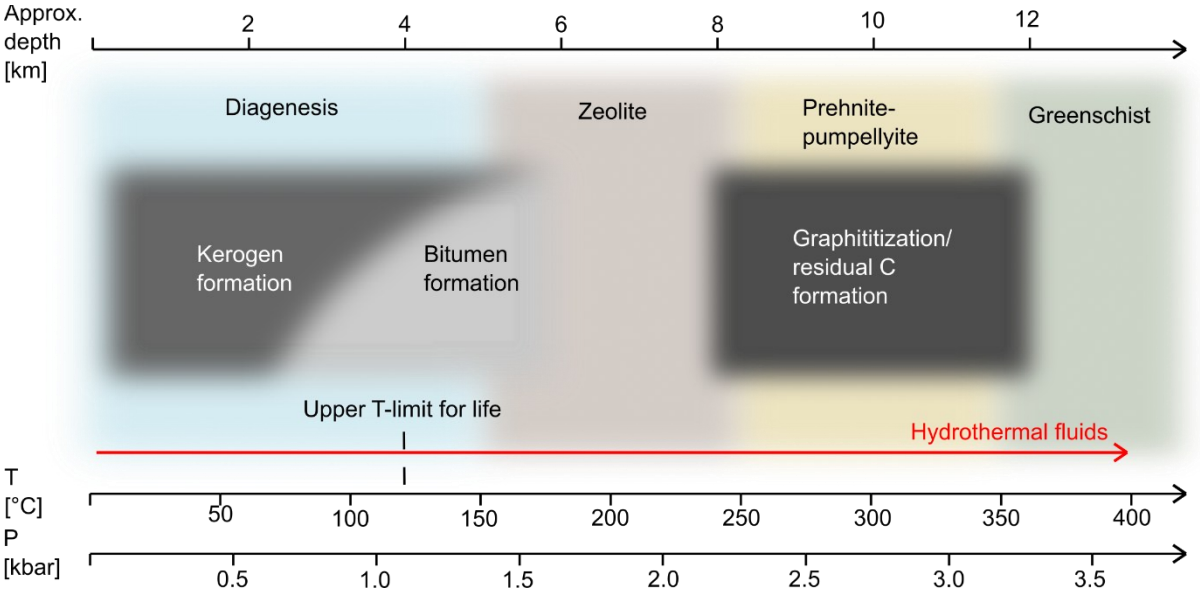

Figure 1.3: Temperature and pressure conditions relevant to the preservation of biosignatures in hydrothermal deposits. The increase in temperature (30°C/km) and pressure (0.27 kbar/km) as a function of depth are given for continental crust since the geothermal gradient is highly variable in the oceanic crust (ca. 40-80°C/km). Note that the heat flow can drastically increase in proximity to hydrothermal vents at oceanic spreading centers (red arrow). Boundaries between metamorphic facies are not sharp, and the relationship between temperature and pressure conditions during metamorphism varies strongly between different plate tectonic settings. Note that diagenetic processes commence at temperatures lower than the upper limit of microbial life and can thus affect, and be affected by, living microbial communities.

1.4.4 (Bio)geochemical signatures

Trace elements

Trace elements partitioning from fluids into minerals is a function of their abundance in the fluid and their compatibility in the mineral. Together, this can be mathematically expressed as the partition coefficient (K)*. Microorganisms can affect K when mineral formation occurs in equilibrium with their cytoplasm (intracellularly), as is the case for many trace elements in magnetite produced by MTB (e.g., Ni, Zn, Cu, Pb: Amor *et al.*, 2015). Also, mediation of mineral formation by organic templates (e.g., cell wall surface, EPS; extracellularly) can affect K in magnetite formed by dissimilatory Fe-reducing bacteria (e.g., Ni, Zn in magnetite: Han *et al.*, 2021), or in sulfide minerals in microbial mats (e.g., As, Zn, Pb, Ni: Labrenz

et al., 2000; Huerta-Diaz *et al.*, 2012; Valdivieso-Ojeda *et al.*, 2014). This suggests that trace element signatures in minerals could be used as fingerprints of microbial activity.

Metals and metalloids also form the active centers of many essential enzymes (e.g., Ni, Mo, Zn: Fraústo da Silva & Williams, 2001), resulting in the enrichment of these elements in organic matter in sediments and rocks (Liermann *et al.*, 2007; Cameron *et al.*, 2012; Reitner *et al.*, 2015; Hickman-Lewis *et al.*, 2020; Cavalazzi *et al.*, 2021). Moreover, the affinity of many trace elements to organic matter can result in their enrichment in living and dead biomass during diagenesis (Huerta-Diaz *et al.*, 2012; Petrash *et al.*, 2016; Sforna *et al.*, 2016). These processes are by no means restricted to "normal" sedimentary environments and may also occur in hydrothermal environments. Indeed, sulfidic stromatolites from the ca. 3.48 Ga Dresser Formation (Pilbara, Western Australia) with enrichments of transition metals and metalloids in early diagenetic pyrite were interpreted to reflect their binding to organic matter (Baumgartner *et al.*, 2020b).

Nevertheless, using trace elements as biosignatures is highly challenging. This is because K is also influenced by other parameters that are usually not well-constrained for paleoenvironments (e.g., mineral precipitation rates and temperature). Also, trace element concentrations in seawater have changed through geological time (Saito *et al.*, 2003; Williams & Fraústo Da Silva, 2003) and are unknown for local paleoenvironments. These problems are amplified in hydrothermal systems, where element concentrations show steep spatial gradients and strong temporal variations (Von Damm, 1995; Kelley *et al.*, 2002). The high capacity of sulfide minerals to abiotically sequester a broad range of metal(loid)s may result in enrichments of trace elements that are commonly associated with biological influence (e.g., Ni) (Raiswell & Plant, 1980; Dellwig *et al.*, 2002; Berner *et al.*, 2013; Gregory *et al.*, 2015; Reitner *et al.*, 2015). Also, trace metals may bind to organic matter of abiotic origin, which may originate from FTT synthesis in specific hydrothermal systems (McCollom *et al.*, 1999; Holm & Charlou, 2001; Rushdi & Simoneit, 2001; McCollom & Seewald, 2007; Proskurowski *et al.*, 2008; McCollom,

2013; Konn *et al.*, 2015; Mißbach *et al.*, 2018; Ménez *et al.*, 2018; Sforna *et al.*, 2018). Finally, mineral-fluid exchange during diagenesis or metamorphism might cause secondary modification of primary trace element signatures (Monecke *et al.*, 2002; Houghton *et al.*, 2004; Petrash *et al.*, 2016; Schad *et al.*, 2021). Future research must address these issues by improving paleoenvironmental proxies and conducting experimental studies to understand the long-term preservation of biogenic trace element fingerprints in minerals under hydrothermal conditions.

Stable isotopes

Metabolic processes are commonly associated with mass-dependent stable isotope fractionation*, leading to different isotope ratios in the products compared to the reactants (Hoefs, 2021). For instance, photo- and chemoautotrophic organisms prefer the lighter over the heavier stable C isotope (^{12}C and ^{13}C, respectively) for carbon fixation. Consequently, biological organic matter is isotopically depleted relative to the inorganic carbon pool, as expressed in negative $\delta^{13}C_{Org}$ values (Hayes, 2001; Schidlowski, 2001; Eigenbrode & Freeman, 2006; Hoefs, 2021). Since heterotrophic organisms usually conserve the isotopic composition of their substrates with only minor variations, modern and ancient biological organic matter typically exhibits $\delta^{13}C$ signatures between ca. -20 and -30‰. Thus, ^{13}C-depleted carbonaceous matter preserved in rocks and minerals may be a valuable fingerprint of life.

Organic compounds in fluids and sediments from modern deep-sea hydrothermal vent sites typically exhibit negative $\delta^{13}C_{Org}$ signatures (ca. -20 to -50‰: Blumenberg *et al.*, 2007; Konn *et al.*, 2009; Jaeschke *et al.*, 2014). However, $\delta^{13}C_{Org}$ values consistent with photo- or chemoautotrophic C fixation do not provide stand-alone evidence for microbial carbon cycling. Similar $\delta^{13}C_{Org}$ values have been reported for abiotic bulk organic matter and organic compounds in carbonaceous meteorites (down to -21.0 and -38.7‰, respectively: Sephton & Gilmour, 2001; Sephton *et al.*, 2003). Significantly, abiotic synthesis of CH_4 and other organic compounds under hydrothermal conditions (e.g., via FTT reactions) can fractionate C isotopes by a magnitude similar to biological fractionation (down to -60‰ in CH_4 and -36‰ in

higher molecular weight compounds: Horita & Berndt, 1999; McCollom & Seewald, 2006). However, compounds from these experiments also yielded highly variable offsets between $\delta^{13}C_{org}$ and $\delta^{13}C_{inorg}$ (30 to -36 ‰: McCollom & Seewald, 2006). Therefore, a consistent offset between $\delta^{13}C_{org}$ and $\delta^{13}C_{inorg}$ of at least 20 to 30‰ across different facies within one system might serve as a biosignature in hydrothermal deposits (cf. Schidlowski 2001).

Another stable isotope system that is relevant for hydrothermal sulfide deposits is sulfur. In non-hydrothermal environments, stable sulfur isotopes (^{32}S, ^{33}S, ^{34}S, ^{36}S) are mainly fractionated during microbial sulfur cycling (Strauss, 1997; Jørgensen *et al.*, 2019; Hoefs, 2021). Substantial kinetic fractionations occur during dissimilatory sulfate reduction and disproportionation of elemental sulfur (Canfield & Thamdrup, 1994; Habicht & Canfield, 1997; Böttcher *et al.*, 2001; Sim *et al.*, 2011). The most commonly analyzed sulfur isotopic ratio is $^{34}S/^{32}S$ because the $^{34}S/^{32}S$ of sulfide species can be fractionated during microbial sulfur cycling by more than -70‰ (Jørgensen *et al.*, 2019). In contrast, the $\delta^{34}S$ signature of volcanogenic H_2S typically ranges from -2 to 2‰ (Ohmoto, 1996; Hoefs, 2021). However, multiple abiotic processes in hydrothermal systems may also substantially fractionate S isotopes. For instance, experiments on thermochemical sulfate reduction at 100 °C yielded $\delta^{34}S$ fractionation ranges of up to ca. 20‰ (Kiyosu & Krouse, 1990; Machel *et al.*, 1995). Similar fractionation factors occur during isotopic exchange between aqueous sulfate and sulfide (Ohmoto & Lasaga, 1982; Ono, 2008). Therefore, only fractionation ranges exceeding ca. 20‰ can be considered robust signals of microbial sulfur cycling in hydrothermal sulfide systems (e.g., -48.0 to 23.1‰: Slack *et al.*, 2019; see also Eldridge *et al.*, 1993; Taylor, 2004; Lode *et al.*, 2017; Present *et al.*, 2017; Velasco-Acebes *et al.*, 2019; Nozaki *et al.*, 2020).

Compared to Phanerozoic hydrothermal sulfide deposits, the range of $\delta^{34}S$ values in Archean records seems to be diminished (-3 to 3‰: Huston *et al.*, 2001; Golding *et al.*, 2011; Wacey *et al.*, 2014). This may point to a purely abiotic sulfide source or microbial sulfur cycling at low sulfate concentrations, as expected for Archean environments (Shen *et al.*, 2001). Indeed, the combined analysis of $\delta^{34}S$, $\Delta^{33}S^*$, and

$\Delta^{36}S$ (i.e., quadruple sulfur isotopes) on Paleoarchean pyrites and barites suggests that microbial sulfur cycling was established as early as ca. 3.5 Ga (Shen *et al.*, 2001, 2009; Philippot *et al.*, 2007; Ueno *et al.*, 2008; Wacey *et al.*, 2011; Baumgartner *et al.*, 2020a; but see Watanabe *et al.*, 2009; Liu *et al.*, 2021). Therefore, applying quadruple sulfur isotopes provides a powerful tool to elucidate microbial sulfur cycling in ancient hydrothermal systems, where traditional approaches can prove challenging.

Fe is widespread in hydrothermal sulfide environments; hence, stable Fe isotopes (^{54}Fe, ^{56}Fe) potentially provide further evidence for geobiological processes in such settings. Fe isotopes are fractionated during partial oxidation and reduction of Fe, producing isotopically enriched Fe(III) minerals ($\delta^{56}Fe>0$) and depleted Fe^{2+}_{aq} ($\delta^{56}Fe<0$) (Johnson *et al.*, 2020). Substantial $\delta^{56}Fe$ variation in natural Fe sulfide minerals (-4 to +4‰) may indicate intense redox cycling and potentially additional stable Fe isotope fractionation linked to pyrite precipitation (e.g., Mansor & Fantle, 2019; Decraene *et al.*, 2021). Microorganisms commonly control redox cycling in the environment and might also influence the degree of this fractionation. For instance, Fe oxidation experiments with anoxygenic phototrophs (Croal *et al.*, 2004), nitrate-reducing Fe(II)-oxidizing bacteria (Kappler *et al.*, 2010), and cyanobacteria (Swanner *et al.*, 2017) revealed that the produced Fe oxides are enriched in ^{56}Fe by 1.5 to 3‰ relative to Fe^{2+}_{aq}. Also, the dissimilatory reduction of Fe(III) minerals releases Fe^{2+}_{aq} depleted in ^{56}Fe by up to ~3‰ (Beard *et al.*, 1999; Crosby *et al.*, 2005; Fortney *et al.*, 2016; Chanda *et al.*, 2021). However, these ranges are similar to those reached by abiotic redox cycling (Toner *et al.*, 2016; Johnson *et al.*, 2020), equilibrium precipitation of Fe minerals in hydrothermal environments (Rouxel *et al.*, 2004, 2018), and isotopic exchange reactions between fluids and pyrite at high temperatures (300-450°C: Pokrovski *et al.*, 2021). Experimental work demonstrates that biogenic magnetite formation by MTB is associated with a mass-independent fractionation* of Fe-isotopes ($\Delta^{57}Fe=0.23$: Amor *et al.*, 2016). However, magnetofossils in the environment do not seem to preserve this isotopic fingerprint (Havas *et al.*, 2021). For these reasons, microbial Fe cycling can currently not be tracked in the geological record based on Fe isotope signatures alone.

1.5 THE PRECAMBRIAN RECORD

While there are many Precambrian VMS and SEDEX deposits, only three localities have been investigated for potential biosignatures in detail: the ca. 3.2 Ga Sulphur Springs Group (Pilbara, Western Australia), the ca. 1.64 Ga Here's Your Chance (H.Y.C.) deposit in Northern Australia, and the ca. 1.43 Ga Gaobanhe massive sulfide deposit in Northern China (Fig. 1.4).

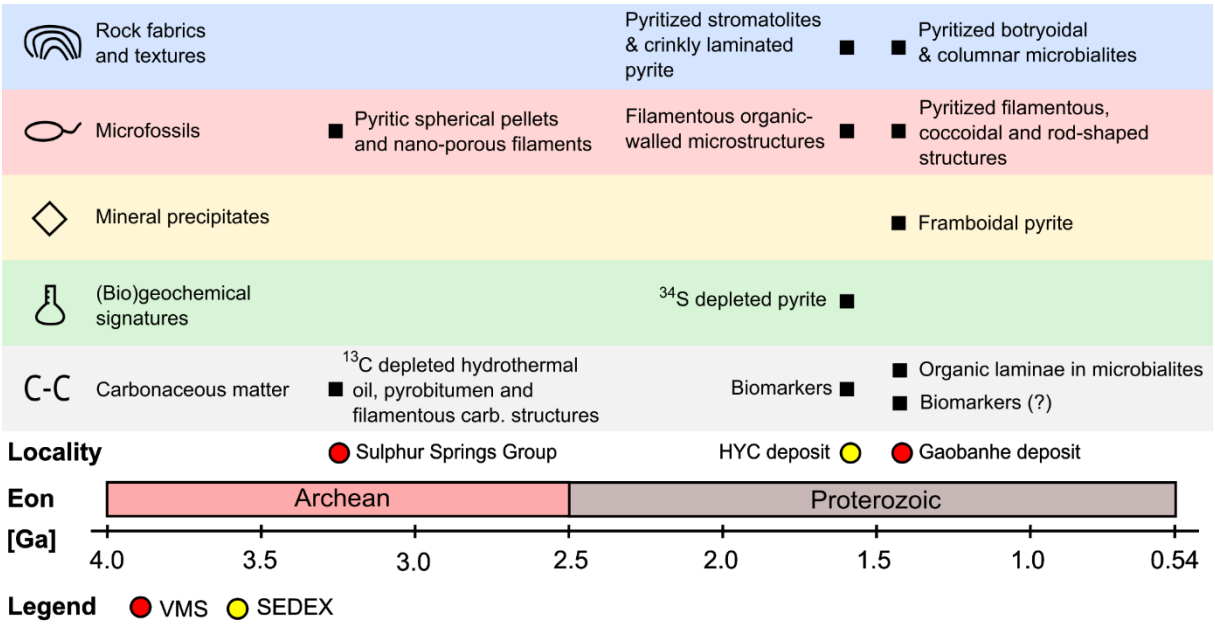

Figure 1.4: Reported microbial biosignatures in Precambrian VMS and SEDEX deposits through geologic time. See the main text for references.

1.5.1 Sulphur Springs Group

The ca. 3.2 Ga Sulphur Springs Group (Pilbara, Western Australia) contains the Earth's oldest recognized VMS deposits and formed in a setting comparable to modern-day volcanic back-arc basins in a water depth of ca. 1000 m (Vearncombe *et al.*, 1995; Brauhart *et al.*, 1998; Huston *et al.*, 2019). Based on its geological setting, mineralogy, and locally occurring mineral textures (dendritic, botryoidal, and colloform sulfide), the upper part of the Sulphur Springs deposit has been interpreted as analog to modern black smoker systems (Vearncombe *et al.*, 1995). The ore mineralization consists mainly of pyrite, sphalerite, chalcopyrite, and galena (Brauhart *et al.*, 1998; Huston *et al.*, 2019), which is consistent with recent hydrothermal sulfide systems and modern VMS deposits (Hannington, 2014).

Notably, primary mineral phases and textures have not been obscured by metamorphism (low-grade prehnite-pumpellyite facies*) (Vearncombe *et al.*, 1995) (Fig. 1.3).

Spherical sulfide minerals in the Sulphur Springs Group were tentatively interpreted as mineralized bacteria (Vearncombe *et al.*, 1995). Notably, colloform chert in the Sulphur Springs deposit contains pyritic filaments interpreted as microfossils of thermophilic, S-cycling prokaryotes living in the subseafloor of a hydrothermal system (Rasmussen, 2000). Their occurrence in paragenetically early chert suggests that the filaments predate the main phase of VMS mineralization and are more likely associated with low-temperature hydrothermal activity (<110°C), consistent with the presence of microbial life (Rasmussen, 2000). These pyrite filaments exhibit a nano-porous texture and are associated with nitrogen-enriched organic matter, which is consistent with a biological origin, but could also be explained by abiotic crystal growth and the localized adsorption of organic matter (Wacey *et al.*, 2014). Hydrothermally-generated oil encapsulated in fluid inclusions and pyrobitumen associated with sulfide minerals in the Sulphur Springs deposits display $\delta^{13}C_{org}$ values between -29.1 and -36.9 ‰, in line with a biological origin (Rasmussen & Buick, 2000). Notably, filamentous ^{13}C-depleted carbonaceous structures ($\delta^{13}C_{org}$ = -26.8 to -34.0 ‰) resembling microbial remains have also been observed in black shales directly overlying the VMS deposit (Duck *et al.*, 2007). In summary, the Sulphur Springs deposit represents a prime target in the search for biosignatures of early life in deep-sea hydrothermal environments. However, the biological origin of the reported filamentous microfossils remains to be further scrutinized.

1.5.2 McArthur (Here's Your Chance; HYC) deposit

The HYC deposit (Northern Territory, Australia) is an unmetamorphosed SEDEX Pb-Zn deposit that occurs within the ca. 1.64 Ga Barney Creek Formation (Page & Sweet, 1998; Logan *et al.*, 2001). The depositional environment of Barney Creek Formation was variably interpreted as a restricted deep marine setting (Bull, 1998; Jackson *et al.*, 2000) or a saline lacustrine system (Crick, 1992; French *et al.*, 2020). Ore

mineralization in the deposit consists of pyrite, sphalerite, and galena precipitated from an oxidized hydrothermal brine rich in sulfate (Logan, 1979; Large *et al.*, 1998).

Black chert in the HYC deposit contains µm-scale filamentous and spheroidal structures interpreted as microfossils (Oehler & Logan, 1977). Moreover, microdigitate and columnar stromatolites with pyritic and siliceous mineralogy, as well as crinkly laminae composed of pyrite, were reported from the deposit (McGoldrick, 1999). The $\delta^{34}S$ signatures of -13 to +15‰ in early diagenetic sulfides suggest that microbial sulfur metabolism was involved in mineral formation (Eldridge *et al.*, 1993). Organic matter in the HYC deposit has experienced significant hydrothermal alteration but still encodes information of ore genetic and geobiological significance (Logan *et al.*, 2001; Chen *et al.*, 2003; Williford *et al.*, 2011; Greenwood *et al.*, 2013; Holman *et al.*, 2014a, 2014b). Preserved organic biosignatures include $\delta^{13}C_{Org}$ characteristics and biomarkers, amongst others indicating the presence of sulfate-reducing and sulfide-oxidizing bacteria in the environment (Logan *et al.*, 2001; Holman *et al.*, 2014b). In summary, the HYC deposit provides rare clues on microbial sulfur cycling in Precambrian hydrothermal sulfide systems.

1.5.3 Gaobanhe massive sulfide deposit

The ca. 1.43 Ga Gaobanhe massive sulfide deposit (North China) is a SEDEX deposit formed in a submerged graben* system on the North China Craton* (Kusky & Li, 2003; Li & Kusky, 2007). Hydrothermal fluid exhalation caused synsedimentary ore mineralization with an upward zonation from pyrite at the bottom to Zn-Pb-sulfide at the top (Kusky & Li, 2003). Rhenium-osmium isotope data and trace-element patterns in the Gaobanhe sulfide phases suggest local hydrothermal overprint during the Mesozoic break-up of the North China Craton (Gao *et al.*, 2020). Nevertheless, the massive sulfide deposits contain the oldest reported morphologically preserved black smoker chimneys reported to date, offering an opportunity to study the association of ancient microbial life with these structures (Li & Kusky, 2007).

The chimney structures contain dome-shaped build-ups of concentric botryoidal and columnar sulfides interlayered with organic matter that are interpreted as

microbialites (Li & Kusky, 2007). Putative pyritic microfossils within the sulfide chimneys include filamentous, coccoidal, and rod-shaped structures locally associated with framboidal pyrite (Li & Kusky, 2007). Perhaps the deposit also preserves biomarkers (Xia *et al.*, 2008), but the provided information does not allow for adequately assessing the quality and validity of the data. Nonetheless, the Gaobanhe deposit is a promising target for studying microbial biosignatures but needs further investigation in greater detail.

1.6 Concluding remarks

Deep-sea hydrothermal sulfide systems might have been crucial for the emergence of life, making ancient deposits from such settings highly relevant to deep-time geobiology and astrobiology. However, reconstructing life in ancient hydrothermal environments is still challenging. Perhaps the most critical problems are (i) the limited number of well-preserved records, (ii) the insufficient understanding of the formation and preservation of geologically stable microbial biosignatures in hydrothermal environments as well as (iii) the large number of hydrothermal processes that may produce pseudo-biosignatures. Candidate microbial biosignatures that can remain stable over geological time scales include rock fabrics and mineral textures (e.g., microbialites, framboidal pyrite), microfossils, biogenic mineral precipitates (e.g., magnetite, pyrite), as well as trace element, stable isotope (C, S, Fe) and biomarker signatures preserved in minerals and associated organic matter. So far, no stand-alone tool is available that unequivocally proves the presence of past microbial life in ancient rocks. Still, a comprehensive model combining mutually consistent biosignatures with a plausible geological scenario for their formation and preservation can result in high confidence for life detection.

Despite the general diversity of potential biosignatures, reported fingerprints of microbial life in Precambrian hydrothermal sulfides are scarce, and many of these findings are still controversially discussed. Of these examples, the HYC deposit currently provides the most comprehensive record because it contains a diverse set of morphologic, textural, and (bio)geochemical biosignatures. Detailed petrographic studies that involve analytical imaging techniques and geochemical approaches will

be essential for identifying features that may be indicative of past microbial life and hence might serve as biosignatures in the future. Equally important are continued experimental efforts to understand the formation and geological stability of (pseudo)biosignatures, allowing to build a more solid framework for the unambiguous identification of microbial fingerprints in ancient hydrothermal deposits. This, in turn, is vital to understanding the emergence of life on Earth and the search for life elsewhere in the universe.

1.7 GLOSSARY

Allochthonous: Rocks, sediment, mineral particles, or organic matter which did not form at the place of deposition but away from their current location.

Craton: Precambrian cores of modern continents; characterized by high crustal thickness and structural rigidity that prevented their subduction and enabled their long-term preservation.

δ-/ Δ-notation: Deviation of an isotopic ratio in a sample from a corresponding isotopic ratio in a reference material in ‰, e.g., for stable sulfur isotopes (Marin-Carbonne *et al.*, 2018):

$$\delta^{3i}S = \left(\frac{\left(\frac{^{3i}S}{^{32}S}\right)_{sample}}{\left(\frac{^{3i}S}{^{32}S}\right)_{standard}} - 1 \right) * 1000$$

$$\Delta^{33}S = \delta^{33}S - 1000 * \left(\left(1 - \frac{\delta^{34}S}{1000} \right) - 1 \right)$$

$$\Delta^{36}S = \delta^{36}S - 1000 * \left(\left(1 - \frac{\delta^{34}S}{1000} \right) - 1 \right)$$

For more information on stable isotope systematics and commonly used reference materials, readers are referred to Hoefs (2021).

Diagenesis: Transformation of sediments into sedimentary rocks through progressive lithification. Diagenetic processes commence immediately after the deposition of the primary sediments and proceed through burial. Diagenesis is poorly defined concerning temperatures, but 150°C is commonly taken as an upper limit.

Endogeneity: Occurring within the analyzed rock or mineral.

Fabric: Components, structural elements, and their geometry within a rock. Commonly used terms to describe fabrics of microbial sediments and microbialites include domal, columnar, layered, laminated, clotted, colloform, botryoidal, fenestral, microdigitate, and peloidal. For examples with images, readers are referred to Grey & Awramik (2020).

Facies (sedimentary): Characteristics of sediments and sedimentary rocks that can be linked to the original depositional environment. Not be confused with metamorphic facies (see below).

Graben: Linear depression of the Earth's continental crust caused by tectonic faulting due to crustal extension.

LUCA: Last Universal Common Ancestor; a hypothetical unicellular organism representing the phylogenetically youngest predecessor of all modern domains of life (bacteria, archaea, eukaryotes).

Mass-dependent (isotope) fractionation: Describes the relative change in the abundance of single isotopes of an element proportional to their mass. The degree of fractionation follows a linear function with a slope governed by the mass differences of the investigated isotope ratios (m_3-m_1 vs. m_2-m_1), as commonly demonstrated in a three-isotope plot (e.g., $^{56}Fe/^{54}Fe$ vs. $^{57}Fe/^{54}Fe$). The magnitude of fractionation increases with the relative mass difference between isotopes.

Mass-independent (isotope) fractionation: A deviation from the linear function of the mass-dependent fractionation that is expressed through the relative difference Δ from this line (e.g., $\Delta^{57}Fe$).

Metamorphism: Pressure- and/or heat-induced structural and mineralogical transformation of rocks. This transformation commonly includes the deformation of the precursor rock (protolith), coarsening of mineral crystals, and the formation of new minerals from the breakdown of existing, no longer stable minerals. Metamorphism does not include chemical changes to the protolith (i.e., it is 'isochemical').

Metamorphic facies: Characteristic assemblage of minerals formed during metamorphic alteration of a primary rock (protolith).

Metasomatism: Chemical alteration of a precursor rock (protolith) in exchange with hydrothermal fluids.

Partition coefficient: Ratio K of the concentration c of an element i in a mineral to the concentration of the same element in solution, normalized to a reference element, e.g., element i in magnetite, normalized to Fe (Amor *et al.*, 2015):

$$K^{i,Fe} = \frac{c^i_{Mag}/c^i_{Sol}}{c^{Fe}_{Mag}/c^{Fe}_{Sol}}$$

Permineralization: Non-destructive replacement of original materials by secondary minerals. Permineralization is typically related to fluids and can account for the detailed preservation of delicate primary features in fossils.

Serpentinization: Hydrothermal alteration of olivine and pyroxene minerals in rocks, yielding serpentine, magnetite, and brucite as well as highly alkaline fluids (pH 9-11) rich in H_2.

Syngenicity: Having formed at the same time as the host rock.

Synsedimentary: Having occurred during sediment deposition.

Taphonomy: The study of how organisms and biogenic materials are altered and/or preserved in the fossil record.

Texture: Morphological features of individual mineral particles within sediment or rock, such as particle size, shape, and organization.

Ultramafic: Rocks that primarily consist of Fe- and Mg-rich minerals (e.g., olivine, pyroxene). Important examples are peridotite (the rock that constitutes Earth's upper mantle) and komatiite (a volcanic rock that was a widespread constituent of the Archean crust).

1.8 REFERENCES

Addadi L, Weiner S (1985) Interactions between acidic proteins and crystals: stereochemical requirements in biomineralization. *Proceedings of the National Academy of Sciences* **82**, 4110–4114.

Akai J, Iida A, Akai K, Chiba A (1997) Mn and Fe minerals of possible biogenic origin from two Precambrian stromatolites in western Australia. *Journal of the Geological Society of Japan* **105**, 484–488.

Alleon J, Bernard S, Le Guillou C, Daval D, Skouri-Panet F, Pont S, Delbes L, Robert F (2016a) Early entombment within silica minimizes the molecular degradation of microorganisms during advanced diagenesis. *Chemical Geology* **437**, 98–108.

Alleon J, Bernard S, Le Guillou C, Marin-Carbonne J, Pont S, Beyssac O, McKeegan KD, Robert F (2016b) Molecular preservation of 1.88 Ga Gunflint organic microfossils as a function of temperature and mineralogy. *Nature Communications* **7**, 11977.

Allwood AC, Grotzinger JP, Knoll AH, Burch IW, Anderson MS, Coleman ML, Kanik I (2009) Controls on development and diversity of Early Archean stromatolites. *Proceedings of the National Academy of Sciences* **106**, 9548–9555.

Allwood AC, Rosing MT, Flannery DT, Hurowitz JA, Heirwegh CM (2018) Reassessing evidence of life in 3,700-million-year-old rocks of Greenland. *Nature* **563**, 241–244.

Amor M, Busigny V, Durand-Dubief M, Tharaud M, Ona-Nguema G, Gélabert A, Alphandéry E, Menguy N, Benedetti MF, Chebbi I, Guyot F (2015) Chemical signature of magnetotactic bacteria. *Proceedings of the National Academy of Sciences* **112**, 1699–1703.

Amor M, Busigny V, Louvat P, Gélabert A, Cartigny P, Durand-Dubief M, Ona-Nguema G, Alphandéry E, Chebbi I, Guyot F (2016) Mass-dependent and -independent signature of Fe isotopes in magnetotactic bacteria. *Science* **352**, 705–708.

Amor M, Mathon FP, Monteil CL, Busigny V, Lefevre CT (2020) Iron-biomineralizing organelle in magnetotactic bacteria: function, synthesis and preservation in ancient rock samples. *Environmental Microbiology* **22**, 3611–3632.

Andrews GF (1988) The selective adsorption of Thiobacilli to dislocation sites on pyrite surfaces. *Biotechnology and Bioengineering* **31**, 378–381.

Arp G, Reimer A, Reitner J (2001) Photosynthesis-Induced Biofilm Calcification and Calcium Concentrations in Phanerozoic Oceans. *Science* **292**, 1701–1704.

Arp G, Reimer A, Reitner J (2003) Microbialite Formation in Seawater of Increased Alkalinity, Satonda Crater Lake, Indonesia. *Journal of Sedimentary Research* **73**, 105–127.

Bai F, Chang L, Pei Z, Harrison RJ, Winklhofer M (2022) Magnetic Biosignatures of Magnetosomal Greigite From Micromagnetic Calculation. *Geophysical Research Letters* **49**, e2022GL098437.

Baumgartner RJ, Caruso S, Fiorentini ML, Van Kranendonk MJ, Martin L, Jeon H, Pagès A, Wacey D (2020a) Sulfidization of 3.48 billion-year-old stromatolites of the Dresser Formation, Pilbara Craton: Constraints from in-situ sulfur isotope analysis of pyrite. *Chemical Geology* **538**, 119488.

Baumgartner RJ, Hu S, Van Kranendonk MJ, Verrall M (2022) Taphonomy of microorganisms and microbial microtextures at sulfidic hydrothermal vents: A case study from the Roman Ruins black smokers, Eastern Manus Basin. *Geobiology* **20**, 479–497.

Baumgartner RJ, Van Kranendonk MJ, Pagès A, Fiorentini ML, Wacey D, Ryan C (2020b) Accumulation of transition metals and metalloids in sulfidized stromatolites of the 3.48 billion–year–old Dresser Formation, Pilbara Craton. *Precambrian Research* **337**, 105534.

Baumgartner RJ, Van Kranendonk MJ, Wacey D, Fiorentini ML, Saunders M, Caruso S, Pages A, Homann M, Guagliardo P (2019) Nano–porous pyrite and organic matter in 3.5-billion-year-old stromatolites record primordial life. *Geology* **47**, 1039–1043.

Beard BL, Johnson CM, Cox L, Sun H, Nealson KH, Aguilar C (1999) Iron Isotope Biosignatures. *Science* **285**, 1889–1892.

Bell EA, Boehnke P, Harrison TM, Mao WL (2015) Potentially biogenic carbon preserved in a 4.1 billion-year-old zircon. *Proceedings of the National Academy of Sciences* **112**, 14518–14521.

Bell MS (2007) Experimental shock decomposition of siderite and the origin of magnetite in Martian meteorite ALH 84001. *Meteoritics & Planetary Science* **42**, 935–949.

Bendt G, Saddeler S, Schulz S (2019) Sulfidation of Magnetite Nanoparticles – Following the Polysulfide Pathway. *European Journal of Inorganic Chemistry* 602–608.

Benzerara K, Bolzoni R, Monteil C, Beyssac O, Forni O, Alonso B, Asta MP, Lefevre C (2020) The gammaproteobacterium Achromatium forms intracellular amorphous calcium carbonate and not (crystalline) calcite. *Geobiology* **19**, 199–213.

Bernard S, Papineau D (2014) Graphitic Carbons and Biosignatures. *Elements* **10**, 435–440.

Berner RA (1970) Sedimentary pyrite formation. *American Journal of Science* **268**, 1–23.

Berner RA (1984) Sedimentary pyrite formation: An update. *Geochimica et Cosmochimica Acta* **48**, 605–615.

Berner ZA, Puchelt H, Nöltner T, Kramar U (2013) Pyrite geochemistry in the Toarcian Posidonia Shale of south-west Germany: Evidence for contrasting trace-element patterns of diagenetic and syngenetic pyrites: *Pyrite element geochemistry*. *Sedimentology* **60**, 548–573.

Beveridge TJ (1989) Role of Cellular Design in Bacterial Metal Accumulation and Mineralization. *Annual Review of Microbiology* **43**, 147–171.

Black M (1933) The algal sedimentation of Andros Island Bahamas. *Philosophical Transactions of the Royal Society B: Biological Sciences* **222**, 165–192.

Blumenberg M, Seifert R, Buschmann B, Kiel S, Thiel V (2012) Biomarkers Reveal Diverse Microbial Communities in Black Smoker Sulfides from Turtle Pits (Mid-Atlantic Ridge, Recent) and Yaman Kasy (Russia, Silurian). *Geomicrobiology Journal* **29**, 66–75.

Blumenberg M, Seifert R, Petersen S, Michaelis W (2007) Biosignatures present in a hydrothermal massive sulfide from the Mid-Atlantic Ridge. *Geobiology* **5**, 435–450.

Böttcher ME, Thamdrup B, Vennemann TW (2001) Oxygen and sulfur isotope fractionation during anaerobic bacterial disproportionation of elemental sulfur. *Geochimica et Cosmochimica Acta* **65**, 1601–1609.

Brasier M, Green O, Lindsay J, Mcloughlin N, Steele A, Stoakes C (2005) Critical testing of Earth's oldest putative fossil assemblage from the ~3.5Ga Apex chert, Chinaman Creek, Western Australia. *Precambrian Research* **140**, 55–102.

Brasier M, McLoughlin N, Green O, Wacey D (2006) A fresh look at the fossil evidence for early Archaean cellular life. *Philosophical Transactions of the Royal Society B: Biological Sciences* **361**, 887–902.

Brasier MD, Green OR, Jephcoat AP, Kleppe AK, Van Kranendonk MJ, Lindsay JF, Steele A, Grassineau NV (2002) Questioning the evidence for Earth's oldest fossils. *Nature* **416**, 76–81.

Brauhart CW, Groves DI, Morant P (1998) Regional alteration systems associated with volcanogenic massive sulfide mineralization at Panorama, Pilbara, Western Australia. *Economic Geology* **93**, 292–302.

Brearley AJ (2003) Magnetite in ALH 84001: An origin by shock-induced thermal decomposition of iron carbonate. *Meteoritics & Planetary Science* **38**, 849–870.

Breier JA, Toner BM, Fakra SC, Marcus MA, White SN, Thurnherr AM, German CR (2012) Sulfur, sulfides, oxides and organic matter aggregated in submarine hydrothermal plumes at 9°50'N East Pacific Rise. *Geochimica et Cosmochimica Acta* **88**, 216–236.

Buick R (1990) Microfossil Recognition in Archean Rocks: An Appraisal of Spheroids and Filaments from a 3500 M.Y. Old Chert-Barite Unit at North Pole, Western Australia. *PALAIOS* **5**, 441–459.

Buick R, Dunlop JSR, Groves DI (1981) Stromatolite recognition in ancient rocks: an appraisal of irregularly laminated structures in an Early Archaean chert-barite unit from North Pole, Western Australia. *Alcheringa: An Australasian Journal of Palaeontology* **5**, 161–181.

Bull SW (1998) Sedimentology of the Palaeoproterozoic Barney Creek formation in DDH BMR McArthur 2, southern McArthur basin, northern territory. *Australian Journal of Earth Sciences* **45**, 21–31.

Burne RV, Moore LS (1987) Microbialites: organosedimentary deposits of benthic microbial communities. *PALAIOS* **2**, 241–254.

Cameron V, House CH, Brantley SL (2012) A First Analysis of Metallome Biosignatures of Hyperthermophilic Archaea. *Archaea* **2012**, 1–12.

Campbell KA (2006) Hydrocarbon seep and hydrothermal vent paleoenvironments and paleontology: Past developments and future research directions. *Palaeogeography, Palaeoclimatology, Palaeoecology* **232**, 362–407.

Canfield DE, Berner RA (1987) Dissolution and pyritization of magnetite in anoxic marine sediments. *Geochimica et Cosmochimica Acta* **51**, 645–659.

Canfield DE, Thamdrup B (1994) The Production of ^{34}S-Depleted Sulfide During Bacterial Disproportionation of Elemental Sulfur. *Science* **266**, 1973–1975.

Cavalazzi B, Lemelle L, Simionovici A, Cady SL, Russell MJ, Bailo E, Canteri R, Enrico E, Manceau A, Maris A, Salomé M, Thomassot E, Bouden N, Tucoulou R, Hofmann A (2021) Cellular remains in a ~3.42-billion-year-old subseafloor hydrothermal environment. *Science Advances* **7**, eabf3963.

Chanda P, Amenabar MJ, Boyd ES, Beard BL, Johnson CM (2021) Stable Fe isotope fractionation during dissimilatory Fe(III) reduction by a thermoacidophile in acidic hydrothermal environments. *Geochimica et Cosmochimica Acta* **292**, 427–451.

Chang SBR, Kirschvink JL (1989) Magnetofossils, the Magnetization of Sediments, and the Evolution of Magnetite Biomineralization. *Annual Review of Earth and Planetary Sciences* **17**, 169–195.

Chang S-BR, Stolz JF, Kirschvink JL (1989) Biogenic Magnetite in Stromatolites. II. Occurrence in Ancient Sedimentary Environments. *Precambrian Research* **43**, 305–315.

Chaudhuri SK, Lack JG, Coates JD (2001) Biogenic Magnetite Formation through Anaerobic Biooxidation of Fe(II). *Applied and Environmental Microbiology* **67**, 2844–2848.

Chen J, Walter MR, Logan GA, Hinman MC, Summons RE (2003) The Paleoproterozoic McArthur River (HYC) Pb/Zn/Ag deposit of northern Australia: organic geochemistry and ore genesis. *Earth and Planetary Science Letters* **210**, 467–479.

Cosmidis J, Benzerara K (2022) Why do microbes make minerals? *Comptes Rendus. Géoscience* **354**, 1–39.

Cosmidis J, Nims CW, Diercks D, Templeton AS (2019) Formation and stabilization of elemental sulfur through organomineralization. *Geochimica et Cosmochimica Acta* **247**, 59–82.

Cosmidis J, Templeton AS (2016) Self-assembly of biomorphic carbon/sulfur microstructures in sulfidic environments. *Nature Communications* **7**, 12812.

Crick IH (1992) Petrological and maturation characteristics of organic matter from the Middle Proterozoic McArthur Basin, Australia. *Australian Journal of Earth Sciences* **39**, 501–519.

Criouet I, Viennet J-C, Jacquemot P, Jaber M, Bernard S (2021) Abiotic formation of organic biomorphs under diagenetic conditions. *Geochemical Perspectives Letters* **16**, 40–46.

Croal LR, Johnson CM, Beard BL, Newman DK (2004) Iron isotope fractionation by Fe(II)-oxidizing photoautotrophic bacteria. *Geochimica et Cosmochimica Acta* **68**, 1227–1242.

Cron B, Henri P, Chan CS, Macalady JL, Cosmidis J (2019) Elemental Sulfur Formation by Sulfuricurvum kujiense Is Mediated by Extracellular Organic Compounds. *Frontiers in Microbiology* **10**, 2710.

Crosby HA, Johnson CM, Roden EE, Beard BL (2005) Coupled Fe(II)−Fe(III) Electron and Atom Exchange as a Mechanism for Fe Isotope Fractionation during Dissimilatory Iron Oxide Reduction. *Environmental Science & Technology* **39**, 6698–6704.

Dahl C (2020) Bacterial Intracellular Sulphur Globules. In: *Bacterial Organelles and Organelle-like Inclusions*, Microbiology Monographs (ed. Jendrossek D). Springer International Publishing, Cham, pp. 19–51.

Deamer D, Damer B (2017) Can Life Begin on Enceladus? A Perspective from Hydrothermal Chemistry. *Astrobiology* **17**, 834–839.

Decraene M-N, Marin-Carbonne J, Thomazo C, Olivier N, Philippot P, Strauss H, Deloule E (2021) Intense biogeochemical iron cycling revealed in Neoarchean micropyrites from stromatolites. *Geochimica et Cosmochimica Acta* **312**, 299–320.

Delacour A, Früh-Green GL, Bernasconi SM, Schaeffer P, Kelley DS (2008) Carbon geochemistry of serpentinites in the Lost City Hydrothermal System (30°N, MAR). *Geochimica et Cosmochimica Acta* **72**, 3681–3702.

Delarue F, Robert F, Sugitani K, Tartèse R, Duhamel R, Derenne S (2017) Investigation of the Geochemical Preservation of ca. 3.0 Ga Permineralized and Encapsulated Microfossils by Nanoscale Secondary Ion Mass Spectrometry. *Astrobiology* **17**, 1192–1202.

Dellwig O, Böttcher ME, Lipinski M, Brumsack H-J (2002) Trace metals in Holocene coastal peats and their relation to pyrite formation (NW Germany). *Chemical Geology* **182**, 423–442.

Dodd MS, Papineau D, Grenne T, Slack JF, Rittner M, Pirajno F, O'Neil J, Little CTS (2017) Evidence for early life in Earth's oldest hydrothermal vent precipitates. *Nature* **543**, 60–64.

Donald R, Southam G (1999) Low temperature anaerobic bacterial diagenesis of ferrous monosulfide to pyrite. *Geochimica et Cosmochimica Acta* **63**, 2019–2023.

Duck LJ, Glikson M, Golding SD, Webb RE (2007) Microbial remains and other carbonaceous forms from the 3.24 Ga Sulphur Springs black smoker deposit, Western Australia. *Precambrian Research* **154**, 205–220.

Duda J-P, Thiel V, Bauersachs T, Mißbach H, Reinhardt M, Schäfer N, Van Kranendonk MJ, Reitner J (2018) Ideas and perspectives: hydrothermally driven redistribution and sequestration of early Archaean biomass – the "hydrothermal pump hypothesis." *Biogeosciences* **15**, 1535–1548.

Duda J-P, Van Kranendonk MJ, Thiel V, Ionescu D, Strauss H, Schäfer N, Reitner J (2016) A Rare Glimpse of Paleoarchean Life: Geobiology of an Exceptionally Preserved Microbial Mat Facies from the 3.4 Ga Strelley Pool Formation, Western Australia. *PLoS ONE* **11**, e0147629.

Dupraz C, Reid RP, Braissant O, Decho AW, Norman RS, Visscher PT (2009) Processes of carbonate precipitation in modern microbial mats. *Earth-Science Reviews* **96**, 141–162.

Durand B (1980) Sedimentary organic matter and kerogen. Definition and quantitative importance of kerogen. In: *Kerogen* (ed. Durand B). Éditions Technip, Paris, pp. 13–34.

Eglinton G, Scott PM, Belsky T, Burlingame AL, Calvin M (1964) Hydrocarbons of Biological Origin from a One-Billion-Year-Old Sediment. *Science* **145**, 263–264.

Ehrlich H, Bailey E, Wysokowski M, Jesionowski T (2021) Forced Biomineralization: A Review. *Biomimetics* **6**, 46.

Eigenbrode JL, Freeman KH (2006) Late Archean rise of aerobic microbial ecosystems. *Proceedings of the National Academy of Sciences* **103**, 15759–15764.

Eldridge CS, Williams N, Walshe JL (1993) Sulfur isotope variability in sediment-hosted massive sulfide deposits as determined using the ion microprobe SHRIMP; II, A study of the H.Y.C. Deposit at McArthur River, Northern Territory, Australia. *Economic Geology* **88**, 1–26.

Fallick AE, Ashton JH, Boyce AJ, Ellam RM, Russell MJ (2001) Bacteria were responsible for the magnitude of the world-class hydrothermal base metal sulfide orebody at Navan, Ireland. *Economic Geology* **96**, 885–890.

Farrimond P, Love GD, Bishop AN, Innes HE, Watson DF, Snape CE (2003) Evidence for the rapid incorporation of hopanoids into kerogen. *Geochimica et Cosmochimica Acta* **67**, 1383–1394.

Ferris FG, Fyfe WS, Beveridge TJ (1987) Bacteria as nucleation sites for authigenic minerals in a metal-contaminated lake sediment. *Chemical Geology* **63**, 225–232.

Flemming H-C, Wuertz S (2019) Bacteria and archaea on Earth and their abundance in biofilms. *Nature Reviews Microbiology* **17**, 247–260.

Foley N, Ayuso RA, Ii RRS (2001) Remnant Colloform Pyrite at the Haile Gold Deposit, South Carolina: A Textural Key to Genesis. *Economic Geology* **96**, 891–902.

Fortney NW, He S, Converse BJ, Beard BL, Johnson CM, Boyd ES, Roden EE (2016) Microbial Fe(III) oxide reduction potential in Chocolate Pots hot spring, Yellowstone National Park. *Geobiology* **14**, 255–275.

Fowler AD, L'Heureux I (1996) Self-Organized Banded Sphalerite and Branching Galena in the Pine Point Ore Deposit, Northwest Territories. *The Canadian Mineralogist* **34**, 1211–1222.

Fraústo da Silva JJR, Williams RJP (2001) *The biological chemistry of the elements - The inorganic chemistry of life*. Oxford University Press, Oxford.

French KL, Birdwell JE, Vanden Berg MD (2020) Biomarker similarities between the saline lacustrine Eocene Green River and the Paleoproterozoic Barney Creek Formations. *Geochimica et Cosmochimica Acta* **274**, 228–245.

Gao B, Zhang L, Jin X, Li W, Bai Y, Sakyi PA (2020) Re-Os geochronology and trace element characteristics of the hydrothermally reworked pyrite of the Gaobanhe sediment-hosted polymetal pyrite deposit in Northern China and its geological significance. *Journal of Geochemical Exploration* **215**, 106561.

Gao S, Huang F, Wang Y, Gao W (2016) A Review of Research Progress in the Genesis of Colloform Pyrite and Its Environmental Indications. *Acta Geologica Sinica - English Edition* **90**, 1353–1369.

García-Ruiz JM, Hyde ST, Carnerup AM, Christy AG, Van Kranendonk MJ, Welham NJ (2003) Self-Assembled Silica-Carbonate Structures and Detection of Ancient Microfossils. *Science* **302**, 1194–1197.

Georgieva MN, Little CTS, Bailey RJ, Ball AD, Glover AG (2018) Microbial-tubeworm associations in a 440 million year old hydrothermal vent community. *Proceedings of the Royal Society B: Biological Sciences* **285**, 20182004.

Georgieva MN, Little CTS, Maslennikov VV, Glover AG, Ayupova NR, Herrington RJ (2021) The history of life at hydrothermal vents. *Earth-Science Reviews* **217**, 103602.

Glikson M, Duck LJ, Golding SD, Hofmann A, Bolhar R, Webb R, Baiano JCF, Sly LI (2008) Microbial remains in some earliest Earth rocks: Comparison with a potential modern analogue. *Precambrian Research* **164**, 187–200.

Golding SD, Duck LJ, Young E, Baublys KA, Glikson M, Kamber BS (2011) Earliest Seafloor Hydrothermal Systems on Earth: Comparison with Modern Analogues. In: *Earliest Life on Earth: Habitats, Environments and Methods of Detection* (eds. Golding SD, Glikson M). Springer Netherlands, Dordrecht, pp. 15–49.

Golubic S, Friedmann I, Schneider J (1981) The Lithobiontic Ecological Niche, with Special Reference to Microorganisms. *Journal of Sedimentary Petrology* **31**, 475–478.

Golubic S, Hofmann HJ (1976) Comparison of Holocene and Mid-Precambrian Entophysalidaceae (Cyanophyta) in Stromatolitic Algal Mats: Cell Division and Degradation. *Journal of Paleontology* **50**, 1074–1082.

Gong J, Myers KD, Munoz-Saez C, Homann M, Rouillard J, Wirth R, Schreiber A, Zuilen MA van (2020) Formation and Preservation of Microbial Palisade Fabric in Silica Deposits from El Tatio, Chile. *Astrobiology* **20**, 500–524.

Greenwood PF, Brocks JJ, Grice K, Schwark L, Jaraula CMB, Dick JM, Evans KA (2013) Organic geochemistry and mineralogy. I. Characterisation of organic matter associated with metal deposits. *Ore Geology Reviews* **50**, 1–27.

Gregory DD, Large RR, Halpin JA, Baturina EL, Lyons TW, Wu S, Danyushevsky L, Sack PJ, Chappaz A, Maslennikov VV, Bull SW (2015) Trace Element Content of Sedimentary Pyrite in Black Shales. *Economic Geology* **110**, 1389–1410.

Grey K, Awramik S (2020) *Handbook for the study and description of microbialites*. Geological Survey of Western Australia Bulletin. Geological Survey of Western Australia, Perth.

Grey K, Sugitani K (2009) Palynology of Archean microfossils (c. 3.0Ga) from the Mount Grant area, Pilbara Craton, Western Australia: Further evidence of biogenicity. *Precambrian Research* **173**, 60–69.

Grosch EG, McLoughlin N (2014) Reassessing the biogenicity of Earth's oldest trace fossil with implications for biosignatures in the search for early life. *Proceedings of the National Academy of Sciences* **111**, 8380–8385.

Grotzinger JP, Rothman DH (1996) An abiotic model for stromatolite morphogenesis. *Nature* **383**, 423–425.

Habicht KS, Canfield DE (1997) Sulfur isotope fractionation during bacterial sulfate reduction in organic-rich sediments. *Geochimica et Cosmochimica Acta* **61**, 5351–5361.

Halama M, Swanner ED, Konhauser KO, Kappler A (2016) Evaluation of siderite and magnetite formation in BIFs by pressure–temperature experiments of Fe(III) minerals and microbial biomass. *Earth and Planetary Science Letters* **450**, 243–253.

Han X, Tomaszewski EJ, Schoenberg R, Konhauser KO, Amor M, Pan Y, Warter V, Kappler A, Byrne JM (2021) Using Zn and Ni behavior during magnetite precipitation in banded iron formations to determine its biological or abiotic origin. *Earth and Planetary Science Letters* **568**, 117052.

Hannington MD (2014) Volcanogenic Massive Sulfide Deposits. In: *Treatise on Geochemistry*. Elsevier, pp. 463–488.

Hannington MD, Galley AG, Herzig PM, Petersen S (1998) Comparison of the TAG mound and stockwork complex with cyprus-type massive sulfide deposits. In: *Proceedings of the Ocean Drilling Program, Scientific Results*, Proceedings of the Ocean Drilling Program (eds. Herzig PM, Humphris SE, Miller DJ, Zierenberg RA). Ocean Drilling Program.

Havas R, Savian JF, Busigny V (2021) Iron isotope signature of magnetofossils and oceanic biogeochemical changes through the Middle Eocene Climatic Optimum. *Geochimica et Cosmochimica Acta* **311**, 332–352.

Hayes JM (2001) Fractionation of the Isotopes of Carbon and Hydrogen in Biosynthetic Processes. In: *Stable isotope geochemistry*, Reviews in Mineralogy and Geochemistry (eds. Valley JW, Cole DR). pp. 225–277.

Hayes JM, Waldbauer JR (2006) The carbon cycle and associated redox processes through time. *Philosophical Transactions of the Royal Society B: Biological Sciences* **361**, 931–950.

Heijlen W, Appel PWU, Frezzotti M-L, Horsewell A, Touret JLR (2006) Metamorphic fluid flow in the northeastern part of the 3.8–3.7Ga Isua Greenstone Belt (SW Greenland): A re-evalution of fluid inclusion evidence for early Archean seafloor-hydrothermal systems. *Geochimica et Cosmochimica Acta* **70**, 3075–3095.

Hickman-Lewis K, Cavalazzi B, Sorieul S, Gautret P, Foucher F, Whitehouse MJ, Jeon H, Georgelin T, Cockell CS, Westall F (2020) Metallomics in deep time and the influence of ocean chemistry on the metabolic landscapes of Earth's earliest ecosystems. *Scientific Reports* **10**, 4965.

Hoefs J (2021) *Stable Isotope Geochemistry*. Springer Textbooks in Earth Sciences, Geography and Environment. Springer International Publishing, Cham.

Hofmann A (2011) Archaean Hydrothermal Systems in the Barberton Greenstone Belt and Their Significance as a Habitat for Early Life. In: *Earliest Life on Earth: Habitats, Environments and Methods of Detection* (eds. Golding SD, Glikson M). Springer Netherlands, Dordrecht, pp. 51–78.

Holm NG, Charlou JL (2001) Initial indications of abiotic formation of hydrocarbons in the Rainbow ultrama¢c hydrothermal system, Mid-Atlantic Ridge. *Earth and Planetary Science Letters* **191**, 8.

Holman AI, Greenwood PF, Brocks JJ, Grice K (2014a) Effects of sulfide minerals on aromatic maturity parameters: Laboratory investigation using micro-scale sealed vessel pyrolysis. *Organic Geochemistry* **76**, 270–277.

Holman AI, Grice K, Jaraula CMB, Schimmelmann A (2014b) Bitumen II from the Paleoproterozoic Here's Your Chance Pb/Zn/Ag deposit: Implications for the analysis of depositional environment and thermal maturity of hydrothermally-altered sediments. *Geochimica et Cosmochimica Acta* **139**, 98–109.

Horita J, Berndt ME (1999) Abiogenic Methane Formation and Isotopic Fractionation Under Hydrothermal Conditions. *Science* **285**, 1055–1057.

Hoshino Y, Flannery DT, Walter MR, George SC (2014) Hydrocarbons preserved in a ~2.7 Ga outcrop sample from the Fortescue Group, Pilbara Craton, Western Australia. *Geobiology* **13**, 99–111.

Houghton JL, Shanks WC, Seyfried WE (2004) Massive sulfide deposition and trace element remobilization in the Middle Valley sediment-hosted hydrothermal system, northern Juan de Fuca Rdge. *Geochimica et Cosmochimica Acta* **68**, 2863–2873.

Huber C, Wächtershäuser G (1997) Activated Acetic Acid by Carbon Fixation on (Fe,Ni)S Under Primordial Conditions. *Science* **276**, 245–247.

Huerta-Diaz MA, Delgadillo-Hinojosa F, Siqueiros-Valencia A, Valdivieso-Ojeda J, Reimer JJ, Segovia-Zavala JA (2012) Millimeter-scale resolution of trace metal distributions in microbial mats from a hypersaline environment in Baja California, Mexico. *Geobiology* **10**, 531–547.

Huston DL, Brauhart CW, Drieberg SL, Davidson GJ, Groves DI (2001) Metal leaching and inorganic sulfate reduction in volcanic-hosted massive sulfide mineral systems: Evidence from the paleo-Archean Panorama district, Western Australia. *Geology* **29**, 687.

Huston DL, Pirajno F, Morant P, Cummins B, Baker D, Mernagh TP (2019) Paleoarchean Mineral Deposits of the Pilbara Craton: Genesis, Tectonic Environment, and Comparisons With Younger Deposits. In: *Earth's Oldest Rocks*. Elsevier, pp. 519–551.

Ionescu D, Zoccarato L, Zaduryan A, Schorn S, Bizic M, Pinnow S, Cypionka H, Grossart H-P (2020) Heterozygous, Polyploid, Giant Bacterium, Achromatium, Possesses an Identical Functional Inventory Worldwide across Drastically Different Ecosystems. *Molecular Biology and Evolution* **38**, 1040–1059.

Ivarsson M, Drake H, Neubeck A, Snoeyenbos-West O, Belivanova V, Bengtson S (2021) Introducing palaeolithobiology. *GFF* **143**, 305–319.

Jackson MJ, Scott DL, Rawlings DJ (2000) Stratigraphic framework for the Leichhardt and Calvert Superbasins: Review and correlations of the pre- 1700 Ma successions between Mt Isa and McArthur River. *Australian Journal of Earth Sciences* **47**, 381–403.

Jaeschke A, Eickmann B, Lang SQ, Bernasconi SM, Strauss H, Früh-Green GL (2014) Biosignatures in chimney structures and sediment from the Loki's Castle low-temperature hydrothermal vent field at the Arctic Mid-Ocean Ridge. *Extremophiles* **18**, 545–560.

Javaux EJ (2019) Challenges in evidencing the earliest traces of life. *Nature* **572**, 451–460.

Javaux EJ, Knoll AH, Walter M (2003) Recognizing and Interpreting the Fossils of Early Eukaryotes. *Origins of Life and Evolution of the Biosphere* **33**, 75–94.

Javaux EJ, Lepot K (2018) The Paleoproterozoic fossil record: Implications for the evolution of the biosphere during Earth's middle-age. *Earth-Science Reviews* **176**, 68–86.

Javaux EJ, Marshall CP, Bekker A (2010) Organic-walled microfossils in 3.2-billion-year-old shallow-marine siliciclastic deposits. *Nature* **463**, 934–938.

Johnson C, Beard B, Weyer S (2020) *Iron Geochemistry: An Isotopic Perspective*. Advances in Isotope Geochemistry. Springer International Publishing, Cham.

Johnson TE, Brown M, Kaus BJP, VanTongeren JA (2014) Delamination and recycling of Archaean crust caused by gravitational instabilities. *Nature Geoscience* **7**, 47–52.

Jones B, Renaut RW (2007) Microstructural changes accompanying the opal-A to opal-CT transition: new evidence from the siliceous sinters of Geysir, Haukadalur, Iceland. *Sedimentology* **54**, 921–948.

Jørgensen BB, Findlay AJ, Pellerin A (2019) The Biogeochemical Sulfur Cycle of Marine Sediments. *Frontiers in Microbiology* **10**, 849.

Kalkowsky E (1908) Oolith und Stromatolith im norddeutschen Buntsandstein. *Zeitschrift der Deutschen geologischen Gesellschaft* **60**, 68–125.

Kappler A, Bryce C, Mansor M, Lueder U, Byrne JM, Swanner ED (2021) An evolving view on biogeochemical cycling of iron. *Nature Reviews Microbiology* **19**, 360–374.

Kappler A, Johnson CM, Crosby HA, Beard BL, Newman DK (2010) Evidence for equilibrium iron isotope fractionation by nitrate-reducing iron(II)-oxidizing bacteria. *Geochimica et Cosmochimica Acta* **74**, 2826–2842.

Kappler A, Pasquero C, Konhauser KO, Newman DK (2005) Deposition of banded iron formations by anoxygenic phototrophic Fe(II)-oxidizing bacteria. *Geology* **33**, 865–868.

Kashefi K, Lovley DR (2003) Extending the Upper Temperature Limit for Life. *Science* **301**, 934–934.

Kelley DS, Baross JA, Delaney JR (2002) Volcanoes, Fluids, and Life at Mid-Ocean Ridge Spreading Centers. *Annual Review of Earth and Planetary Sciences* **30**, 385–491.

Kesler SE, Gesink JA, Haynes FM (1989) Evolution of mineralizing brines in the east Tennessee Mississippi Valley-type ore field. *Geology* **17**, 466–469.

Kirschvink JL, Chang S-BR (1984) Ultrafine-grained magnetite in deep-sea sediments: Possible bacterial magnetofossils. *Geology* **12**, 559–562.

Kiyosu Y, Krouse HR (1990) The role of organic acid in the abiogenic reduction of sulfate and the sulfur isotope effect. *Geochemical Journal* **24**, 21–27.

Knoll AH, Barghoorn ES (1974) Ambient Pyrite in Precambrian Chert: New Evidence and a Theory. *Proceedings of the National Academy of Sciences* **71**, 2329–2331.

Knoll AH, Barghoorn ES (1977) Archean Microfossils Showing Cell Division from the Swaziland System of South Africa. *Science* **198**, 396–398.

Knoll AH, Bergmann KD, Strauss JV (2016) Life: the first two billion years. *Philosophical Transactions of the Royal Society B: Biological Sciences* **371**, 20150493.

Köhler I, Konhauser KO, Papineau D, Bekker A, Kappler A (2013) Biological carbon precursor to diagenetic siderite with spherical structures in iron formations. *Nature Communications* **4**, 1741.

Konhauser KO, Jones B, Phoenix VR, Ferris G, Renaut RW (2004) The Microbial Role in Hot Spring Silicification. *AMBIO: A Journal of the Human Environment* **33**, 552–558.

Konn C, Charlou JL, Donval JP, Holm NG, Dehairs F, Bouillon S (2009) Hydrocarbons and oxidized organic compounds in hydrothermal fluids from Rainbow and Lost City ultramafic-hosted vents. *Chemical Geology* **258**, 299–314.

Konn C, Charlou JL, Holm NG, Mousis O (2015) The Production of Methane, Hydrogen, and Organic Compounds in Ultramafic-Hosted Hydrothermal Vents of the Mid-Atlantic Ridge. *Astrobiology* **15**, 381–399.

Kopp RE, Kirschvink JL (2008) The identification and biogeochemical interpretation of fossil magnetotactic bacteria. *Earth-Science Reviews* **86**, 42–61.

Kotopoulou E, Godelitsas A, Göttlicher J, Steininger R, Price R, Fike DA, Amend JP, Gilhooly WP, Druschell G, Nomikou P, Gamaletsos PN, Lozios S (2022) Metastable Iron (Mono)sulfides in the Shallow-Sea Hydrothermal Sediments of Milos, Greece. *ACS Earth and Space Chemistry* **6**, 920–931.

Kucha H, Schroll E, Stumpfl EF (2005) Fossil sulphate-reducing bacteria in the Bleiberg lead-zinc deposit, Austria. *Mineralium Deposita* **40**, 123–126.

Kusky TM, Li J (2003) Paleoproterozoic tectonic evolution of the North China Craton. *Journal of Asian Earth Sciences* **22**, 383–397.

Labrenz M, Druschel GK, Thomsen-Ebert T, Gilbert B, Welch SA, Kemner KM, Logan GA, Summons RE, De Stasio G, Bond PL, Lai B, Kelly SD, Banfield JF (2000) Formation of Sphalerite (ZnS) Deposits in Natural Biofilms of Sulfate-Reducing Bacteria. *Science* **290**, 1744–1747.

Lam KP, Hitchcock AP, Obst M, Lawrence JR, Swerhone GDW, Leppard GG, Tyliszczak T, Karunakaran C, Wang J, Kaznatcheev K, Bazylinski DA, Lins U (2010) Characterizing magnetism of individual magnetosomes by X-ray magnetic circular dichroism in a scanning transmission X-ray microscope. *Chemical Geology* **270**, 110–116.

Large RR, Bull SW, Cooke DR, McGoldrick PJ (1998) A genetic model for the H.Y.C. Deposit, Australia; based on regional sedimentology, geochemistry, and sulfide-sediment relationships. *Economic Geology* **93**, 1345–1368.

Lepland A, Arrhenius G, Cornell D (2002) Apatite in early Archean Isua supracrustal rocks, southern West Greenland: its origin, association with graphite and potential as a biomarker. *Precambrian Research* **118**, 221–241.

Lepland A, Van Zuilen M, Philippot P (2011) Fluid-deposited graphite and its geobiological implications in early Archean gneiss from Akilia, Greenland. *Geobiology* **9**, 2–9.

Lepot K (2020) Signatures of early microbial life from the Archean (4 to 2.5 Ga) eon. *Earth-Science Reviews* **209**, 103296.

Lepot K, Benzerara K, Philippot P (2011) Biogenic versus metamorphic origins of diverse microtubes in 2.7Gyr old volcanic ashes: Multi-scale investigations. *Earth and Planetary Science Letters* **312**, 37–47.

Lepot K, Williford KH, Ushikubo T, Sugitani K, Mimura K, Spicuzza MJ, Valley JW (2013) Texture-specific isotopic compositions in 3.4Gyr old organic matter support selective preservation in cell-like structures. *Geochimica et Cosmochimica Acta* **112**, 66–86.

Li J, Kusky TM (2007) World's largest known Precambrian fossil black smoker chimneys and associated microbial vent communities, North China: Implications for early life. *Gondwana Research* **12**, 84–100.

Liermann LJ, Hausrath EM, Anbar AD, Brantley SL (2007) Assimilatory and dissimilatory processes of microorganisms affecting metals in the environment. *Journal of Analytical Atomic Spectrometry* **22**, 867.

Lin W, Paterson GA, Zhu Q, Wang Y, Kopylova E, Li Y, Knight R, Bazylinski DA, Zhu R, Kirschvink JL, Pan Y (2017) Origin of microbial biomineralization and magnetotaxis during the Archean. *Proceedings of the National Academy of Sciences* **114**, 2171–2176.

Little CTS, Glynn SEJ, Mills RA (2004) Four-Hundred-and-Ninety-Million-Year Record of Bacteriogenic Iron Oxide Precipitation at Sea-Floor Hydrothermal Vents. *Geomicrobiology Journal* **21**, 415–429.

Little CTS, Herrington RJ, Maslennikov VV, Zaykov VV (1998) The fossil record of hydrothermal vent communities. In: *Modern Ocean Floor Processes and the Geological Record*, Geological Society Special Publications (eds. Mills RA, Harrison K). London, pp. 259–270.

Little CTS, Johannessen KC, Bengtson S, Chan CS, Ivarsson M, Slack JF, Broman C, Thorseth IH, Grenne T, Rouxel OJ, Bekker A (2021) A late Paleoproterozoic (1.74 Ga) deep-sea, low-temperature, iron-oxidizing microbial hydrothermal vent community from Arizona, USA. *Geobiology* **19**, 228–249.

Liu L, Ireland TR, Holden P (2021) SHRIMP 4-S isotope systematics of two pyrite generations in the 3.49 Ga Dresser Formation. *Geochemical Perspectives Letters* **17**, 45–49.

Liu W, Zhang X, Wang W (2020) Microbial Imprints on Sulfide Minerals in Submarine Hydrothermal Deposits of the East Pacific Rise. *Journal of Geophysical Research: Biogeosciences* **125**, e2020JG005736.

Lode S, Piercey SJ, Layne GD, Piercey G, Cloutier J (2017) Multiple sulphur and lead sources recorded in hydrothermal exhalites associated with the Lemarchant volcanogenic massive sulphide deposit, central Newfoundland, Canada. *Mineralium Deposita* **52**, 105–128.

Logan GA, Hinman MC, Walter MR, Summons RE (2001) Biogeochemistry of the 1640 Ma McArthur River (HYC) lead-zinc ore and host sediments, Northern Territory, Australia. *Geochimica et Cosmochimica Acta* **65**, 2317–2336.

Logan RG (1979) *The Geology and Mineralogical Zoning of the H.Y.C. Ag-Pb-Zn Deposit, McArthur River, Northern Territory, Australia* (Master thesis).

Lovley DR, Stolzt JF, Phillips EJP (1987) Anaerobic production of magnetite by a dissimilatory iron-reducing microorganism. *Nature* **330**, 252–254.

Lowe DR (1994) Abiological origin of described stromatolites older than 3.2 Ga. *Geology* **22**, 387–390.

Lowenstam H (1981) Minerals formed by organisms. *Science* **211**, 1126–1131.

Luque FJ, Crespo-Feo E, Barrenechea JF, Ortega L (2012) Carbon isotopes of graphite: Implications on fluid history. *Geoscience Frontiers* **3**, 197–207.

Machel HG, Krouse HR, Sassen R (1995) Products and distinguishing criteria of bacterial and thermochemical sulfate reduction. *Applied Geochemistry* **10**, 373–389.

MacLeod F, S. Kindler G, Lun Wong H, Chen R, P. Burns B (2019) Asgard archaea: Diversity, function, and evolutionary implications in a range of microbiomes. *AIMS Microbiology* **5**, 48–61.

Manning-Berg A, Wood R, Williford K, Czaja A, Kah L (2019) The Taphonomy of Proterozoic Microbial Mats and Implications for Early Diagenetic Silicification. *Geosciences* **9**, 40.

Manning-Berg AR, Kah LC (2017) Proterozoic microbial mats and their constraints on environments of silicification. *Geobiology* **15**, 469–483.

Mansor M, Berti D, Hochella MF, Murayama M, Xu J (2019) Phase, morphology, elemental composition, and formation mechanisms of biogenic and abiogenic Fe-Cu-sulfide nanoparticles: A comparative study on their occurrences under anoxic conditions. *American Mineralogist* **104**, 703–717.

Mansor M, Fantle MS (2019) A novel framework for interpreting pyrite-based Fe isotope records of the past. *Geochimica et Cosmochimica Acta* **253**, 39–62.

Mansor M, Xu J (2020) Benefits at the nanoscale: a review of nanoparticle-enabled processes favouring microbial growth and functionality. *Environmental Microbiology* **22**, 3633–3649.

Marin-Carbonne J, Remusat L, Sforna MC, Thomazo C, Cartigny P, Philippot P (2018) Sulfur isotope's signal of nanopyrites enclosed in 2.7 Ga stromatolitic organic remains reveal microbial sulfate reduction. *Geobiology* **16**, 121–138.

Marlow J, Peckmann J, Orphan V (2015) Autoendoliths: a distinct type of rock-hosted microbial life. *Geobiology* **13**, 303–307.

Marshall CP, Love GD, Snape CE, Hill AC, Allwood AC, Walter MR, Van Kranendonk MJ, Bowden SA, Sylva SP, Summons RE (2007) Structural characterization of kerogen in 3.4Ga Archaean cherts from the Pilbara Craton, Western Australia. *Precambrian Research* **155**, 1–23.

Maslennikov VV, Maslennikova SP, Large RR, Danyushevsky LV, Herrington RJ, Ayupova NR, Zaykov VV, Lein AYu, Tseluyko AS, Melekestseva IYu, Tessalina SG (2017) Chimneys in Paleozoic massive sulfide mounds of the Urals VMS deposits: Mineral and trace element comparison with modern black, grey, white and clear smokers. *Ore Geology Reviews* **85**, 64–106.

McCollom T, Seewald J (2006) Carbon isotope composition of organic compounds produced by abiotic synthesis under hydrothermal conditions. *Earth and Planetary Science Letters* **243**, 74–84.

McCollom TM (2003) Formation of meteorite hydrocarbons from thermal decomposition of siderite (FeCO3). *Geochimica et Cosmochimica Acta* **67**, 311–317.

McCollom TM (2013) Laboratory Simulations of Abiotic Hydrocarbon Formation in Earth's Deep Subsurface. *Reviews in Mineralogy and Geochemistry* **75**, 467–494.

McCollom TM, Donaldson C (2019) Experimental Constraints on Abiotic Formation of Tubules and Other Proposed Biological Structures in Subsurface Volcanic Glass. *Astrobiology* **19**, 53–63.

McCollom TM, Ritter G, Simoneit BRT (1999) Lipid Synthesis Under Hydrothermal Conditions by Fischer- Tropsch-Type Reactions. *Origins of Life and Evolution of the Biosphere* **29**, 153–166.

McCollom TM, Seewald JS (2007) Abiotic Synthesis of Organic Compounds in Deep-Sea Hydrothermal Environments. *Chemical Reviews* **107**, 382–401.

McGoldrick P (1999) Northern Australian "Sedex" Zn-Pb deposits: microbial oases in Proterozoic seas. In: *Mineral Deposits: Processes to Processing* (ed. Stanley CJ). A.A. Balkema, Rotterdam, Brookfield.

McKay DS, Gibson EK, Thomas-Keprta KL, Vali H, Romanek CS, Clemett SJ, Chillier XDF, Maechling CR, Zare RN (1996) Search for Past Life on Mars: Possible Relic Biogenic Activity in Martian Meteorite ALH84001. *Science* **273**, 924–930.

McLoughlin N, Brasier MD, Wacey D, Green OR, Perry RS (2007) On Biogenicity Criteria for Endolithic Microborings on Early Earth And Beyond. *Astrobiology* **7**, 10–26.

McLoughlin N, Wilson LA, Brasier MD (2008) Growth of synthetic stromatolites and wrinkle structures in the absence of microbes – implications for the early fossil record. *Geobiology* **6**, 95–105.

McMahon S (2019) Earth's earliest and deepest purported fossils may be iron-mineralized chemical gardens. *Proceedings of the Royal Society B: Biological Sciences* **286**, 20192410.

Ménez B, Pisapia C, Andreani M, Jamme F, Vanbellingen QP, Brunelle A, Richard L, Dumas P, Réfrégiers M (2018) Abiotic synthesis of amino acids in the recesses of the oceanic lithosphere. *Nature* **564**, 59–63.

Milesi V, Guyot F, Brunet F, Richard L, Recham N, Benedetti M, Dairou J, Prinzhofer A (2015) Formation of CO2, H2 and condensed carbon from siderite dissolution in the 200–300°C range and at 50MPa. *Geochimica et Cosmochimica Acta* **154**, 201–211.

Milesi V, McCollom TM, Guyot F (2016) Thermodynamic constraints on the formation of condensed carbon from serpentinization fluids. *Geochimica et Cosmochimica Acta* **189**, 391–403.

Miot J, Benzerara K, Morin G, Kappler A, Bernard S, Obst M, Férard C, Skouri-Panet F, Guigner J-M, Posth N, Galvez M, Brown GE, Guyot F (2009) Iron biomineralization by anaerobic neutrophilic iron-oxidizing bacteria. *Geochimica et Cosmochimica Acta* **73**, 696–711.

Mißbach H, Duda J-P, Kerkhof AM van den, Lüders V, Pack A, Reitner J, Thiel V (2021) Ingredients for microbial life preserved in 3.5 billion-year-old fluid inclusions. *Nature Communications* **12**, 1101.

Mißbach H, Schmidt BC, Duda J-P, Lünsdorf NK, Goetz W, Thiel V (2018) Assessing the diversity of lipids formed via Fischer-Tropsch-type reactions. *Organic Geochemistry* **119**, 110–121.

Moeller K, Schoenberg R, Grenne T, Thorseth IH, Drost K, Pedersen RB (2014) Comparison of iron isotope variations in modern and Ordovician siliceous Fe oxyhydroxide deposits. *Geochimica et Cosmochimica Acta* **126**, 422–440.

Mojzsis SJ, Arrhenius G, McKeegan KD, Harrison TM, Nutman AP, Friend CRL (1996) Evidence for life on Earth before 3,800 million years ago. *Nature* **384**, 55–59.

Monecke T, Kempe U, Go J (2002) Genetic significance of the trace element content in metamorphic and hydrothermal quartz: a reconnaissance study. *Earth and Planetary Science Letters* **202**, 709–724.

Mycke B, Michaelis W, Degens ET (1988) Biomarkers in sedimentary sulfides of precambrian age. *Organic Geochemistry* **13**, 619–625.

Nims C, Cron B, Wetherington M, Macalady J, Cosmidis J (2019) Low frequency Raman Spectroscopy for micron-scale and in vivo characterization of elemental sulfur in microbial samples. *Scientific Reports* **9**, 7971.

Nims C, Lafond J, Alleon J, Templeton AS, Cosmidis J (2021) Organic biomorphs may be better preserved than microorganisms in early Earth sediments. *Geology* **49**, 629–634.

Nozaki T, Nagase T, Ushikubo T, Shimizu K, Ishibashi J, and the D/V Chikyu Expedition 909 Scientists (2020) Microbial sulfate reduction plays an important role at the initial stage of subseafloor sulfide mineralization. *Geology* **49**, 222–227.

O'Brien CE, Giovannelli D, Govenar B, Luther GW, Lutz RA, Shank TM, Vetriani C (2015) Microbial biofilms associated with fluid chemistry and megafaunal colonization at post-eruptive deep-sea hydrothermal vents. *Deep Sea Research Part II: Topical Studies in Oceanography* **121**, 31–40.

Oehler JH, Logan RG (1977) Microfossils, cherts, and associated mineralization in the Proterozoic McArthur (H.Y.C.) lead-zinc-silver deposit. *Economic Geology* **72**, 1393–1409.

Ohfuji H, Rickard D (2005) Experimental syntheses of framboids—a review. *Earth-Science Reviews* **71**, 147–170.

Ohmoto H (1996) Formation of volcanogenic massive sulfide deposits: The Kuroko perspective. *Ore Geology Reviews* **10**, 135–177.

Ohmoto H, Lasaga AC (1982) Kinetics of reaetions between aqueous sulfates and sulfides in hydrothermal systems. *Geochimica et Cosmochimica Acta* **46**, 1727–1745.

Ono S (2008) Multiple-Sulphur Isotope Biosignatures. *Space Science Reviews* **135**, 203–220.

Ortega L, Millward D, Luque FJ, Barrenechea JF, Beyssac O, Huizenga J-M, Rodas M, Clarke SM (2010) The graphite deposit at Borrowdale (UK): A catastrophic mineralizing event associated with Ordovician magmatism. *Geochimica et Cosmochimica Acta* **74**, 2429–2449.

Page RW, Sweet IP (1998) Geochronology of basin phases in the western Mt Isa Inlier, and correlation with the McArthur Basin. *Australian Journal of Earth Sciences* **45**, 219–232.

Papineau D, De Gregorio BT, Cody GD, Fries MD, Mojzsis SJ, Steele A, Stroud RM, Fogel ML (2010a) Ancient graphite in the Eoarchean quartz–pyroxene rocks from Akilia in

southern West Greenland I: Petrographic and spectroscopic characterization. *Geochimica et Cosmochimica Acta* **74**, 5862–5883.

Papineau D, De Gregorio BT, Cody GD, O'Neil J, Steele A, Stroud RM, Fogel ML (2011) Young poorly crystalline graphite in the >3.8-Gyr-old Nuvvuagittuq banded iron formation. *Nature Geoscience* **4**, 376–379.

Papineau D, De Gregorio BT, Stroud RM, Steele A, Pecoits E, Konhauser K, Wang J, Fogel ML (2010b) Ancient graphite in the Eoarchean quartz-pyroxene rocks from Akilia in southern West Greenland II: Isotopic and chemical compositions and comparison with Paleoproterozoic banded iron formations. *Geochimica et Cosmochimica Acta* **74**, 5884–5905.

Papineau D, She Z, Dodd MS, Iacoviello F, Slack JF, Hauri E, Shearing P, Little CTS (2022) Metabolically diverse primordial microbial communities in Earth's oldest seafloor-hydrothermal jasper. *Science Advances* **8**, eabm2296.

Park Y, Faivre D (2022) Diversity of Microbial Metal Sulfide Biomineralization. *ChemPlusChem* **87**, e2021004.

Peter JM, Scott SD (1988) Mineralogy, Composition, and Fluid-Inclusion Microthermometry of Seafloor Hydrothermal Deposits in the Southern Trough of Guaymas Basin, Gulf of California. *Canadian Mineralogist* **26**, 567–587.

Peters KE, Walters CC, Moldowan JM (2005a) *The Biomarker Guide - Volume 1: Biomarkers and Isotopes in the Environment and Human History*, 2nd ed. Cambridge University Press, Cambridge.

Peters KE, Walters CC, Moldowan JM (2005b) *The Biomarker Guide - Volume 2: Biomarkers and Isotopes in Petroleum Exploration and Earth History*, 2nd ed. Cambridge University Press, Cambridge.

Petrash DA, Robbins LJ, Shapiro RS, Mojzsis SJ, Konhauser KO (2016) Chemical and textural overprinting of ancient stromatolites: Timing, processes, and implications for their use as paleoenvironmental proxies. *Precambrian Research* **278**, 145–160.

Philippot P, Van Zuilen M, Lepot K, Thomazo C, Farquhar J, Van Kranendonk MJ (2007) Early Archaean Microorganisms Preferred Elemental Sulfur, Not Sulfate. *Science* **317**, 1534–1537.

Picard A, Gartman A, Clarke DR, Girguis PR (2018) Sulfate-reducing bacteria influence the nucleation and growth of mackinawite and greigite. *Geochimica et Cosmochimica Acta* **220**, 367–384.

Picard A, Gartman A, Cosmidis J, Obst M, Vidoudez C, Clarke DR, Girguis PR (2019) Authigenic metastable iron sulfide minerals preserve microbial organic carbon in anoxic environments. *Chemical Geology* **530**, 119343.

Picard A, Gartman A, Girguis PR (2016) What Do We Really Know about the Role of Microorganisms in Iron Sulfide Mineral Formation? *Frontiers in Earth Science* **4**.

Picard A, Gartman A, Girguis PR (2021) Interactions Between Iron Sulfide Minerals and Organic Carbon: Implications for Biosignature Preservation and Detection. *Astrobiology* **21**, 587–604.

Pinti DL, Mineau R, Clement V (2009) Hydrothermal alteration and microfossil artefacts of the 3,465-million-year-old Apex chert. *Nature Geoscience* **2**, 640–643.

Pirajno F (2010) *Hydrothermal processes and mineral systems*. Springer, Dordrecht.

Pokrovski GS, Blanchard M, Saunier G, Poitrasson F (2021) Mechanisms and rates of pyrite formation from hydrothermal fluid revealed by iron isotopes. *Geochimica et Cosmochimica Acta* **304**, 281–304.

Popa R, Kinkle BK, Badescu A (2004) Pyrite Framboids as Biomarkers for Iron-Sulfur Systems. *Geomicrobiology Journal* **21**, 193–206.

Posth NR, Canfield DE, Kappler A (2014) Biogenic Fe(III) minerals: From formation to diagenesis and preservation in the rock record. *Earth-Science Reviews* **135**, 103–121.

Posth NR, Köhler I, D. Swanner E, Schröder C, Wellmann E, Binder B, Konhauser KO, Neumann U, Berthold C, Nowak M, Kappler A (2013) Simulating Precambrian banded iron formation diagenesis. *Chemical Geology* **362**, 66–73.

Poulton SW, Krom MD, Raiswell R (2004) A revised scheme for the reactivity of iron (oxyhydr)oxide minerals towards dissolved sulfide. *Geochimica et Cosmochimica Acta* **68**, 3703–3715.

Prange A, Chauvistré R, Modrow H, Hormes J, Trüper HG, Dahl C (2002) Quantitative speciation of sulfur in bacterial sulfur globules: X-ray absorption spectroscopy reveals at least three different species of sulfur. *Microbiology* **148**, 267–276.

Present TM, Bergmann KD, Myers C, Slotznick SP, Creveling JR, Zieg J, Fischer WW, Knoll AH, Grotzinger JP (2017) Pyrite-walled tube structures in a Mesoproterozoic sediment-hosted metal sulfide deposit. *Geological Society of America Bulletin* **130**, 598–616.

Proskurowski G, Lilley MD, Seewald JS, Fru h-Green GL, Olson EJ, Lupton JE, Sylva SP, Kelley DS (2008) Abiogenic Hydrocarbon Production at Lost City Hydrothermal Field. *Science* **319**, 604–607.

Qian G, Brugger J, Skinner WM, Chen G, Pring A (2010) An experimental study of the mechanism of the replacement of magnetite by pyrite up to 300°C. *Geochimica et Cosmochimica Acta* **74**, 5610–5630.

Qian G, Brugger J, Testemale D, Skinner W, Pring A (2013) Formation of As(II)-pyrite during experimental replacement of magnetite under hydrothermal conditions. *Geochimica et Cosmochimica Acta* **100**, 1–10.

Raiswell R, Plant J (1980) The incorporation of trace elements into pyrite during diagenesis of black shales, Yorkshire, England. *Economic Geology* **75**, 684–699.

Rasmussen B (2000) Filamentous microfossils in a 3,235-million-year-old volcanogenic massive sulphide deposit. *Nature* **405**, 676–679.

Rasmussen B, Buick R (2000) Oily old ores: Evidence for hydrothermal petroleum generation in an Archean volcanogenic massive sulfide deposit. *Geology* **28**, 731–734.

Rasmussen B, Fletcher IR, Brocks JJ, Kilburn MR (2008) Reassessing the first appearance of eukaryotes and cyanobacteria. *Nature* **455**, 1101–1104.

Rasmussen B, Muhling JR, Fischer WW (2021) Ancient Oil as a Source of Carbonaceous Matter in 1.88-Billion-Year-Old Gunflint Stromatolites and Microfossils. *Astrobiology* **21**, 655–672.

Reeves EP, Yoshinaga MY, Pjevac P, Goldenstein NI, Peplies J, Meyerdierks A, Amann R, Bach W, Hinrichs K-U (2014) Microbial lipids reveal carbon assimilation patterns on hydrothermal sulfide chimneys: Microbial lipids on hydrothermal sulfide structures. *Environmental Microbiology* **16**, 3515–3532.

Reid RP, James NP, Macintyre IG, Dupraz CP, Burne RV (2003) Shark Bay stromatolites: Microfabrics and reinterpretation of origins. *Facies* **49**, 299–324.

Reinhardt M, Goetz W, Duda J-P, Heim C, Reitner J, Thiel V (2019) Organic signatures in Pleistocene cherts from Lake Magadi (Kenya), analogs for early Earth hydrothermal deposits. *Biogeosciences* **16**, 2443–2465.

Reitner J (1993) Modern cryptic microbialite/metazoan facies from Lizard Island (Great Barrier Reef, Australia) formation and concepts. *Facies* **29**, 3–39.

Reitner J (2011) Microbial mats. In: *Encyclopedia of Geobiology* (eds. Reitner J, Thiel V). Springer, Berlin, pp. 606–608.

Reitner J, Blumenberg M, Walliser E-O, Schäfer N, Duda J-P (2015) Methane-derived carbonate conduits from the late Aptian of Salinac (Marne Bleues, Vocontian Basin, France): Petrology and biosignatures. *Marine and Petroleum Geology* **66**, 641–652.

Reitner J, Peckmann J, Reimer A, Schumann G, Thiel V (2005) Methane-derived carbonate build-ups and associated microbial communities at cold seeps on the lower Crimean shelf (Black Sea). *Facies* **51**, 66–79.

Revan MK, Genç Y, Maslennikov VV, Maslennikova SP, Large RR, Danyushevsky LV (2014) Mineralogy and trace-element geochemistry of sulfide minerals in hydrothermal chimneys from the Upper-Cretaceous VMS deposits of the eastern Pontide orogenic belt (NE Turkey). *Ore Geology Reviews* **63**, 129–149.

Reysenbach A-L, Cady SL (2001) Microbiology of ancient and modern hydrothermal systems. *Trends in Microbiology* **9**, 79–86.

Rickard DT (1975) Kinetics and Mechanism of Pyrite Formation at Low Temperatures. *American Journal of Science* **275**, 636–652.

Riding R (2000) Microbial carbonates: the geological record of calcified bacterial-algal mats and biofilms: *Microbial carbonates*. *Sedimentology* **47**, 179–214.

Riding R (2011) Microbialites, stromatolites, and thrombolites. In: *Encyclopedia of Geobiology* (eds. Reitner J, Thiel V). Springer Netherlands, Dordrecht, pp. 635–654.

Rojas-Chapana J, Tributsch H (2004) Interfacial activity and leaching patterns of Leptospirillum ferrooxidans on pyrite. *FEMS Microbiology Ecology* **47**, 19–29.

Rouillard J, García-Ruiz J-M, Gong J, Zuilen MA van (2018) A morphogram for silica-witherite biomorphs and its application to microfossil identification in the early earth rock record. *Geobiology* **16**, 279–296.

Rouillard J, García-Ruiz JM, Kah L, Gérard E, Barrier L, Nabhan S, Gong J, Zuilen MA (2019) Identifying microbial life in rocks: Insights from population morphometry. *Geobiology* **18**, 282–305.

Rouxel O, Fouquet Y, Ludden JN (2004) Subsurface processes at the lucky strike hydrothermal field, Mid-Atlantic ridge: evidence from sulfur, selenium, and iron isotopes. *Geochimica et Cosmochimica Acta* **68**, 2295–2311.

Rouxel O, Toner B, Germain Y, Glazer B (2018) Geochemical and iron isotopic insights into hydrothermal iron oxyhydroxide deposit formation at Loihi Seamount. *Geochimica et Cosmochimica Acta* **220**, 449–482.

Rouzaud J-N, Deldicque D, Charon É, Pageot J (2015) Carbons at the heart of questions on energy and environment: A nanostructural approach. *Comptes Rendus Geoscience* **347**, 124–133.

Rumble D, Hoering TC (1986) Carbon isotope geochemistry of graphite vein deposits from New Hampshire, U.S.A. *Geochimica et Cosmochimica Acta* **50**, 1239–1247.

Rushdi AI, Simoneit BRT (2001) Lipid formation by aqueous Fischer-Tropsch-Type synthesis over a temperature range of 100 to 400 °C. *Origins of Life and Evolution of the Biosphere* **31**, 103–118.

Russell MJ (1996) The generation at hot springs of sedimentary ore deposits, microbialites and life. *Ore Geology Reviews* **10**, 199–214.

Russell MJ, Daniel RM, Hall AJ, Sherringham JA (1994) A hydrothermally precipitated catalytic iron sulphide membrane as a first step toward life. *Journal of Molecular Evolution* **39**, 231–243.

Russell MJ, Hall AJ, Martin W (2010) Serpentinization as a source of energy at the origin of life: Serpentinization and the emergence of life. *Geobiology* **8**, 355–371.

Saito MA, Sigman DM, Morel FMM (2003) The bioinorganic chemistry of the ancient ocean: the co-evolution of cyanobacterial metal requirements and biogeochemical cycles at the Archean–Proterozoic boundary? *Inorganica Chimica Acta* **356**, 308–318.

Schad M, Halama M, Jakus N, Robbins LJ, Warchola TJ, Tejada J, Kirchhof R, Lalonde SV, Swanner ED, Planavsky NJ, Thorwarth H, Mansor M, Konhauser KO, Kappler A (2021) Phosphate remobilization from banded iron formations during metamorphic mineral transformations. *Chemical Geology* **584**, 120489.

Schidlowski M (2001) Carbon isotopes as biogeochemical recorders of life over 3.8 Ga of Earth history: evolution of a concept. *Precambrian Research* **106**, 117–134.

Schieber J (2002) Sedimentary Pyrite: A window into the microbial past. *Geology* **30**, 531–534.

Schiffbauer JD, Yin L, Bodnar RJ, Kaufman AJ, Meng F, Hu J, Shen B, Yuan X, Xiao S (2007) Ultrastructural and Geochemical Characterization of Archean–Paleoproterozoic Graphite Particles: Implications for Recognizing Traces of Life in Highly Metamorphosed Rocks. *Astrobiology* **7**, 684–704.

Schopf J, Packer B (1987) Early Archean (3.3-billion to 3.5-billion-year-old) microfossils from Warrawoona Group, Australia. *Science* **237**, 70–73.

Schroll E, Rantitsch G (2005) Sulphur isotope patterns from the Bleiberg deposit (Eastern Alps) and their implications for genetically affiliated lead-zinc deposits. *Mineralogy and Petrology* **84**, 1–18.

Semikhatov MA, Gebelein CD, Cloud P, Awramik SM, Benmore WC (1979) Stromatolite morphogenesis—progress and problems. *Canadian Journal of Earth Sciences* **19**, 992–1015.

Sephton MA, Gilmour I (2001) Compound-specific isotope analysis of the organic constituents in carbonaceous chondrites. *Mass Spectrometry Reviews* **20**, 111–120.

Sephton MA, Verchovsky AB, Bland PA, Gilmour I, Grady MM, Wright IP (2003) Investigating the variations in carbon and nitrogen isotopes in carbonaceous chondrites. *Geochimica et Cosmochimica Acta* **67**, 2093–2108.

Sforna MC, Brunelli D, Pisapia C, Pasini V, Malferrari D, Ménez B (2018) Abiotic formation of condensed carbonaceous matter in the hydrating oceanic crust. *Nature Communications* **9**, 5049.

Sforna MC, Daye M, Philippot P, Somogyi A, Zuilen MA van, Medjoubi K, Gérard E, Jamme F, Dupraz C, Braissant O, Glunk C, Visscher PT (2016) Patterns of metal distribution in hypersaline microbialites during early diagenesis: Implications for the fossil record. *Geobiology* **15**, 259–279.

Sforna MC, Zuilen MA van, Philippot P (2014) Structural characterization by Raman hyperspectral mapping of organic carbon in the 3.46 billion-year-old Apex chert, Western Australia. *Geochimica et Cosmochimica Acta* **124**, 18–33.

Shen Y, Buick R, Canfield DE (2001) Isotopic evidence for microbial sulphate reduction in the early Archaean era. *Nature* **410**, 77–81.

Shen Y, Farquhar J, Masterson A, Kaufman AJ, Buick R (2009) Evaluating the role of microbial sulfate reduction in the early Archean using quadruple isotope systematics. *Earth and Planetary Science Letters* **279**, 383–391.

Sim MS, Bosak T, Ono S (2011) Large Sulfur Isotope Fractionation Does Not Require Disproportionation. *Science* **333**, 74–77.

Simoneit BRT (1993) Aqueous high-temperature and high-pressure organic geochemistry of hydrothermal vent systems. *Geochimica et Cosmochimica Acta* **57**, 3231–3243.

Simoneit BRT, Lein AYu, Peresypkin VI, Osipov GA (2004) Composition and origin of hydrothermal petroleum and associated lipids in the sulfide deposits of the Rainbow field (Mid-Atlantic Ridge at 36°N). *Geochimica et Cosmochimica Acta* **68**, 2275–2294.

Slack JF, Shanks WC, Ridley WI, Dusel-Bacon C, DesOrmeau JW, Ramezani J, Fayek M (2019) Extreme sulfur isotope fractionation in the Late Devonian Dry Creek volcanogenic massive sulfide deposit, central Alaska. *Chemical Geology* **513**, 226–238.

Southam G, Saunders JA (2005) The Geomicrobiology of Ore Deposits. *Economic Geology* **100**, 1067–1084.

Spang A, Saw JH, Jørgensen SL, Zaremba-Niedzwiedzka K, Martijn J, Lind AE, Eijk R van, Schleper C, Guy L, Ettema TJG (2015) Complex archaea that bridge the gap between prokaryotes and eukaryotes. *Nature* **521**, 173–179.

Strauss H (1997) The isotopic composition of sedimentary sulfur through time. *Palaeogeography, Palaeoclimatology, Palaeoecology* **132**, 97–118.

Suarez-Gonzalez P, Benito MI, Quijada IE, Mas R, Campos-Soto S (2019) 'Trapping and binding': A review of the factors controlling the development of fossil agglutinated microbialites and their distribution in space and time. *Earth-Science Reviews* **194**, 182–215.

Sugitani K, Grey K, Allwood A, Nagaoka T, Mimura K, Minami M, Marshall CP, Van Kranendonk MJ, Walter MR (2007) Diverse microstructures from Archaean chert from the Mount Goldsworthy–Mount Grant area, Pilbara Craton, Western Australia: Microfossils, dubiofossils, or pseudofossils? *Precambrian Research* **158**, 228–262.

Summons RE, Welander PV, Gold DA (2021) Lipid biomarkers: molecular tools for illuminating the history of microbial life. *Nature Reviews Microbiology* **20**, 174–185.

Suzuki Y, Inagaki F, Takai K, Nealson KH, Horikoshi K (2004) Microbial Diversity in Inactive Chimney Structures from Deep-Sea Hydrothermal Systems. *Microbial Ecology* **47**, 186–196.

Swanner ED, Bayer T, Wu W, Hao L, Obst M, Sundman A, Byrne JM, Michel FM, Kleinhanns IC, Kappler A, Schoenberg R (2017) Iron Isotope Fractionation during Fe(II) Oxidation Mediated by the Oxygen-Producing Marine Cyanobacterium *Synechococcus* PCC 7002. *Environmental Science & Technology* **51**, 4897–4906.

Taylor BE (2004) Biogenic and thermogenic sulfate reduction in the Sullivan Pb–Zn–Ag deposit, British Columbia (Canada): Evidence from micro-isotopic analysis of carbonate and sulfide in bedded ores. *Chemical Geology* **204**, 215–236.

Thiel J, Byrne JM, Kappler A, Schink B, Pester M (2019) Pyrite formation from FeS and H2S is mediated through microbial redox activity. *Proceedings of the National Academy of Sciences* **116**, 6897–6902.

Thomas-Keprta KL, Bazylinski DA, Kirschvink JL, Clemett SJ, Mckay DS, Wentworth SJ, Vali H, Jr EKG, Romanek CS (2000) Elongated prismatic magnetite crystals in ALH84001 carbonate globules: Potential Martian magnetofossils. *Geochimica et Cosmochimica Acta* **64**, 4049–4081.

Thorseth IH, Torsvik T, Torsvik V, Daae FL, Pedersen RB (2001) Diversity of life in ocean floor basalt. *Earth and Planetary Science Letters* **194**, 31–37.

Toner BM, Lesniewski RA, Marlow JJ, Briscoe LJ, Santelli CM, Bach W, Orcutt BN, Edwards KJ (2013) Mineralogy Drives Bacterial Biogeography of Hydrothermally Inactive Seafloor Sulfide Deposits. *Geomicrobiology Journal* **30**, 313–326.

Toner BM, Rouxel OJ, Santelli CM, Bach W, Edwards KJ (2016) Iron Transformation Pathways and Redox Micro-Environments in Seafloor Sulfide-Mineral Deposits: Spatially Resolved Fe XAS and δ57/54Fe Observations. *Frontiers in Microbiology* **7**.

Tornos F, Velasco F, Menor-Salván C, Delgado A, Slack JF, Escobar JM (2014) Formation of recent Pb-Ag-Au mineralization by potential sub-surface microbial activity. *Nature Communications* **5**, 4600.

Treiman AH (2003) Submicron Magnetite Grains and Carbon Compounds in Martian Meteorite ALH84001: Inorganic, Abiotic Formation by Shock and Thermal Metamorphism. *Astrobiology* **3**, 369–392.

Trichet J, Défarge C (1995) Non-biologically supported organomineralization. In: *Proceedings 7th International Symposium on Biomineralization*, Bulletin de l'Institut Océanographique de Monaco. pp. 203–236.

Ueno Y, Ono S, Rumble D, Maruyama S (2008) Quadruple sulfur isotope analysis of ca. 3.5Ga Dresser Formation: New evidence for microbial sulfate reduction in the early Archean. *Geochimica et Cosmochimica Acta* **72**, 5675–5691.

Valdivieso-Ojeda JA, Huerta-Diaz MA, Delgadillo-Hinojosa F (2014) High enrichment of molybdenum in hypersaline microbial mats of Guerrero Negro, Baja California Sur, Mexico. *Chemical Geology* **363**, 341–354.

Van Dover CL (2000) *The Ecology of Deep-Sea Hydrothermal Vents*. Princeton University Press, Princeton.

Van Dover CL (2019) Inactive Sulfide Ecosystems in the Deep Sea: A Review. *Frontiers in Marine Science* **6**, 461.

Van Kranendonk M, Philippot P, Lepot K, Bodorkos S, Pirajno F (2008) Geological setting of Earth's oldest fossils in the ca. 3.5 Ga Dresser Formation, Pilbara Craton, Western Australia. *Precambrian Research* **167**, 93–124.

Van Kranendonk MJ (2011) Morphology as an Indicator of Biogenicity for 3.5–3.2 Ga Fossil Stromatolites from the Pilbara Craton, Western Australia. In: *Advances in Stromatolite Geobiology*, Lecture Notes in Earth Sciences (eds. Reitner J, Quéric N-V, Arp G). Springer Berlin Heidelberg, Berlin, Heidelberg, pp. 537–554.

Vandenbroucke M, Largeau C (2007) Kerogen origin, evolution and structure. *Organic Geochemistry* **38**, 719–833.

Vearncombe S, Barley ME, Groves DI, McNaughton NJ, Mikucki EJ, Vearncombe JR (1995) 3.26 Ga black smoker-type mineralization in the Strelley Belt, Pilbara Craton, Western Australia. *Journal of the Geological Society* **152**, 587–590.

Velasco-Acebes J, Tornos F, Kidane AT, Wiedenbeck M, Velasco F, Delgado A (2019) Isotope geochemistry tracks the maturation of submarine massive sulfide mounds (Iberian Pyrite Belt). *Mineralium Deposita* **54**, 913–934.

Von Damm KL (1995) Controls on the Chemistry and Temporal Variability of Seafloor Hydrothermal Fluids. In: *Geophysical Monograph Series* (eds. Humphris SE, Zierenberg RA, Mullineaux LS, Thomson RE). American Geophysical Union, Washington, D. C., pp. 222–247.

Wacey D, Kilburn MR, Saunders M, Cliff J, Brasier MD (2011a) Microfossils of sulphur-metabolizing cells in 3.4-billion-year-old rocks of Western Australia. *Nature Geoscience* **4**, 698–702.

Wacey D, Noffke N, Cliff J, Barley ME, Farquhar J (2015) Micro-scale quadruple sulfur isotope analysis of pyrite from the ~3480Ma Dresser Formation: New insights into sulfur cycling on the early Earth. *Precambrian Research* **258**, 24–35.

Wacey D, Noffke N, Saunders M, Guagliardo P, Pyle DM (2018a) Volcanogenic Pseudo-Fossils from the ~3.48 Ga Dresser Formation, Pilbara, Western Australia. *Astrobiology* **18**, 539–555.

Wacey D, Saunders M, Brasier MD, Kilburn MR (2011b) Earliest microbially mediated pyrite oxidation in ~3.4 billion-year-old sediments. *Earth and Planetary Science Letters* **301**, 393–402.

Wacey D, Saunders M, Cliff J, Kilburn MR, Kong C, Barley ME, Brasier MD (2014) Geochemistry and nano-structure of a putative ~3240 million-year-old black smoker biota, Sulphur Springs Group, Western Australia. *Precambrian Research* **249**, 1–12.

Wacey D, Saunders M, Kong C (2018b) Remarkably preserved tephra from the 3430 Ma Strelley Pool Formation, Western Australia: Implications for the interpretation of Precambrian microfossils. *Earth and Planetary Science Letters* **487**, 33–43.

Wacey D, Saunders M, Kong C, Brasier A, Brasier M (2016) 3.46 Ga Apex chert 'microfossils' reinterpreted as mineral artefacts produced during phyllosilicate exfoliation. *Gondwana Research* **36**, 296–313.

Wächtershäuser G (1990) Evolution of the first metabolic cycles. *Proceedings of the National Academy of Sciences* **87**, 200–204.

Watanabe Y, Farquhar J, Ohmoto H (2009) Anomalous Fractionations of Sulfur Isotopes During Thermochemical Sulfate Reduction. *Science* **324**, 370–373.

Weiner S, Dove PM (2003) An Overview of Biomineralization Processes and the Problem of the Vital Effect. *Reviews in Mineralogy and Geochemistry* **54**, 1–29.

Weiss MC, Sousa FL, Mrnjavac N, Neukirchen S, Roettger M, Nelson-Sathi S, Martin WF (2016) The physiology and habitat of the last universal common ancestor. *Nature Microbiology* **1**, 16116.

Westall F (2005) Life on the Early Earth: A Sedimentary View. *Science* **308**, 366–367.

Westall F, Folk RL (2003) Exogenous carbonaceous microstructures in Early Archaean cherts and BIFs from the Isua Greenstone Belt: implications for the search for life in ancient rocks. *Precambrian Research* **126**, 313–330.

Widdel F, Schnell S, Heising S, Ehrenreich A, Assmus B, Schink B (1993) Ferrous iron oxidation by anoxygenic phototrophic bacteria. *Nature* **362**, 834–836.

Wilkin RT, Barnes HL (1997) Formation processes of framboidal pyrite. *Geochimica et Cosmochimica Acta* **61**, 323–339.

Williams RJ. P, Fraústo Da Silva JJR (2003) Evolution was Chemically Constrained. *Journal of Theoretical Biology* **220**, 323–343.

Williford KH, Grice K, Logan GA, Chen J, Huston D (2011) The molecular and isotopic effects of hydrothermal alteration of organic matter in the Paleoproterozoic McArthur River Pb/Zn/Ag ore deposit. *Earth and Planetary Science Letters* **301**, 382–392.

Wilson NSF, Zentilli M, Spiro B (2003) A Sulfur, Carbon, Oxygen, and Strontium Isotope Study of the Volcanic-Hosted El Soldado Manto-Type Copper Deposit, Chile: Essential Role of Bacteria and Petroleum. *Economic Geology* **98**, 163–174.

Xia X, Lian W, Yuan C, Yan F, Yuan J (2008) Mineralization of a Proterozoic Sulfide Black Smoker Chimney and Thermophilous Microorganisms in Eastern Hebei, China. *Acta Geologica Sinica* **82**, 858–863.

Xu J, Murayama M, Roco CM, Veeramani H, Michel FM, Rimstidt JD, Winkler C, Hochella MF (2016) Highly-defective nanocrystals of ZnS formed via dissimilatory bacterial sulfate reduction: A comparative study with their abiogenic analogues. *Geochimica et Cosmochimica Acta* **180**, 1–14.

Zawaski MJ, Kelly NM, Orlandini OF, Nichols CIO, Allwood AC, Mojzsis SJ (2020) Reappraisal of purported ca. 3.7 Ga stromatolites from the Isua Supracrustal Belt (West Greenland) from detailed chemical and structural analysis. *Earth and Planetary Science Letters* **545**, 116409.

Zuilen MA van (2019) The Significance of Carbonaceous Matter to Understanding Life Processes on Early Earth. In: *Earth's Oldest Rocks*. Elsevier, pp. 945–963.

Zuilen MA van, Lepland A, Arrhenius G (2002) Reassessing the evidence for the earliest traces of life. *Nature* **418**, 627–630.

Zuilen MA van, Lepland A, Teranes J, Finarelli J, Wahlen M, Arrhenius G (2003) Graphite and carbonates in the 3.8 Ga old Isua Supracrustal Belt, southern West Greenland. *Precambrian Research* **126**, 331–348.

CHAPTER 2 – OBJECTIVES AND STRUCTURE

The literature review provided in *Chapter 1* (Runge et al., 2023, *Geobiology*) revealed that the biosignature record in ancient hydrothermal sulfides is poorly explored, significantly limiting our understanding of life's emergence and early evolution. Microbial biominerals emerged as a promising research avenue because they can differ from their abiotic counterparts in many characteristics (e.g., size, shape, crystallinity, trace-element and isotopic signatures, and association with organic matter) providing potentially detectable biosignatures in ancient rocks. Nevertheless, the distinction between abiogenic and biogenic minerals is challenging because their characteristics are also influenced by environmental conditions and altered by diagenetic processes (i.e., their taphonomy). These problems are exacerbated in hydrothermal systems, where steep physical and chemical gradients drive complex and interacting mineral (trans)formation processes, including precipitation and dissolution, at any time, not only after burial (Fig. 2.1). Identifying biogenic minerals and their transformation products in ancient hydrothermal sulfides, thus, has unique and complex challenges that necessitate research into taphonomic processes in these environments. To date, these processes have been poorly explored.

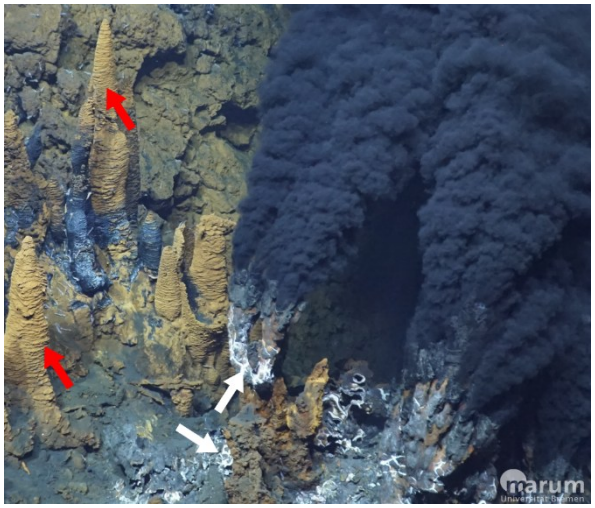

Figure 2.1: Microbial life at the Rainbow Hydrothermal Field (Mid-Atlantic Ridge). Hydrothermal systems harbor unique microbial ecosystems independent of energy from sunlight. Sulfide dissolved in reducing hydrothermal fluids fuels chemoautotrophic sulfur oxidation at the interface with oxygenated seawater, forming white elemental sulfur deposits (white arrow). The oxidative weathering of reduced hydrothermal Fe(II) sulfides to Fe(III) (oxyhydr)oxides (red arrow) is commonly driven by iron-oxidizing bacteria. However, the taphonomy of biogenic sulfur and iron minerals in these environments remains poorly explored (image recorded during research cruise M190, RV Meteor, July 2023. MARUM, University of Bremen).

Figure 2.2: Work packages (WPs) of this Ph.D. project. A: abiotic experiments were conducted with magnetite nanoparticles synthesized by anoxic titration of Fe(II)- and Fe(III)-chloride in HCl by $NHOH_4$ (WP I, published in Runge et al., 2023, *Earth and Planetary Science Letters*). B: biological experiments were conducted with biogenic magnetite from cultures of the Fe(III)-reducing bacterium *Geobacter sulfurreducens* (WP II, published in Runge et al. 2024, *Communications Earth & Environment*). C: sediment-hosted massive sulfides from the Devonian (~390 Ma) Rammelsberg deposit were studied as a Phanerozoic analog for Precambrian records (here: polished slab of the *Banded Ore* from the Rammelsberg deposit) (WP III, Runge et al., in revision for *Chemical Geology*).

This study takes a geobiological approach to deciphering the taphonomy of microbial biosignatures by combining experimental geomicrobiology with petrographic and stable isotope analysis of a Phanerozoic analog for Precambrian hydrothermal sulfides. We integrate various experimental methods with abiogenic and biogenic sulfur and iron minerals (such as microbial culturing and high-temperature mineral incubation) and analytical techniques (including scanning electron microscopy, secondary ion mass spectrometry, and Raman spectroscopy). This approach aims to constrain the (trans)formation of abiogenic and biogenic sulfur and iron minerals under conditions relevant to sulfidic hydrothermal systems over different temporal and spatial scales. Specifically, this thesis addresses three selected research questions (Q 1 to Q 3) with corresponding targeted work packages (WP I to WP III) (Fig. 2.2, Tab. 2.1). The results of each WP are reported in separate scientific manuscripts (*Chapters 3 to 5*).

The final *Chapter 6* ('Conclusions and Perspectives') synthesizes and critically discusses the main results of this thesis. It derives a framework for assessing the biogenicity of ancient minerals based on the integrated analysis of experimental products, recent and Phanerozoic analogs, and Precambrian hydrothermal sulfides. This framework will substantially help distinguish between abiogenic and biogenic minerals and their transformation products in recent sediments and ancient rocks,

contributing to a more robust reconstruction of the evolution of life in deep time. This chapter further highlights continuing challenges and future research directions for understanding the taphonomy of microbial biosignatures in hydrothermal systems.

Table 2.1: Research questions (Q), corresponding work packages (WP), and chapters of this thesis.

Q 1 What are the mechanisms and products of sulfur and iron mineral (trans)formation under sulfidic hydrothermal conditions?	**WP I** *(Chapter 3*; Runge et al., 2023, *Earth and Planetary Science Letters*) presents experiments constraining the mechanisms and products of mineral transformation reactions under conditions relevant to hydrothermal sulfide systems. Magnetite was chosen as the target mineral because its biologically mediated production is (i) well established in laboratory settings, (ii) common in hydrothermal systems, (iii) dating back to the Archean, and (iv) associated with various mineral properties that differ from its abiogenic counterpart.
Q 2 Does the hydrothermal alteration of microbial biominerals produce distinct taphonomic fingerprints?	**WP II** (*Chapter 4*; Runge et al., 2024, *Communications Earth & Environment*) expands on WP1 by comparing the hydrothermal sulfidation of abiogenic and biogenic magnetite. This study constrains the role of microbial organic matter in the transformation of biogenic magnetite under hydrothermal conditions and characterizes the morphology of the resulting taphonomic products.
Q 3 Can biosignatures of microbial sulfur and iron cycling be preserved in hydrothermal sulfide systems?	**WP III** (*Chapter 5*; Runge et al., in revision for *Chemical Geology*) presents a textural (SEM) and in-situ (SIMS) triple sulfur ($\delta^{34}S$, $\Delta^{33}S$) and iron ($\delta^{56}Fe$) isotope analysis of pyrite in the metamorphic ~390 Ma Rammelsberg sediment-hosted massive sulfides, as a Phanerozoic analog for Precambrian hydrothermal sulfide systems.

REFERENCES

Runge, E., Mansor, M., Chiu, T.-H., Shuster, J., Fischer, S., Kappler, A., and Duda, J.-P., 2024, Hydrothermal sulfidation of biogenic magnetite produces framboid-like pyrite: Communications Earth & Environment, v. 5, p. 252.

Runge, E.A., Mansor, M., Kappler, A., and Duda, J.-P., 2023a, Microbial biosignatures in ancient hydrothermal sulfides: Geobiology, v. 21, p. 355–377.

Runge, E.A., Mansor, M., Shuster, J., Fischer, S., Liu, Y., Lunter, D.J., Kappler, A., and Duda, J.-P., 2023b, Sulfidation of nano-magnetite to pyrite: Implications for interpreting paleoenvironmental proxies and biosignature records in hydrothermal sulfide deposits: Earth and Planetary Science Letters, v. 617, p. 118261, doi:10.1016/j.epsl.2023.118261.

CHAPTER 3 – WORK PACKAGE I

Sulfidation of nano-magnetite to pyrite: implications for interpreting paleoenvironmental proxies and biosignature records in hydrothermal sulfide deposits

Eric A. Runge[1,2†], Muammar Mansor[3], Jeremiah Shuster[4], Stefan Fischer[4], Yali Liu[5], Dominique J. Lunter[5], Andreas Kappler[3,6], and Jan-Peter Duda[1,2,†]

[1]*Sedimentology and Organic Geochemistry, Department of Geosciences, Tübingen University, Germany*
[2]*Geobiology, Geoscience Center, Göttingen University, Germany*
[3]*Geomicrobiology, Department of Geosciences, Tübingen University, Germany*
[4]*Tuebingen Structural Microscopy Core Facility, Tübingen University, Germany*
[5]*Pharmaceutical Technology, Department of Pharmacy and Biochemistry, Tübingen University, Germany*
[6]*Cluster of Excellence EXC 2124, Controlling Microbes to Fight Infection, Tübingen University, Germany*

†corresponding authors

Published in: *Earth and Planetary Science Letters*, 617, 118261 (2023)

3.1 ABSTRACT

Nano-magnetite is a potential archive for biosignatures and paleoenvironmental proxies in hydrothermal systems. However, sulfidic diagenesis at hydrothermal conditions potentially drives the rapid transformation of magnetite to Fe sulfide minerals. The identity and characteristics of transformation products from these reactions are crucial for interpreting biosignature records and paleoenvironmental proxies associated with Fe minerals in sulfide deposits. To constrain the preservation and transformation of magnetite in hydrothermal sulfide habitats, we incubated synthetic nano-magnetite in anoxic artificial seawater at a sulfide:Fe ratio of 4:1 as well as at different pH (7, 10) and temperatures (20-80°C), and in presence or absence of added S^0. Experimental products were analyzed by means of sequential Fe extraction, μ-X-ray diffraction (μ-XRD), Raman spectroscopy, and scanning electron microscopy (SEM). After 46 days, nano-magnetite was only detected at 20°C (pH ~10). Fe(III)-containing mackinawite and greigite formed at pH ~10 and ≥20°C. At pH ~7 and 80°C, magnetite was transformed to pyrite within only 19 days, with faster rates in the presence of polysulfides, which formed from the sulfide-mediated reduction of Fe(III) and in the presence of S^0. Our results demonstrate a potential taphonomic bias against nano-magnetite in sulfidic hydrothermal habitats and suggest that pyrite-associated paleoenvironmental proxies and biosignature records of Fe- and S-cycling microorganisms in hydrothermal deposits are affected by diagenetic fluid-mineral interactions.

3.2 INTRODUCTION

Nano-magnetite in natural environments forms via abiotic Fe(II)-catalyzed transformation of Fe(III) (oxyhydr)oxides or is driven by Fe-cycling microorganisms, such as dissimilatory Fe(III)-reducing bacteria (DIRB) or magnetotactic bacteria (MTB) (Amor et al., 2020; Hansel et al., 2005; Kirschvink and Chang, 1984). Abiotic and biogenic magnetite differ in morphology, crystallographic structure, magnetic properties, redox state, trace metal content, and stable isotopic fingerprints (e.g., Kirschvink and Chang, 1984; Thomas-Keprta et al., 2000; Carvallo et al., 2008; Lam et al., 2010; Amor et al., 2016, 2022; Han et al., 2021). Thus, nano-magnetite is a potential archive for biosignatures of Fe cycling microorganisms. Moreover, the presence of nano-magnetite in sediments and rocks alongside its morphologic, geochemical, and isotopic characteristics has been used to infer past biological productivity, availability of nutrients and substrates, diagenetic redox conditions, climate change, ocean circulation and stratification, as well as paleomagnetic reconstructions (e.g., Chang et al., 2012; Havas et al., 2021; Hesse, 1994; Kopp and Kirschvink, 2008; Schumann et al., 2008; Yamazaki and Kawahata, 1998). However, these applications require a robust understanding of diagenetic processes affecting the preservation of nano-magnetite in different marine environments.

In marine sediments, both abiotic and biogenic magnetite are produced in anoxic to suboxic zones. These precipitates are typically nm-sized and highly reactive due to their large relative surface area (Byrne et al., 2015; Hansel et al., 2005). This affects their preservation potential during sulfidic diagenesis driven by sulfur cycling microbes (SCM); while µm-sized sedimentary magnetite can be preserved for 1000s of years after burial in sulfidic zones (Canfield and Berner, 1987), experimentally synthesized nm-sized magnetite has a half-life of only 72 days at 1 mM dissolved sulfide, pH 7.5, and 25°C (Poulton et al., 2004). Magnetite-producing MTB and DIRB are also widespread in hydrothermal sulfide systems (Roh et al., 2006; Sylvan et al., 2012). In these habitats, sulfide is not only supplied by SCM but also from fluids containing high concentrations of volcanogenic sulfide (Früh-Green et al., 2022). Elevated temperatures and high sulfide concentrations potentially drive the rapid

sulfidation of magnetite in hydrothermal sulfide systems, which are among the most ancient microbial habitats on Earth (Van Kranendonk et al., 2008; Mißbach et al., 2021; Runge et al., 2022).

For hydrothermal sulfide deposits, the implications are twofold: biosignatures and environmental proxies associated with magnetite might be diagenetically altered or erased. On the other hand, the sulfidation of primary magnetite may yield distinct transformation products that might be subject for use as biosignatures and paleoenvironmental proxies themselves. Textural, trace element, and isotopic characteristics of pyrite, for example, are commonly used to trace microbial Fe- and S- cycling, fluid composition and temperature, as well as redox conditions in hydrothermal sulfide environments (e.g., Baumgartner et al., 2020; Li and Kusky, 2007; Nozaki et al., 2020; Ohmoto, 1972; Revan et al., 2014; Rouxel et al., 2004; Vearncombe et al., 1995). This highlights the importance of understanding the formation and diagenetic history of Fe sulfides in such habitats. Previous experiments on magnetite sulfidation were conducted at temperatures ≥125°C (Bendt et al., 2019; Qian et al., 2013, 2010), excess Fe conditions (Nie et al., 2023), or excluded the characterization of transformation products (Poulton et al., 2004). Microbial activity and biogenic mineral formation, however, are limited to temperatures of ≤121°C (Kashefi and Lovley, 2003), which occur along a mixing gradient from hot, acidic and sulfide-rich endmember fluids (~400°C; pH 2-5) to seawater (2-4°C; pH 8) in hydrothermal systems (Früh-Green et al., 2022). The stability of nano-magnetite and the identity and characteristics of its transformation products during in-situ sulfidation under conditions in such mixing zones have not been constrained so far.

Here, we simulate the sulfidic diagenesis of nano-magnetite in hydrothermal systems by incubating synthetic nanoparticles in anoxic artificial seawater at different sulfide:Fe ratios (4:1 and 1:4), pH (~7 and ~10), temperatures (20–80°C), and in the presence or absence of added S^0, an important oxidant in pyrite forming reactions under anoxic conditions (Benning et al., 2000; Mansor and Fantle, 2019) that commonly co-occurs with Fe oxyhydr(oxides) in hydrothermal sulfide systems

(Kelley et al., 2002). The results of our multi-analytical approach, combining sequential Fe extraction, μ-X-ray diffraction (μ-XRD), Raman spectroscopy, and the structural characterization of experimental products by scanning electron microscopy (SEM), demonstrate the rapid transformation of nano-magnetite to pyrite and suggest a strong in-situ taphonomic bias against primary magnetite preservation in hydrothermal sulfidic systems.

3.3 MATERIALS AND METHODS

3.3.1 Synthesis of magnetite nanoparticles

Magnetite nanoparticles were synthesized by dropwise titration of 100 mL anoxic solution containing 0.2 M $FeCl_3$: 0.1 M $FeCl_2$ in 0.3 M HCl with 100 g of anoxic 20% NaOH in a N_2-filled anoxic chamber while stirring at 600 rpm. The resulting suspension containing magnetite particles was further stirred at 600 rpm for 15 min. A magnet was placed against the bottle to hold the magnetic particles in place while the supernatant was removed and replaced by anoxic ultrapure H_2O (Milli-Q, Merck Millipore). This suspension was sonicated for 5 min and again replaced by anoxic ultrapure water. This washing procedure was repeated twice. The successful synthesis of the magnetite nanoparticles was confirmed using μ-X-ray diffraction (μ-XRD) (Fig. 3.S1) and an average crystallite size of 12 nm was calculated based on XRD reflections using the Scherrer equation as detailed in (Mansor et al., 2019).

3.3.2 Experimental setups

The preparation of incubation experiments, sampling, and sample preparation for analysis were conducted in N_2-filled anoxic chamber. Batch experiments were prepared in triplicate with total volumes of 50 mL in 100 mL-volume serum bottles closed with butyl stoppers to prevent the presence of oxygen. Artificial seawater was prepared using 17.30 g/L NaCl, 8.61 g/L $MgCl_2 \cdot 6H_2O$, 0.03 g/L $MgSO_4 \cdot 7H_2O$, 0.99 g/L $CaCl_2 \cdot 2H_2O$, 0.39 g/L KCl, 0.06 g/L KBr, 0.25 g/L NH_4Cl, and 1.85 g/L $NaHCO_3$. The pH of the resulting solution was adjusted to 7 using 0.5 mL of 1 M HCl, and dissolved O_2 was degassed by purging with 50/50 N_2/CO_2. An anoxic 1 M sulfide solution was made by dissolving Na_2S in O_2-free H_2O.

Batch experiments were prepared in triplicate with total volumes of 50 mL in 100 mL-volume serum bottles closed with butyl stoppers. The magnetite suspension and the sulfide solution were added to the artificial seawater at 60 mM sulfide and 15 mM Fe (4:1 molar ratio), representative of hydrothermal fluids in a modern black smoker environment (Hannington et al., 2005). This composition resulted in an initial pH of 10.3 that, during the experiment, remained constant at 20 and 40°C, and slightly decreased to 9.2 and 9.5 at 60 and 80°C, respectively (Fig. 3.S2). Two additional setups were prepared that further contained (i) 200 mM MOPS buffer, and (ii) 200 mM MOPS buffer and 62 mM (100 mg) elemental sulfur (S^0, Sigma Aldrich, product # 13803), respectively. These experiments had a starting pH of 7.0, which slightly increased to 7.4 during the experiment (Fig. 3.S2). The serum bottles for the pH ~10 experiments were incubated at 20, 40, 60, or 80°C, and the pH ~7 experiments were incubated at 80°C. Sampling for geochemical analysis was done after 0, 19, 30, or 46 days. For μ-XRD, Raman spectroscopy, and scanning electron microscopy (SEM), samples were taken after 19, 30, or 46 days.

3.3.3 Geochemical analyses

Aliquots (0.5 mL) of the mineral suspension were centrifuged for 5 min. at 12,100 × *g* to separate the minerals from the "liquid" phase (this phase contains both the combined dissolved and colloidal Fe that did not settle during centrifugation). Fe concentrations in both fractions were quantified spectrophotometrically using the ferrozine assay (Stookey, 1970). Supernatants were acidified with 1 M HCl before analysis. Sequential Fe extraction of the solid phase using 6 M HCl (reactive Fe minerals: magnetite, mackinawite, and greigite) and 8 M HNO_3 (pyrite) was used to determine the extent of pyritization over time (Heron et al., 1994; Huerta-Diaz and Morse, 1990; Poulton and Canfield, 2005). Extraction with 6 M HCl was conducted for 24 hrs in an anoxic chamber in the presence of Ti(III)-citrate to prevent oxidation of dissolved sulfide to S^0, which could reduce Fe extraction yields (Rickard et al., 2006). Solid residues from the 6 M HCl extraction step were extracted with 8 M HNO_3 for >2 hrs. Polysulfides in the liquid phase were analyzed via UV-VIS spectroscopy in 1 mL plastic cuvettes using a spectral range of 250-500 nm.

3.3.4 µ-X-ray diffraction (µ-XRD)

Aliquots for µ-XRD measurements were taken in an N_2-filled anoxic chamber. Mineral pellets were harvested by centrifugation and washed three times with anoxic ultrapure water to remove residual salts before drying. Dry samples were stored in N_2-filled preserving jars until µ-XRD analysis under ambient atmospheric conditions (Boursiquot et al., 2001; Zhang et al., 2020). µ-XRD was performed on dry material using a Bruker's D8 Discover GADDS XRD² micro-diffractometer equipped with a standard sealed tube with a Co-anode (Co Kα radiation, λ = 0.179 nm) at 30 kV/30mA. The total time measurement was 240 seconds at two detector positions (15° and 40°). Phase identification was validated using the Match! Software for phase identification from powder diffraction (Match!, Crystal Impact, Bonn, Germany, version 3.11.5.203) with the Crystallography Open Database (COD-Inorg REV211633 2018.19.25).

3.3.5 Raman spectroscopy

For Raman spectroscopy, aliquots from suspended samples were dried onto glass slides in an anoxic chamber. Glass slides were transported to the instrument in N_2-filled jars. Raman spectra were acquired with an Alpha 500R Confocal Raman Microscope (WITec GmbH, Ulm, Germany), which was equipped with a 532 nm excitation laser, an UHTS 300 spectrometer and a DV401-BV CCD camera. The optical grating was 600 g/mm for recording the spectra in the range of 0 to 3790 cm^{-1}. Herein, a 40× objective with a numerical aperture of 0.6 was used (EC Epiplan-neofluor, Carl Zeiss, Germany). The laser power was adjusted to 1 mW using an optical power meter (PM100D, Thorlabs GmbH, Dachau, Germany) to avoid excessive heating that potentially induces mineral transformation. Per sample, three spots were analyzed using 10 integrations for 10 to 20 seconds each. Spectra from these three spot measurements were combined into a composite spectrum, and relative intensities were normalized to 100. Magnetite and pyrite were identified using the software CrystalSleuth, the RRUFF database (https://rruff.info/; accessed 15 August 2022) and mackinawite (FeS_m) and greigite were compared to reference patterns from (Bourdoiseau et al., 2011, 2008).

3.3.6 Scanning electron microscopy (SEM)

For SEM analysis, samples were washed with anoxic Milli-Q water and dried onto carbon adhesive tabs attached to aluminium stubs in an anoxic chamber. The dried samples were coated with 8 nm of gold using a BAL-TEC SCD 005 sputter coater. The morphological characterization of the minerals was performed using a Crossbeam 550L SEM (Zeiss, Oberkochen, Germany) operating at an acceleration voltage of 2 kV and working distances of 3.7 mm. All micrographs were taken using the Secondary Electron Secondary Ion (SESI) detector.

3.4 RESULTS

3.4.1 Mineralogical analysis

After 46 days of incubation, magnetite was detected only at pH ~10 and 20°C (Fig. 3.1). FeS_m was present in all experiments at pH ~10 (Fig. 3.1). The shifted band positions of FeS_m in our experiment (255 to 257 $cm^{-1}$and 315 to 317 cm^{-1}) relative to Fe(II)-mackinawite (208 and 282 cm^{-1}) indicates the presence of Fe(III) in the crystal structure (Bourdoiseau et al., 2008; Sanden et al., 2021). Greigite was only detected in experiments at pH ~10 and ≤40°C after 46 days (Fig. 3.1), although it formed at 60°C after 7 days (Fig. 3.S3B). Pyrite was only detected after 46 days at pH ~7 (80°C) in both the presence and absence of S^0 (Fig. 3.1).

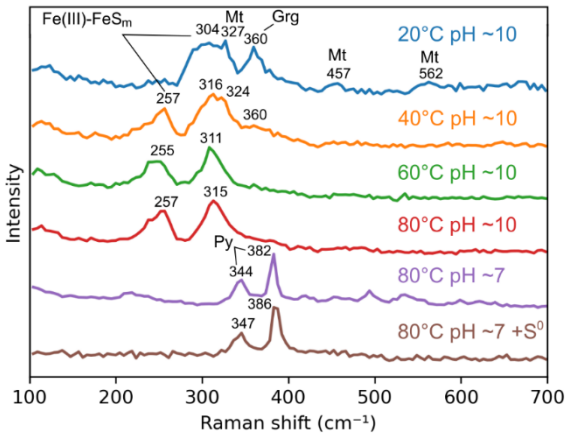

Figure 3.1: Raman spectra of minerals from the incubation experiments after 46 days at a sulfide:Fe ratio of 4:1. Fe(III)-FeS_m: Fe(III)-containing mackinawite; Mt: magnetite; Grg: greigite; Py: pyrite.

3.4.2 Geochemical analysis

In experiments at pH ~10, $Fe(II)_{aq}$ was generally low (≤100 µM) compared to the initial total Fe concentration (15 mM) and decreased slightly over time (Fig. 3.2B; Tab. 3.S1). At 80°C and pH ~10, the fraction of HNO_3 extractable Fe ($Fe[HNO_3/(HCl+HNO_3)]$) slightly increased to 0.1 over 46 days (Fig. 3.2B; Tab. 3.S1), suggesting minor pyrite formation and/or cross-contamination from the 6 M HCl fraction. In experiments at pH ~7, $Fe(II)_{aq}$ was initially higher (~300 µM) compared to ones at pH ~10, and then dropped to ~24 µM within the first 19 days (Fig. 3.2B; Tab. S1). 6 M HCl extraction of the solid phase from these experiments after 19 days yielded black residues that were soluble in HNO_3, suggesting the presence of pyrite (Huerta-Diaz and Morse, 1990). The fraction of HNO_3-extractable Fe ($Fe[HNO_3/(HCl+HNO_3)]$) at pH ~7 increased to ~1 within 46 days, indicating near-complete transformation of magnetite to pyrite with faster reaction rates in the presence of added S^0 (Fig. 3.2B). The yellowish coloring of the liquid phases and UV-VIS spectroscopy revealed that polysulfides formed in the experiments at pH ~7, but not at pH ~10 (Fig. 3.3).

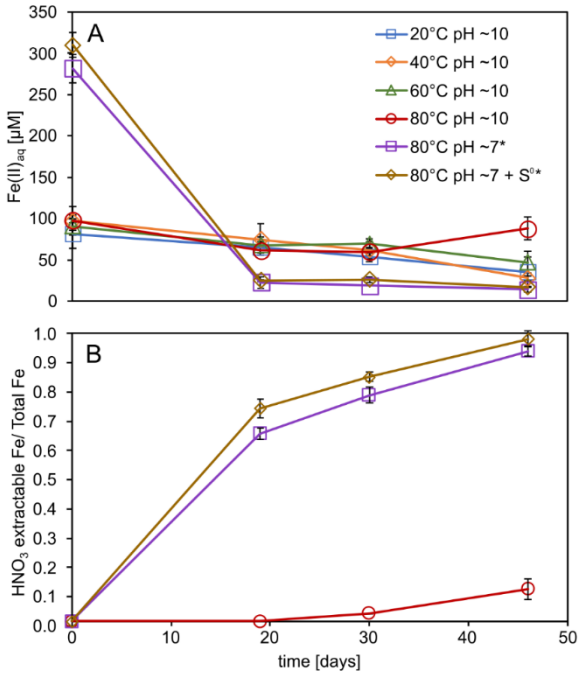

Figure 3.2: Fe geochemistry of batch experiments. The error bars represent standard deviations of triplicate analysis. A: aqueous phase (combined dissolved and colloidal Fe); B: pyritization extent at a sulfide:Fe ratio of 4:1 as determined via sequential Fe extraction of the solid phase using 6 M HCl (magnetite/FeS_m/greigite) and 8 M HNO_3 (pyrite). *Denotes samples in which colloidal particles were not fully removed by centrifugation.

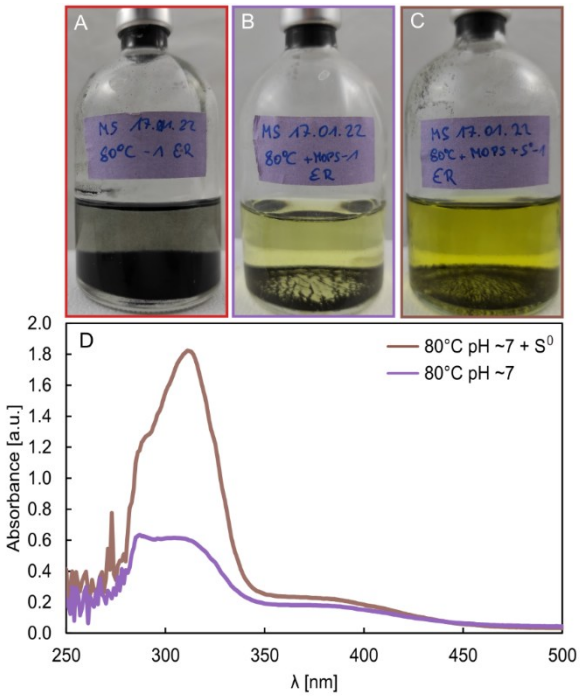

Figure 3.3: Photographs of experimental bottles and UV-VIS spectra of dissolved polysulfides in experiments (80°C, 19 days). No polysulfides were found in the experiments at pH ~10 (A). Polysulfides formation in experiments at pH ~7 was apparent from the yellow coloration (B, C). Note that the liquid in the experiment with added S^0 (C) has a more intense coloration than the experiment without added S^0 (B), indicating increased formation of polysulfides in the presence of added S^0. This is supported by a higher UV-VIS absorbance in the presence of S^0 (D). The difference in the peak position between both experiments at pH ~7 (D) may be due to variations in polysulfide chain-lengths.

3.4.3 SEM

Experiments at pH ~7 contained rosette-like structures comprised of 10s of nm sized platy crystals (Fig. 3.4A-C) that are characteristic of FeS_m (Csákberényi-Malasics et al., 2012; Picard et al., 2018). Pyrite crystals in both experiments at pH ~7 were roughly bi-pyramidal in shape and ca. 2-5 µm in size (Fig. 3.4, e.g., D, I). All pyrite crystals from the experiment without additional S^0 exhibited poorly developed surfaces and had a dendritic habit (Fig. 3.4A-F). Dendritic pyrite also occurred in the presence of added S^0 but was much less prominent; instead, most pyrite crystals appeared more rounded with smoother crystal faces (Fig. 3.4G-L). Notably, pyrite crystals in experiments with added S^0 showed abundant nm-sized surface-bound globules of unknown composition (Fig. 3.4J-L). Over time, these globules increased in size from individual particles (after 19 days) to particle aggregates (after 30 d) (Fig. 3.4J-K). After 46 days, these aggregates were no longer present (Fig. 3.4L).

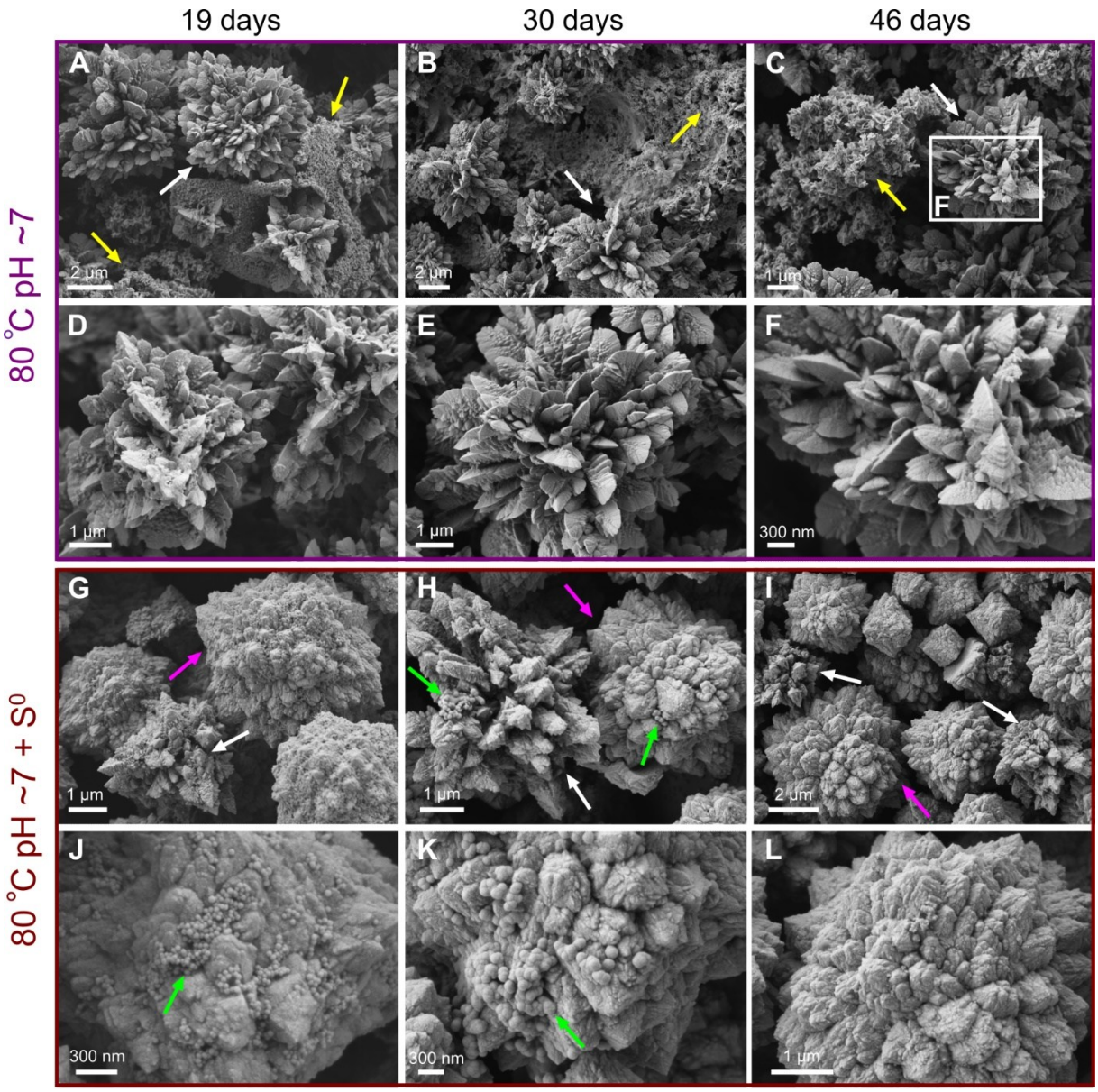

Figure 3.4: SEM micrographs of samples taken throughout the incubation experiments at pH ~7. Pyrite crystals from experiments without added S^0 (purple frame) exclusively exhibited a distinct dendritic habit (A-F; white arrows) and were associated with platy nm-sized particles, likely FeS_m (A-C; yellow arrows). Note that this dendritic habit is still well-preserved after 46 days (F; white arrow). In contrast, most pyrite crystals in experiments without added S^0 (brown frame) appeared more rounded (G-L; pink arrows), although some dendritic pyrite crystals also occur in these experiments (G-I, white arrows). Pyrite crystals from this experiment also contained globular precipitates of unknown composition that were 100s of nanometres in size (H, J-L; green arrows). These precipitates appeared to coalesce over time and become incorporated into pyrite crystals after 46 days (L).

3.5 DISCUSSION

3.5.1 Mineral (trans)formation

We suggest that the removal of magnetite from our experiments is driven by reductive dissolution in presence of excess sulfide (Eq. 1; Poulton et al., 2004). If this is the case, magnetite will dissolve at a much slower rate at excess Fe conditions. Therefore, we performed additional experiments with an equivalent setup to the pH ~10, 60°C runs but varied the S:Fe ratio between 4 and 0.25. Raman spectroscopy of the resulting minerals demonstrates the presence of magnetite and absence of Fe sulfides after 7 days with excess Fe (Fig. 3.S3A). At excess sulfide conditions, in contrast, magnetite signals are strongly diminished while Fe(III)-containing mackinawite (Fe(III)-FeS_m) and greigite are present (Fig. 3.S3B). Therefore, we consider reductive dissolution by sulfide as the key-mechanism for the removal of magnetite from our experiments at excess sulfide conditions.

Eq. 1: $Fe_3O_4 + 4HS^- + 4H^+ \rightarrow 3FeS_m + 4H_2O + S^0$

At pH ~10, the formation of Fe(III)-containing mackinawite (FeS_m) was most likely due to rapid reprecipitation after magnetite dissolution driven by excess sulfide (Eq. 1). The incorporation of Fe(III) into the FeS_m structure may be due to a release of $Fe(III)_{aq}$ from magnetite during mineral dissolution, as previously observed during the reduction of sulfate green-rust $[Fe(II)_4Fe(III)_2(OH)_{12}SO_4 \bullet 8H_2O]$ by sulfate-reducing bacteria (Langumier et al., 2009). Therefore, we suggest that the formation of Fe(III)-containing FeS_m at pH ~10 is the result of a dissolution-reprecipitation mechanism. The exclusive detection of greigite in experiments at pH ~10 and ≤40°C after 46 days (Fig. 3.1) suggests a rate-dependent removal of greigite at higher temperatures, perhaps via reduction to FeS or transformation to pyrite.

At pH ~7, the high initial concentration of $Fe(II)_{aq}$ (Fig. 3.2A; Tab. 3.S1) compared to pH ~10 experiments can be explained by the presence of dissolved or colloidal Fe(II), or both. It is unlikely that this difference is controlled by the solubility of FeS which is independent of pH above pH 6 (Rickard and Luther, 2007). However, it has been demonstrated that colloidal FeS precursors to crystalline FeS_m aggregate upon pH

increase via oriented assembly, suggesting that the formation of FeS_m is promoted at higher pH (Matamoros-Veloza et al., 2018b, 2018a). We therefore attribute the higher initial concentration of $Fe(II)_{aq}$ at pH 7 mainly to the presence of colloidal FeS. The subsequent decrease of $Fe(II)_{aq}$ to ~25 µM after 19 days (pH ~7) (Fig. 3.2A; Tab. 3.S1) is then most likely due to aggregation of colloidal FeS into FeS_m particles that are large enough to settle during centrifugation (Mirabello et al., 2020). We therefore suggest that the growth of initial Fe sulfides in pH ~7 experiments was driven by the assembly of colloidal FeS.

Pyrite can form via reaction of FeS_{aq} precursors with H_2S_{aq} ("H_2S pathway", Eq. 2; Rickard, 1997), surface-mediated sulfidation of Fe (oxyhydr)oxides (Ferric Hydroxide Surface "FHS pathway", Eq. 3a-e; Peiffer et al., 2015), or oxidation of FeS_{aq} by dissolved polysulfides ("polysulfide pathway", Eq. 4, Rickard, 1975). Pyritization via the H_2S pathway is likely of minor importance in our experiments, due the limited abundance of $H_2S_{(aq)}$ from the speciation of $H_2S_{(aq)}/HS^-$ at pH 7 and the fact that the required reactions will be kinetically inhibited under strict anoxic conditions (Benning et al., 2000; Mansor and Fantle, 2019). The FHS pathway requires the presence of Fe (oxyhydr)oxide surfaces to proceed (Peiffer et al., 2015). However, at excess sulfide conditions, magnetite nanoparticles were mostly transformed to Fe sulfides within 7 days even at 60°C (Fig. 3.S3A). At the conditions in our pyrite-forming experiments (80°C, excess sulfide) the removal of magnetite was likely even faster, while pyrite formation proceeded over 46 days (Fig. 3.2B). Therefore, the FHS pathway was most likely not quantitatively important in our experiments. In contrast, the higher abundance of polysulfides in the presence of added S^0 (Fig. 3.3) was associated with a faster pyritization rate (Fig. 3.2B), indicating a rate control of polysulfide availability on pyrite formation. For these reasons, we consider the polysulfide pathway the dominant pyrite formation mechanism in our experiments.

Eq. 2 $FeS_{aq} + H_2S \rightarrow FeS_2 + H_2$

Eq. 3a $>Fe^{III}OH + HS^- \leftrightarrow >Fe^{III}S^- + H_2O$

Eq. 3b $>Fe^{III}S^- \leftrightarrow >Fe^{II}S^{\bullet}$

Eq. 3c $>Fe^{II}S^{\bullet} + H_2O \leftrightarrow >Fe^{II}OH_2^{+} + S^{\bullet-}$

Eq. 3d $>Fe^{II}OH_2^{+} + 2S^{\bullet-} \rightarrow H_2O + >Fe^{II}S_2^{-}$

Eq. 3e $>Fe^{II}S_2^{-} \rightarrow FeS_{2,aq}$ + new surface site

Eq. 4 $FeS_{aq} + S_2^{2-} \rightarrow FeS_2 + S^{2-}$

3.5.2 Polysulfide formation

Polysulfide formation can occur via a reaction of HS^- or H_2S_{aq} with S^0 (Eq. 5; Rickard, 1975). This reaction is consistent with the more intense coloration of polysulfides in the experiment with added S^0 (Fig. 3.3) since sulfide was added in equal amounts to all experiments. However, polysulfides also formed at pH ~7 without added S^0, but not at pH ~10 (Fig. 3.3), suggesting polysulfide formation was also controlled by pH in addition to S^0 abundance. Eq. 5 predicts favorable conditions for polysulfide formation at higher pH, which is inconsistent with our observation (Fig. 3.3). Another possible pathway for polysulfide formation is the oxidation of HS^- on surfaces of Fe(III) mineral surfaces, which are more protonated at pH ~7 than at pH ~10, making surface-mediated oxidation of HS^- more efficient than in circumneutral solutions (Yao and Millero, 1996). Thus, oxidation of HS^- at the magnetite's surface led to formation of polysulfides as well as S^0, which in turn could promote even more polysulfide formation via the reaction between remaining HS^- and newly formed S^0 (Eq. 5).

Eq. 5 $H_2S + S^0 \leftrightarrow S_2^{2-} + 2H^+$

3.5.3 Pyrite crystal growth

The exclusive presence of dendritic pyrite in experiments without added S^0 and the dominance of rounded pyrite in experiments with added S^0 (Fig. 3.4) suggests different particle growth mechanisms and/or reaction kinetics as a function of S^0 abundance. Dendritic pyrite is known from experimental synthesis and black smoker chimneys in the environment, and commonly used as indicator for formation temperatures ≤250°C and rapid crystal growth at high degrees of supersaturation (Murowchick and Barnes, 1987; Wang et al., 2022). This suggests that the growth of dendritic pyrite in our experiments was fast, most likely driven by early surface-

mediated polysulfide formation at pH ~7 and Fe_{aq} from rapidly dissolving magnetite at excess sulfide conditions. The presence of rounded pyrite crystals in experiments with S^0 (Fig. 3.4G-L) is consistent with expected reaction kinetics since S^0 facilitates the formation of polysulfides and thus pyrite (Berg et al., 2020; Rickard, 1975). Therefore, dendritic pyrite in both experiments might reflect the initial precipitation of approximately 2-5 µm-sized pyrite crystals. The presence of surface-associated globules on rounded pyrite crystals (Fig. 3.4J-L), in contrast, indicates a second stage of crystal growth proceeding at a faster rate in the presence of added S^0. Since magnetite surfaces were no longer available, polysulfides formed via Eq. 5 during this stage. The transformation of these globules from individual particles (after 19 days) to larger aggregates (after 30 days) indicates an assembly mechanism for their growth. After 46 days, these aggregates were no longer visible (Fig. 3.4L), suggesting their progressive incorporation into pyrite crystals. Thus, the growth of dendritic to rounded pyrite in the presence of added S^0 seems to proceed via attachment of nanocrystals followed by recrystallization (Gong et al., 2013). This mechanism seems to proceed without a visible increase in particle size (Fig. 3.4G-L), similar to skeletal growth (Salas et al., 2021).

3.5.4 Geological implications

A significant portion of magnetite in marine sediments is produced by DIRB and MTB (Amor et al., 2020; Kirschvink and Chang, 1984), which are widespread in hydrothermal systems (Roh et al., 2006; Sylvan et al., 2012) and might have emerged as early as in the Archean (Johnson et al., 2008; Lin et al., 2017). Indeed, syngenetic magnetite associated with organic matter is present in Earth's oldest hydrothermal sulfide deposits, that is, the ~3.2 Ga Sulphur Springs Group of Western Australia (Baumgartner et al., 2022). Hence, magnetite and its diagenetic transformation products might provide biosignature records in ancient hydrothermal sulfide systems, which are among the most ancient microbial habitats on Earth (Van Kranendonk et al., 2008; Mißbach et al., 2021; Runge et al., 2022). Our study demonstrates that nano-magnetite is rapidly transformed to Fe sulfides under conditions relevant to sulfidic hydrothermal habitats (Fig. 3.5), suggesting that any

structural or geochemical information on paleoenvironmental conditions or microbial processes associated with nano-magnetite is rapidly erased or altered at hydrothermal temperatures as low as 80°C. This likely results in a substantial taphonomic bias against authigenic Fe oxides in sulfidic hydrothermal systems throughout geological time.

Our results suggest that pyrite in hydrothermal deposits can be a secondary product from early diagenetic magnetite sulfidation (Fig. 3.5). The formation of dendritic pyrite in our experiments indicated rapid growth of initial pyrite crystals. In common marine sediments, sulfide is only supplied at a low rate by SCM, resulting in slow magnetite dissolution and a reduced supply of Fe_{aq} (cf. Canfield and Berner, 1987). In hydrothermal systems, however, magnetite sulfidation and dendritic pyrite formation may be driven by abundant sulfide from both biogenic and volcanogenic sources (Früh-Green et al., 2022), causing rapid magnetite dissolution. This implies that morphological, trace element, and isotopic characteristics of some pyrites in sulfide deposits may not record primary signals but be the result of a diagenetic interaction of a magnetite precursor with hydrothermal fluids. Moreover, the observed pyrite growth mechanisms in presence of added S^0 would produce zoned crystals (Salas et al., 2021), which may record geochemical and isotopic signals from multiple growth stages and, hence, time-averaged signals in bulk analysis. Thus, our study highlights the importance of a detailed understanding of diagenetic mineral (trans)formation for interpreting paleoenvironmental and biosignature records of Fe- and S-cycling microorganisms in hydrothermal sulfides.

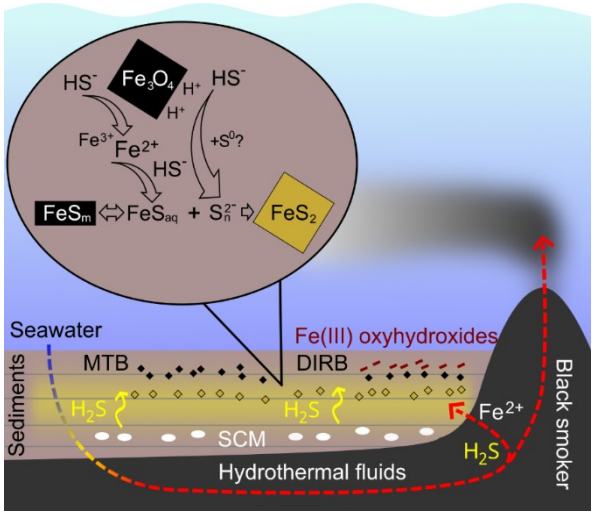

Figure 3.5: Sulfidation of nano-magnetite to pyrite in a hydrothermal sulfide system. Nano-magnetite derives from MTB or reduction of Fe(III) oxyhydroxides by DIRB. During early diagenesis, volcanogenic and/or biogenic (from SCM) sulfide (H_2S/HS^-) in hydrothermal fluids causes reductive dissolution of magnetite in the sediment, yielding Fe^{2+} and minor Fe^{3+}. The reaction of Fe^{2+} and Fe^{3+} with HS^- leads to nucleation of Fe(III)-containing FeS_m. Polysulfides (S_n^{2-}) dominantly form via oxidation of HS^- during interaction with protonated magnetite surfaces and/or oxidation of HS^- by S^0. These polysulfides oxidize FeS_{aq} to pyrite (FeS_2).

3.6 Conclusions

We experimentally demonstrated the rapid sulfidation of nano-magnetite to pyrite under conditions similar to those prevailing in sulfidic hydrothermal habitats. The transformation of magnetite to pyrite occurred within 19 days (80°C, pH ~7) and was faster in the presence of added S^0. This transformation proceeds via a multistep process, involving (i) reductive dissolution of magnetite by aqueous sulfide, (ii) reprecipitation of Fe(III)-containing FeS_m, (iii) transformation of Fe(III)-containing FeS_m to pyrite via the polysulfide pathway, and (iv) pyrite growth via particle attachment. Our findings strongly suggest that sulfidic diagenesis of nano-magnetite in hydrothermal habitats drives pyrite formation, likely resulting in a substantial preservation bias against authigenic magnetite in hydrothermal sulfide systems. Thus, magnetite sulfidation is an important process to consider when interpreting paleoenvironmental proxies and biosignatures of Fe- and S-cycling microorganisms in hydrothermal deposits throughout geological time.

3.7 Acknowledgements

This study was supported by the DFG (SPP 1833, Emmy Noether Programme; DU 1450/3-2, DU 1450/7-1; JPD, ER; INST 37/1027-1 FUGG; AK) as well as by the German Excellence Strategy of the German Federal and State Governments (EXC2124, 390838134; Tübingen Structural Microscopy Core Facility; AK, MM, SF, JS).

3.8 References

Amor, M., Busigny, V., Louvat, P., Gélabert, A., Cartigny, P., Durand-Dubief, M., Ona-Nguema, G., Alphandéry, E., Chebbi, I., Guyot, F., 2016. Mass-dependent and -independent signature of Fe isotopes in magnetotactic bacteria. Science 352, 705–708. https://doi.org/10.1126/science.aad7632

Amor, M., Tharaud, M., Gélabert, A., Komeili, A., 2020. Single-cell determination of iron content in magnetotactic bacteria: implications for the iron biogeochemical cycle. Environ Microbiol 22, 823–831. https://doi.org/10.1111/1462-2920.14708

Amor, M., Wan, J., Egli, R., Carlut, J., Gatel, C., Andersen, I.M., Snoeck, E., Komeili, A., 2022. Key Signatures of Magnetofossils Elucidated by Mutant Magnetotactic Bacteria and Micromagnetic Calculations. JGR Solid Earth 127, e2021JB023239. https://doi.org/10.1029/2021JB023239

Baumgartner, R.J., Teece, B.L., Rasmussen, B., Muhling, J., Rickard, W.D.A., Pejcic, B., Hu, S., Bourdet, J., Caruso, S., Van Kranendonk, M.J., Grice, K., 2022. Exceptional preservation of organic matter and iron-organic colloidal mineralization in hydrothermal black smoker-type sulfide mineralization from the Paleoarchean seafloor. Chemical Geology 121296. https://doi.org/10.1016/j.chemgeo.2022.121296

Baumgartner, R.J., Van Kranendonk, M.J., Pagès, A., Fiorentini, M.L., Wacey, D., Ryan, C., 2020. Accumulation of transition metals and metalloids in sulfidized stromatolites of the 3.48 billion–year–old Dresser Formation, Pilbara Craton. Precambrian Research 337, 105534. https://doi.org/10.1016/j.precamres.2019.105534

Bendt, G., Saddeler, S., Schulz, S., 2019. Sulfidation of Magnetite Nanoparticles – Following the Polysulfide Pathway. European Journal of Inorganic Chemistry 602–608.

Benning, L.G., Wilkin, R.T., Barnes, H.L., 2000. Reaction pathways in the Fe–S system below 100°C. Chemical Geology 167, 25–51. https://doi.org/10.1016/S0009-2541(99)00198-9

Berg, J.S., Duverger, A., Cordier, L., Laberty-Robert, C., Guyot, F., Miot, J., 2020. Rapid pyritization in the presence of a sulfur/sulfate-reducing bacterial consortium. Sci Rep 10, 8264. https://doi.org/10.1038/s41598-020-64990-6

Bourdoiseau, J.-A., Jeannin, M., Rémazeilles, C., Sabot, R., Refait, P., 2011. The transformation of mackinawite into greigite studied by Raman spectroscopy: Transformation of mackinawite into greigite. J. Raman Spectrosc. 42, 496–504. https://doi.org/10.1002/jrs.2729

Bourdoiseau, J.-A., Jeannin, M., Sabot, R., Rémazeilles, C., Refait, Ph., 2008. Characterisation of mackinawite by Raman spectroscopy: Effects of crystallisation, drying and oxidation. Corrosion Science 50, 3247–3255. https://doi.org/10.1016/j.corsci.2008.08.041

Boursiquot, S., Mullet, M., Abdelmoula, M., Génin, J.-M., Ehrhardt, J.-J., 2001. The dry oxidation of tetragonal FeS 1- x mackinawite. Physics and Chemistry of Minerals 28, 600–611. https://doi.org/10.1007/s002690100193

Byrne, J.M., Muhamadali, H., Coker, V.S., Cooper, J., Lloyd, J.R., 2015. Scale-up of the production of highly reactive biogenic magnetite nanoparticles using *Geobacter*

sulfurreducens. J. R. Soc. Interface. 12, 20150240. https://doi.org/10.1098/rsif.2015.0240

Canfield, D.E., Berner, R.A., 1987. Dissolution and pyritization of magnetite in anoxic marine sediments. Deep Sea Research Part B. Oceanographic Literature Review 51, 645–659. https://doi.org/10.1016/0198-0254(87)90182-8

Carvallo, C., Sainctavit, P., Arrio, M.-A., Menguy, N., Wang, Y., Ona-Nguema, G., Brice-Profeta, S., 2008. Biogenic vs. abiogenic magnetite nanoparticles: A XMCD study. American Mineralogist 93, 880–885. https://doi.org/10.2138/am.2008.2713

Chang, L., Roberts, A.P., Williams, W., Fitz Gerald, J.D., Larrasoaña, J.C., Jovane, L., Muxworthy, A.R., 2012. Giant magnetofossils and hyperthermal events. Earth and Planetary Science Letters 351–352, 258–269. https://doi.org/10.1016/j.epsl.2012.07.031

Csákberényi-Malasics, D., Rodriguez-Blanco, J.D., Kis, V.K., Rečnik, A., Benning, L.G., Pósfai, M., 2012. Structural properties and transformations of precipitated FeS. Chemical Geology 294–295, 249–258. https://doi.org/10.1016/j.chemgeo.2011.12.009

Früh-Green, G.L., Kelley, D.S., Lilley, M.D., Cannat, M., Chavagnac, V., Baross, J.A., 2022. Diversity of magmatism, hydrothermal processes and microbial interactions at mid-ocean ridges. Nat Rev Earth Environ 3, 852–871. https://doi.org/10.1038/s43017-022-00364-y

Gong, M., Kirkeminde, A., Ren, S., 2013. Symmetry-Defying Iron Pyrite (FeS2) Nanocrystals through Oriented Attachment. Sci Rep 3, 2092. https://doi.org/10.1038/srep02092

Han, X., Tomaszewski, E.J., Schoenberg, R., Konhauser, K.O., Amor, M., Pan, Y., Warter, V., Kappler, A., Byrne, J.M., 2021. Using Zn and Ni behavior during magnetite precipitation in banded iron formations to determine its biological or abiotic origin. Earth and Planetary Science Letters 568, 117052. https://doi.org/10.1016/j.epsl.2021.117052

Hannington, M.D., De Ronde, C.E.J., Petersen, S., 2005. Sea-Floor Tectonics and Submarine Hydrothermal Systems. Economic Geology 100th Anniversary Volume, 111–141. https://doi.org/10.5382/AV100.06

Hansel, C.M., Benner, S.G., Fendorf, S., 2005. Competing Fe(II)-Induced Mineralization Pathways of Ferrihydrite. Environ. Sci. Technol. 39, 7147–7153. https://doi.org/10.1021/es050666z

Havas, R., Savian, J.F., Busigny, V., 2021. Iron isotope signature of magnetofossils and oceanic biogeochemical changes through the Middle Eocene Climatic Optimum. Geochimica et Cosmochimica Acta 311, 332–352. https://doi.org/10.1016/j.gca.2021.07.007

Heron, Gorm., Crouzet, Catherine., Bourg, A.C.M., Christensen, T.H., 1994. Speciation of Fe(II) and Fe(III) in Contaminated Aquifer Sediments Using Chemical Extraction Techniques. Environ. Sci. Technol. 28, 1698–1705. https://doi.org/10.1021/es00058a023

Hesse, P.P., 1994. Evidence for bacterial palaeoecological origin of mineral magnetic cycles in oxic and sub-oxic Tasman Sea sediments. Marine Geology 117, 1–17. https://doi.org/10.1016/0025-3227(94)90003-5

Huerta-Diaz, M.A., Morse, J.W., 1990. A Quantitative Method for Determination of Trace Metal Concentrations in Sedimentary Pyrite. Marine Chemistry 29, 119–144.

Johnson, C.M., Beard, B.L., Roden, E.E., 2008. The Iron Isotope Fingerprints of Redox and Biogeochemical Cycling in Modern and Ancient Earth. Annu. Rev. Earth Planet. Sci. 36, 457–493. https://doi.org/10.1146/annurev.earth.36.031207.124139

Kashefi, K., Lovley, D.R., 2003. Extending the Upper Temperature Limit for Life. Science 301, 934–934. https://doi.org/10.1126/science.1086823

Kelley, D.S., Baross, J.A., Delaney, J.R., 2002. Volcanoes, Fluids, and Life at Mid-Ocean Ridge Spreading Centers. Annu. Rev. Earth Planet. Sci. 30, 385–491. https://doi.org/10.1146/annurev.earth.30.091201.141331

Kirschvink, J.L., Chang, S.-B.R., 1984. Ultrafine-grained magnetite in deep-sea sediments: Possible bacterial magnetofossils. Geology 12, 559–562.

Kopp, R.E., Kirschvink, J.L., 2008. The identification and biogeochemical interpretation of fossil magnetotactic bacteria. Earth-Science Reviews 86, 42–61. https://doi.org/10.1016/j.earscirev.2007.08.001

Lam, K.P., Hitchcock, A.P., Obst, M., Lawrence, J.R., Swerhone, G.D.W., Leppard, G.G., Tyliszczak, T., Karunakaran, C., Wang, J., Kaznatcheev, K., Bazylinski, D.A., Lins, U., 2010. Characterizing magnetism of individual magnetosomes by X-ray magnetic circular dichroism in a scanning transmission X-ray microscope. Chemical Geology 270, 110–116. https://doi.org/10.1016/j.chemgeo.2009.11.009

Langumier, M., Sabot, R., Obame-Ndong, R., Jeannin, M., Sablé, S., Refait, Ph., 2009. Formation of Fe(III)-containing mackinawite from hydroxysulphate green rust by sulphate reducing bacteria. Corrosion Science 51, 2694–2702. https://doi.org/10.1016/j.corsci.2009.07.001

Li, J., Kusky, T.M., 2007. World's largest known Precambrian fossil black smoker chimneys and associated microbial vent communities, North China: Implications for early life. Gondwana Research 12, 84–100. https://doi.org/10.1016/j.gr.2006.10.024

Lin, W., Paterson, G.A., Zhu, Q., Wang, Y., Kopylova, E., Li, Y., Knight, R., Bazylinski, D.A., Zhu, R., Kirschvink, J.L., Pan, Y., 2017. Origin of microbial biomineralization and magnetotaxis during the Archean. Proc Natl Acad Sci USA 114, 2171–2176. https://doi.org/10.1073/pnas.1614654114

Mansor, M., Berti, D., Hochella, M.F., Murayama, M., Xu, J., 2019. Phase, morphology, elemental composition, and formation mechanisms of biogenic and abiogenic Fe-Cu-sulfide nanoparticles: A comparative study on their occurrences under anoxic conditions. American Mineralogist 104, 703–717. https://doi.org/10.2138/am-2019-6848

Mansor, M., Fantle, M.S., 2019. A novel framework for interpreting pyrite-based Fe isotope records of the past. Geochimica et Cosmochimica Acta 253, 39–62. https://doi.org/10.1016/j.gca.2019.03.017

Matamoros-Veloza, A., Cespedes, O., Johnson, B.R.G., Stawski, T.M., Terranova, U., de Leeuw, N.H., Benning, L.G., 2018a. A highly reactive precursor in the iron sulfide system. Nat Commun 9, 3125. https://doi.org/10.1038/s41467-018-05493-x

Matamoros-Veloza, A., Stawski, T.M., Benning, L.G., 2018b. Nanoparticle Assembly Leads to Mackinawite Formation. Crystal Growth & Design 18, 6757–6764. https://doi.org/10.1021/acs.cgd.8b01025

Mirabello, G., Ianiro, A., Bomans, P.H.H., Yoda, T., Arakaki, A., Friedrich, H., de With, G., Sommerdijk, N.A.J.M., 2020. Crystallization by particle attachment is a colloidal assembly process. Nat. Mater. 19, 391–396. https://doi.org/10.1038/s41563-019-0511-4

Mißbach, H., Duda, J.-P., van den Kerkhof, A.M., Lüders, V., Pack, A., Reitner, J., Thiel, V., 2021. Ingredients for microbial life preserved in 3.5 billion-year-old fluid inclusions. Nat Commun 12, 1101. https://doi.org/10.1038/s41467-021-21323-z

Murowchick, J.B., Barnes, H.L., 1987. Effects of temperature and degree of supersaturation on pyrite morphology. American Mineralogist 72, 1241–1250.

Nie, M., Li, X., Ding, Y., Pan, Y., Cai, Y., Liu, Y., Liu, J., 2023. Effect of Stoichiometry on Nanomagnetite Sulfidation. Environ. Sci. Technol. acs.est.2c08179. https://doi.org/10.1021/acs.est.2c08179

Nozaki, T., Nagase, T., Ushikubo, T., Shimizu, K., Ishibashi, J., and the D/V Chikyu Expedition 909 Scientists, 2020. Microbial sulfate reduction plays an important role at the initial stage of subseafloor sulfide mineralization. Geology 49, 222–227. https://doi.org/10.1130/G47943.1

Ohmoto, H., 1972. Systematics of Sulfur and Carbon Isotopes in Hydrothermal Ore Deposits. Economic Geology 67, 551–578.

Peiffer, S., Behrends, T., Hellige, K., Larese-Casanova, P., Wan, M., Pollok, K., 2015. Pyrite formation and mineral transformation pathways upon sulfidation of ferric hydroxides depend on mineral type and sulfide concentration. Chemical Geology 400, 44–55. https://doi.org/10.1016/j.chemgeo.2015.01.023

Picard, A., Gartman, A., Clarke, D.R., Girguis, P.R., 2018. Sulfate-reducing bacteria influence the nucleation and growth of mackinawite and greigite. Geochimica et Cosmochimica Acta 220, 367–384. https://doi.org/10.1016/j.gca.2017.10.006

Poulton, S.W., Canfield, D.E., 2005. Development of a sequential extraction procedure for iron: implications for iron partitioning in continentally derived particulates. Chemical Geology 214, 209–221. https://doi.org/10.1016/j.chemgeo.2004.09.003

Poulton, S.W., Krom, M.D., Raiswell, R., 2004. A revised scheme for the reactivity of iron (oxyhydr)oxide minerals towards dissolved sulfide. Geochimica et Cosmochimica Acta 68, 3703–3715. https://doi.org/10.1016/j.gca.2004.03.012

Qian, G., Brugger, J., Skinner, W.M., Chen, G., Pring, A., 2010. An experimental study of the mechanism of the replacement of magnetite by pyrite up to 300°C. Geochimica et Cosmochimica Acta 74, 5610–5630. https://doi.org/10.1016/j.gca.2010.06.035

Qian, G., Brugger, J., Testemale, D., Skinner, W., Pring, A., 2013. Formation of As(II)-pyrite during experimental replacement of magnetite under hydrothermal conditions. Geochimica et Cosmochimica Acta 100, 1–10. https://doi.org/10.1016/j.gca.2012.09.034

Revan, M.K., Genç, Y., Maslennikov, V.V., Maslennikova, S.P., Large, R.R., Danyushevsky, L.V., 2014. Mineralogy and trace-element geochemistry of sulfide minerals in hydrothermal chimneys from the Upper-Cretaceous VMS deposits of the eastern Pontide orogenic belt (NE Turkey). Ore Geology Reviews 63, 129–149. https://doi.org/10.1016/j.oregeorev.2014.05.006

Rickard, D., 1997. Kinetics of pyrite formation by the H2S oxidation of iron (II) monosulfide in aqueous solutions between 25 and 125°C: The rate equation. Geochimica et Cosmochimica Acta 61, 115–134. https://doi.org/10.1016/S0016-7037(96)00321-3

Rickard, D., Griffith, A., Oldroyd, A., Butler, I.B., Lopez-Capel, E., Manning, D.A.C., Apperley, D.C., 2006. The composition of nanoparticulate mackinawite, tetragonal iron(II) monosulfide. Chemical Geology 235, 286–298. https://doi.org/10.1016/j.chemgeo.2006.07.004

Rickard, D., Luther, G.W., 2007. Chemistry of Iron Sulfides. Chem. Rev. 107, 514–562. https://doi.org/10.1021/cr0503658

Rickard, D.T., 1975. Kinetics and Mechanism of Pyrite Formation at Low Temperatures. American Journal of Science 275, 636–652.

Roh, Y., Gao, H., Vali, H., Kennedy, D.W., Yang, Z.K., Gao, W., Dohnalkova, A.C., Stapleton, R.D., Moon, J.-W., Phelps, T.J., Fredrickson, J.K., Zhou, J., 2006. Metal Reduction and Iron Biomineralization by a Psychrotolerant Fe(III)-Reducing Bacterium, *Shewanella* sp. Strain PV-4. Appl Environ Microbiol 72, 3236–3244. https://doi.org/10.1128/AEM.72.5.3236-3244.2006

Rouxel, O., Fouquet, Y., Ludden, J.N., 2004. Subsurface processes at the lucky strike hydrothermal field, Mid-Atlantic ridge: evidence from sulfur, selenium, and iron isotopes. Geochimica et Cosmochimica Acta 68, 2295–2311. https://doi.org/10.1016/j.gca.2003.11.029

Runge, E.A., Mansor, M., Kappler, A., Duda, J.-P., 2022. Microbial biosignatures in ancient hydrothermal sulfides. Geobiology 12539.

Salas, P., Ruprecht, P., Hernández, L., Rabbia, O., 2021. Out-of-sequence skeletal growth causing oscillatory zoning in arc olivines. Nat Commun 12, 4069. https://doi.org/10.1038/s41467-021-24275-6

Sanden, S.A., Szilagyi, R.K., Li, Y., Kitadai, N., Webb, S.M., Yano, T., Nakamura, R., Hara, M., McGlynn, S.E., 2021. Electrochemically induced metal- *vs*. ligand-based redox changes in mackinawite: identification of a Fe^{3+} - and polysulfide-containing intermediate. Dalton Trans. 50, 11763–11774. https://doi.org/10.1039/D1DT01684A

Schumann, D., Raub, T.D., Kopp, R.E., Guerquin-Kern, J.-L., Wu, T.-D., Rouiller, I., Smirnov, A.V., Sears, S.K., Lücken, U., Tikoo, S.M., Hesse, R., Kirschvink, J.L., Vali, H., 2008. Gigantism in unique biogenic magnetite at the Paleocene–Eocene Thermal Maximum. Proc. Natl. Acad. Sci. U.S.A. 105, 17648–17653. https://doi.org/10.1073/pnas.0803634105

Stookey, L.L., 1970. Ferrozine - A New Spectrophotometric Feagent for Iron. Anal. Chem. 42, 779–781. https://doi.org/10.1021/ac60289a016

Sylvan, J.B., Toner, B.M., Edwards, K.J., 2012. Life and Death of Deep-Sea Vents: Bacterial Diversity and Ecosystem Succession on Inactive Hydrothermal Sulfides. mBio 3, e00279-11. https://doi.org/10.1128/mBio.00279-11

Thomas-Keprta, K.L., Bazylinski, D.A., Kirschvink, J.L., Clemett, S.J., Mckay, D.S., Wentworth, S.J., Vali, H., Jr, E.K.G., Romanek, C.S., 2000. Elongated prismatic magnetite crystals in ALH84001 carbonate globules: Potential Martian magnetofossils. Geochimica et Cosmochimica Acta 64, 4049–4081.

Van Kranendonk, M., Philippot, P., Lepot, K., Bodorkos, S., Pirajno, F., 2008. Geological setting of Earth's oldest fossils in the ca. 3.5 Ga Dresser Formation, Pilbara Craton, Western Australia. Precambrian Research 167, 93–124. https://doi.org/10.1016/j.precamres.2008.07.003

Vearncombe, S., Barley, M.E., Groves, D.I., McNaughton, N.J., Mikucki, E.J., Vearncombe, J.R., 1995. 3.26 Ga black smoker-type mineralization in the Strelley Belt, Pilbara Craton, Western Australia. Journal of the Geological Society 152, 587–590. https://doi.org/10.1144/gsjgs.152.4.0587

Wang, S., Li, C., Li, B., Dang, Y., Ye, J., Zhu, Z., Zhang, L., Shi, X., 2022. Constraints on fluid evolution and growth processes of black smoker chimneys by pyrite geochemistry: A case study of the Tongguan hydrothermal field, South Mid-Atlantic Ridge. Ore Geology Reviews 140, 104410. https://doi.org/10.1016/j.oregeorev.2021.104410

Yamazaki, T., Kawahata, H., 1998. Organic carbon flux controls the morphology of magnetofossils in marine sediments. Geol 26, 1064–1066. https://doi.org/10.1130/0091-7613(1998)026<1064:OCFCTM>2.3.CO;2

Yao, W., Millero, F.J., 1996. Oxidation of hydrogen sulfide by hydrous Fe(III) oxides in seawater. Marine Chemistry 52, 1–16. https://doi.org/10.1016/0304-4203(95)00072-0

Zhang, Q., Appel, E., Stanjek, H., Byrne, J.M., Berthold, C., Sorwat, J., Rösler, W., Seemann, T., 2020. Humidity related magnetite alteration in an experimental setup. Geophysical Journal International 224, 69–85. https://doi.org/10.1093/gji/ggaa394

3.9 SUPPLEMENTARY MATERIALS

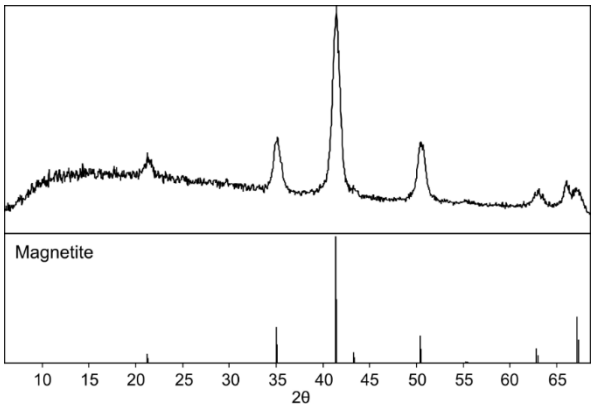

Figure 3.S1: μ-X-ray diffractogram of synthesized magnetite nanoparticles (top) and reflections of a reference magnetite from the Crystallography Open Database (COD-Inorg REV211633 2018.19.25) (bottom).

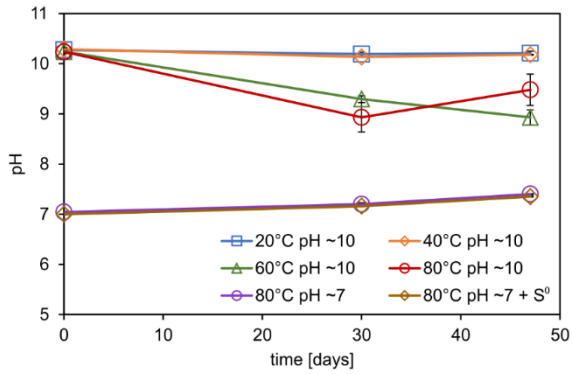

Figure 3.S2: pH of the incubation experiments over time. Data points are given as averages from experimental duplicates. The error bars represent the range of pH values per duplicate.

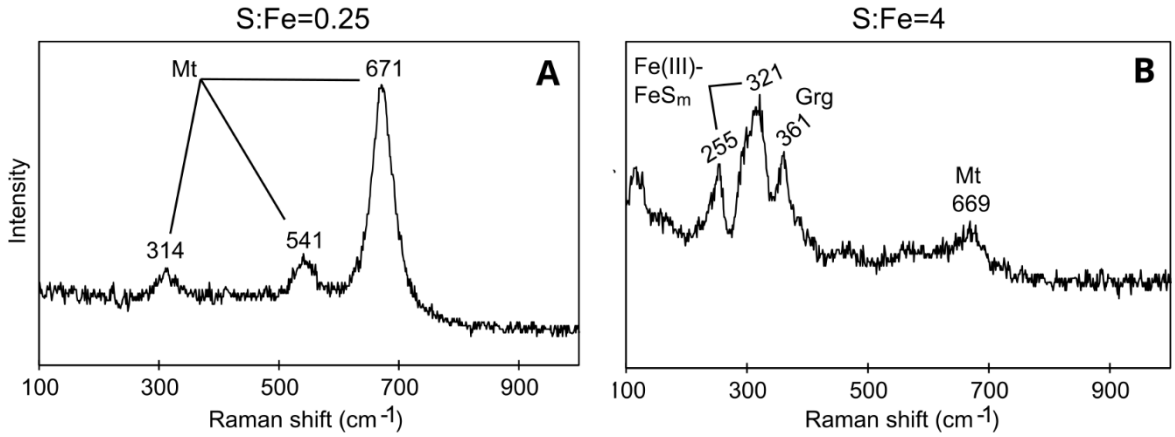

Figure 3.S3: Raman spectroscopy of mineral products after 7 days from additional incubation experiments at pH ~10, 60°C. Fe(III)-FeS_m: Fe(III)-containing mackinawite, Grg: greigite, Mt: magnetite. Mt peak intensities at excess S (A) are strongly diminished as compared to excess Fe conditions (B), and/or masked by newly formed Fe sulfides.

Table 3.S1: Fe concentrations in liquid and solid phases of the incubation experiments. Reported concentrations are mean values of experimental triplicates. *Denotes samples in which colloidal particles were not fully removed by centrifugation.

Experiment	Parameter		0 days	19 days	30 days	46 days
20°C pH 10	$Fe(II)_{aq}$	[µM]	81	65	53	35
	1σ		18	7	2	18
	Fe (HCl)	[mM]	15.0	14.0	34.4	13.0
	1σ		1.3	0.6	8.1	1.0
	Fe (HNO_3)	[mM]	n.d.	n.d.	n.d.	n.d.
	1σ		n.d.	n.d.	n.d.	n.d.
	Fe [HNO_3/(HCl + HNO_3)]		n.d.	n.d.	n.d.	n.d.
	1σ		n.d.	n.d.	n.d.	n.d.
40°C pH 10	$Fe(II)_{aq}$	[µM]	97	75	62	28
	1σ		17	19	3	3
	Fe (HCl)	[mM]	16.9	13.6	27.5	13.5
	1σ		0.5	0.3	5.6	0.7
	Fe (HNO_3)	[mM]	n.d.	n.d.	n.d.	n.d.
	1σ		n.d.	n.d.	n.d.	n.d.
	Fe [HNO_3/(HCl + HNO_3)]		n.d.	n.d.	n.d.	n.d.
	1σ		n.d.	n.d.	n.d.	n.d.
60°C pH 10	$Fe(II)_{aq}$	[µM]	91	68	70	47
	1σ		5	10	5	14
	Fe (HCl)	[mM]	14.0	18.1	42.6	13.8
	1σ		1.1	4.7	3.3	2.0
	Fe (HNO_3)	[mM]	n.d.	n.d.	n.d.	n.d.
	1σ		n.d.	n.d.	n.d.	n.d.
	Fe [HNO_3/(HCl + HNO_3)]		n.d.	n.d.	n.d.	n.d.
	1σ		n.d.	n.d.	n.d.	n.d.
80°C pH 10	$Fe(II)_{aq}$	[µM]	98	62	60	88
	1σ		7	6	12	13
	Fe (HCl)	[mM]	15.4	18.2	34.4	13.2
	1σ		1.1	3.9	9.3	0.8
	Fe (HNO_3)	[mM]	n.d.	n.d.	1.0	1.7
	1σ		n.d.	n.d.	0.2	0.6
	Fe [HNO_3/(HCl + HNO_3)]		n.d.	n.d.	0.03	0.11
	1σ		n.d.	n.d.	0.00	0.04
80°C pH 7	$Fe(II)_{aq}$	[µM]	282*	23	19	15
	1σ		17	7	1	4
	Fe (HCl)	[mM]	12	2.4	2.5	0.6
	1σ		0.6	0.1	0.3	0.2
	Fe (HNO_3)	[mM]	n.d.	4.6	9.2	9.1
	1σ		n.d.	0.2	0.5	0.2

	Fe [HNO_3/(HCl + HNO_3)]		n.d.	0.65	0.79	0.94
	1σ		n.d.	0.02	0.03	0.02
80°C pH 7 + S^0	$Fe(II)_{aq}$	[µM]	310*	25	26	17
	1σ		15	1	4	1
	Fe (HCl)	[mM]	13	1.9	2.3	0.4
	1σ		1.6	0.0	0.3	0.1
	Fe (HNO_3)	[mM]	0	5.7	12.7	13.2
	1σ		0	1.1	1.4	4.1
	Fe [HNO_3/(HCl + HNO_3)]		n.d.	0.74	0.85	0.98
	1σ		n.d.	0.03	0.02	0.03

CHAPTER 4 – WORK PACKAGE II

Hydrothermal sulfidation of biogenic magnetite produces framboid-like pyrite

Eric Runge[1,2,†], Muammar Mansor[3], Tsz Ho Chiu[3], Jeremiah Shuster[4,5], Stefan Fischer[4], Andreas Kappler[3,6], and Jan-Peter Duda[1,2,†]

[1]*Sedimentology and Organic Geochemistry, Department of Geosciences, Tübingen University, Tübingen, Germany*
[2]*Department of Geobiology, Geoscience Center, University of Göttingen, Göttingen, Germany*
[3]*Geomicrobiology, Department of Geosciences, Tübingen University, Tübingen, Germany*
[4]*Tübingen Structural Microscopy Core Facility, Tübingen University, Tübingen, Germany*
[5]*Department of Earth Sciences, Western University, London, Canada*
[6]*Cluster of Excellence EXC 2124, Controlling Microbes to Fight Infection, Tübingen University, Tübingen, Germany*

†corresponding authors

Published in: *Communications Earth & Environment*, 5, 252 (2024)

4.1 Abstract

Biogenic magnetite is a potential biosignature for microbial iron cycling in hydrothermal sulfide systems, critical environments for unraveling the emergence and early evolution of life. However, the preservation potential of biogenic magnetite under hydrothermal conditions is poorly understood. Here, we show that the hydrothermal sulfidation of abiogenic and biogenic magnetite (sulfide/iron = 4, 80°C) yields pyrite with various distinct morphologies, including framboid-like spheroids. We demonstrate that the variability in pyrite morphologies resulted from the modulation of pyritization rates by interrelated effects between organic matter and elemental sulfur (crystalline or colloidal). Notably, framboid-like pyrite, commonly considered a potential fingerprint of microbial sulfur cycling, was exclusively produced from the hydrothermal sulfidation of biogenic (i.e., organic matter-associated) magnetite produced by iron-cycling microorganisms. Thus, framboid-like pyrite can additionally be a taphonomic fingerprint of microbial iron cycling, enabling a better understanding of the evolution of Earth's biosphere in deep time.

4.2 Introduction

Hydrothermal systems are prime environmental candidates for life's emergence due to their potential role in prebiotic organic synthesis [1–3], their steep physical and chemical gradients establishing disequilibrium conditions [4,5], and their existence on Earth for at least 3.77 billion years [2,6–10]. Hydrothermal systems potentially occurred in past surface environments on early Mars [11] and in modern subsurface oceans of Enceladus [12], underscoring their astrobiological significance. Therefore, understanding the proliferation of a microbial biosphere under hydrothermal conditions is crucial. This task requires tools for unraveling the interactions of minerals, organic compounds, and microorganisms in hydrothermal systems on the early Earth. Microbial biosignatures in early Earth's rock record are our only archive for investigating these interactions in deep time [10]. Thus, better constraining the formation and preservation of microbial biosignatures in ancient hydrothermal deposits is fundamental for understanding the emergence and subsequent evolution of life on our planet and beyond.

Nano-magnetite [Fe_3O_4] is an essential piece in this puzzle due to its ubiquitous bio-mediated formation in early Earth's oceans and its potential role in catalyzing vital prebiotic chemical reactions in hydrothermal systems [1,13,14]. On modern Earth, nano-magnetite forms by abiotic Fe(II)-driven transformation of Fe(III) (oxyhydr)oxides or via iron-cycling microorganisms, such as dissimilatory Fe(III)-reducing prokaryotes or magnetotactic bacteria [15–17]. Dissimilatory Fe(III)-reducing prokaryotes and magnetotactic bacteria are thought to have emerged in the Archean [18,19], and commonly occur in modern hydrothermal sulfide environments [20–23]. Indeed, strain 121 (*Geogemma barossii*), one of the most heat-tolerant microorganisms known on Earth to date, is a magnetite-producing Fe(III)-reducing archaeon isolated from a black smoker system [24], highlighting the role of magnetite biomineralization under hydrothermal conditions. Biogenic magnetite has specific morphologic, crystallographic, magnetic, and geochemical properties that differ from abiogenic magnetite [15,25–31]. Biogenic magnetite is also closely associated with organic matter, namely the cells and extracellular polymeric substances of microorganisms involved

in its formation [28,30]. These properties make biogenic magnetite a potential biosignature of iron-cycling microorganisms in hydrothermal environments.

In hydrothermal environments, magnetite might be affected by sulfide delivered from hot and acidic fluids (up to ~400°C; pH 2-5) [32] and microbial sulfur cycling [33], likely exerting a dominant control on its preservation [34]. This is because sulfide can drive the rapid reductive dissolution of nano-magnetite [34–40]. Magnetite sulfidation leads to the formation of secondary iron sulfides, including mackinawite [FeS_m], greigite [Fe_3S_4], and pyrite [FeS_2] [34,35,39]. The mechanisms and rates of these reactions, and the potential transformation of secondary iron sulfides to pyrite, are affected by temperature, solution E_h and pH, sulfur/iron ratio, magnetite stoichiometry, and the presence of trace metal(loid)s [34,39–48]. Moreover, elemental sulfur [S^0], a ubiquitous intermediate sulfur species in hydrothermal systems, can strongly affect magnetite pyritization rates and pyrite morphology [34]. This implies that diagenetic processes in hydrothermal sulfide systems substantially alter biosignatures associated with magnetite.

Previous studies have not considered the interrelated effects of sulfur species (i.e., sulfide, S^0, polysulfides) with organic matter (e.g., microbial biomass) that would be present during the hydrothermal sulfidation of biogenic magnetite. Organic matter is known to affect the surface reactivity and aggregation behavior of Fe(III) (oxyhydr)oxides, including magnetite, and secondary Fe (mono)sulfides [47,49–53]. This potentially influences the textural and geochemical characteristics of the resulting pyrite, which commonly serves as a biosignature of sulfur-cycling microorganisms. For instance, pyrite exhibiting a framboidal morphology is widely used to track microbial sulfur cycling, especially if it encodes ^{34}S-depleted sulfur stable isotope signatures ($\delta^{34}S_{source}$ - $\delta^{34}S_{pyrite}$ >20‰) [54–57]. Framboidal pyrite from modern and ancient environments is commonly associated with organic matter, suggesting an essential role of organic templates in its formation [55,56]. However, experimental work on pyrite formation in active sulfur- and iron-cycling microbial cultures, as well as abiotic diagenesis of biogenic FeS (i.e., in the presence of microbial biomass but no living cells) at high temperatures (75-150°C), yielded <1 to 5 µm sized pyrite spheroids that

do not show the typical raspberry-like texture commonly seen in framboids [58–61]. Furthermore, some experimental studies without organic matter demonstrated abiotic formation pathways for framboidal pyrite (see review by [62]). Nevertheless, while the direct role of microorganisms influencing framboid formation is elusive, Organic matter appears to have a strong impact on pyrite morphology in natural environments. However, the identity and morphology of iron sulfides from the sulfidation of biogenic magnetite under hydrothermal conditions have not been constrained.

Here, we demonstrate experimentally that abiogenic and biogenic magnetite sulfidation under sulfidic hydrothermal conditions (60 mM sulfide, 15 mM iron, in anoxic artificial seawater at 80°C, pH 7.5) yields various pyrite morphologies, including framboid-like spheroids. With μ-X-ray diffraction (μ-XRD), Raman spectroscopy, geochemical analysis ($Fe(II)_{aq}$ and sequential iron extraction), ultraviolet-visible (UV-Vis) spectroscopy, and scanning electron microscopy (SEM) supported by focused ion beam (FIB) milling, we show that the interrelated effects of organic matter and S^0 (62 mM) on magnetite sulfidation rates and mechanisms control the variability of pyrite morphotypes. Notably, our study demonstrates that framboid-like pyrite results from the hydrothermal sulfidation of biogenic magnetite but not abiogenic magnetite. Thus, framboid-like pyrite may not only fingerprint microbial sulfur cycling but also record microbial iron cycling in hydrothermal sulfide systems.

4.3 Results

4.3.1 Mineralogical analyses

After 7 days of incubation, magnetite was neither detected by μ-XRD nor by Raman spectroscopy in any experimental setup (Figs. 4.1,4.2). Instead, pyrite formed in all experiments as indicated by characteristic Raman bands at 330 to 333 cm^{-1} and 366 to 371 cm^{-1} (Fig. 4.2). Pyrite is absent from μ-XRD patterns in experiments with abiogenic magnetite crystalline S^0 (Fig. 4.1). Also, pyrite was not detected by μ-XRD in any experiment with biogenic magnetite (Fig. 4.1). This could be due to a pyrite content below the limit of detection or a poor degree of crystallinity. Mineral products

from experiments with abiogenic magnetite also showed Raman bands characteristic of Fe(III)-containing mackinawite (Fe(III)-FeS_m: 310 to 319 cm^{-1}) [63], but only in the absence of S^0 (Fig. 4.2). In contrast, all experiments with biogenic magnetite contained Fe(III)-FeS_m (Fig. 4.2).

After 21 days of incubation, the mineralogical composition of experiments with abiogenic magnetite remained unchanged (Figs. 4.1,4.2). The appearance of µ-XRD reflections characteristic for pyrite in experiments with both abiogenic and biogenic magnetite (+S^0) may reflect an increasing degree of crystallinity (Fig. 4.1). In experiments with biogenic magnetite and S^0, Fe(III)-FeS_m was no longer detected using Raman spectroscopy (Fig. 4.2). In contrast, µ-XRD reflections characteristic of FeS_m are still present (Fig. 4.1). This is most likely due to the limited spot size during in-situ analysis by Raman spectroscopy.

After 35 days of incubation, pyrite was detected in experiments with biogenic magnetite (no S^0) using µ-XRD (Fig. 4.1). Overall, µ-XRD reflections characteristic of pyrite are broader in the presence of S^0 (Fig. 4.1), indicating greater variability in d-spacing consistent with a lower degree of crystallinity.

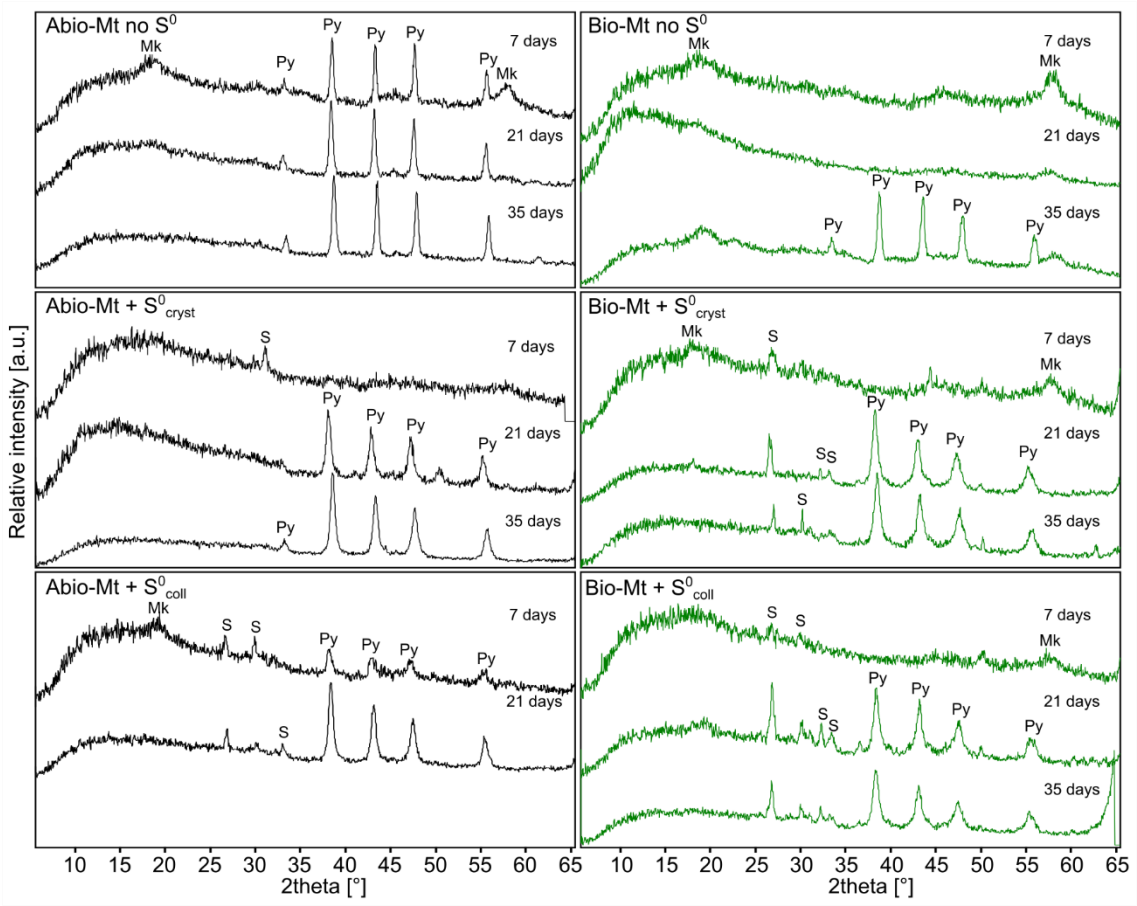

Figure 4.1: µ-XRD patterns for sulfidation experiments with abiogenic magnetite (Abio-Mt, black) and biogenic magnetite (Bio-Mt, green). Mk: Mackinawite; Py: Pyrite; S: S^0. Please note that one sample from the experiment with abiogenic magnetite and colloidal S^0 (35 days) could not be analyzed due to technical problems with the instrument.

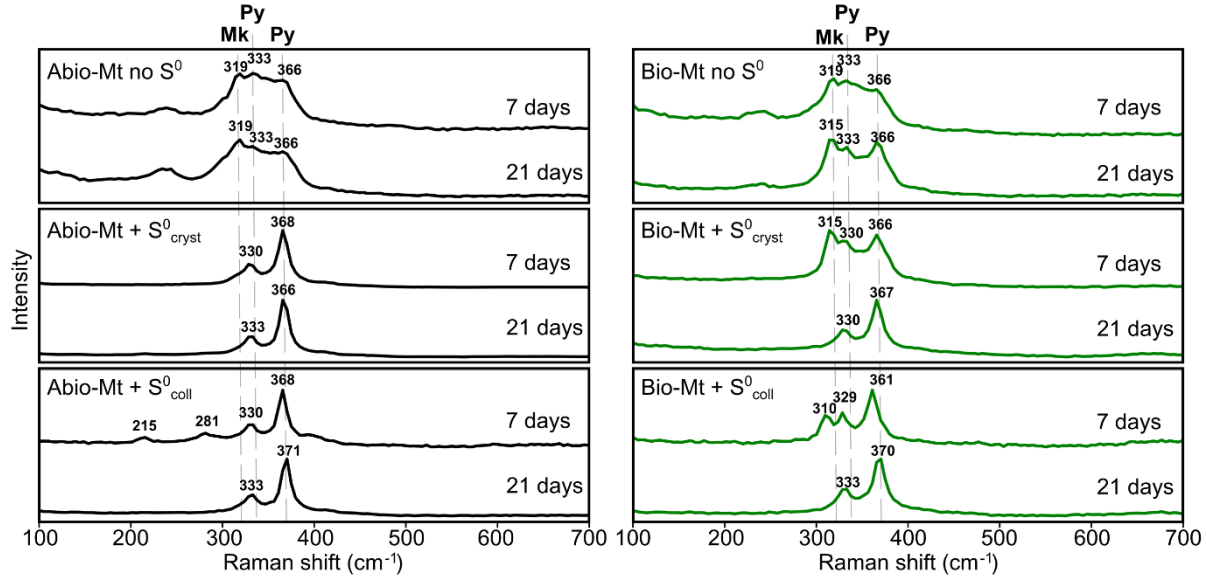

Figure 4.2: Raman spectra for sulfidation experiments with abiogenic magnetite (Abio-Mt, black) and biogenic magnetite (Bio-Mt, green). Mk: Fe(III)-FeS_m, Py: Pyrite. Note that Fe(III)-FeS_m was detected in

experiments with biogenic magnetite and S^0 after 7 days but not in experiments with abiogenic magnetite.

4.3.2 Geochemical analysis

In experiments with and without crystalline S^0, $Fe(II)_{aq}$ was between 43–74 µM at t_0 and decreased to <10 µM during the experiment (Fig. 4.3A, Supplementary Data 4.1). Much higher $Fe(II)_{aq}$ concentrations occurred in the presence of colloidal S^0 (304 µM and 105 µM with abiogenic and biogenic magnetite, respectively; Fig. 4.3A). After 3 days of incubation, $Fe(II)_{aq}$ concentrations in experiments with colloidal S^0 were in the range of the other experiments (Fig. 4.3A).

Sequential iron extraction on the solid phase indicated a much faster increase in the degree of pyritization [$Fe(HNO_3)$/[$Fe(HCl)$+$Fe(HNO_3)$]] in the presence of S^0 for both abiogenic and biogenic magnetite (Fig. 4.3B, Tab. 4.1, Supplementary Data 4.1). Pyritization proceeded faster in experiments with colloidal S^0 than with crystalline S^0 for both abiogenic and biogenic magnetite (Fig. 4.3B, Tab. 4.1). Regardless of the presence of S^0, pyritization rates were slower with biogenic magnetite (Fig. 4.3B, Tab. 4.1).

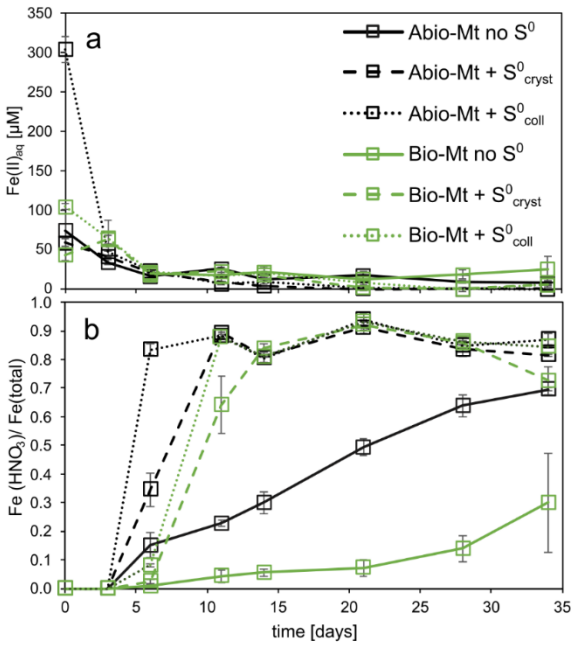

Figure 4.3: Iron geochemistry of sulfidation experiments with abiogenic magnetite (Abio-Mt) and biogenic magnetite (Bio-Mt). The error bars represent the standard deviations of a minimum of experimental duplicates. A: Aqueous phase ($Fe(II)_{aq}$: combined dissolved and colloidal iron); B: Degree of pyritization (DOP) as determined via sequential iron extraction of the solid phase using 6 M HCl (magnetite/FeS_m/greigite) and 8 M HNO_3 (pyrite).

Table 4.1: Degree of pyritization (DOP) after 6 days inferred from sequential iron extraction ($Fe(HNO_3)/Fe(HCl)+Fe(HNO_3)$; see also Fig. 3). Note the faster pyritization rates, indicated by higher DOP, in experiments with abiogenic magnetite and S^0, compared to equivalent experiments with biogenic magnetite or without S^0.

Experiment	DOP (6 days)	SD (1σ)	Apparent pyrite grain size [µm]	Pyrite morphology
Abio-Mt, no S^0	0.15	0.04	2-3	Cubic-euhedral
Abio-Mt, crystalline S^0	0.35	0.06	3-5	Dendritic-octahedral
Abio-Mt, colloidal S^0	0.83	0.02	3-5	Dendritic-octahedral
Bio-Mt, no S^0	0.01	0.00	Nano-crystalline	Nano-crystalline
Bio-Mt, crystalline S^0	0.03	0.01	3-5	Framboid-like spheroid
Bio-Mt, colloidal S^0	0.08	0.00	3-5	Framboid-like spheroid

4.3.3 Ultraviolet-visible (UV-Vis) spectroscopy

At the start (t_0), experiments with colloidal S^0 showed increased UV-Vis absorbances across the analyzed spectrum (250-500 nm) compared to all other experiments (Fig. 4.4A). This is likely due to the presence of colloidal FeS in the supernatant. After 3 days, a yellow coloration of the supernatant indicated the presence of polysulfides in experiments with S^0 (Supplementary Figure 4.1; [64]), supported by UV absorption peaks at 280 and 314 nm (Fig. 4.4B, [48,65]). Experiments with S^0 showed higher absorbances than experiments without S^0, which indicates a higher abundance of dissolved polysulfides (Fig. 4.4B-D; [65]). In the presence of colloidal S^0, the absorbance of peaks characteristic of polysulfides was higher than in the presence of crystalline S^0 (Figs. 4.4B-D, Supplementary Figure 4.1). Generally, experiments with biogenic magnetite showed higher polysulfide abundances than equivalent experiments with abiogenic magnetite (Figs. 4.4B-D, Supplementary Figure 4.1). Polysulfide abundances and the 314 to 280 nm absorbance peak ratio in all experiments increased over time (Figs. 4.4B-E).

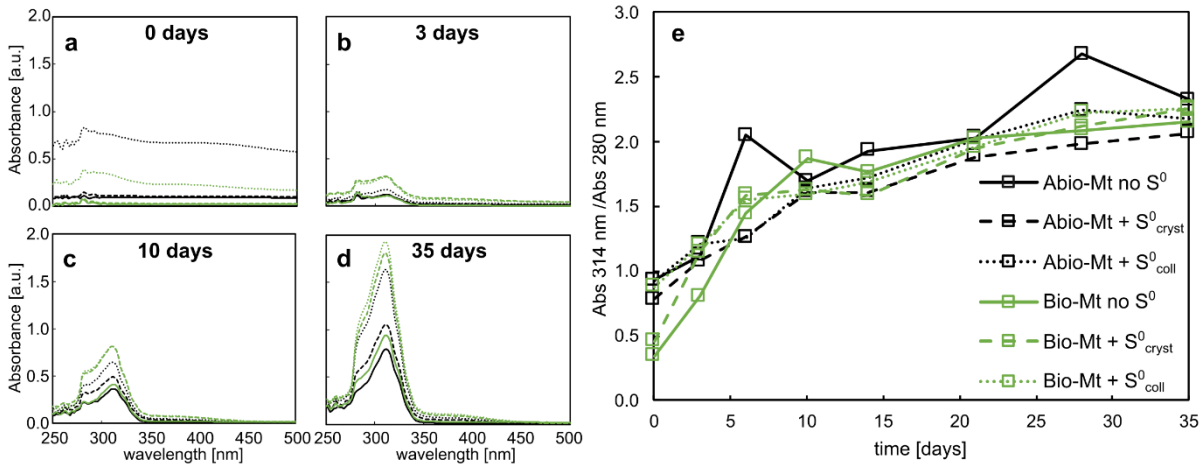

Figure 4.4: UV-Vis spectra of the supernatants in sulfidation experiments with abiogenic magnetite (Abio-Mt) and biogenic magnetite (Bio-Mt). A: Increased absorbance in experiments with colloidal S^0, particularly with abiogenic magnetite, likely due to the presence of colloidal FeS (see also Fig. 4.3A). B-D: Absorption peaks at 280 and 314 nm showing the presence of dissolved polysulfides after 3, 10, and 35 days (B, C, D, respectively). Note that polysulfide abundances are higher in experiments with biogenic magnetite than abiogenic magnetite, with S^0 than no S^0, and with colloidal S^0 than crystalline S^0. E: Ratios of absorbance peaks at 314 and 280 nm.

4.3.4 Scanning electron microscopy (SEM) and focused ion beam (FIB) milling

After 7 days of incubation, all experiments contained platy crystals characteristic of FeS_m (Fig. 4.5A-F, [66,67]). Experiments with abiogenic magnetite but without S^0 further contained µm-sized cubic-euhedral pyrite (Fig. 4.5A). In the presence of both crystalline and colloidal S^0, experiments with abiogenic magnetite contained octahedral-dendritic pyrite (Fig. 4.5B, C). No pyrite was observed in experiments with biogenic magnetite, irrespective of the presence of S^0 (Figs. 4.5D-F). Since Raman spectroscopy and sequential extraction, but not µ-XRD, indicated the presence of pyrite (Figs. 4.1-4.3), the precipitates appear to be nano-crystalline.

After 21 days of incubation (Fig. 4.5G-L), no morphological changes in the precipitates from experiments with abiogenic magnetite were observed (Figs. 4.5G-I). Also, pyrite remained undetected in experiments with biogenic magnetite but without S^0 (Figs. 4.5J). However, samples from experiments with biogenic magnetite and crystalline and colloidal S^0 contained ~3-5 µm sized pyrite spheroids (Figs. 4.5K-L). FIB sections milled after 47 days of incubation revealed remnant internal grain boundaries within the pyrite spheroids, demonstrating that they consist of aggregates of nm-sized pyrite crystals (Fig. 4.6).

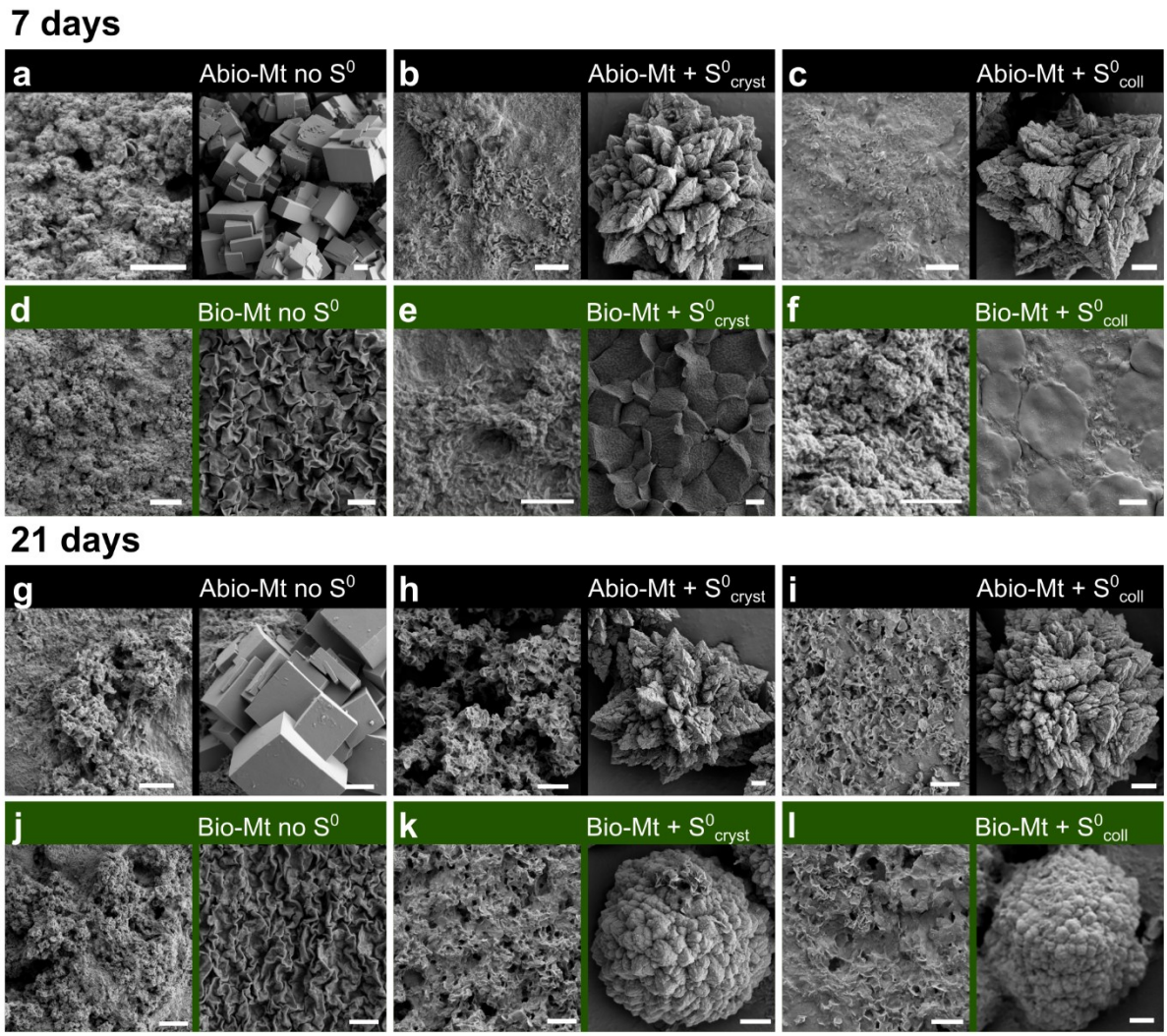

Figure 4.5: SEM images of products from sulfidation of abiogenic magnetite (Abio-Mt, black boxes) and biogenic magnetite (Bio-Mt, green boxes). A-F: SEM images after 7 days. G-L: SEM images after 21 days. FeS_m formed in all experiments. Cubic-euhedral pyrite formed in experiments with neither organic matter (OM) nor S^0 (A, G). In experiments with biogenic magnetite, no pyrite was observed after 7 days, irrespective of the presence of S^0 (D-F). Dendritic-octahedral pyrite formed in experiments without OM but with the addition of S^0 (B, C, H, I). Framboid-like pyrite spheroids only formed in experiments with OM and S^0 after 21 days (K, L). All scale bars are 1 µm.

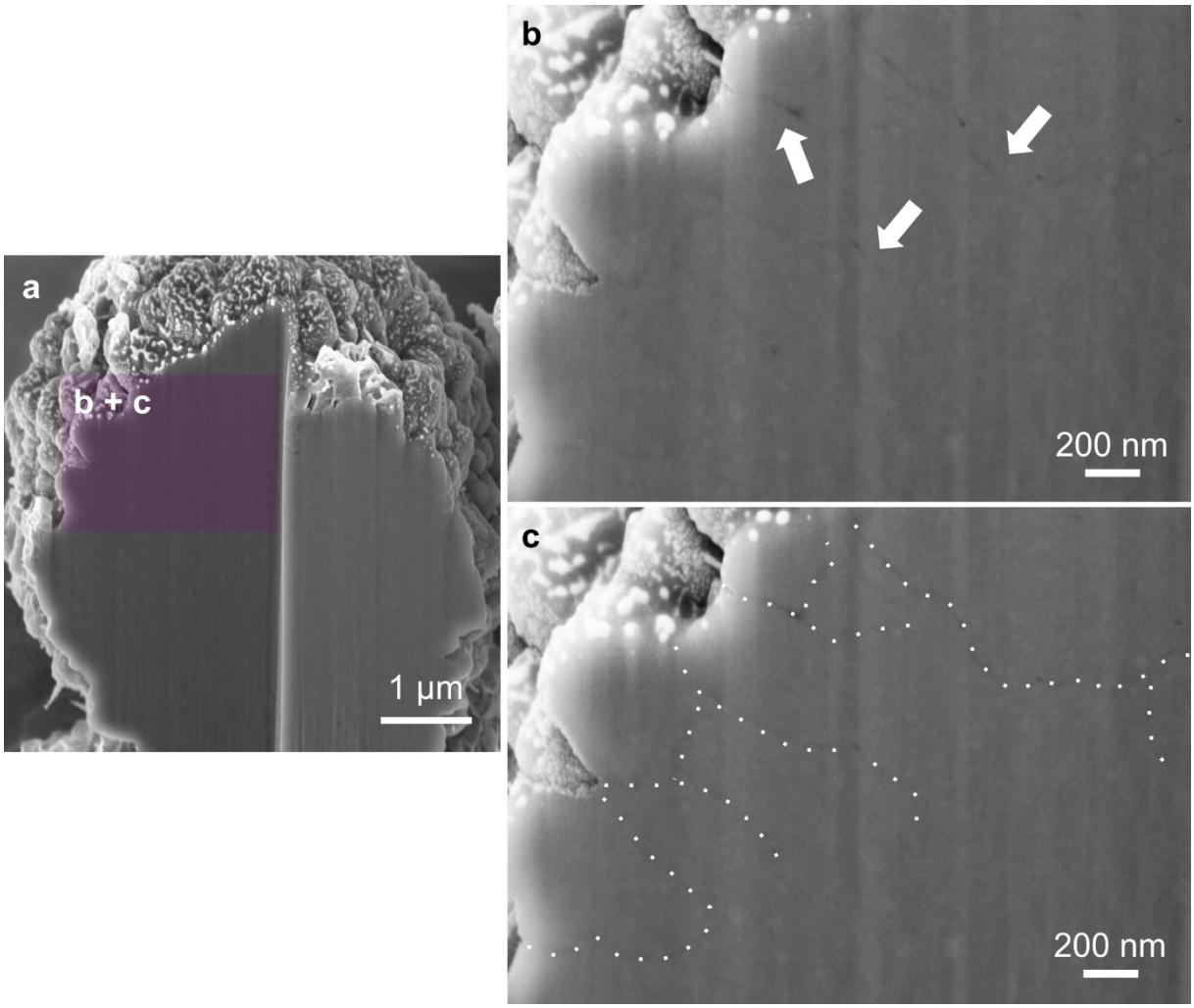

Figure 4.6: SEM images after focused ion-beam (FIB) milling of a framboid-like pyrite spheroid after 47 days of incubation. A: overview of the FIB section. Note the presence of remnant grain boundaries near the edges of the spheroid (white arrows in B, white dotted lines in C).

4.4 Discussion

4.4.1 Magnetite dissolution

The absence of µ-XRD reflections and Raman bands characteristic for magnetite after 7 days (Figs. 4.1-4.2) suggests rapid sulfidation of the magnetite precursor in all experiments. This most likely proceeds via the reductive dissolution of magnetite driven by excess aqueous sulfide [34,36], as supported by the initial increase in $Fe(II)_{aq}$ (Fig. 4.3A). $Fe(II)_{aq}$ likely represents the combined presence of dissolved Fe^{2+}, colloidal FeS particles, and aqueous FeS complexes (Figs. 4.3A, [45,68]). The presence of colloidal FeS in the supernatant is further supported by increased UV-Vis absorbance in these experiments (Fig. 4.4A). Accordingly, the higher $Fe(II)_{aq}$ concentration in experiments

with colloidal S^0 (Fig. 4.3A) is either due to an increased Fe^{2+} release from magnetite dissolution or a higher abundance of colloidal and/or aqueous FeS. An increased liberation of Fe^{2+} is readily explained by a faster dissolution rate of colloidal S^0 compared to crystalline S^0 [69,70], which would release more reactive S species into the system, promoting magnetite dissolution. This is also consistent with higher polysulfide abundances in the presence of colloidal S^0 compared to crystalline S^0 (Fig. 4.4B-D). Polysulfides generated in this process could also complex Fe^{2+}, leading to a higher abundance of aqueous FeS species [71].

We also observed lower initial $Fe(II)_{aq}$ in experiments with biogenic magnetite relative to equivalent setups with abiogenic magnetite (Fig. 4.3A). This could be due to the complexation of $Fe(II)_{aq}$ with organic molecules adsorbed to mineral surfaces (Supplementary Figure 4.2, [50]). Alternatively, OM may passivate surfaces or promote the aggregation of magnetite and FeS_m, lowering their dissolution rate and, thus, $Fe(II)_{aq}$ release [47,51,72]. The rapid decrease in $Fe(II)_{aq}$ after 3 days is likely due to the aggregation of colloidal FeS [73]. Subsequently, $Fe(II)_{aq}$ remains low because FeS is poorly soluble at pH 7.5 [74].

4.4.2 Polysulfide formation

The higher abundance of polysulfides in the presence of S^0 in our experiments suggests the oxidation of aqueous sulfide by S^0 as a relevant process (Fig. 4.4B-D). Indeed, this process is known to yield stable polysulfides at pH >7 [70,75], which agrees with our experiment (pH 7.5). In contrast, the possible formation of polysulfides via oxidation of sulfide by Fe(III) in magnetite is most effective at neutral pH [34,45,76] and hence is likely not the dominant mechanism in the case of our experiments. The higher abundance of polysulfides in experiments with colloidal S^0 relative to crystalline S^0 is likely due to the larger reactive surface of colloidal S^0 (Fig. 4.4B-D, [69,70]). Higher abundances of polysulfides in experiments with biogenic magnetite might suggest that organic matter drives the oxidation of aqueous sulfide to secondary S^0 [77], which then further reacts with sulfide to polysulfides.

4.4.3 Controls on pyritization rate

FeS_m in our experiments co-exists with pyrite after 7 days and disappears after 21 days (Figs. 4.1-4.2, 4.5), suggesting that pyritization proceeds via a FeS_m precursor. The faster pyritization rate in experiments with added S^0 (i.e., at a high polysulfide abundance, Figs. 4.3-4.4) indicates that pyrite in our experiments dominantly forms via the polysulfide pathway (Eq. 1), consistent with previous magnetite sulfidation experiments under anoxic conditions [34,39]. Pyrite formation via the polysulfide pathway predicts a change in the polysulfide speciation (i.e., chain length) over time (Eq. 1, [48]). We speculate that the asymptotic increase in the 314 to 280 nm UV absorption peak ratio during our experiments (Fig. 4.4E) indicates an overall shift towards shorter polysulfide chain lengths, although individual polysulfide species cannot be discriminated with this technique alone.

$$FeS_{aq} + S_n^{2-} \rightarrow FeS_2 + S_{(n-1)}^{2-} \quad (1)$$

Pyritization rates in experiments with biogenic magnetite were systematically slower than in equivalent setups with abiogenic magnetite, irrespective of the addition of S^0 (Fig. 4.3). This is consistent with previous studies demonstrating an inhibitory effect of organic compounds on pyrite formation [47,49,51,52] and demonstrates that organic matter has an additional control on reaction rates. Organic matter may protect S^0 or FeS_m against dissolution, potentially resulting in a decreased formation of polysulfides and, consequently, pyrite [78,79]. Moreover, organic matter sulfurization may act as a sink for polysulfides in experiments with biogenic magnetite, which would not be available for pyrite formation [80]. However, biogenic magnetite experiments showed increased abundances of polysulfides at slower pyritization rates (Figs. 4.3-4.4); hence, pyritization is not limited by polysulfide abundance. More likely, pyritization is inhibited by the sorption of organic matter to FeS_m, decreasing mineral reactivity towards aqueous (poly)sulfide and limiting its aggregation and/or growth [47,79]. This, in turn, may slow down FeS_m transformation to pyrite, especially at the nm scale [81]. This likely explains the inhibition of pyrite formation in the experiment with biogenic magnetite and no S^0.

4.4.4 Rate control on pyrite morphology

In our experiments with abiogenic magnetite, there is a clear relationship between pyritization rate and morphology (Figs. 4.5,4.7). Octahedral-dendritic pyrite formed in the presence of S^0 and at faster pyritization rates are morphologically identical to previously reported pyrites from sulfidation of abiogenic magnetite (Fig. 4.5B, C, H, I, [34]). These crystals likely reflect high degrees of supersaturation, resulting in rapid nucleation [34,82,83]. In contrast, cubic-euhedral pyrite is generally associated with lower degrees of supersaturation and slower growth rates, allowing for well-developed crystal faces [82]. This is consistent with μ-XRD data, showing higher degrees of crystallinity than octahedral-dendritic pyrite produced in experiments with abiogenic magnetite and S^0 (Fig. 4.1).

The slower pyrite growth rates in our experiments with abiogenic magnetite and without S^0 likely resulted from the lower abundance of polysulfides (Figs. 4.4B-D, Supplementary Figure 4.1). Notably, the resulting cubic-euhedral pyrite in this study exhibits a distinctly different habitus than octahedral-dendritic pyrite that formed in previous magnetite sulfidation experiments at equivalent conditions (sulfide/Fe=4, 62 mM S^0) but slightly lower pH (~7 [34] vs. 7.5 in the present study). This effect may be due to pH-dependent polysulfide formation in magnetite suspensions. In our experiments at pH 7.5, the surface-mediated polysulfide formation was muted [76], possibly yielding an overall lower abundance of polysulfides than at pH 7. This may have inhibited the dominant polysulfide pathway for pyrite formation in our experiments at pH 7.5 without S^0, yielding slower pyritization rates. Hence, this highlights that variations of only 0.5 pH units can substantially affect pyrite morphology.

4.4.5 Influence of organic matter on pyrite morphology

Biological organic matter, such as cell walls, microbial extracellular polymeric substances, or intracellular materials, can provide nucleation sites and templates for pyrite formation [55,56,59]. Furthermore, organic compounds may promote pyrite spheroid nucleation in anoxic experimental systems by increasing E_h [59], substantially influencing pyrite morphology [84]. Organic matter also appears to strongly control

pyrite morphology in our experiments. For instance, the slowest pyritization rates were observed in experiments with biogenic magnetite but without S^0 (Fig. 4.3). Here, pyrite was evidenced with Raman spectroscopy, µ-XRD, and sequential extraction but is not visible in SEM even after 21 days, supporting slow growth to only very small particle sizes (Figs. 4.5-4.7). Organic matter was suggested to inhibit the growth and transformation of ferrihydrite in the presence of Fe(II) or sulfide via particle aggregation and Ostwald ripening [47,53,85]. Possibly, a similar mechanism affects nanoparticulate pyrite or its precursors, such as FeS_m, in our experiment. On the other hand, experiments with biogenic magnetite and S^0 contained ~3-5 µm-sized pyrite spheroids after 21 days, while no such spheroids were observed after the sulfidation of abiogenic magnetite (Figs. 4.5-4.7). Based on our data, it cannot be resolved whether templating effects or organic matter-induced kinetic effects primarily drive pyrite spheroid formation. However, the pyritization of biogenic magnetite likely proceeds via a complex interplay of these factors, with organic matter playing a key role in controlling pyrite morphology.

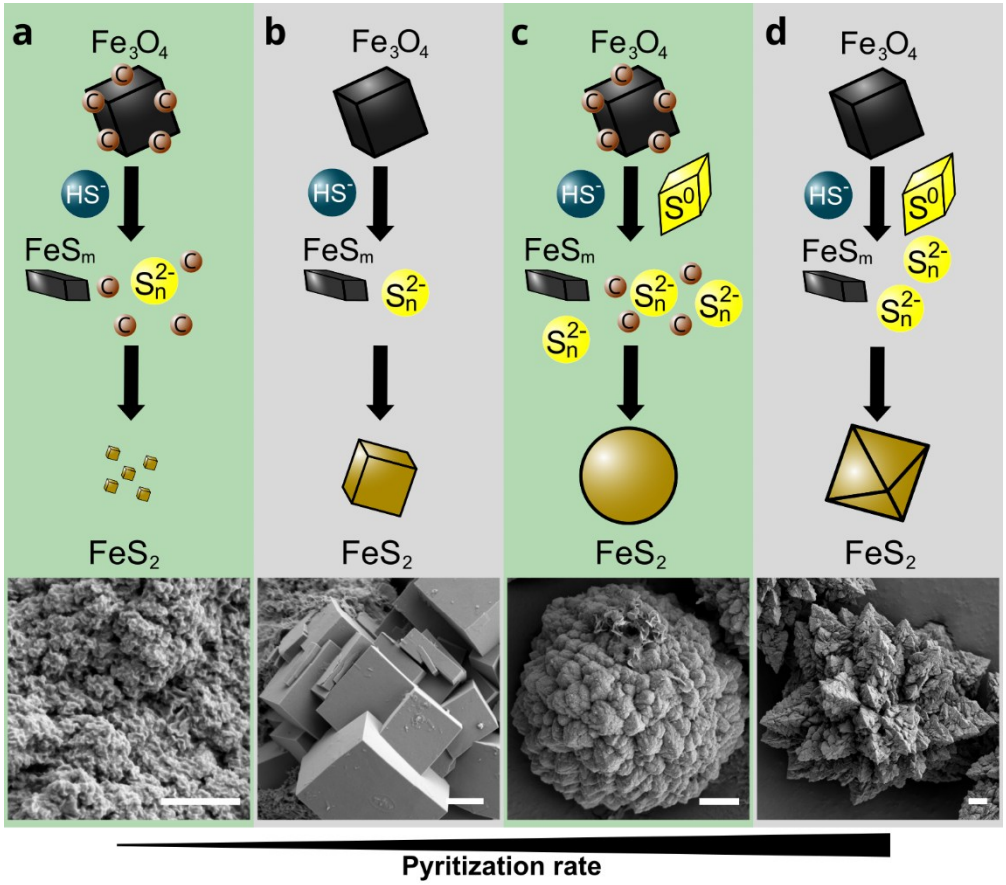

Figure 4.7: Pyrite morphology after sulfidation of abiogenic and biogenic magnetite as a function of pyritization rate and the presence of organic matter (OM). Magnetite is reductively dissolved by aqueous HS^- (and H_2S, not shown), releasing Fe^{2+} (and minor Fe^{3+}, not shown), which reprecipitates as Fe(III)-FeS_m. A: Sulfidation of magnetite in the presence of OM but without S^0 yields the slowest pyritization rates, resulting in nanoparticulate pyrite (not observed in SEM). B: Without OM and S^0, pyrite growth is slow, yielding cubic-euhedral pyrite. C: In the presence of OM and S^0, the pyritization rate is high, and OM mediates the formation of pyrite spheroids. D: In the absence of OM but in the presence of S^0, pyritization rates are the highest, yielding octahedral-dendritic pyrite. All scale bars are 1 μm.

Spheroids vs. framboids – similarities and differences

Framboidal pyrite is commonly used to track microbial sulfur cycling in modern and ancient environments. This, however, requires that the analyzed precipitates are pristine products of primary geomicrobiological processes. While lacking the diagnostic raspberry-like internal texture, pyrite spheroids in our experiment approximate pyrite framboids in anoxic and sulfidic sediments [86] concerning the overall spherical habit, aggregational texture, and size (~3-5 μm). Moreover, the organic matter-mediated formation of pyrite spheroids in our experiment is broadly analogous to mechanisms proposed for generating pyrite framboids in sedimentary deposits, including sulfate-reducing biofilms or microbial mats [54–56]. This suggests that in the presence of biogenic (i.e., organic matter-associated) precursor iron minerals and S^0, framboid-like pyrite spheroids could form in the same environments as true framboids. Moreover, petrographic observations suggest that diagenetic and hydrothermal alteration of pyrite framboids can induce infilling and recrystallization processes that drive their textural evolution towards spherical precipitates that do not exhibit pristine internal textures [87]. Indeed, some pyrite in ancient rocks described as framboids show an overall spherical habit but lack the internal texture of pristine framboids (e.g., [10,57,88]). While our findings do not refute that these precipitates are indeed infilled or recrystallized framboids [10,89], we suggest that some of such pyrite may have been originally pyrite spheroids, particularly in hydrothermal environments.

4.4.6 Spheroids as biosignatures for iron cycling microorganisms?

We demonstrated that the hydrothermal sulfidation of biogenic magnetite can drive the formation of framboid-like pyrite. Consistent with previous experimental studies

[59], this indicates that microbial sulfur cycling is not necessarily the critical mechanism for forming framboid-like pyrite, meaning that such precipitates may not be specific biosignatures for sulfur-cycling microorganisms. Instead, framboid-like pyrite may be the product of the diagenetic transformation of biogenic iron minerals, such as magnetite produced by dissimilatory Fe(III)-reducing prokaryotes or magnetotactic bacteria, under sulfidic conditions (Fig. 4.7C). Framboid-like pyrite may result from the sulfidation of biogenic magnetite irrespective of whether reduced sulfur species are biogenic (i.e., from microbial sulfur cycling) or abiogenic (e.g., volcanogenic) in origin. This means framboid-like pyrite may be a promising taphonomic fingerprint of precursor biominerals resulting from microbial iron cycling, particularly in hydrothermal sulfide systems.

4.5 Conclusions

We demonstrated that sulfidation of abiogenic and biogenic magnetite yields pyrite under sulfidic hydrothermal conditions. Pyritization rates and pyrite morphology were strongly controlled by S^0 (S^0 promoting pyritization; cubic-euhedral without S^0, octahedral-dendritic with S^0), pH (octahedral-dendritic at pH 7, cubic euhedral at pH 7.5), and organic matter (inhibiting pyritization). Notably, S^0 and organic matter promoted the formation of ~3-5 μm pyrite spheroids that resembled pyrite framboids, demonstrating that framboid-like pyrite can form via the hydrothermal sulfidation of biogenic magnetite under sulfidic conditions. This suggests that some framboid-like pyrite in ancient rocks may represent original pyrite spheroids rather than recrystallized or infilled pyrite framboids, particularly in hydrothermal deposits. Moreover, our study highlights the need to constrain the impact of diagenetic processes on pyrite morphologies. Framboid-like pyrite may represent a taphonomic product from the sulfidation of biogenic magnetite. Therefore, framboid-like pyrite is not only a potential fingerprint of microbial sulfur cycling but can also record microbial iron cycling in hydrothermal systems.

4.6 METHODS

4.6.1 Starting materials

For experiments with abiogenic magnetite (i.e., without organic matter), we synthesized magnetite nanoparticles in an N_2-filled anoxic chamber according to previously described procedures [34]. For experiments with biogenic magnetite (i.e., with organic matter), we prepared magnetite nanoparticles via dissimilatory Fe(III) reduction of 2-line ferrihydrite by *Geobacter sulfurreducens*. The 2-line ferrihydrite was prepared by reaction of $Fe(NO_3)_3 \cdot 9H_2O$ (40 g) with KOH (1 M) until pH 7.0 [90]. The material was centrifuged (26000 × *g*; 10 min) and washed three times in Milli-Q H_2O to remove nitrate ions and then purged with N_2 to remove O_2. A dense culture of *G. sulfurreducens* was inoculated at 10% (v/v) in a total volume of 100 mL growth medium in a 200 mL serum bottle and closed with butyl stoppers. The growth medium contained 30 mM $NaHCO_3$, 25 mM Na acetate, 40 mM Na fumarate, and 1 mL each of SL-10 trace element solution, seven vitamin solution, and selenite-tungstate solution [91]. In the late exponential phase (after ~48 h, OD_{600} ~0.5), the cells were centrifuged at (5300 × *g*; 20 min) and washed in 50 mL of 10 mM HEPES buffer solution (pH 7.0) three times. The resulting cell pellets were resuspended in 10 mM HEPES buffer solution and then added at OD_{600} = 0.38 to a Fe(III)-reduction medium containing 10 mM HEPES buffer, 25 mM Na acetate, and 50 mM 2-line ferrihydrite at 30°C for three days. The dissimilatory Fe(III)-reduction was conducted in 25 mL total volume in 50 mL serum bottles closed with butyl stoppers. Anoxic and sterile conditions were maintained during all steps in the preparation of biogenic magnetite.

Both abiogenic and biogenic magnetite were washed by holding the particles in place, placing a hand-magnet to the outside of the serum bottle, decanting the supernatant, adding ~80 mL O_2-free ultrapure H_2O (Milli-Q, Merck Millipore), and sonicating for 5 minutes. This procedure was repeated two times. The total organic carbon contents (TOC) of the abiogenic and biogenic magnetite suspensions were determined as the sum of the dissolved organic carbon (DOC) in the liquid phase and the organic carbon content of the solid phase (Supplementary Table 1). After centrifugation at 12,100 × *g*

for 5 minutes, the DOC of the liquid phase was analyzed using a Multi N/C analyzer 2100S (Analytik Jena GmbH) as the non-purgeable organic carbon after acidification with 50 µL of 2 M HCl. For organic carbon analyses of the solid phase, samples were dried at 50 °C and powdered with a ball mill. Double determination analysis was conducted using a Vario Cube Elemental Analyzer (Elementar Analysesysteme GmbH), and quantification was done using the sulfanilamide standard. The resulting TOC of the abiogenic and biogenic magnetite suspensions were 0.98 mM and 9.29 mM, respectively. The average crystallite sizes of the synthesized abiogenic and biogenic magnetite (confirmed by µ-XRD; Supplementary Figure 4.2), as calculated using the Scherrer equation [92], were 12 nm and 9 nm, respectively.

Artificial seawater was prepared using 17.30 g/L NaCl, 8.61 g/L $MgCl_2 \bullet 6H_2O$, 0.03 g/L $MgSO_4 \bullet 7H_2O$, 0.99 g/L $CaCl_2 \bullet 2H_2O$, 0.39 g/L KCl, 0.06 g/L KBr, 0.25 g/L NH_4Cl, and 1.85 g/L $NaHCO_3$. The pH of the resulting solution was adjusted to 7.0 using 1 M HCl, and dissolved O_2 was degassed by purging with 50/50 N_2/CO_2. An anoxic 1 M sulfide solution was made by dissolving Na_2S in O_2-free ultrapure H_2O. Colloidal S^0 was prepared by dropwise addition of 10 mL concentrated H_2SO_4 to 30 mL 3 M Na-thiosulfate [$Na_2S_2O_3 \times 5H_2O$] solution, which was immersed in an ice bath. Precipitation of colloidal S^0 in this process yielded a yellow suspension. The aggregation of colloidal S^0 was induced by the addition of 40 mL saturated NaCl solution. To remove excess NaCl, the colloidal S^0 was allowed to settle overnight, the supernatant was removed, and 50 mL of 2% NaCl was added. This process was repeated three times. The resulting suspension was transferred to a serum bottle and purged with N_2 to remove O_2. The concentration of the colloidal S^0 stock was determined gravimetrically after drying an aliquot at 60°C.

4.6.2 Experimental setups

The preparation of incubation experiments, sampling, and sample preparation for analysis were conducted in an N_2-filled anoxic chamber. Batch experiments were prepared with total volumes of 50 mL in 100 mL-volume serum bottles closed with butyl stoppers to prevent the presence of oxygen. We used a minimum of two experimental replicates for chemical analysis (pH, sequential Fe extraction). At least

one additional replicate per setup was prepared for mineralogical analysis (Raman spectroscopy, μ-XRD) and SEM.

The magnetite suspensions and the sulfide solution were added to the artificial seawater at 60 mM sulfide and 15 mM iron (4:1 molar ratio). This mixing ratio resulted in 0.14 mM and 1.3 mM added TOC from abiogenic and biogenic magnetite, respectively. To each experimental setup, 100 mM MOPS buffer was added, which resulted in an average initial pH of 7.46±0.06 (Supplementary Figure 4.3). During the experiment, the pH remained constant within ±0.1 pH units (i.e., decreased to 7.38±0.03; Supplementary Figure 4.3). For both abiogenic and biogenic magnetite experiments, we prepared two additional setups that further contained 62 mM of commercially available crystalline S^0 (100 mg, Sigma Aldrich, product # 13803) or pre-synthesized colloidal S^0 (suspended in 2% NaCl solution), respectively. Light microscopy observations indicate that crystalline S^0 particles were ~30 μm while colloidal S^0 particles were ≤ 5 μm in size. All serum bottles were incubated at 80°C.

4.6.3 Geochemical analyses

Aliquots (0.5 mL) of the mineral suspension were centrifuged for 5 minutes at 12,100 × *g* to separate the minerals from the aqueous phase (this phase contains both the combined dissolved and colloidal iron that did not settle during centrifugation). Concentrations of Fe^{2+} in the aqueous phase and total iron in the solid phase were quantified spectrophotometrically using the ferrozine assay [93]. Supernatants were acidified with 1 M HCl before analysis. Sequential iron extraction of the solid phase using 6 M HCl (reactive iron minerals: magnetite, mackinawite, and greigite) and 8 M HNO_3 (pyrite) was used to determine the degree of pyritization over time [94,95]. Extraction with 6 M HCl was conducted for 24 hours in an anoxic chamber in the presence of Ti(III)-citrate to prevent oxidation of dissolved sulfide to S^0, which could reduce iron extraction yields [96]. Solid residues from the 6 M HCl extraction step were extracted with 8 M HNO_3 for >2 hrs. Centrifuged aliquots of the liquid phase were analyzed in duplicates for the presence of polysulfides via UV-Vis spectroscopy in 96-well plates using a spectral range of 250-500 nm. The resulting spectra were normalized using a Milli-Q blank.

4.6.4 µ-X-ray diffraction (µ-XRD)

Aliquots for µ-XRD measurements were taken in an N_2-filled anoxic chamber. Mineral pellets were harvested by centrifugation and washed three times with anoxic ultrapure water to remove residual salts before drying. Dry samples were stored in N_2-filled preserving jars until µ-XRD analysis under ambient atmospheric conditions [97,98]. µ-XRD was performed on dry material using a Bruker's D8 Discover GADDS XRD² micro-diffractometer equipped with a standard sealed tube with a copper-anode (Co Kα radiation, λ = 0.179 nm) at 30 kV/30mA. The total time measurement was 240 seconds at two detector positions (15° and 40°). Phase identification was validated using the Match! Software for phase identification from powder diffraction (Match!, Crystal Impact, Bonn, Germany, version 3.11.5.203) with the Crystallography Open Database (COD-Inorg REV211633 2018.19.25).

4.6.5 Raman spectroscopy

Aliquots from suspended samples were dried onto glass slides in an anoxic chamber. Glass slides were transported to the instrument in N_2-filled jars. Raman spectra were acquired with an Alpha 500R Confocal Raman Microscope (WITec GmbH, Ulm, Germany), which was equipped with a 532 nm excitation laser, a UHTS 300 spectrometer, and a DV401-BV CCD camera. The optical grating was 600 g/mm for recording the spectra from 0 to 3790 cm^{-1}. A 40× objective with a numerical aperture of 0.6 was used (EC Epiplan-neofluor, Carl Zeiss, Germany). The laser power was adjusted to ≤1 mW using an optical power meter (PM100D, Thorlabs GmbH, Dachau, Germany) to avoid heat-induced mineral transformation. Three spots were analyzed per sample using up to 10 integrations of 10 to 20 seconds each. Spectra from these three spot measurements were combined into a composite spectrum, and relative intensities were normalized to 100. Pyrite was identified using the software CrystalSleuth, the RRUFF database (https://rruff.info/; accessed 16 August 2023), and Fe(III)- FeS_m was compared to reference patterns from Bourdoiseau et al. (2008) [63].

4.6.6 Scanning electron microscopy (SEM) and focused-ion beam (FIB) milling

Aliquots from experimental duplicates were pooled and washed three times with anoxic Milli-Q water. These samples were dried onto a carbon adhesive tab attached to an aluminum stub in an anoxic chamber. Once dry, the samples were coated with 8 nm of gold using a BAL-TEC SCD 005 sputter coater to reduce charging effects during analysis. Morphological characterization of experimental products was performed using a Crossbeam 550L SEM (Zeiss, Oberkochen, Germany) operating at an acceleration voltage of 2 kV and working distances of 5.2 mm. All micrographs were taken using the Secondary Electron Secondary Ion (SESI) detector.

FIB milling was performed on a Zeiss Crossbeam 550L. A SEM stub was coated with a thin layer of Tempfix (Plano G3305). The coated stub was held at a temperature of approx. 40 °C and the anoxically dried sample was sprinkled onto its surface. After reaching room temperature, the sample was sputter-coated with 8 nm of platinum. A cross-section through the object of interest was made using the 300 pA – 30 kV FIB probe. In a second step, the surface of the cross-section was polished using the 2 pA – 30 kV FIB probe. Images were generated using the InLens detector at an acceleration voltage of 5 kV and a probe current of 100 pA.

4.7 Acknowledgements

We thank François Guyot and two anonymous reviewers for their constructive feedback. This study was supported by the DFG (SPP 1833, Emmy Noether Programme; DU 1450/3-2, DU 1450/7-1; JPD, ER; INST 37/1027-1 FUGG; AK) as well as by the German Excellence Strategy of the German Federal and State Governments (EXC2124, 390838134; Tübingen Structural Microscopy Core Facility; AK, MM, SF, JS). We thank James M. Byrne for advice on preparing biogenic magnetite and Prachi Joshi, Aude Picard, and Julie Cosmidis for helpful discussions on the experimental design. Jorinel-Manuel Domingos kindly provided colloidal S^0. Eva Voggenreiter and Johann Holdt helped with TOC analysis. Dominique J. Lunter and Hans Schönfelder are thanked for their assistance with Raman spectroscopy.

4.8 References

1. McCollom, T. M. & Seewald, J. S. Abiotic Synthesis of Organic Compounds in Deep-Sea Hydrothermal Environments. *Chem. Rev.* **107**, 382–401 (2007).

2. Russell, M. J., Hall, A. J. & Martin, W. Serpentinization as a source of energy at the origin of life: Serpentinization and the emergence of life. *Geobiology* **8**, 355–371 (2010).

3. Mißbach, H. *et al.* Assessing the diversity of lipids formed via Fischer-Tropsch-type reactions. *Organic Geochemistry* **119**, 110–121 (2018).

4. Baross, J. A. & Hoffman, S. E. Submarine hydrothermal vents and associated gradient environments as sites for the origin and evolution of life. *Origins Life Evol Biosphere* **15**, 327–345 (1985).

5. Martin, W., Baross, J., Kelley, D. & Russell, M. J. Hydrothermal vents and the origin of life. *Nat Rev Microbiol* **6**, 805–814 (2008).

6. Rasmussen, B. Filamentous microfossils in a 3,235-million-year-old volcanogenic massive sulphide deposit. *Nature* **405**, 676–679 (2000).

7. Van Kranendonk, M., Philippot, P., Lepot, K., Bodorkos, S. & Pirajno, F. Geological setting of Earth's oldest fossils in the ca. 3.5 Ga Dresser Formation, Pilbara Craton, Western Australia. *Precambrian Research* **167**, 93–124 (2008).

8. Dodd, M. S. *et al.* Evidence for early life in Earth's oldest hydrothermal vent precipitates. *Nature* **543**, 60–64 (2017).

9. Duda, J.-P. *et al.* Ideas and perspectives: hydrothermally driven redistribution and sequestration of early Archaean biomass – the "hydrothermal pump hypothesis". *Biogeosciences* **15**, 1535–1548 (2018).

10. Runge, E. A., Mansor, M., Kappler, A. & Duda, J.-P. Microbial biosignatures in ancient hydrothermal sulfides. *Geobiology* 12539 (2022).

11. Franz, H. B. *et al.* Large sulfur isotope fractionations in Martian sediments at Gale crater. *Nature Geosci* **10**, 658–662 (2017).

12. Hsu, H.-W. *et al.* Ongoing hydrothermal activities within Enceladus. *Nature* **519**, 207–210 (2015).

13. Li, Y.-L., Konhauser, K. O. & Zhai, M. The formation of magnetite in the early Archean oceans. *Earth and Planetary Science Letters* **466**, 103–114 (2017).

14. Ozturk, S. F. & Sasselov, D. D. On the origins of life's homochirality: Inducing enantiomeric excess with spin-polarized electrons. *Proc. Natl. Acad. Sci. U.S.A.* **119**, e2204765119 (2022).

15. Kirschvink, J. L. & Chang, S.-B. R. Ultrafine-grained magnetite in deep-sea sediments: Possible bacterial magnetofossils. *Geology* **12**, 559–562 (1984).

16. Hansel, C. M., Benner, S. G. & Fendorf, S. Competing Fe(II)-Induced Mineralization Pathways of Ferrihydrite. *Environ. Sci. Technol.* **39**, 7147–7153 (2005).

17. Amor, M., Tharaud, M., Gélabert, A. & Komeili, A. Single-cell determination of iron content in magnetotactic bacteria: implications for the iron biogeochemical cycle. *Environ Microbiol* **22**, 823–831 (2020).

18. Vargas, M., Kashefi, K., Blunt-Harris, E. L. & Lovley, D. R. Microbiological evidence for Fe(III) reduction on early Earth. *Nature* **395**, 65–67 (1998).

19. Lin, W. *et al.* Origin of microbial biomineralization and magnetotaxis during the Archean. *Proc Natl Acad Sci USA* **114**, 2171–2176 (2017).

20. Suzuki, Y., Inagaki, F., Takai, K., Nealson, K. H. & Horikoshi, K. Microbial Diversity in Inactive Chimney Structures from Deep-Sea Hydrothermal Systems. *Microbial Ecology* **47**, 186–196 (2004).

21. Roh, Y. *et al.* Metal Reduction and Iron Biomineralization by a Psychrotolerant Fe(III)-Reducing Bacterium, *Shewanella* sp. Strain PV-4. *Appl Environ Microbiol* **72**, 3236–3244 (2006).

22. Lin, J. T. *et al.* Magnetite formation from ferrihydrite by hyperthermophilic archaea from Endeavour Segment, Juan de Fuca Ridge hydrothermal vent chimneys. *Geobiology* **12**, 200–211 (2014).

23. Nakano, S. *et al.* Bullet-shaped magnetosomes and metagenomic-based magnetosome gene profiles in a deep-sea hydrothermal vent chimney. *Front. Microbiol.* **14**, 1174899 (2023).

24. Kashefi, K. & Lovley, D. R. Extending the Upper Temperature Limit for Life. *Science* **301**, 934–934 (2003).

25. Thomas-Keprta, K. L. *et al.* Elongated prismatic magnetite crystals in ALH84001 carbonate globules: Potential Martian magnetofossils. *Geochimica et Cosmochimica Acta* **64**, 4049–4081 (2000).

26. Carvallo, C. *et al.* Biogenic vs. abiogenic magnetite nanoparticles: A XMCD study. *American Mineralogist* **93**, 880–885 (2008).

27. Lam, K. P. *et al.* Characterizing magnetism of individual magnetosomes by X-ray magnetic circular dichroism in a scanning transmission X-ray microscope. *Chemical Geology* **270**, 110–116 (2010).

28. Amor, M. *et al.* Chemical signature of magnetotactic bacteria. *Proceedings of the National Academy of Sciences* **112**, 1699–1703 (2015).

29. Amor, M. *et al.* Key Signatures of Magnetofossils Elucidated by Mutant Magnetotactic Bacteria and Micromagnetic Calculations. *JGR Solid Earth* **127**, e2021JB023239 (2022).

30. Han, X. *et al.* Using Zn and Ni behavior during magnetite precipitation in banded iron formations to determine its biological or abiotic origin. *Earth and Planetary Science Letters* **568**, 117052 (2021).

31. Kappler, A., Thompson, A. & Mansor, M. Impact of Biogenic Magnetite Formation and Transformation on Biogeochemical Cycles. *Elements* **19**, 222–227 (2023).

32. Früh-Green, G. L. *et al.* Diversity of magmatism, hydrothermal processes and microbial interactions at mid-ocean ridges. *Nat Rev Earth Environ* **3**, 852–871 (2022).

33. Reysenbach, A.-L. & Cady, S. L. Microbiology of ancient and modern hydrothermal systems. *Trends in Microbiology* **9**, 79–86 (2001).

34. Runge, E. A. *et al.* Sulfidation of nano-magnetite to pyrite: Implications for interpreting paleoenvironmental proxies and biosignature records in hydrothermal sulfide deposits. *Earth and Planetary Science Letters* **617**, 118261 (2023).

35. Canfield, D. E. & Berner, R. A. Dissolution and pyritization of magnetite in anoxic marine sediments. *Deep Sea Research Part B. Oceanographic Literature Review* **51**, 645–659 (1987).

36. Poulton, S. W., Krom, M. D. & Raiswell, R. A revised scheme for the reactivity of iron (oxyhydr)oxide minerals towards dissolved sulfide. *Geochimica et Cosmochimica Acta* **68**, 3703–3715 (2004).

37. Qian, G., Brugger, J., Skinner, W. M., Chen, G. & Pring, A. An experimental study of the mechanism of the replacement of magnetite by pyrite up to 300°C. *Geochimica et Cosmochimica Acta* **74**, 5610–5630 (2010).

38. Qian, G., Brugger, J., Testemale, D., Skinner, W. & Pring, A. Formation of As(II)-pyrite during experimental replacement of magnetite under hydrothermal conditions. *Geochimica et Cosmochimica Acta* **100**, 1–10 (2013).

39. Bendt, G., Saddeler, S. & Schulz, S. Sulfidation of Magnetite Nanoparticles – Following the Polysulfide Pathway. *European Journal of Inorganic Chemistry* 602–608 (2019).

40. Nie, M. *et al.* Effect of Stoichiometry on Nanomagnetite Sulfidation. *Environ. Sci. Technol.* acs.est.2c08179 (2023) doi:10.1021/acs.est.2c08179.

41. Benning, L. G., Wilkin, R. T. & Barnes, H. L. Reaction pathways in the Fe–S system below 100°C. *Chemical Geology* **167**, 25–51 (2000).

42. Gong, M., Kirkeminde, A. & Ren, S. Symmetry-Defying Iron Pyrite (FeS2) Nanocrystals through Oriented Attachment. *Sci Rep* **3**, 2092 (2013).

43. Peiffer, S. *et al.* Pyrite formation and mineral transformation pathways upon sulfidation of ferric hydroxides depend on mineral type and sulfide concentration. *Chemical Geology* **400**, 44–55 (2015).

44. Wan, M., Schröder, C. & Peiffer, S. Fe(III):S(-II) concentration ratio controls the pathway and the kinetics of pyrite formation during sulfidation of ferric hydroxides. *Geochimica et Cosmochimica Acta* **217**, 334–348 (2017).

45. Hockmann, K., Planer-Friedrich, B., Johnston, S. G., Peiffer, S. & Burton, E. D. Antimony mobility in sulfidic systems: Coupling with sulfide-induced iron oxide transformations. *Geochimica et Cosmochimica Acta* **282**, 276–296 (2020).

46. Baya, C. *et al.* Influence of trace level As or Ni on pyrite formation kinetics at low temperature. *Geochimica et Cosmochimica Acta* **300**, 333–353 (2021).

47. Wang, Q. *et al.* Transformations of Ferrihydrite–Extracellular Polymeric Substance Coprecipitates Driven by Dissolved Sulfide: Interrelated Effects of Carbon and Sulfur Loadings. *Environ. Sci. Technol.* acs.est.2c06921 (2023) doi:10.1021/acs.est.2c06921.

48. Domingos, J. M. *et al.* Inferred pyrite growth via the particle attachment pathway in the presence of trace metals. *Geochem. Persp. Let.* **26**, 14–19 (2023).

49. Wilkin, R. T. & Barnes, H. L. Pyrite formation by reactions of iron monosulfides with dissolved inorganic and organic sulfur species. *Geochimica et Cosmochimica Acta* **60**, 4167–4179 (1996).

50. Morse, J. W. & Wang, Q. Pyrite formation under conditions approximating those in anoxic sediments: II. Influence of precursor iron minerals and organic matter. *Marine Chemistry* **57**, 187–193 (1997).

51. Rickard, D., Butler, I. B. & Oldroyd, A. A novel iron sulphide mineral switch and its implications for Earth and planetary science. *Earth and Planetary Science Letters* **189**, 85–91 (2001).

52. ThomasArrigo, L. K., Bouchet, S., Kaegi, R. & Kretzschmar, R. Organic matter influences transformation products of ferrihydrite exposed to sulfide. *Environ. Sci.: Nano* **7**, 3405–3418 (2020).

53. Hiemstra, T., Mendez, J. C. & Li, J. Evolution of the reactive surface area of ferrihydrite: time, pH, and temperature dependency of growth by Ostwald ripening. *Environ. Sci.: Nano* **6**, 820–833 (2019).

54. Popa, R., Kinkle, B. K. & Badescu, A. Pyrite Framboids as Biomarkers for Iron-Sulfur Systems. *Geomicrobiology Journal* **21**, 193–206 (2004).

55. Maclean, L. C. W. *et al.* A high-resolution chemical and structural study of framboidal pyrite formed within a low-temperature bacterial biofilm. *Geobiology* **6**, 471–480 (2008).

56. Wacey, D. *et al.* Uncovering framboidal pyrite biogenicity using nano-scale CNorg mapping. *Geology* **43**, 27–30 (2015).

57. Duda, J.-P. *et al.* A Rare Glimpse of Paleoarchean Life: Geobiology of an Exceptionally Preserved Microbial Mat Facies from the 3.4 Ga Strelley Pool Formation, Western Australia. *PLoS ONE* **11**, e0147629 (2016).

58. Duverger, A. *et al.* Mechanisms of Pyrite Formation Promoted by Sulfate-Reducing Bacteria in Pure Culture. *Front. Earth Sci.* **8**, 588310 (2020).

59. Duverger, A., Bernard, S., Viennet, J., Miot, J. & Busigny, V. Formation of pyrite spherules from mixtures of biogenic FeS and organic compounds during experimental diagenesis. *Geochem Geophys Geosyst* (2021) doi:10.1029/2021GC010056.

60. Berg, J. S. *et al.* Rapid pyritization in the presence of a sulfur/sulfate-reducing bacterial consortium. *Sci Rep* **10**, 8264 (2020).

61. Truong, C. *et al.* Production of carbon-containing pyrite spherules induced by hyperthermophilic Thermococcales: a biosignature? *Front. Microbiol.* **14**, 1145781 (2023).

62. Ohfuji, H. & Rickard, D. Experimental syntheses of framboids—a review. *Earth-Science Reviews* **71**, 147–170 (2005).

63. Bourdoiseau, J.-A., Jeannin, M., Sabot, R., Rémazeilles, C. & Refait, Ph. Characterisation of mackinawite by Raman spectroscopy: Effects of crystallisation, drying and oxidation. *Corrosion Science* **50**, 3247–3255 (2008).

64. Steudel, R. & Chivers, T. The role of polysulfide dianions and radical anions in the chemical, physical and biological sciences, including sulfur-based batteries. *Chem. Soc. Rev.* **48**, 3279–3319 (2019).

65. Vorlicek, T. P., Kahn, M. D., Kasuya, Y. & Helz, G. R. Capture of molybdenum in pyrite-forming sediments: role of ligand-induced reduction by polysulfides. *Geochimica et Cosmochimica Acta* **68**, 547–556 (2004).

66. Csákberényi-Malasics, D. *et al.* Structural properties and transformations of precipitated FeS. *Chemical Geology* **294–295**, 249–258 (2012).

67. Picard, A., Gartman, A., Clarke, D. R. & Girguis, P. R. Sulfate-reducing bacteria influence the nucleation and growth of mackinawite and greigite. *Geochimica et Cosmochimica Acta* **220**, 367–384 (2018).

68. Noël, V. *et al.* FeS colloids – formation and mobilization pathways in natural waters. *Environ. Sci.: Nano* **7**, 2102–2116 (2020).

69. Hartler, N., Libert, J. & Teder, A. Rate of Sulfur Dissolution in Aqueous Sodium Sulfide. *Ind. Eng. Chem. Proc. Des. Dev.* **6**, 398–406 (1967).

70. Avetisyan, K., Buchshtav, T. & Kamyshny, A. Kinetics and mechanism of polysulfides formation by a reaction between hydrogen sulfide and orthorhombic cyclooctasulfur. *Geochimica et Cosmochimica Acta* **247**, 96–105 (2019).

71. Chadwell, S. J., Rickard, D. & Luther, G. W. Electrochemical Evidence for Metal Polysulfide Complexes: Tetrasulfide (S2-4) Reactions with Mn2+, Fe2+, Co2+, Ni2+, Cu2+, and Zn2+. *Electroanalysis* **13**, 21–29 (2001).

72. Illés, E. & Tombácz, E. The effect of humic acid adsorption on pH-dependent surface charging and aggregation of magnetite nanoparticles. *Journal of Colloid and Interface Science* **295**, 115–123 (2006).

73. Matamoros-Veloza, A., Stawski, T. M. & Benning, L. G. Nanoparticle Assembly Leads to Mackinawite Formation. *Crystal Growth & Design* **18**, 6757–6764 (2018).

74. Ma, H. *et al.* Secondary Mineral Formation and Carbon Dynamics during FeS Oxidation in the Presence of Dissolved Organic Matter. *Environ. Sci. Technol.* **56**, 14120–14132 (2022).

75. Rickard, D. T. Kinetics and Mechanism of Pyrite Formation at Low Temperatures. *American Journal of Science* **275**, 636–652 (1975).

76. Yao, W. & Millero, F. J. Oxidation of hydrogen sulfide by hydrous Fe(III) oxides in seawater. *Marine Chemistry* **52**, 1–16 (1996).

77. Yu, Z.-G., Peiffer, S., Göttlicher, J. & Knorr, K.-H. Electron Transfer Budgets and Kinetics of Abiotic Oxidation and Incorporation of Aqueous Sulfide by Dissolved Organic Matter. *Environ. Sci. Technol.* **49**, 5441–5449 (2015).

78. Cosmidis, J., Nims, C. W., Diercks, D. & Templeton, A. S. Formation and stabilization of elemental sulfur through organomineralization. *Geochimica et Cosmochimica Acta* **247**, 59–82 (2019).

79. Picard, A. *et al.* Authigenic metastable iron sulfide minerals preserve microbial organic carbon in anoxic environments. *Chemical Geology* **530**, 119343 (2019).

80. Raven, M. R., Sessions, A. L., Adkins, J. F. & Thunell, R. C. Rapid organic matter sulfurization in sinking particles from the Cariaco Basin water column. *Geochimica et Cosmochimica Acta* **190**, 175–190 (2016).

81. Son, S., Pil Hyun, S., Charlet, L. & Kwon, K. D. Thermodynamic stability reversal of iron sulfides at the nanoscale: Insights into the iron sulfide formation in low-temperature aqueous solution. *Geochimica et Cosmochimica Acta* 31 (2022).

82. Murowchick, J. B. & Barnes, H. L. Effects of temperature and degree of supersaturation on pyrite morphology. *American Mineralogist* **72**, 1241–1250 (1987).

83. Wang, S. *et al.* Constraints on fluid evolution and growth processes of black smoker chimneys by pyrite geochemistry: A case study of the Tongguan hydrothermal field, South Mid-Atlantic Ridge. *Ore Geology Reviews* **140**, 104410 (2022).

84. Butler, I. B. & Rickard, D. Framboidal pyrite formation via the oxidation of iron (II) monosulfide by hydrogen sulphide. *Geochimica et Cosmochimica Acta* **64**, 2665–2672 (2000).

85. ThomasArrigo, L. K., Byrne, J. M., Kappler, A. & Kretzschmar, R. Impact of Organic Matter on Iron(II)-Catalyzed Mineral Transformations in Ferrihydrite–Organic Matter Coprecipitates. *Environ. Sci. Technol.* **52**, 12316–12326 (2018).

86. Rickard, D. Sedimentary pyrite framboid size-frequency distributions: A meta-analysis. *Palaeogeography, Palaeoclimatology, Palaeoecology* **522**, 62–75 (2019).

87. Liu, K. *et al.* Morphology of framboidal pyrite and its textural evolution: Evidence from the Logatchev area, Mid-Atlantic Ridge. *Ore Geology Reviews* **141**, 104630 (2022).

88. Reitner, J., Blumenberg, M., Walliser, E.-O., Schäfer, N. & Duda, J.-P. Methane-derived carbonate conduits from the late Aptian of Salinac (Marne Bleues, Vocontian Basin, France): Petrology and biosignatures. *Marine and Petroleum Geology* **66**, 641–652 (2015).

89. Wilkin, R. T., Barnes, H. L. & Brantley, S. L. The size distribution of framboidal pyrite in modern sediments: An indicator of redox conditions. *Geochimica et Cosmochimica Acta* **60**, 3897–3912 (1996).

90. Schwertmann, U. & Cornell, R. M. *Iron Oxides in the Laboratory*. (Wiley, 2000).

91. Tomaszewski, E. J. *et al.* Complexation by cysteine and iron mineral adsorption limit cadmium mobility during metabolic activity of *Geobacter sulfurreducens*. *Environ. Sci.: Processes Impacts* **22**, 1877–1887 (2020).

92. Mansor, M., Berti, D., Hochella, M. F., Murayama, M. & Xu, J. Phase, morphology, elemental composition, and formation mechanisms of biogenic and abiogenic Fe-Cu-sulfide nanoparticles: A comparative study on their occurrences under anoxic conditions. *American Mineralogist* **104**, 703–717 (2019).

93. Stookey, L. L. Ferrozine - A New Spectrophotometric Feagent for Iron. *Anal. Chem.* **42**, 779–781 (1970).

94. Heron, Gorm., Crouzet, Catherine., Bourg, A. C. M. & Christensen, T. H. Speciation of Fe(II) and Fe(III) in Contaminated Aquifer Sediments Using Chemical Extraction Techniques. *Environ. Sci. Technol.* **28**, 1698–1705 (1994).

95. Huerta-Diaz, M. A. & Morse, J. W. A Quantitative Method for Determination of Trace Metal Concentrations in Sedimentary Pyrite. *Marine Chemistry* **29**, 119–144 (1990).

96. Rickard, D. *et al.* The composition of nanoparticulate mackinawite, tetragonal iron(II) monosulfide. *Chemical Geology* **235**, 286–298 (2006).

97. Boursiquot, S., Mullet, M., Abdelmoula, M., Génin, J.-M. & Ehrhardt, J.-J. The dry oxidation of tetragonal FeS 1- x mackinawite. *Physics and Chemistry of Minerals* **28**, 600–611 (2001).

98. Zhang, Q. *et al.* Humidity related magnetite alteration in an experimental setup. *Geophysical Journal International* **224**, 69–85 (2020).

4.9 SUPPLEMENTARY MATERIALS

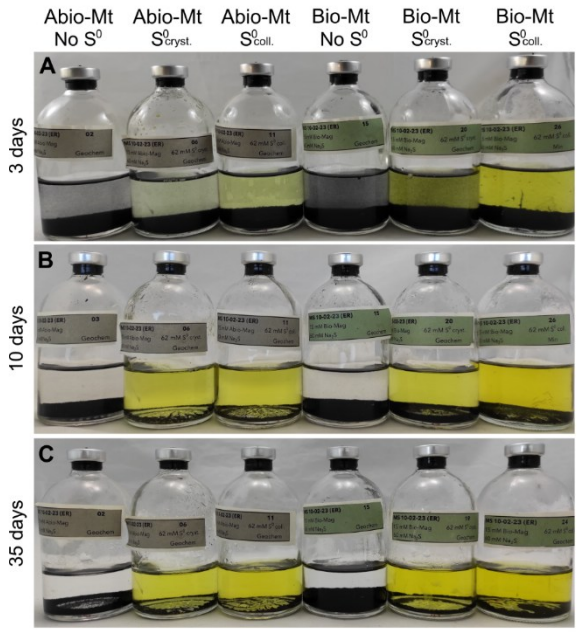

Supplementary Figure 4.1: Photographs of sulfidation experiments with abiogenic magnetite (Abio-Mt) and biogenic magnetite (Bio-Mt). Photographs after 3, 10, and 35 days are shown in panel A, B, C, respectively. The yellow color of the supernatant in experiments with S^0 indicates the presence of dissolved polysulfides[1].

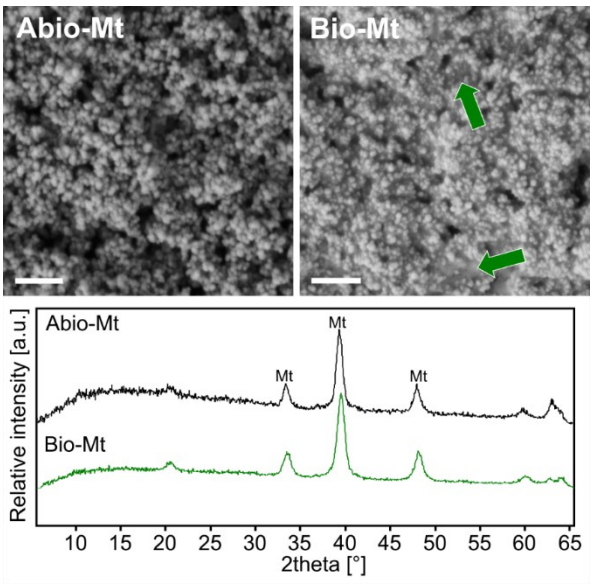

Supplementary Figure 4.2: SEM images and µ-XRD patterns of the abiogenic magnetite (Abio-Mt) and biogenic magnetite (Bio-Mt) used as starting materials for the sulfidation experiments. Scale bars are 300 nm. Note the pore space filling material in the biogenic magnetite, likely organic matter derived from G. sulfurreducens cultures (green arrows).

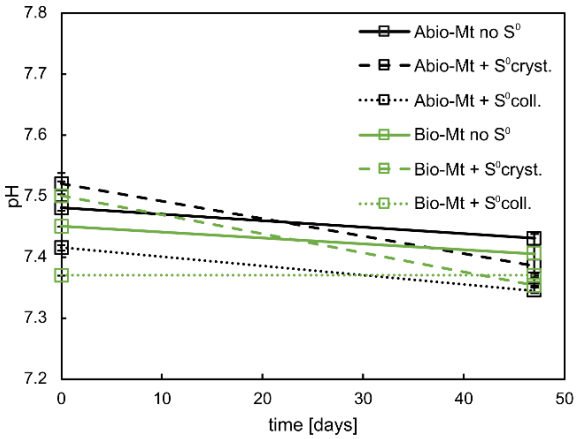

Supplementary Figure 4.3: pH of the sulfidation experiments with abiogenic magnetite (Abio-Mt) and biogenic magnetite (Bio-Mt) over time. Data points are given as averages of least two experimental replicates. The error bars represent the range of pH values among replicates.

Supplementary Table 4.1: Organic carbon concentrations of the abiogenic magnetite (Abio-Mt) and biogenic (Bio-Mt) magnetite suspensions used for the sulfidation experiments. Note that total organic carbon (TOC) concentrations in Bio-Mt are ~10x higher than in Abio-Mt and that organic carbon in Bio-Mt is primarily associated with the solid phase (i.e., low DOC/solid OC).

	DOC [mmol/L]	Solid OC [mmol/L]	TOC [mmol/L]	DOC/solid OC
Abio-Mt	0.9	0.1	1.0	7.2
Bio-Mt	3.8	5.5	9.3	0.7

Supplementary Table 2: Iron concentrations in liquid and solid phases of the sulfidation experiments. Reported concentrations are mean values of a minimum of experimental duplicates, except for analyses denoted with an *, where only one analysis was available. Fe (HNO3) concentrations were not determined (n.d.) when the mineral pellet was completely dissolved in 6 M HCl. <LOD = below limit of detection.

Experiment	Parameter		0 days	3 days	6 days	11 days	14 days	21 days	28 days	35 days
Abio-Mt, no S^0	$Fe(II)_{aq}$	[µM]	74	34	16	26	12	17	9	8
	1σ		22	3	6	5	1	5	1	3
	Fe (HCl)	[mM]	15.3	15.8	12.4	13.2	10.6	9.3	6.0	5.1
	1σ		1.0	0.1	1.2	0.6	0.6	0.3	0.4	0.1
	Fe (HNO_3)	[mM]	n.d.	n.d.	2.2	3.9	4.5	9.2	10.7	11.7
	1σ		n.d.	n.d.	0.5	0.1	0.6	1.3	1.0	0.5
	Fe [HNO_3/(HCl + HNO_3)]		0.00	0.00	0.15	0.23	0.30	0.49	0.64	0.70
	1σ		0.00	0.00	0.04	0.01	0.04	0.03	0.04	0.00
Abio-Mt, crystalline S^0	$Fe(II)_{aq}$	[µM]	59	41	21	9	4	<LOD	<LOD	<LOD
	1σ		5	1	1	4	0	n.d.	n.d.	n.d.
	Fe (HCl)	[mM]	14.0	14.1	7.3	1.4	2.4	1.2	2.0	2.4
	1σ		0.0	0.2	0.0	0.0	0.2	0.3	0.3	0.3
	Fe (HNO_3)	[mM]	n.d.	n.d.	3.9	11.7	10.4	12.5	10.3	10.5
	1σ		n.d.	n.d.	1.0	0.9	0.8	0.2	0.0	1.3
	Fe [HNO_3/(HCl + HNO_3)]		0.00	0.00	0.35	0.89	0.81	0.91	0.84	0.82
	1σ		0.00	0.00	0.06	0.01	0.00	0.02	0.02	0.00
Abio-Mt, colloidal S^0	$Fe(II)_{aq}$	[µM]	304	47	23	7	9	2	<LOD	<LOD
	1σ		17	0	4	0	3	1	n.d.	n.d.
	Fe (HCl)	[mM]	13.2	12.2	1.8	1.5	2.8	0.8	2.1	1.7
	1σ		0.3	0.1	0.2	0.1	0.1	0.3	0.1	0.3
	Fe (HNO_3)	[mM]	n.d.	n.d.	9.0	11.6	11.4	12.8	11.7	10.9
	1σ		n.d.	n.d.	0.1	0.3	0.4	0.1	0.0	0.9
	Fe [HNO_3/(HCl + HNO_3)]		0.00	0.00	0.83	0.88	0.80	0.94	0.85	0.87

	1σ		0.00	0.00	0.02	0.01	0.02	0.02	0.01	0.02
Bio-Mt, no S^0	$Fe(II)_{aq}$	[µM]	43*	40*	19	17	21	12	19	25
	1σ		n.d.	n.d.	4	2	6	3	5	16
	Fe (HCl)	[mM]	16.9*	16.8*	13.8	13.9	15.3	16.3	15.3	11.5
	1σ		n.d.	n.d.	3.6	4.3	3.1	4.6	5.7	7.6
	Fe (HNO_3)	[mM]	n.d.	n.d.	0.1	0.6	0.9	1.2	2.5	4.2
	1σ		n.d.	n.d.	0.0	0.3	0.1	0.4	0.8	1.8
	Fe [HNO_3/(HCl + HNO_3)]		0.00	0.00	0.01	0.04	0.06	0.07	0.14	0.30
	1σ		0.00	0.00	0.00	0.02	0.01	0.03	0.05	0.17
Bio-Mt, crystalline S^0	$Fe(II)_{aq}$	[µM]	43	63	19	22	18	2	<LOD	6
	1σ		7	5	6	5	1	2	n.d.	3
	Fe (HCl)	[mM]	11.6	12.4	11.4	5.0	2.0	0.9	1.7	3.2
	1σ		0.4	0.6	0.5	1.5	0.2	0.2	0.1	1.0
	Fe (HNO_3)	[mM]	n.d.	n.d.	0.3	8.9	10.6	10.6	10.3	8.3
	1σ		n.d.	n.d.	0.1	1.3	0.2	0.9	0.7	0.9
	Fe [HNO_3/(HCl + HNO_3)]		0.00	0.00	0.03	0.64	0.84	0.92	0.86	0.73
	1σ		0.00	0.00	0.01	0.10	0.02	0.02	0.01	0.05
Bio-Mt, colloidal S^0	$Fe(II)_{aq}$	[µM]	105	65	22	16	21	8	<LOD	6
	1σ		4	23	0	2	7	2	n.d.	1
	Fe (HCl)	[mM]	11.2	12.7	10.7	1.4	2.4	0.9	1.8	1.9
	1σ		3.0	0.7	0.8	0.0	0.3	0.1	0.1	0.1
	Fe (HNO_3)	[mM]	n.d.	n.d.	0.9	9.6	10.1	12.3	11.5	10.5
	1σ		n.d.	n.d.	0.0	0.2	0.3	0.4	0.2	0.5
	Fe [HNO_3/(HCl + HNO_3)]		0.00	0.00	0.08	0.88	0.81	0.93	0.86	0.85
	1σ		0.00	0.00	0.00	0.00	0.02	0.01	0.01	0.00

CHAPTER 5 – WORK PACKAGE III

Stable isotope fingerprints of microbial sulfur and iron cycling preserved in ancient metamorphic hydrothermal sulfide deposits

Eric Runge[1,2†], Muammar Mansor[3], Virgil Pasquier[4], Thomas Bovay[4], Johanna Marin-Carbonne[4], Vanessa Fichtner[1], Andreas Kappler[3,5], and Jan-Peter Duda[1,2]

[1]Department of Geobiology, Geoscience Center, University of Göttingen, Göttingen, Germany
[2]Sedimentology and Organic Geochemistry, Department of Geosciences, Tübingen University, Tübingen, Germany
[3]Geomicrobiology, Department of Geosciences, Tübingen University, Tübingen, Germany
[4]Institute of Earth Sciences, Université de Lausanne, Lausanne, Switzerland
[5]Cluster of Excellence EXC 2124, Controlling Microbes to Fight Infection, Tübingen University, Tübingen, Germany

†corresponding author

In revision for *Chemical Geology*

5.1 Abstract

Sulfur and iron stable isotope compositions in pyrite are widely employed for tracing microbial sulfur and iron cycling through geological time. In hydrothermal sulfide systems, however, sulfur and iron pools can be affected by both microbial and abiotic processes, limiting the applicability of the respective stable isotopes as biosignatures. Moreover, the diagenetic and metamorphic stability of sulfur and iron isotope signatures in pyrite under hydrothermal conditions is insufficiently understood. Here, we employed coupled in-situ Secondary Ion Mass Spectrometry (SIMS) triple sulfur ($\delta^{34}S$ and $\Delta^{33}S$) and iron ($\delta^{56}Fe$) isotope analysis on pyrite precipitates of various morphologies in ~390 Ma sediment-hosted massive sulfides to better understand the preservation of stable isotope biosignatures in hydrothermal systems. Detailed petrographic analysis revealed that framboidal pyrite formed before euhedral pyrite. $\delta^{34}S$ and $\Delta^{33}S$ signatures of the pyrites (-15.13 to +18.77‰ and -0.21 to +0.26‰, respectively) can be explained by either microbial or thermochemical sulfate reduction. However, the isotopically lightest framboidal pyrite $\delta^{34}S$ value (-15.13‰) likely originated from microbial sulfur cycling. The same pyrites show highly variable $\delta^{56}Fe$ compositions (-1.30 to +2.19‰), indicating precipitation from a diagenetically fractionated iron pool not fully equilibrated with hydrothermal fluids. The lower median $\delta^{56}Fe$ value in framboidal versus euhedral pyrite points to a variable expression of kinetic and equilibrium fractionation. This may reflect differences in precipitation rates between multiple pyrite generations recording early diagenetic (microbial) processes and hydrothermal overprint of the system, consistent with textural evidence for framboid recrystallization and overgrowth. Notably, the equal presence of $\delta^{56}Fe$ evidence across morphotypes highlights that geobiological studies should include morphologically diverse pyrite to avoid false-negative biosignature detection. Taken together, our results demonstrate that sulfur and iron stable isotope signatures indicative of microbial sulfur and iron cycling might be rare but still detectable in hydrothermal sulfides despite extensive alteration of the precursor sediment by sulfidic and iron-rich hydrothermal fluids in the environment and by greenschist metamorphism during later stages in the rock's

history. Our study highlights the challenges and potentials of coupled textural and in-situ stable isotope analysis for tracing microbial sulfur and iron cycling in hydrothermal sulfide systems through Earth's history.

5.2 Introduction

Hydrothermal sulfide systems are among the most ancient habitats on Earth and, thus, may provide an essential window into the emergence and evolution of microbial metabolism (Rasmussen, 2000; Georgieva et al., 2021; Mißbach et al., 2021; Baumgartner et al., 2022; Runge et al., 2023a; Weimann et al., 2024). The ancient equivalents of these environments are volcanogenic and sediment-hosted massive sulfide deposits (Huston et al., 2010; Wilkinson, 2014; Tornos et al., 2015). In sedimentary systems, iron sulfide mineral formation (including pyrite) is commonly mediated by microbial iron and sulfur cycling (Rickard, 1969; Strauss, 1997; Canfield et al., 1998; Donald and Southam, 1999; Picard et al., 2016; Thiel et al., 2019; Berg et al., 2020; Gorlas et al., 2022; Bronner et al., 2023; Truong et al., 2023; Runge et al., 2024). Since these processes can occur at temperatures exceeding 100°C (e.g., Jørgensen et al., 1992; Kashefi and Lovley, 2003), pyrite in hydrothermal environments may also record signatures of microbial sulfur and iron cycling. However, in these settings, pyrite commonly precipitates abiotically from iron-rich and sulfidic hydrothermal fluids (Schoonen and Barnes, 1991; Butler et al., 2004; Wang et al., 2022; Früh-Green et al., 2022) or may result from the abiotic sulfidation of magnetite (Canfield and Berner, 1987; Qian et al., 2010, 2013; Bendt et al., 2019; Runge et al., 2023b, 2024) at relative high temperature. Thus, gleaning information on past microbial processes from ancient hydrothermal sulfides depends on our ability to distinguish biogenic from abiogenic pyrite, as well as primary pyrite from subsequent generations.

Sulfur and iron stable isotope ratios ($^{56}Fe/^{54}Fe$, $^{33}S/^{32}S$, $^{34}S/^{32}S$) in pyrite are among the most applied tools for deciphering the biogenicity of pyrite in modern and ancient environments (Butler et al., 2004; Eickmann et al., 2014; Duda et al., 2016; Marin-Carbonne et al., 2020; Nozaki et al., 2020, 2024; Baumgartner et al., 2020; Pokrovski et al., 2021; Decraene et al., 2021; Moreras-Marti et al., 2022; Dupeyron et al., 2023; Reinhardt et al., 2024). In the case of stable sulfur isotopes, the largest fractionation is associated with microbial sulfur cycling (MSC) (Canfield, 2001). Microbial sulfate reduction (MSR), possibly in conjunction with re-oxidation of sulfide and subsequent

elemental sulfur disproportionation, can cause isotope fractionation approaching equilibrium ($\Delta^{34}S_{sulfate\text{-}sulfide}$ = 70‰ at 20°C: Canfield and Thamdrup, 1994; Sim et al., 2011a). Accordingly, strongly ^{34}S-depleted sulfide minerals in volcanogenic and sediment-hosted deposits throughout the geological record were interpreted as evidence for MSC (Eldridge et al., 1993; Taylor, 2004; Present et al., 2017; Lode et al., 2017; Slack et al., 2019; Velasco-Acebes et al., 2019). However, the true fractionation during MSR can vary between 0 and 70‰, depending on the microbial strain and environmental parameters, such as carbon and sulfur availability or temperature (Chambers et al., 1975; Habicht et al., 2002; Farquhar et al., 2003; Bradley et al., 2016; Sim et al., 2023).

At temperatures ≥100°C, thermochemical sulfate reduction (TSR) dominates and can also cause substantial sulfur isotope fractionation via a kinetic isotope effect (KIE; maximum $\Delta^{34}S_{sulfate\text{-}py} \approx$ 20‰ at 100°C: Kiyosu and Krouse, 1990; Machel et al., 1995). Theoretical estimates suggest that the equilibrium isotope effect (EIE) between sulfate and sulfide ($\Delta^{34}S_{sulfate\text{-}py}$) at 100°C is ≈ 43‰, giving an upper limit for sulfur isotope fractionation in TSR systems (Eldridge et al., 2016). Notably, MSR or TSR occurring under closed system conditions (when sulfate reduction rates exceed the resupply of sulfate) would produce ^{34}S-enriched sulfate in the residual porewater (Zaback et al., 1993; Jørgensen et al., 2004; Paiste et al., 2022). This can lead to pyrite that is isotopically close to, or even heavier than, the initial sulfate source. Therefore, sulfide minerals in hydrothermal systems may be ^{34}S-enriched even in the presence of MSC, suggesting biological activity remains undetected in many cases.

Minor sulfur isotopes (^{33}S and ^{36}S) might help disentangle microbial from abiotic sulfur cycling in hydrothermal deposits. For instance, the theoretical relationship between the fractionation factors (α) for $^{33}S/^{32}S$ and $^{34}S/^{32}S$ ratios during mass-dependent equilibrium fractionation is related by the exponent $^{33}\theta$ and described by the function:

$$\alpha^{33/32}_{sulfate-sulfide} = \left(\alpha^{34/32}_{sulfate-sulfide}\right)^{^{33}\theta} \quad (1)$$

However, the exponent $^{33}\theta$ (0.515 at low-temperature equilibrium) varies slightly between different mass-dependent fractionation processes, resulting in deviations from the theoretical EIE expressed as non-zero $\Delta^{33}S$ (Farquhar et al., 2007). For instance, MSR, chemolithotrophic sulfide oxidation, and sulfur disproportionation are associated with $^{33}\theta$ between 0.5077 and 0.5187, corresponding to positive $\Delta^{33}S$ deviations in the produced sulfur species of up to ca. +0.23‰ (Johnston, 2005; Sim et al., 2011b; Zerkle et al., 2016; Moreras-Marti et al., 2022). Experimental TSR using single organic compounds as reductants even demonstrated $\Delta^{33}S$ values of up to +13‰ in the products, although fractionation of this magnitude has not been reported from natural environments (Watanabe et al., 2009; Oduro et al., 2011). In contrast, $\Delta^{33}S$ deviations associated with abiotic sulfide oxidation by O_2 are minor (0.037 ± 0.014‰: Eldridge and Farquhar, 2018). Therefore, minor sulfur isotopes may provide a powerful means to reconstruct sulfur cycling in hydrothermal systems.

The largest $\delta^{56}Fe$ variations in Earth's surface environments are caused by early diagenetic redox reactions (Johnson et al., 2020; Dauphas et al., 2024). More specifically, partial oxidation (abiotic or biotic) of Fe(II) generates a ^{56}Fe enriched Fe(III) pool, which then rapidly precipitates as Fe(III) (oxyhydr)oxide minerals with positive $\delta^{56}Fe$ signatures under circumneutral conditions (Johnson et al., 2020). Partial reduction of Fe(III) minerals generates Fe(II) with a negative $\delta^{56}Fe$ signature of down to -3‰ in equilibrium (Dauphas et al., 2017; Johnson et al., 2020). This can occur biologically during microbial dissimilatory Fe(III) reduction (Beard et al., 1999; Chanda et al., 2021; Crosby et al., 2005; Fortney et al., 2016) or abiotically through the oxidation of chemical reductants such as sulfide (McAnena et al., 2024), which is considered a critical process in sulfidic low-temperature and hydrothermal systems (Canfield and Berner, 1987; Poulton et al., 2004; Runge et al., 2023b, 2024).

If microbial Fe(III) reduction occurs in a closed system, the initial production of a light (i.e., ^{54}Fe enriched) Fe(II) pool can drive the residual iron pool towards heavier $\delta^{56}Fe$ compositions (Chever et al., 2015). Similarly, while the reductive dissolution of iron-bearing mineral particles initially yields isotopically light Fe(II), $\delta^{56}Fe$ compositions will progressively approach values closer to the iron source (Chever et al., 2015;

McAnena et al., 2024). Moreover, the precipitation of isotopically light FeS can increase the δ^{56}Fe value of the residual iron pool (Butler et al., 2005; Severmann et al., 2006; Sivan et al., 2011; Roy et al., 2012). The δ^{56}Fe values of pyrite are additionally influenced KIE and EIE, where the KIE results in a more negative fractionation at faster precipitation rates, and the EIE causes a more positive fractionation at lower temperatures (Butler et al., 2005; Polyakov et al., 2007; Guilbaud et al., 2011; Syverson et al., 2013; Rolison et al., 2018; Mansor and Fantle, 2019). This inverse relationship between KIE and EIE during precipitation can diminish the apparent stable iron isotope fractionation, potentially blurring redox-dependent signals in hydrothermal pyrite. Nonetheless, large δ^{56}Fe ranges in pyrite exceeding 3‰ most likely reflect extensive iron cycling mediated by low-temperature microbial activity; hence, a large δ^{56}Fe variation is best interpreted as a biosignature.

The alteration of minerals by diagenetic hydrothermal fluids can affect sulfur and iron stable isotope records. For instance, in-situ sulfur isotope analysis of modern and ancient hydrothermal sulfides by secondary ion mass spectrometry (SIMS) indicates that high-temperature fluids can drive the recrystallization of framboidal pyrite and its associated evolution of δ^{34}S values towards heavier compositions (Liu et al., 2022; Nozaki et al., 2024). Moreover, the overgrowth of early diagenetic pyrite with secondary hydrothermal generations is common in these systems (Eldridge et al., 1988; Nozaki et al., 2020, 2024; Meng et al., 2022; Martin et al., 2023). Notably, the few published stable iron isotope studies on sulfide minerals in ancient volcanogenic and sediment-hosted deposits did not reveal evidence for microbial iron cycling (Gagnevin et al., 2012; Otake et al., 2021), in contrast to studies on their modern counterparts (i.e., seafloor hydrothermal sulfide systems) (Toner et al., 2016). This suggests that ancient deposits may have experienced a more intense alteration of their initial iron isotope records. For instance, mineral alteration associated with diagenetic hydrothermal fluids can increase δ^{56}Fe by preferentially leaching the lighter isotope (^{54}Fe) (Rouxel et al., 2003). Moreover, pyrite precipitation experiments at 300–450 °C demonstrated an increase in δ^{56}Fe value in pyrite over time due to EIE with $Fe(II)_{aq}$ during recrystallization (Syverson et al., 2013; Pokrovski et al., 2021).

Such exchange reactions can significantly alter $\delta^{56}Fe$ signatures even at temperatures as low as 80°C (Mansor and Fantle, 2019). These examples suggest a potential preservation bias against stable isotope signatures of microbial sulfur and iron cycling. At the same time, they highlight that bulk analysis of isotopically zoned precipitates might yield mixed signals, potentially blurring microbial signatures (Marin-Carbonne et al., 2020; Nozaki et al., 2024). This underlines the need to assess the preservation potential of isotopic biosignatures in minerals from hydrothermal sulfide systems by textural and in-situ stable isotope analysis.

Here, we assess the preservation of isotopic signatures indicative of microbial sulfur and iron cycling recorded in pyrite precipitates of various morphologies (framboidal, subhedral, euhedral) in the 390-million-year-old Rammelsberg deposit (Germany), a well-characterized example of sediment-hosted massive sulfides. We couple textural analysis by scanning electron microscopy (SEM) with in-situ SIMS triple sulfur ($\delta^{34}S$, $\Delta^{33}S$) and iron isotope data ($\delta^{56}Fe$) to reveal that pyrite from the Rammelsberg deposit preserves isotopic signatures of early diagenetic microbial redox cycling despite extensive hydrothermal alteration of the precursor sediment and later greenschist metamorphism. We emphasize the importance of coupled textural and in-situ sulfur and iron isotope analysis for reconstructing microbial redox cycling in ancient hydrothermal sulfide systems, including some of the oldest rocks on Earth.

5.3 Geological context

The Rammelsberg sediment-hosted hydrothermal sulfide deposit is located in the Harz Mountains, Northern Germany. The sulfide ore body occurs within a sedimentary succession deposited in the Goslar Trough – a continentally influenced semi-restricted marine basin that formed during regional extension before the Variscan orogeny (Ramdohr, 1953; Paul, 1975; Sperling, 1986; Walcher, 1986; Sáez et al., 2011; Moreno et al., 2019) (Fig. 5.1). The Rammelsberg deposit is hosted within the 'Wissenbacher Schiefer', a local subunit of the Middle Eifelian to Middle Givetian Goslar Formation (Buchholz and Luppold, 2008) (Fig. 5.1). The ore equivalent horizon (i.e., the unmineralized lateral extension of the ore body; Fig. 5.1) dominantly consists of shales (with minor carbonate and pyrite) interbedded with siltstones and fine-

grained sandstones, interpreted as distal turbiditic sediments (Walcher, 1986; Large and Walcher, 1999; Sáez et al., 2011; Moreno et al., 2019). Redox-sensitive trace element characteristics (V, Mo, U) in the shales suggest oxic bottom waters with the redox boundary below the sediment surface (Sáez et al., 2011). Organic carbon (C_{org}) contents are relatively low (<1 wt.%) – however, this may result from the conversion of an originally larger organic carbon pool into carbonates during TSR (Sáez et al., 2011).

The formation of the Rammelsberg sulfide ore body was tightly coupled to the subsidence of the Rhenohercynian basin (Large and Walcher, 1999; Moreno et al., 2019). Accordingly, deeply rooted extensional faults acted as fluid pathways, channeling metal-rich hydrothermal brines to the seafloor. The 'Kniest' zone crosscuts the footwall shale horizon and likely served as the central feeder zone during ore formation (Large and Walcher, 1999; Moreno et al., 2019). The cyclic intercalation of the sulfide ores with partially replaced black shale layers and fragments demonstrates that the ore formation proceeded in several pulses and syngenetically to the deposition of the Wissenbacher Schiefer (Large and Walcher, 1999; Sáez et al., 2011). The major minerals in the ore body are sphalerite [ZnS], galena [PbS], barite [$BaSO_4$], chalcopyrite [$CuFeS_2$], and pyrite [FeS_2], with pyrite as the dominant iron sulfide (Large and Walcher, 1999; Sáez et al., 2011; Moreno et al., 2019). Microthermometric analysis of fluid inclusions in the Kniest and sulfur isotope pairs between sphalerite, galena, and chalcopyrite in the ore body suggest minimum temperatures of 130–180 °C for the mineralizing brine (Nielsen, 1985; Muchez and Stassen, 2006). Sulfur input from hydrothermal sources is evident by the higher content of pyrite of the Rammelsberg deposit (up to 25 wt.-%) compared to the ore equivalent horizon in the Wissenbacher Schiefer, which only has minor authigenic framboidal and euhedral pyrite (Walcher, 1986; Sáez et al., 2011). The fluid circulation was also associated with hydrothermal iron input, as evidenced by iron enrichment in chlorites from the Kniest compared to the ore equivalent horizon (Large and Walcher, 1999). Fe:S ratios in the ore equivalent horizon exceed the stoichiometry of pyrite, partly due to iron carbonates of possible hydrothermal origin

(Large and Walcher, 1999; Sáez et al., 2011). Hydrothermal alteration of the ore equivalent horizon is also reflected in increased carbonate and silica content near the Kniest (Large and Walcher, 1999). Deformation of the Rammelsberg deposit occurred during the Variscan orogeny, although at a low metamorphic grade (up to 260 °C: Ramdohr, 1953; Muchez and Stassen, 2006).

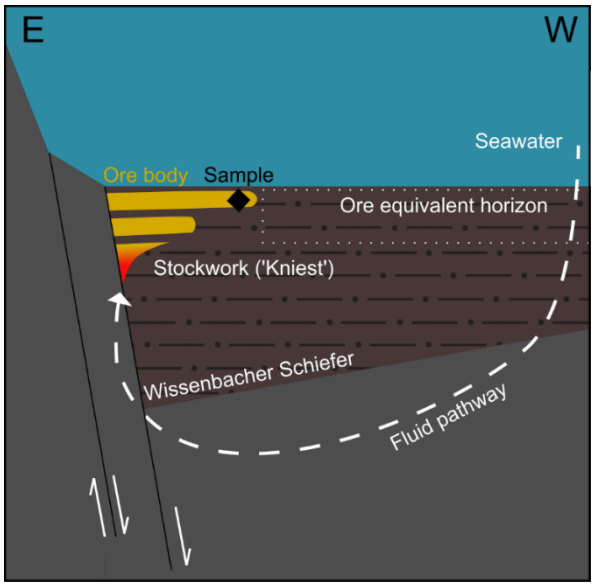

Figure 5.1: Schematic of the Goslar Trough during the initial rift stage of the Variscan orogeny (not to scale). Hydrothermal fluid circulation and sulfide ore formation occurred during the Middle Eifelian Wissenbacher Schiefer deposition. The analyzed sample (black diamond) originates from the ore body. Redrawn after Sáez et al. (2011) and Moreno et al. (2019).

5.4 Materials and methods

5.4.1 Reflected light (RL) and scanning electron microscopy (SEM)

Reflected light (RL) microscopy images were recorded using a Keyence VHX-6000 digital microscope at Tübingen University. For scanning electron microscopy (SEM), polished thin sections were coated with ~30 nm of gold using a BAL-TEC SCD 005 sputter coater to reduce charging effects during imaging. Textural characterization of the samples was performed using a Crossbeam 550L SEM (Zeiss, Oberkochen, Germany) operating at an acceleration voltage of 20 kV and working distances of 9.1 mm. All micrographs were taken using the backscattered electron detector (BSD). The textural classification of the analyzed pyrite grains was based on SEM observation of the following criteria: framboidal pyrites are spherical grains with or without an internal raspberry-like texture, subhedral pyrites are irregularly shaped grains with up to one clearly developed crystal face, and euhedral pyrites are grains with more than one clearly developed crystal face.

5.4.2 Secondary ion mass spectrometry (SIMS)

In total, 60 pyrite grains were analyzed for their iron isotope composition using the SIMS instrument (Cameca IMS 1280-HR) at the SwissSIMS facility of the University of Lausanne. 26 out of 60 pyrite grains were additionally analyzed for their sulfur isotope composition using the same instrument. The sample was cut from a polished petrographic thin section using a diamond wire saw and embedded in indium filled in an aluminum sample mount. The topography of the sample mount's surface was assessed using a white light microscope and was less than 3 µm. Two reference standard grains (Balmat and Ruttan pyrite, Whitehouse and Fedo, 2007; Pasquier et al., 2024) were included in each sample mount, and the mounts were gold-coated before analysis.

SIMS analyses of iron isotope compositions followed the procedure detailed in Decraene et al. (2021). Pyrite grains were sputtered by a 3 nA primary O^- beam focused to a 2.5-3 µm spot. The isotopes of ^{52}Cr, ^{54}Fe, ^{56}Fe, and ^{57}Fe were measured in multicollection mode with three off-axis Faraday cups and one electron multiplier for ^{52}Cr. The mass resolving power (MRP) was set at ~6800 to resolve interferences on $^{54}Fe^+$ ($^{53}CrH^+$, MRP: +6088) and $^{56}Fe^+$ ($^{55}MnH^+$, MRP: +5118). The mass of $^{52}Cr^+$ was measured to correct the $^{54}Cr^+$ isobaric interference on $^{54}Fe^+$ (Marin-Carbonne et al., 2011), as some samples display relatively high Cr content. Iron isotope compositions are reported as per mil variations of $^{56}Fe/^{54}Fe$ ratios measured in the samples normalized to that of the international reference material (Institute for Reference Materials and Measurements-014, IRMM-014; Eq. 1). The uncertainties associated with the $\delta^{56}Fe$ values presented in this study are shown as 2SD.

$$\delta^{56}Fe = \left[\frac{\left(\frac{^{56}Fe}{^{54}Fe}\right)_{sample}}{\left(\frac{^{56}Fe}{^{54}Fe}\right)_{IRMM-014}} - 1 \right] * 1000 \qquad (1)$$

One analysis consisted of the 90s of pre-sputtering, during which centering of the primary beam and calibration of the Faraday cups was performed, followed by 40 cycles of analyses (total of 300 s). Balmat ($\delta^{56}Fe_{true}$ = -0.40 ± 0.01‰: Whitehouse and

Fedo, 2007) was used as a primary standard to correct the instrumental mass fractionation (IMF) $\alpha=(^{56}Fe/^{54}Fe)_{meas}/(^{56}Fe/^{54}Fe)_{true}$, defined as the ratio between iron isotopic ratio measured by SIMS and the true ratio determined by Multi Collector Inductively Coupled Plasma Mass Spectrometry (MC-ICP-MS). The reproducibility was ±0.19‰ (2SD, July 2022 session).

SIMS analysis of sulfur isotope compositions followed an established routine procedure (Whitehouse, 2013). A Cs^+ primary beam of 1.09 nA intensity was focused to a spot of approximately 15-20 µm. The typical $^{32}S^-$ intensity was between 8.2 x 10^8 and 1.3 x 10^9 counts per second for sulfide. The ^{32}S-, $^{33}S^-$ and $^{34}S^-$ were measured in multicollection mode with three off-axis Faraday cups. The mass resolution was set to ~5000 to resolve the isobaric interferences due to the hydride contribution on $^{33}S^-$ ($^{32}SH^-$, MRP: +3911). A typical analysis consisted of two minutes of pre-sputtering in raster mode and data acquisition in 40 cycles of five seconds each. The background of the detectors was measured during the pre-sputtering and was then corrected for each analysis. The internal precision achieved under these conditions was better than ±0.16‰ for $\delta^{34}S$ and better than ±0.12‰ for $\delta^{33}S$ values (2σ). Several reference pyrite materials (Maine: $\delta^{34}S$ = -20.61 ± 0.05‰, $\delta^{33}S$ = -10.63 ± 0.02‰; Spain: $\delta^{34}S$ = -1.56 ± 0.26‰, $\delta^{33}S$ = -0.78 ± 0.13‰; and Balmat: $\delta^{34}S$ = +15.84 ± 0.92‰, $\delta^{33}S$ = +8.12 ± 0.48‰; Muller et al., 2017) were measured to determine IMF and the reference mass discrimination line, from which $\Delta^{33}S$ values were calculated. The reproducibility was found to be ±0.17‰ (2σ) for $\delta^{34}S$ and ±0.28‰ (2σ) for $\delta^{33}S$ values. Sulfur isotope compositions are reported as per mil variations of $^{34}S/^{32}S$ and $^{33}S/^{32}S$ ratios measured in the samples normalized to that of the international reference material (Vienna-Canyon Diablo Troilite, V-CDT; Eq. 2) as follows: The uncertainties associated with the $\delta^{33}S$ and $\delta^{34}S$ values presented in this study are shown as 2SD.

$$\delta^{3x}S = \left[\frac{\left(\frac{^{3x}S}{^{32}S}\right)_{sample}}{\left(\frac{^{3x}S}{^{32}S}\right)_{V-CDT}} - 1\right] * 1000 \qquad (2)$$

The $\Delta^{33}S$ values were calculated according to Eq. 3. The uncertainties associated with the $\Delta^{33}S$ values presented in this article are shown as the square root of the sum of the squared internal and external errors for each sulfur isotope.

$$\Delta^{33}S = \delta^{33}S - 1000 * \left[(1 + \frac{\delta^{34}S}{1000})^{0.516}) - 1\right] \quad (3)$$

5.5 RESULTS

5.5.1 Reflected Light (RL) microscopy and Scanning Electron Microscopy (SEM)

Petrographic analysis by RL microscopy revealed the presence of layers rich in pyrite, chalcopyrite, sphalerite, and galena (Fig. 5.2A). Chalcopyrite exhibited radial crystals (Fig. 5.2B, C), and pyrite occurred as framboidal, subhedral, and euhedral grains (Fig. 5.2B-D). Framboidal pyrite was generally ca. 10 to 15 μm in size (Fig. 5.3A). Notably, some framboidal pyrite did not show the characteristic raspberry-like internal texture formed by aggregation of individual microcrystals (Fig. 5.3A-B). Subhedral and euhedral pyrite were 10 to several tens of μm in diameter (Figs. 5.3C-D). Euhedral pyrite occasionally overgrows framboidal pyrite (Fig. 5.3B) and displays growth zonation (Fig. 5.3D).

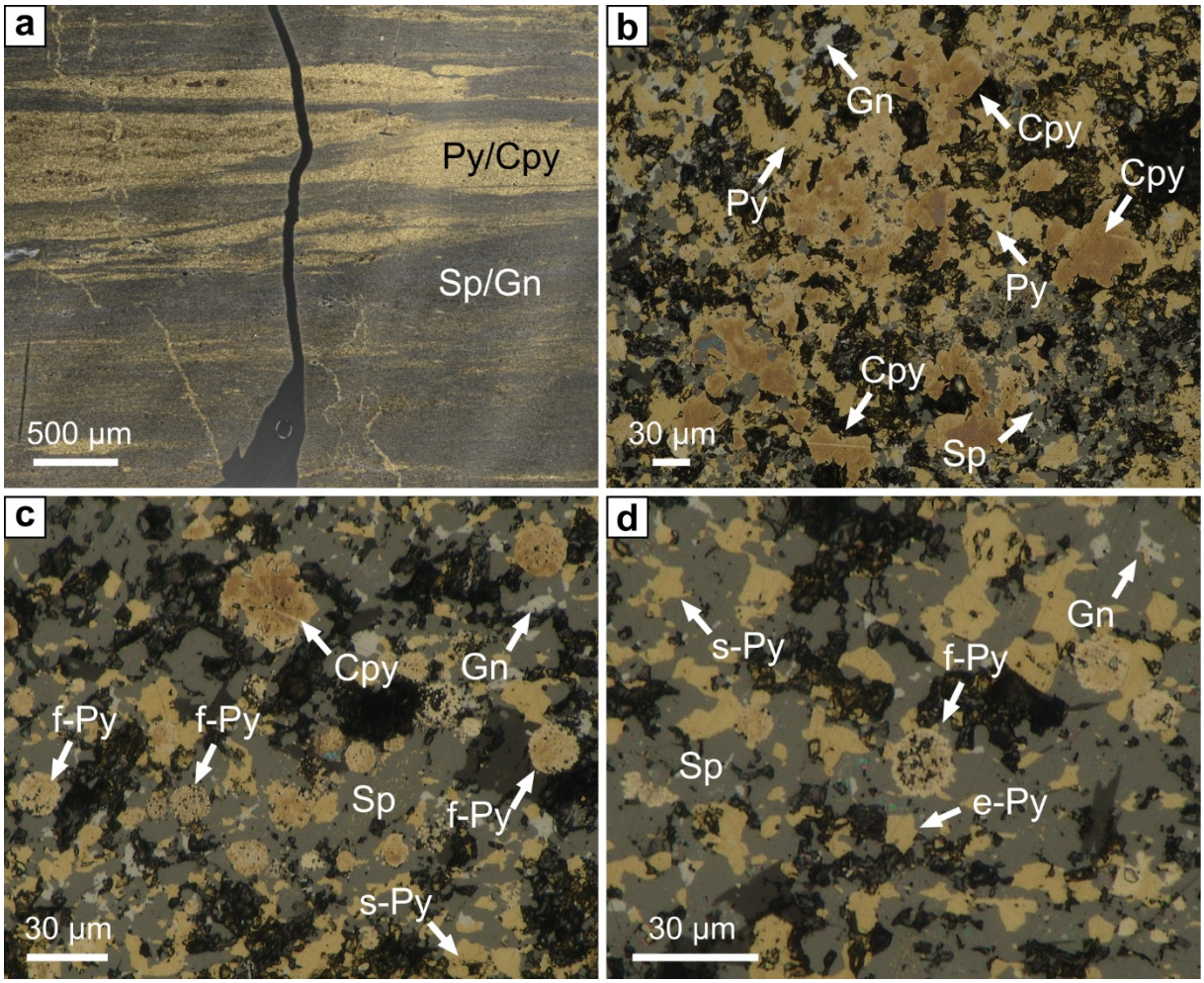

Figure 5.2: Reflected light (RL) microscopy images of sulfides in the Rammelsberg deposit. A: Layered sulfide ore consisting of alternating (chalco)pyrite (golden colors; Py/Cpy) and sphalerite with accessory galena (greyish colors; Sp/Gn); B-D: Close-up views of chalcopyrite, sphalerite (Sp), and galena (Gn), as well as of framboidal, subhedral, and euhedral pyrite (f-Py, s-Py, and e-Py, respectively).

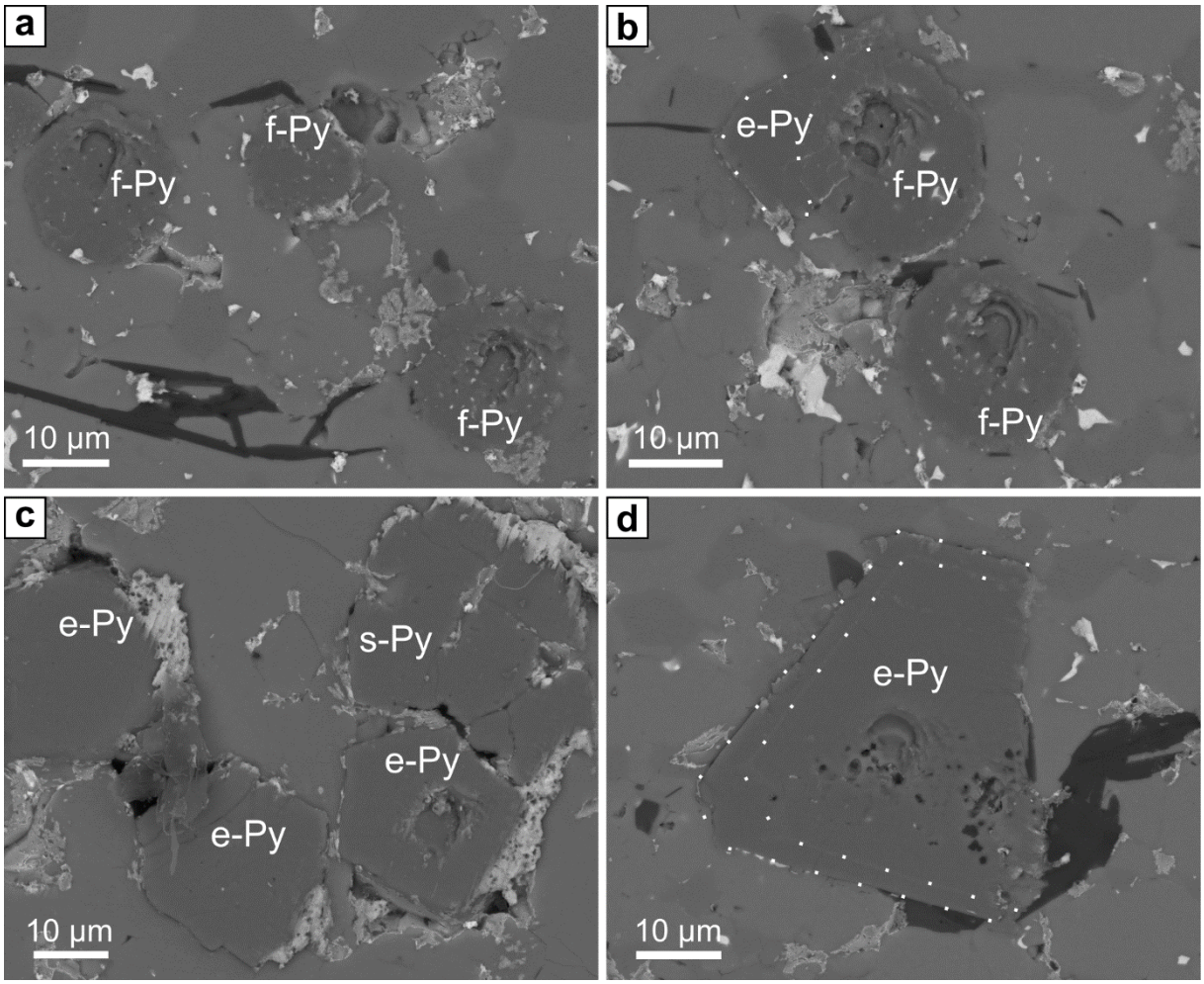

Figure 5.3: Scanning electron microscopy (SEM) photographs of pyrite textures in the Rammelsberg deposit. A: framboidal pyrite (f-Py); B: framboidal pyrite with euhedral pyrite (e-Py) overgrowth (white dotted line), indicating an earlier formation of framboidal pyrite; C: subhedral (s-Py) and euhedral pyrite; D: euhedral pyrite with growth zonation (white dotted line), indicating a pyrite generation postdating euhedral pyrite. Note that framboidal pyrite appears recrystallized and is generally smaller than subhedral and euhedral pyrite. The pits in the pyrite grains are the secondary ion mass spectrometry analysis (SIMS) spots (~5 µm each).

5.5.2 Secondary Ion Mass Spectrometry (SIMS)

Table 5.1: Iron and sulfur isotope compositions of pyrite morphotypes in the Rammelsberg deposit.

	Framboidal	Subhedral	Euhedral	All
δ^{56}Fe Min [‰]	-1.15	-0.73	-1.30	-1.30
δ^{56}Fe Max [‰]	1.99	2.19	1.71	2.19
δ^{56}Fe Average [‰]	0.46	0.75	0.79	0.57
δ^{56}Fe Median [‰]	0.39	0.86	1.00	0.77
δ^{56}Fe 1SD [‰]	0.81	0.76	0.97	0.82
δ^{56}Fe n	36	14	7	57
δ^{34}S Min [‰]	-15.13	9.29	-0.30	-15.13
δ^{34}S Max [‰]	17.01	18.49	18.77	18.77
δ^{34}S Average [‰]	12.16	14.60	11.92	12.67
δ^{34}S Median [‰]	14.99	15.42	15.03	14.99
δ^{34}S 1SD [‰]	8.28	3.29	7.56	7.10
δ^{34}S n	14	6	6	26
Δ^{33}S Min [‰]	-0.03	-0.15	-0.21	-0.21
Δ^{33}S Max [‰]	0.21	0.18	0.26	0.26
Δ^{33}S Average [‰]	0.10	0.03	0.04	0.07
Δ^{33}S Median [‰]	0.09	0.02	0.06	0.09
Δ^{33}S 1SD [‰]	0.07	0.13	0.20	0.12
Δ^{33}S n	14	6	6	26

Microscale δ^{34}S values in pyrite ranged from -15.13‰ to +18.77‰ (median = +14.99‰; average ± 1SD = +12.67 ± 7.10‰; n = 26; Tab. 5.1, Fig. 5.4), displaying a unimodal distribution (Fig. 5.5). The δ^{34}S values of framboidal pyrite varied between -15.13‰ and +17.01‰ (median = +14.99‰; average ± 1SD = +12.16 ± 8.28‰; n = 14), while subhedral pyrite ranged from +9.29 to +18.49‰ (median = +15.42‰; average ± 1SD = +14.60 ± 3.29‰; n = 6) and euhedral pyrite from -0.30 to +18.77‰ (median = +15.03‰; average ± 1SD = +11.92 ± 7.56‰; n = 6) (Tab. 5.1; Fig. 5.4).

The analyzed pyrite grains showed large variations in microscale δ^{56}Fe values ranging from -1.30 to +2.19‰ (median = +0.77‰; average ± 1SD = +0.57 ± 0.82‰; n = 57; Tab. 5.1; Fig. 5.4), displaying a bimodal distribution (Fig. 5.5). The δ^{56}Fe value of framboidal pyrite varied between -1.15 and +1.99‰ (median = +0.39‰; average ± 1SD = +0.46 ± 0.81‰; n = 36), while subhedral pyrite ranged from -0.73 to +2.19‰ (median =

+0.86‰; average ± 1SD = +0.75 ± 0.76‰; n = 14) and euhedral pyrite from -1.30 to +1.71‰ (median = +1.00‰; average ± 1SD = +0.79 ± 0.97‰; n = 7) (Tab. 5.1; Fig. 5.4).

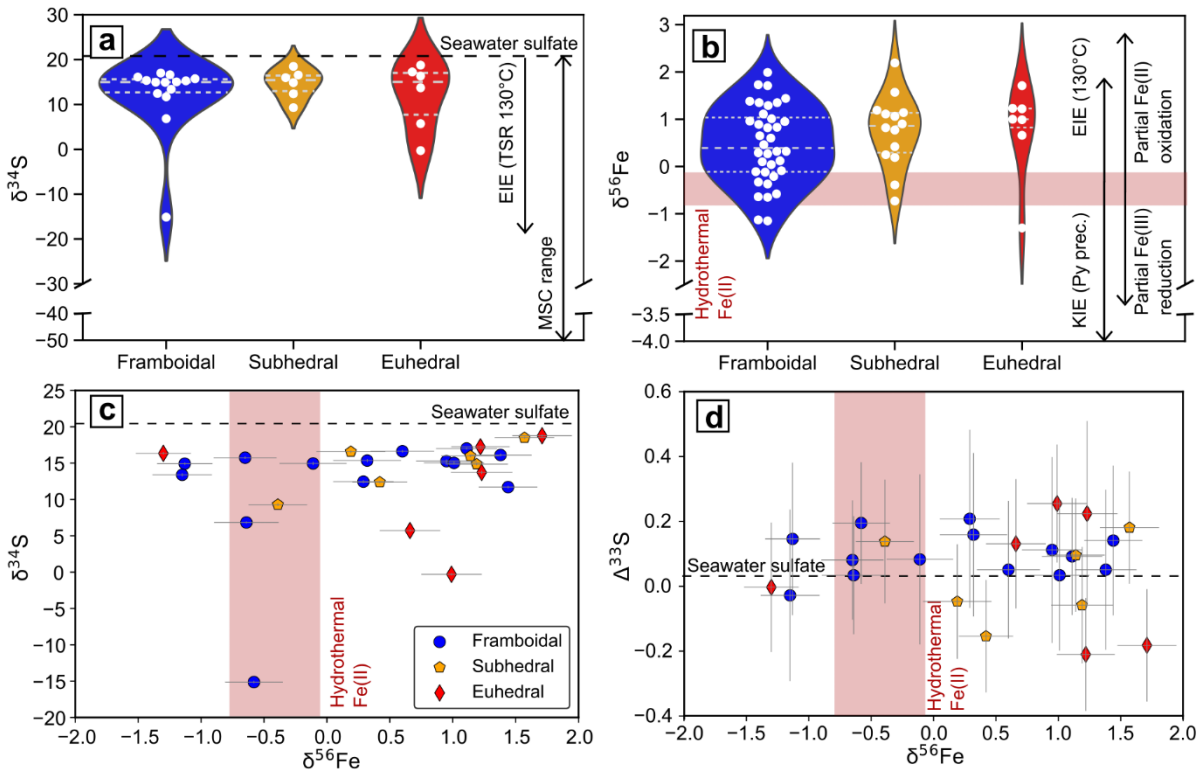

Figure 5.4: Pyrite sulfur ($\delta^{34}S$) and iron ($\delta^{56}Fe$) isotope composition for framboidal (blue), subhedral (yellow), and euhedral (red) pyrite in the Rammelsberg deposit. A, B: Violin plots of sulfur isotope composition and systematics. Starting from middle-Eifelian seawater ($\delta^{34}S$= +20.4‰; Wu et al., 2014), equilibrium isotope effects (EIE) during thermochemical sulfate reduction (TSR) can generate pyrite with down to $\delta^{34}S \approx$ -19‰ at 130°C (Eldridge et al., 2016), the minimum fluid temperature reconstruction for Rammelsberg system (Muchez and Stassen, 2006). Microbial sulfur cycling (MSC) could generate pyrite down to $\delta^{34}S \approx$ -50‰. B: Violin plots of iron isotope composition and systematics. Kinetic isotope effects (KIE) during pyrite precipitation can generate pyrite with $\delta^{56}Fe <$ -3.5‰ relative to the hydrothermal Fe(II) source (-0.8 to -0.1‰) (Mansor and Fantle, 2019). EIE between pyrite and hydrothermal Fe(II) during pyrite precipitation and mineral-fluid-interactions can generate pyrite with up to $\delta^{56}Fe$ = +1.8‰ at 130°C ($\Delta^{56}Fe_{pyrite\text{-}Fe(II)}$ = 1.9‰: Syverson et al., 2013; Mansor and Fantle, 2019). Iron redox reactions affecting pyrite precursors can generate pyrite with $\delta^{56}Fe$ = -3 to +3‰ (Johnson et al., 2020). C: $\delta^{56}Fe$ vs. $\delta^{34}S$ cross plot. D: $\delta^{56}Fe$ vs. $\Delta^{33}S$ cross plot. The violin plot's middle lines represent the median values.

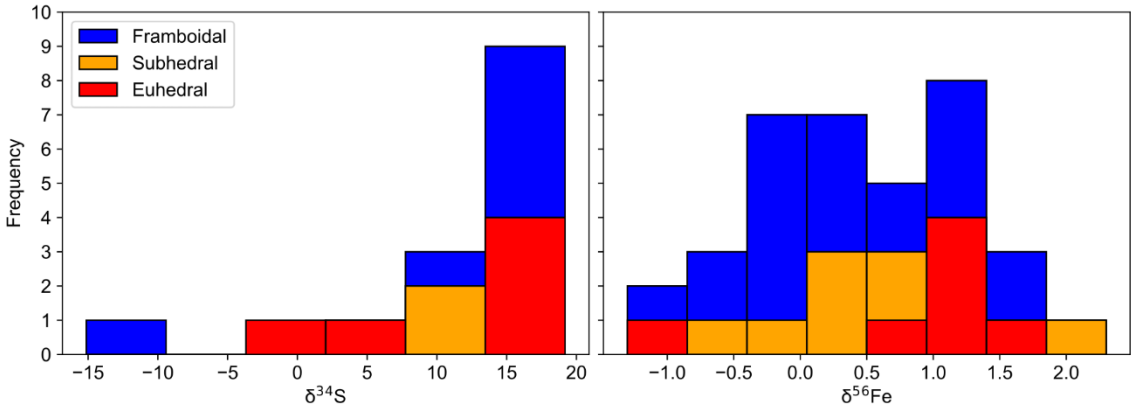

Figure 5.5: Histograms of sulfur ($\delta^{34}S$) and iron ($\delta^{56}Fe$) isotope compositions of the different pyrite morphotypes from the Rammelsberg deposit. Note that $\delta^{34}S$ displays an unimodal distribution while $\delta^{56}Fe$ displays a bimodal distribution. Each histogram's number of bins (k) was calculated according to the Rice rule ($k = 2 \times n^{1/3}$).

5.6 Discussion

5.6.1 Spatial relations and growth sequence of pyrite

The co-occurrence of multiple pyrite morphotypes in hydrothermal systems is commonly interpreted as a growth sequence (e.g., early diagenetic framboids vs. late diagenetic/hydrothermal euhedral grains: Eldridge et al., 1988, 1993; Sawlowicz, 1993; Nozaki et al., 2024). Indeed, the Rammelsberg deposit formed in a sediment-hosted hydrothermal sulfide system characterized by deposition of silt- and clay-rich sediments affected by repeated pulses of sulfidic hydrothermal fluid circulation (Ramdohr, 1953; Large and Walcher, 1999; Sáez et al., 2011). Therefore, pyrite in the Rammelsberg deposit could have formed in multiple generations, driven by (microbial) low-temperature processes and hot, metal-rich fluids. Accordingly, overgrowths of euhedral on framboidal pyrite demonstrate that the latter formed earlier (Fig. 5.3B). Moreover, some large euhedral grains exhibit a growth zonation, indicating a pyrite generation postdating euhedral pyrite (Fig. 5.3D). This suggests that the relative influence of different pyrite formation mechanisms might even vary during the growth of individual pyrite grains, as implied by commonly observed zonation features in pyrite (e.g., Marin-Carbonne et al., 2014; Reinhardt et al., 2024).

The absence of the characteristic raspberry-like internal texture in framboidal pyrite (Figs. 5.2C-D, 5.3A-B) suggests that some of these grains may represent primary

spheroidal pyrite, which is commonly observed in pyritization experiments in the presence of organic matter or sulfur- and iron-cycling microorganisms (Duverger et al., 2020, 2021; Berg et al., 2020; Truong et al., 2023; Runge et al., 2024). However, considering the presence of multiple pyrite generations, it seems plausible that most of these framboidal grains were recrystallized or infilled by a secondary generation of pyrite due to interaction with sulfidic fluids, as previously suggested (Ramdohr, 1953; Runge et al., 2023a). These observations demonstrate a complex pyrite formation sequence from early framboidal to later euhedral pyrite.

5.6.2 Hydrothermal versus microbial sulfide sources: Insights from triple sulfur isotopes ($\delta^{34}S, \Delta^{33}S$)

Due to the complex pyrite formation sequence in the Rammelsberg deposit, bulk (bio)geochemical approaches may not allow for resolving potential isotopic variabilities but yield average compositions, even in the case of isolated grains. Microscale in-situ approaches, such as those presented here, could be much better suited to disentangle potential stable isotopic fingerprints of microbial redox cycling in pyrite from hydrothermally influenced environments (Eldridge et al., 1988, 1993; Marin-Carbonne et al., 2020; Nozaki et al., 2020, 2024).

The range of $\delta^{34}S$ values in pyrite measured in this study ($\delta^{34}S \approx$ -15 to +19‰: Tab. 1) is consistent with previously analyzed bulk and in-situ pyrite $\delta^{34}S$ values from the Rammelsberg deposit (-20‰ to +20‰: Anger et al., 1966; Nielsen, 1985; Eldridge et al., 1988; Large and Walcher, 1999) and comparable to other Phanerozoic sediment-hosted hydrothermal sulfides (e.g., Buschendorf et al., 1963; Goodfellow, 1987; Kelley et al., 2004). In the Rammelsberg deposit, this range was interpreted to reflect a co-occurrence of sulfide from MSC ($\delta^{34}S_{pyrite} < 0$‰) and TSR ($\delta^{34}S_{pyrite} \approx$ +5 to +20‰) of seawater ($\delta^{34}S_{sulfate}$ = +20.4 ± 0.30‰; Wu et al., 2014) or sedimentary sulfate in the deep subsurface (Eldridge et al., 1988; Sáez et al., 2011).

The co-occurrence of sulfide from MSR and TSR in pyrite from the Rammelsberg deposit is plausible since periods of low-temperature marine sedimentation (conducive to MSC) likely alternated with periods of hydrothermal fluid circulation

(conducive to TSR) (Large and Walcher, 1999). Also, the broad $\delta^{34}S_{pyrite}$ range indicates that igneous sulfide was not the dominant pyrite sulfur source in the Rammelsberg system ($\delta^{34}S \approx 0‰$: Hoefs, 2021). The most positive $\delta^{34}S$ pyrite signatures measured in this study (ca. +10 to +19‰) instead require either the (near) complete reduction of seawater sulfate or the partial reduction of a sulfate reservoir enriched in ^{34}S relative to seawater. This enrichment could have resulted from Rayleigh distillation in the porewater under closed system conditions. On the other hand, the isotopically lightest pyrite sulfur in our sample ($\delta^{34}S$ = -15.13 ± 0.18‰) would require a fractionation of $\Delta^{34}S_{sulfate\text{-}pyrite} \approx 35‰$, assuming the contemporaneous seawater sulfate as the original sulfur source ($\delta^{34}S$ = +20.4 ± 0.30‰; Wu et al., 2014). Notably, closed-system reduction of ^{34}S-enriched porewater sulfate would require even greater degrees of fractionation to explain this $\delta^{34}S$ composition. Assuming the theoretically determined equilibrium fractionation factor at 100 °C ($^{34}\alpha_{py\text{-}sulfate}$ = 0.957; Eldridge et al., 2016), representing the maximum possible fractionation achieved by TSR, this pyrite is consistent with TSR or MSC in the precursor sediment of the Rammelsberg deposit (Fig. 5.4A). However, TSR and MSC cannot be distinguished based on our $\delta^{34}S$ data alone since their possible ranges of $\Delta^{34}S_{sulfate\text{-}pyrite}$ at equilibrium overlap considerably (0 to 70 ‰ vs. 0 to 43 ‰; Canfield, 2001; Eldridge et al., 2016).

To further investigate the role of TSR and MSC in the Rammelsberg system, we modeled the evolution of sulfide $\delta^{34}S$ vs. $\Delta^{33}S$ during Rayleigh isotope distillation (Fig. 5.6), which is expected to occur under closed system conditions (Sansjofre et al., 2016; Thomazo et al., 2019). Closed system conditions could have been favored in the Rammelsberg system via sediment burial and the semi-restricted paleogeographic situation of the Goslar Trough, limiting exchange with the seawater sulfate pool (Walcher, 1986; Sáez et al., 2011; Moreno et al., 2019). We assumed an initial $\delta^{34}S_{sulfate}$ value of +20.4 ± 0.30‰ and $\Delta^{33}S$ = +0.026 ± 0.094‰ for the co-eval middle Eifelian seawater as derived from carbonate-associated sulfate (Wu et al., 2014). Equilibrium fractionation factors were applied for TSR in the range of minimum fluid temperature estimates in the Rammelsberg system (130°C and 180°C), as well as low-temperature MSR ($^{34}\alpha_{py\text{-}sulfate}$ = 0.961, 0.968 and 0.930, respectively; $^{33}\lambda$ of 0.515) (Farquhar et al.,

2003; Eldridge et al., 2016). Within the 2σ uncertainty of $\Delta^{33}S$ measured on the standard (±0.28‰), the model shows that most of our data points are consistent with Rayleigh distillation during either TSR or MSR. Therefore, our triple sulfur isotope data cannot conclusively distinguish TSR from MSC as sulfide sources for most analyzed pyrite grains, suggesting Rayleigh distillation during either process is a possible scenario.

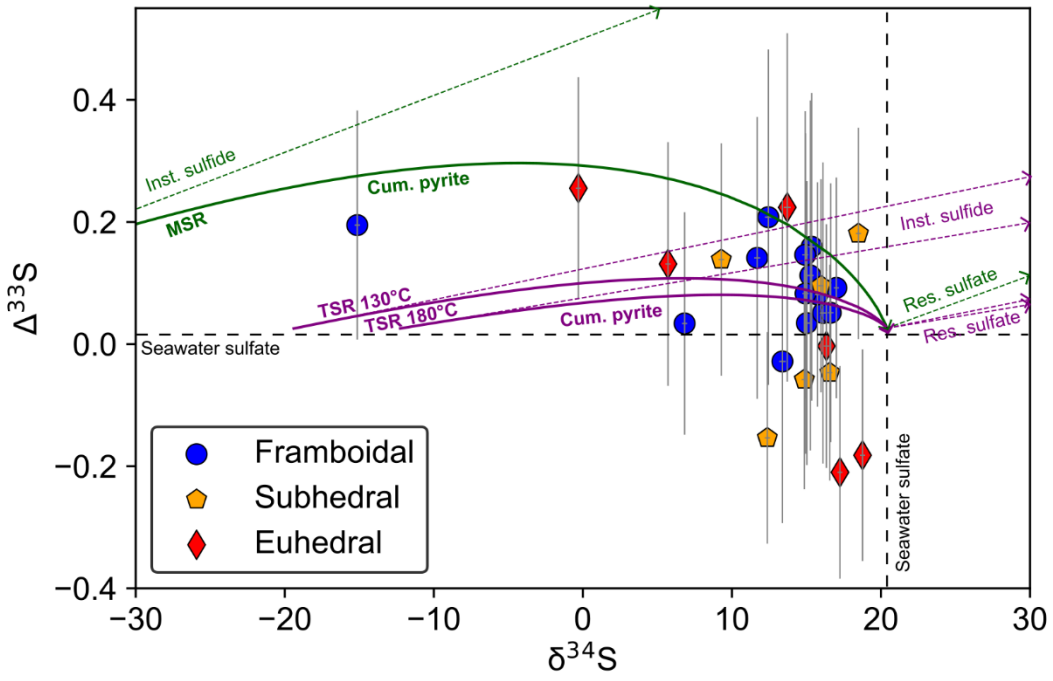

Figure 5.6: Triple sulfur isotope plot and model results for Rayleigh distillation during thermochemical sulfate reduction (TSR) and microbial sulfate reduction (MSR) in a closed system. The modeled fractionation trends are achieved using an initial $\delta^{34}S_{sulfate}$ = +20.4‰, $\Delta^{33}S$ = +0.026‰ for middle Eifelian seawater (Wu et al., 2014).We assumed equilibrium conditions for both TSR (at 130°C and 180°C) and MSR ($^{34}\alpha^{TSR\ 130°C}_{py\text{-}sulfate}$ = 0.961, $^{34}\alpha^{TSR\ 180°C}_{py\text{-}sulfate}$ = 0.968, $^{34}\alpha^{MSR}_{py\text{-}sulfate}$ = 0.930, $^{33}\lambda$ = 0.515). Instantaneous sulfide corresponds to sulfide formed at the respective time point. Cumulative pyrite corresponds to pyrite compositions predicted by the model.

An essential role of TSR in the Rammelsberg system is supported by an organic carbon depletion relative to the ore equivalent horizon alongside the presence of secondary carbonates, likely due to carbon oxidation during TSR (Machel et al., 1995; Sáez et al., 2011; Cai et al., 2022). Moreover, chalcopyrite in the Rammelsberg deposit, most likely a hydrothermal precipitate, is consistently heavy (i.e., $\delta^{34}S$ = ~13‰; Eldridge et al., 1988). This supports a TSR origin of the hydrothermal sulfide. TSR also generally produces nodular or euhedral pyrite grains, possibly exhibiting growth zonation (Liang et al., 2024), as observed in the Rammelsberg deposit (Fig. 5.3D). However, it seems unlikely that TSR alone explains the entire observed $\delta^{34}S_{pyrite}$ variability. The most negative $\delta^{34}S$ value (-15.13‰) presented in this study can only be explained by TSR at 130°C, but not at 180°C (Fig. 5.6). These fluid temperatures represent minimum values, and TSR at higher temperatures would decrease the expected EIE (Eldridge et al., 2016). Moreover, at temperatures relevant to the Rammelsberg system (<200°C), isotope exchange between sulfate and sulfide is also kinetically inhibited (Ohmoto and Lasaga, 1982). Therefore, equilibrium is less likely to be attained before quenching of the system (i.e., pyrite precipitation), limiting the expression of the EIE via TSR. Apparent fractionations during TSR are also commonly diminished by quantitative consumption of porewater sulfate in a closed system (Machel et al., 1995; Machel, 2001; Meshoulam et al., 2016). The multiple generations and morphological variety of pyrite provide further evidence against TSR as the only driver for pyritization (Figs. 5.2-5.3). These considerations render TSR a possible, yet unlikely, scenario for explaining such a negative $\delta^{34}S$ value (-15.13‰). Notably, this value appears in framboidal pyrite (Figs. 4-6), which is demonstrably an early phase (Fig. 5.3B). This is consistent with a synsedimentary to early diagenetic origin, which is expected for microbially derived sulfide. For these reasons, the overall $\delta^{34}S$ variability in the Rammelsberg system most likely requires both TSR and MSC, consistent with previous interpretations (Anger et al., 1966; Nielsen, 1985; Eldridge et al., 1988; Large and Walcher, 1999).

Notably, the possible co-occurrence of TSR and MSC signals is not reflected in morphotypes with distinct $\delta^{34}S$ compositions. Rather, the median $\delta^{34}S$ compositions

of framboidal, subhedral, and euhedral pyrite are similar (Tab. 1). This suggests that not all pyrite with $\delta^{34}S > 0‰$ initially formed from TSR-derived sulfide. Instead, it seems plausible that an early diagenetic MSC-derived pyrite generation with initial $\delta^{34}S$ compositions of < 0‰ experienced isotope exchange with ^{34}S-enriched ($\delta^{34}S > 0‰$) fluids during periods of hydrothermal activity, consistent with evidence for framboid recrystallization (Fig. 5.3A-B) (Eldridge et al., 1988; Nozaki et al., 2020, 2024; Liu et al., 2022; Meng et al., 2022; Martin et al., 2023). At the same time, a secondary generation of subhedral and euhedral pyrite may have inherited heavy $\delta^{34}S$ values caused by closed-system TSR (Eldridge et al., 1988; Paiste et al., 2024). Both processes may have resulted in the unimodal $\delta^{34}S$ distribution around near-seawater $\delta^{34}S$ values, independent of pyrite morphology, that is observed in this study (Fig. 5.5). Such an evolution is consistent with previous interpretations from the Rammelsberg deposit and other sediment-hosted hydrothermal sulfide deposits, as well as sedimentary basins affected by TSR (Eldridge et al., 1988; Lyons et al., 2006; Sáez et al., 2011; Paiste et al., 2024). In concert, the most likely scenario is a two-step process involving early diagenetic pyrite formation driven by MSC during low-temperature conditions followed by, or alternating with, periods of hydrothermal fluid circulation when TSR-derived sulfide drove recrystallization and formation of the secondary pyrite generation.

5.6.3 Hydrothermal versus early diagenetic pyrite formation - insights from iron isotopes ($\delta^{56}Fe$)

This two-step model of MSC during early diagenesis and TSR in episodes of hydrothermal fluid circulation allows for different predictions concerning the iron cycle during pyrite formation in the Rammelsberg system: either hydrothermal Fe(II) delivery was involved in secondary pyrite formation with TSR-derived sulfide, or hydrothermal fluids drove the pyritization of sedimentary iron-bearing precursors, or both.

If pyrite precipitated from hydrothermal Fe(II), differences in $\delta^{56}Fe$ between our analyzed pyrite grains should reflect a variable expression of KIE and EIE as a function of precipitation rate (Syverson et al., 2013; Mansor and Fantle, 2019;

Pokrovski et al., 2021). Pyrite formation rates depend on various parameters, including temperature, pH, E_h, pyrite saturation, iron/sulfide ratio, type and stoichiometry of the iron source, trace metal abundance, as well as content and composition of organic matter (Berner, 1984; Canfield et al., 1992; Benning et al., 2000; Wan et al., 2017; Baya et al., 2021; Nie et al., 2023; Wang et al., 2023; Domingos et al., 2023; Runge et al., 2023b, 2024). Notably, these parameters also exert a strong control on pyrite morphology (Murowchick and Barnes, 1987; Wang and Morse, 1996; Wang et al., 2022; Domingos et al., 2023; Runge et al., 2023b, 2024). Framboidal pyrite in sediments and sedimentary rocks is usually considered an early diagenetic microbially-induced precipitate characterized by rapid nucleation (e.g., Rickard, 2019). On the other hand, large euhedral pyrite grains, such as presented here (e.g., Fig. 5.3D), commonly result from either the slow growth of small euhedral grains or form as a later transformation product from framboid recrystallization (Sawlowicz, 1993; Domingos et al., 2023). Accordingly, framboidal pyrite may reflect dominant expression of KIE (i.e., lower δ^{56}Fe), while euhedral pyrite expresses a stronger EIE (i.e., higher δ^{56}Fe) (Butler et al., 2005; Polyakov et al., 2007; Guilbaud et al., 2011; Syverson et al., 2013; Rolison et al., 2018; Mansor and Fantle, 2019).

Rate-controlled variations of δ^{56}Fe in pyrite are consistent with framboidal pyrite showing a lower median δ^{56}Fe than euhedral pyrite (+0.39‰ vs. +1.00‰, respectively; Tab. 5.1; Fig. 5.4). Subhedral pyrite (+0.86‰) may represent an intermediate phase but considering the 2σ uncertainty of the instrumental mass fractionation, it is not significantly different from framboidal and euhedral pyrite. Variations in pyritization rates may occur among different microenvironments within a sedimentary body and over time during progressive diagenesis, potentially leading to the co-occurrence of various pyrite morphotypes after compaction (Chang et al., 2022). Thus, framboidal, subhedral, and euhedral pyrite may have formed simultaneously but at different rates, resulting in variable expression of KIE and EIE between paragenetic pyrite morphotypes. However, textural evidence for framboid recrystallization and overgrowth by euhedral pyrite implies that the δ^{56}Fe variability

between pyrite morphotypes more likely reflects the variable expression of KIE and EIE between different pyrite generations.

This raises the question of whether pyrite precipitation from hydrothermal fluids can explain the overall $\delta^{56}Fe$ variability in the Rammelsberg system. To address this question, we assume the typical $\delta^{56}Fe$ value of hydrothermal $Fe(II)_{aq}$ (-0.8 to -0.1‰: Severmann et al., 2004; Johnson et al., 2008; Rouxel et al., 2008) as an approximation of the hydrothermal iron source composition in the Rammelsberg system. At the lower minimum fluid temperature estimate of 130°C (Muchez and Stassen, 2006), the apparent isotope fractionation during pyrite precipitation should only be ca. -1.9‰ relative to the hydrothermal Fe(II) (Syverson et al., 2013; Mansor and Fantle, 2019). This would result in $\delta^{56}Fe$ compositions similar to previously analyzed pyrite from seafloor hydrothermal sulfides, which typically display a narrow range of $\delta^{56}Fe$ between ca. -2.0 and 0.0‰ (Rouxel et al., 2004, 2008; Dauphas et al., 2017). Hence, while some pyrite compositions in our sample could be explained by direct precipitation from hydrothermal Fe(II), this model fails to explain the overall $\delta^{56}Fe$ variability and the strongly positive values we observed (Tab. 5.1; Figs. 5.4-5.5). In contrast, sedimentary pyrite usually displays much larger $\delta^{56}Fe$ variations (ca. -4‰ to +4‰: Mansor and Fantle, 2019; Dupeyron et al., 2023). Thus, the range and the median of $\delta^{56}Fe$ values displayed here indicate either a sedimentary origin or a combination of sedimentary and hydrothermal signals for most pyrite grains, lending support to the two-step model for pyrite formation inferred from the sulfur isotope data.

Sedimentary pyrite forms via the reaction of aqueous FeS (FeS_{aq}) with polysulfides or H_2S (Rickard, 1975, 1997; Luther, 1991) or surface-mediated sulfidation of Fe(III) (oxyhydr)oxides (Peiffer et al., 2015; Wan et al., 2017). The FeS_{aq} precursor commonly results from mackinawite (FeS_m) dissolution (Rickard, 1997). FeS_m, in turn, can either precipitate from negative $\delta^{56}Fe$ pore water $Fe(II)_{aq}$ or positive $\delta^{56}Fe$ Fe(II) after the complete reduction of Fe(III) (oxyhydr)oxide minerals (Crosby et al., 2007; Guilbaud et al., 2011; Marin-Carbonne et al., 2020). Hence, the $\delta^{56}Fe$ variation in sedimentary pyrite might reflect the pyritization of isotopically different precursors, consistent

with the bimodal distribution of $\delta^{56}Fe$ values (Marin-Carbonne et al., 2020; Decraene et al., 2021) (Fig. 5.5). If the $\delta^{56}Fe$ variation in our sample results from different precursors, the heavier and lighter pyrite endmembers would approximate the composition of the Fe(III)- and Fe(II)-derived precursor, respectively. The difference between these endmembers ($\Delta^{56}Fe_{Fe(III)-Fe(II)}$) in our sample is 3.49‰, which is similar to equilibrium fractionation at low temperatures (3‰; Dauphas et al., 2017; Johnson et al., 2020). One possible source for isotopically heavy Fe(III)-bearing endmember is the total reductive dissolution of magnetite (Poulton et al., 2004; Runge et al., 2023b, 2024), which is an accessory mineral in the Rammelsberg deposit (Ramdohr, 1953). The isotopically lighter Fe(II) endmember, on the other hand, could have resulted from partial reduction of primary Fe(III)-bearing minerals by microbial Fe(III) reduction or reducing hydrothermal fluids, producing Fe(II)-bearing pyrite precursors phases like FeS_m or greigite [Fe_3S_4] (Beard et al., 1999; Butler et al., 2005; McAnena et al., 2024). Therefore, the pyritization of isotopically different precursors best explains the overall $\delta^{56}Fe$ variability in the Rammelsberg system. Notably, the similar $\delta^{56}Fe$ ranges between framboidal, subhedral, and euhedral pyrite (Figs. 5.4,5.5) suggest this could apply to all observed pyrite morphotypes.

In summary, while a variable expression of KIE and EIE may explain the different median compositions of framboidal and euhedral pyrite, we interpret the wide range of $\delta^{56}Fe$ in our sample to result from pyritization of isotopically different pyrite precursors produced during early diagenesis. The production of these precursors requires redox reactions involving iron, which are dominantly driven by microbial iron cycling in marine sediments (Picard et al., 2016; Berg et al., 2020; Planavsky et al., 2021; Kappler et al., 2021), consistent with periods of low-temperature conditions in the Rammelsberg system. Thus, the $\delta^{56}Fe$ variability in our sample is best explained by a model involving a microbially driven fractionation of the sedimentary iron pool in the Rammelsberg system. While it cannot be ruled out that the $\delta^{56}Fe$ record in pyrite was modified by partial equilibration with hydrothermal Fe(II), this suggests a better preservation of $\delta^{56}Fe$ than $\delta^{34}S$ records in pyrite during hydrothermal alteration, as previously observed (Marin-Carbonne et al., 2020).

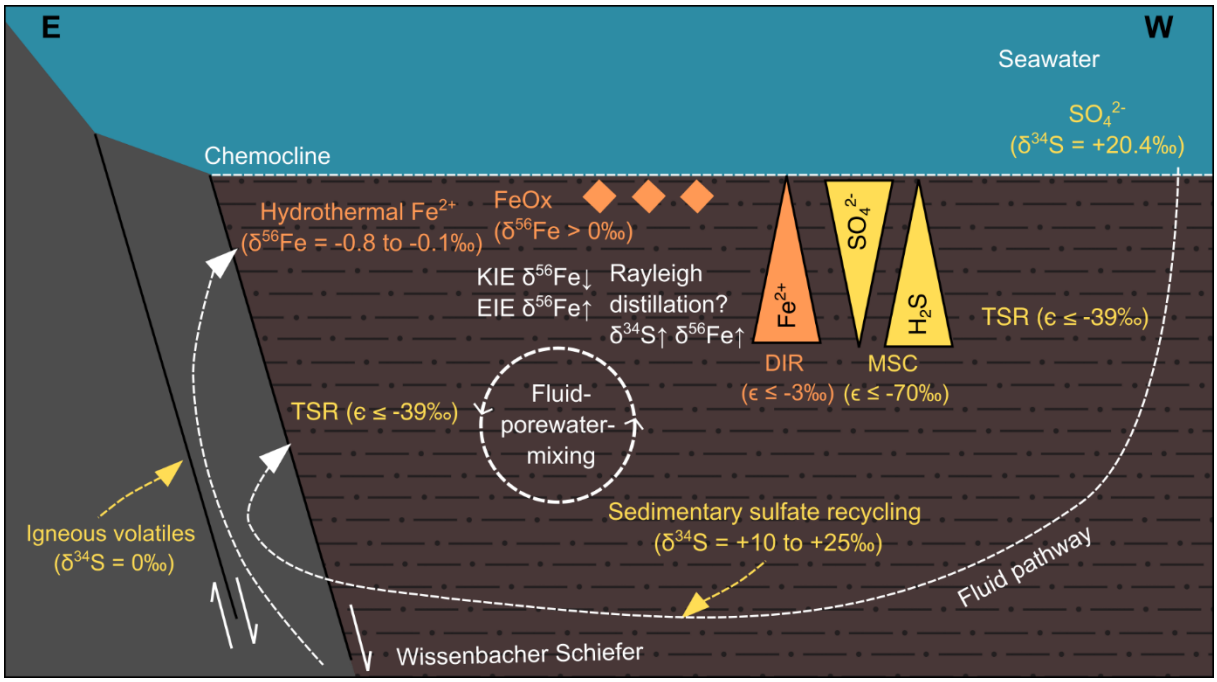

Figure 5.7: Sulfur ($\delta^{34}S$) and iron ($\delta^{56}Fe$) isotope systematics in the Rammelsberg system. Yellow features denote reservoirs and processes affecting the sulfur pool. Orange features denote reservoirs and processes affecting the iron pool. FeOx: Iron (oxyhydr)oxides, KIE: Kinetic Isotope Effect, EIE: Equilibrium Isotope Effect, DIR: Dissimilatory Fe(III)-reduction, MSC: Microbial Sulfur Cycling, TSR: Thermochemical Sulfate Reduction. Geological context, isotopic compositions of reservoirs, and fractionation factors (ε) associated with relevant processes were compiled from Anger et al. (1966); Eldridge et al. (1988); Ono, 2008; Sáez et al. (2011); Mansor and Fantle, (2019); Hoefs, (2021).

5.6.4 Implications for biosignature preservation in hydrothermal systems

Volcanogenic and sediment-hosted massive sulfide deposits commonly show large bulk and in-situ $\delta^{34}S$ variations ($\Delta^{34}S_{py}$ > ~30‰) (Eldridge et al., 1988, 1993; Taylor, 2004; Present et al., 2017; Lode et al., 2017; Slack et al., 2019; Velasco-Acebes et al., 2019; Nozaki et al., 2020, 2024; Liu et al., 2022). Typically, these $\delta^{34}S$ signatures are specific to pyrite with certain textures and commonly interpreted as follows: (i) an early framboidal pyrite with low-$\delta^{34}S$, resulting from MSC, and (ii) a late euhedral pyrite with high $\delta^{34}S$ values, precipitated from a hydrothermal sulfur source. While our in-situ data support this view for sulfur, this may not be true for the hitherto poorly explored $\delta^{56}Fe$ record of sediment-hosted massive sulfide deposits. Instead, our $\delta^{56}Fe$ data can entirely be explained by early diagenetic iron cycling and seem less affected by hydrothermal alteration, consistent with previous observations from sedimentary pyrite (Marin-Carbonne et al., 2020). Moreover, $\delta^{56}Fe$ evidence for the sulfidation of Fe(III) (oxyhydr)oxides in some pyrite grains lends support to the idea

that pyrite in hydrothermal sulfide environments may inherit biosignatures from its precursor minerals (Runge et al., 2023a, 2023b, 2024). Thus, our study highlights the importance of multi-proxy and in-situ approaches when interpreting stable isotope records of iron and sulfur cycling in hydrothermal environments.

The consistently large variability of $\delta^{56}Fe$ ranges between pyrite morphotypes, suggesting a role of microbial iron cycling, implies that information on past microbial life can be gleaned from pyrite grains of various morphologies and is not restricted to selected early diagenetic phases (i.e., framboidal pyrite). It is commonly noted that the identification of biosignatures based on morphological features alone can lead to false positive life detection (e.g., Brasier et al., 2002; García-Ruiz et al., 2003; Cosmidis and Templeton, 2016; McMahon, 2019). This is highlighted by the fact that framboidal pyrite in this study resembles spheroidal pyrite, which may result from the abiotic sulfidation of organic matter associated precursors (Duverger et al., 2021; Runge et al., 2024). On the other hand, our coupled textural and microscale stable isotope data stress that negligence of mineral morphotypes not commonly associated with life (i.e., subhedral and euhedral pyrite) can lead to false negatives.

Our textural and in-situ stable isotope data in pyrites from the Rammelsberg deposit were consistent with microbial redox cycling of sulfur and iron in the precursor sediment. Remarkably, these potential biosignatures survived pervasive hydrothermal alteration of the precursor sediment and low-grade post-depositional metamorphism (Ramdohr, 1953; Muchez and Stassen, 2006; Runge et al., 2023a). Up to 3.5 billion-years-old deposits in the Barberton Greenstone Belt and Pilbara Craton (South Africa and Western Australia, respectively) represent the oldest geological record of sulfidic hydrothermal systems. This includes the Bien Venue Formation, the Sulphur Springs Group, and the Dresser Formation, which hosts some of the oldest well-preserved evidence for life on Earth (Vearncombe et al., 1995; Van Kranendonk et al., 2008; Hofmann, 2011; Mißbach et al., 2021; Weimann et al., 2024; Baumgartner et al., 2024). Notably, these deposits experienced no more than greenschist facies metamorphism (Buick et al., 2002; Kohler and Anhaeusser, 2002; Terabayashi et al., 2003; Tice et al., 2004), similar to the Rammelsberg deposit (Ramdohr, 1953; Muchez

and Stassen, 2006). Hence, textural analysis coupled with in-situ iron and sulfur isotope signatures in pyrite from these localities could provide promising targets for studying microbial iron and sulfur cycling in Earth's most ancient hydrothermal sulfide systems.

5.7 CONCLUSIONS

By integrating textural evidence with coupled in-situ SIMS triple sulfur ($\delta^{34}S$ and $\Delta^{33}S$) and iron isotope ($\delta^{56}Fe$) data, we conclude that pyrite in the 390 Ma Rammelsberg sediment-hosted hydrothermal sulfide deposit preserves evidence for early diagenetic microbial sulfur and iron cycling. Phase relations between framboidal and euhedral pyrite establish that framboidal pyrite is the earlier generation. While the bulk of our $\delta^{34}S$ and $\Delta^{33}S$ compositions are consistent with both hydrothermal (igneous and/or TSR) or microbial sulfide sources, the isotopically lightest pyrite ($\delta^{34}S$ = -15.13‰; framboidal) in the Rammelsberg deposit is best explained by microbial sulfur cycling. Differences in median $\delta^{56}Fe$ between framboidal and euhedral pyrite suggest differential expression of KIE and EIE due to varying pyritization rates between earlier and later formed pyrite. However, the overall $\delta^{56}Fe$ variability in our sample reflects a diagenetically fractionated iron pool, most likely affected by microbial iron cycling. In concert, our data imply a multigenerational sequence of early diagenetic pyrite, recording microbial sulfur and iron cycling and hydrothermal overprint of the system, consistent with textural evidence for framboid recrystallization and overgrowth. This alteration demonstrably affected the sulfur isotope record in pyrite but allowed for preserving iron isotope signals of early diagenetic processes. The equal presence of evidence for microbial iron cycling between framboidal, subhedral, and euhedral pyrite, as indicated by similar $\delta^{56}Fe$ ranges, highlights that focusing geobiological studies exclusively on mineral morphotypes commonly associated with microbial activity (i.e., framboidal pyrite) can lead to false-negative life detection. Our results suggest that textural evidence and stable isotope signatures of early diagenetic microbial redox cycling can be preserved in sediment-hosted massive sulfides – despite pervasive alteration of the precursor sediments by hydrothermal fluids and later greenschist metamorphism.

Hence, coupled in-situ sulfur and iron isotope analysis of pyrite provides a challenging but powerful means to track biogeochemical cycles throughout the geological record, perhaps including some of the oldest rocks on Earth.

5.8 Acknowledgments

This study was supported by the DFG (SPP 1833, Emmy Noether Programme; DU 1450/3-2, DU 1450/7-1; JPD, ER; INST 37/1027-1 FUGG; AK) and the German Excellence Strategy of the German Federal and State Governments (EXC2124, 390838134; Tübingen Structural Microscopy Core Facility; AK, MM). We thank Jeremiah Shuster and Stefan Fischer for their SEM work and Axel Hackmann for his support in thin section preparation. Eckart Walcher provided valuable insights into the Wissenbacher Schiefer and the ore genesis in the Rammelsberg deposit.

5.9 References

Anger, G., Nielson, H., Puchelt, H., and Ricke, W., 1966, Sulfur isotopes in the Rammelsberg ore deposit (Germany): Economic Geology, v. 61, p. 511–536, doi:10.2113/gsecongeo.61.3.511.

Baumgartner, R.J. et al., 2022, Exceptional preservation of organic matter and iron-organic colloidal mineralization in hydrothermal black smoker-type sulfide mineralization from the Paleoarchean seafloor: Chemical Geology, p. 121296, doi:10.1016/j.chemgeo.2022.121296.

Baumgartner, R.J., Caruso, S., Fiorentini, M.L., Van Kranendonk, M.J., Martin, L., Jeon, H., Pagès, A., and Wacey, D., 2020, Sulfidization of 3.48 billion-year-old stromatolites of the Dresser Formation, Pilbara Craton: Constraints from in-situ sulfur isotope analysis of pyrite: Chemical Geology, v. 538, p. 119488, doi:10.1016/j.chemgeo.2020.119488.

Baumgartner, R.J., Van Kranendonk, M.J., Caruso, S., Campbell, K.A., Dobson, M.J., Teece, B.L., Verrall, M., Homann, M., Lalonde, S., and Visscher, P.T., 2024, Pyritic stromatolites from the Paleoarchean Dresser Formation, Pilbara Craton: Resolving biogenicity and hydrothermally influenced ecosystem dynamics: Geobiology, v. 22, p. e12610, doi:10.1111/gbi.12610.

Baya, C. et al., 2021, Influence of trace level As or Ni on pyrite formation kinetics at low temperature: Geochimica et Cosmochimica Acta, v. 300, p. 333–353, doi:10.1016/j.gca.2021.01.042.

Beard, B.L., Johnson, C.M., Cox, L., Sun, H., Nealson, K.H., and Aguilar, C., 1999, Iron Isotope Biosignatures: Science, v. 285, p. 1889–1892, doi:10.1126/science.285.5435.1889.

Bendt, G., Saddeler, S., and Schulz, S., 2019, Sulfidation of Magnetite Nanoparticles – Following the Polysulfide Pathway: European Journal of Inorganic Chemistry, p. 602–608.

Benning, L.G., Wilkin, R.T., and Barnes, H.L., 2000, Reaction pathways in the Fe–S system below 100°C: Chemical Geology, v. 167, p. 25–51, doi:10.1016/S0009-2541(99)00198-9.

Berg, J.S., Duverger, A., Cordier, L., Laberty-Robert, C., Guyot, F., and Miot, J., 2020, Rapid pyritization in the presence of a sulfur/sulfate-reducing bacterial consortium: Scientific Reports, v. 10, p. 8264, doi:10.1038/s41598-020-64990-6.

Berner, R.A., 1984, Sedimentary pyrite formation: An update: Geochimica et Cosmochimica Acta, v. 48, p. 605–615, doi:10.1016/0016-7037(84)90089-9.

Bradley, A.S., Leavitt, W.D., Schmidt, M., Knoll, A.H., Girguis, P.R., and Johnston, D.T., 2016, Patterns of sulfur isotope fractionation during microbial sulfate reduction: Geobiology, v. 14, p. 91–101.

Brasier, M.D., Green, O.R., Jephcoat, A.P., Kleppe, A.K., Van Kranendonk, M.J., Lindsay, J.F., Steele, A., and Grassineau, N.V., 2002, Questioning the evidence for Earth's oldest fossils: Nature, v. 416, p. 76–81, doi:10.1038/416076a.

Bronner, R. et al., 2023, Co-reduction of Fe(III) and S0 drives Fe-S biomineral formation and phosphate mobilisation: Geochemical Perspectives Letters, v. 24, p. 27–32, doi:10.7185/geochemlet.2301.

Buchholz, P., and Luppold, F.W., 2008, Litho-und Biostratigrafie des älteren Mitteldevons im Oberharz: Zeitschrift der Deutschen Gesellschaft für Geowissenschaften, v. 159, p. 263–281.

Buick, R. et al., 2002, Geochronology and stratigraphic relationships of the Sulphur Springs Group and Strelley Granite: a temporally distinct igneous province in the Archaean Pilbara Craton, Australia: Precambrian Research, v. 114, p. 87–120, doi:10.1016/S0301-9268(01)00221-2.

Buschendorf, F., Nielsen, H., Puchelt, H., and Ricke, W., 1963, Schwefel-Isotopen-Untersuchungen am Pyrit-Sphalerit-Barit-Lager Meggen/Lenne (Deutschland) und an verschiedenen Devon-Evaporiten: Geochimica et Cosmochimica Acta, v. 27, p. 501–523.

Butler, I.B., Archer, C., Vance, D., Oldroyd, A., and Rickard, D., 2005, Fe isotope fractionation on FeS formation in ambient aqueous solution: Earth and Planetary Science Letters, v. 236, p. 430–442, doi:10.1016/j.epsl.2005.05.022.

Butler, I.B., Böttcher, M.E., Rickard, D., and Oldroyd, A., 2004, Sulfur isotope partitioning during experimental formation of pyrite via the polysulfide and hydrogen sulfide pathways: implications for the interpretation of sedimentary and hydrothermal pyrite isotope records: Earth and Planetary Science Letters, v. 228, p. 495–509, doi:10.1016/j.epsl.2004.10.005.

Cai, C., Li, H., Li, K., and Wang, D., 2022, Thermochemical sulfate reduction in sedimentary basins and beyond: A review: Chemical Geology, v. 607, p. 121018, doi:10.1016/j.chemgeo.2022.121018.

Canfield, D.E., 2001, Biogeochemistry of Sulfur Isotopes, *in* Valley, J.W. and Cole, D.R. eds., Reviews in Mineralogy and Geochemistry, Mineralogical society of America.

Canfield, D.E., and Berner, R.A., 1987, Dissolution and pyritization of magnetite in anoxic marine sediments: Geochimica et Cosmochimica Acta, v. 51, p. 645–659, doi:10.1016/0198-0254(87)90182-8.

Canfield, D.E., Raiswell, R., and Bottrell, S., 1992, The Reactivity of Sedimentary Iron Minerals Toward Sulfide: American Journal of Science, v. 292, p. 659–683.

Canfield, D.E., and Thamdrup, B., 1994, The Production of ^{34}S-Depleted Sulfide During Bacterial Disproportionation of Elemental Sulfur: Science, v. 266, p. 1973–1975, doi:10.1126/science.11540246.

Canfield, D.E., Thamdrup, B., and Fleischer, S., 1998, Isotope fractionation and sulfur metabolism by pure and enrichment cultures of elemental sulfur-disproportionating bacteria: Limnology and Oceanography, v. 43, p. 253–264, doi:10.4319/lo.1998.43.2.0253.

Chambers, L.A., Trudinger, P.A., Smith, J.W., and Burns, M.S., 1975, Fractionation of sulfur isotopes by continuous cultures of Desulfovibrio desulfuricans: Canadian Journal of Microbiology, v. 21, p. 1602–1607.

Chanda, P., Amenabar, M.J., Boyd, E.S., Beard, B.L., and Johnson, C.M., 2021, Stable Fe isotope fractionation during dissimilatory Fe(III) reduction by a thermoacidophile in acidic hydrothermal environments: Geochimica et Cosmochimica Acta, v. 292, p. 427–451, doi:10.1016/j.gca.2020.09.025.

Chang, J., Li, Y., and Lu, H., 2022, The Morphological Characteristics of Authigenic Pyrite Formed in Marine Sediments: Journal of Marine Science and Engineering, v. 10, p. 1533, doi:10.3390/jmse10101533.

Chever, F., Rouxel, O.J., Croot, P.L., Ponzevera, E., Wuttig, K., and Auro, M., 2015, Total dissolvable and dissolved iron isotopes in the water column of the Peru upwelling regime: Geochimica et Cosmochimica Acta, v. 162, p. 66–82, doi:10.1016/j.gca.2015.04.031.

Cosmidis, J., and Templeton, A.S., 2016, Self-assembly of biomorphic carbon/sulfur microstructures in sulfidic environments: Nature Communications, v. 7, p. 12812, doi:10.1038/ncomms12812.

Crosby, H.A., Johnson, C.M., Roden, E.E., and Beard, B.L., 2005, Coupled Fe(II)–Fe(III) Electron and Atom Exchange as a Mechanism for Fe Isotope Fractionation during Dissimilatory Iron Oxide Reduction: Environmental Science & Technology, v. 39, p. 6698–6704, doi:10.1021/es0505346.

Crosby, H.A., Roden, E.E., Johnson, C.M., and Beard, B.L., 2007, The mechanisms of iron isotope fractionation produced during dissimilatory Fe(III) reduction by *Shewanella putrefaciens* and *Geobacter sulfurreducens*: Geobiology, v. 5, p. 169–189, doi:10.1111/j.1472-4669.2007.00103.x.

Dauphas, N., Heard, A.W., Rego, E.S., Rouxel, O., Marin-Carbonne, J., Pasquier, V., Bekker, A., and Rowley, D., 2024, Past and present dynamics of the iron biogeochemical cycle, *in* Treatise in Geochemistry, Elsevier, p. arXiv:2312.09044, doi:10.1016/B978-0-323-99762-1.00059-0.

Dauphas, N., John, S.G., and Rouxel, O., 2017, Iron Isotope Systematics: Reviews in Mineralogy and Geochemistry, v. 82, p. 415–510, doi:10.2138/rmg.2017.82.11.

Decraene, M.-N., Marin-Carbonne, J., Thomazo, C., Olivier, N., Philippot, P., Strauss, H., and Deloule, E., 2021, Intense biogeochemical iron cycling revealed in Neoarchean micropyrites from stromatolites: Geochimica et Cosmochimica Acta, v. 312, p. 299–320, doi:10.1016/j.gca.2021.07.020.

Domingos, J.M., Runge, E., Dreher, C., Chiu, T.-H., Shuster, J., Fischer, S., Kappler, A., Duda, J.-P., Xu, J., and Mansor, M., 2023, Inferred pyrite growth via the particle attachment pathway in the presence of trace metals: Geochemical Perspectives Letters, v. 26, p. 14–19, doi:10.7185/geochemlet.2318.

Donald, R., and Southam, G., 1999, Low temperature anaerobic bacterial diagenesis of ferrous monosulfide to pyrite: Geochimica et Cosmochimica Acta, v. 63, p. 2019–2023, doi:10.1016/S0016-7037(99)00140-4.

Duda, J.-P., Van Kranendonk, M.J., Thiel, V., Ionescu, D., Strauss, H., Schäfer, N., and Reitner, J., 2016, A Rare Glimpse of Paleoarchean Life: Geobiology of an Exceptionally Preserved Microbial Mat Facies from the 3.4 Ga Strelley Pool Formation, Western

Australia (J. M. Senko, Ed.): PLoS ONE, v. 11, p. e0147629, doi:10.1371/journal.pone.0147629.

Dupeyron, J., Decraene, M.-N., Marin-Carbonne, J., and Busigny, V., 2023, Formation pathways of Precambrian sedimentary pyrite: Insights from in situ Fe isotopes: Earth and Planetary Science Letters, v. 609, p. 118070, doi:10.1016/j.epsl.2023.118070.

Duverger, A., Berg, J.S., Busigny, V., Guyot, F., Bernard, S., and Miot, J., 2020, Mechanisms of Pyrite Formation Promoted by Sulfate-Reducing Bacteria in Pure Culture: Frontiers in Earth Science, v. 8, p. 588310, doi:10.3389/feart.2020.588310.

Duverger, A., Bernard, S., Viennet, J., Miot, J., and Busigny, V., 2021, Formation of pyrite spherules from mixtures of biogenic FeS and organic compounds during experimental diagenesis: Geochemistry, Geophysics, Geosystems, doi:10.1029/2021GC010056.

Eickmann, B., Thorseth, I.H., Peters, M., Strauss, H., Bröcker, M., and Pedersen, R.B., 2014, Barite in hydrothermal environments as a recorder of subseafloor processes: a multiple-isotope study from the Loki's Castle vent field: Geobiology, v. 12, p. 308–321, doi:10.1111/gbi.12086.

Eldridge, C.S., Compston, W., Williams, I.S., Both, R.A., Walshe, J.L., and Ohmoto, H., 1988, Sulfur isotope variability in sediment-hosted massive sulfide deposits as determined using the ion microprobe SHRIMP; I, An example from the Rammelsberg orebody: Economic Geology, v. 83, p. 443–449, doi:10.2113/gsecongeo.83.2.443.

Eldridge, D.L., and Farquhar, J., 2018, Rates and multiple sulfur isotope fractionations associated with the oxidation of sulfide by oxygen in aqueous solution: Geochimica et Cosmochimica Acta, v. 237, p. 240–260, doi:10.1016/j.gca.2018.06.030.

Eldridge, D.L., Guo, W., and Farquhar, J., 2016, Theoretical estimates of equilibrium sulfur isotope effects in aqueous sulfur systems: Highlighting the role of isomers in the sulfite and sulfoxylate systems: Geochimica et Cosmochimica Acta, v. 195, p. 171–200, doi:10.1016/j.gca.2016.09.021.

Eldridge, C.S., Williams, N., and Walshe, J.L., 1993, Sulfur isotope variability in sediment-hosted massive sulfide deposits as determined using the ion microprobe SHRIMP; II, A study of the H.Y.C. Deposit at McArthur River, Northern Territory, Australia: Economic Geology, v. 88, p. 1–26, doi:10.2113/gsecongeo.88.1.1.

Farquhar, J., Johnston, D.T., and Wing, B.A., 2007, Implications of conservation of mass effects on mass-dependent isotope fractionations: Influence of network structure on sulfur isotope phase space of dissimilatory sulfate reduction: Geochimica et Cosmochimica Acta, v. 71, p. 5862–5875, doi:10.1016/j.gca.2007.08.028.

Farquhar, J., Johnston, D.T., Wing, B.A., Habicht, K.S., Canfield, D.E., Airieau, S., and Thiemens, M.H., 2003, Multiple sulphur isotopic interpretations of biosynthetic pathways: implications for biological signatures in the sulphur isotope record: Geobiology, v. 1, p. 27–36, doi:10.1046/j.1472-4669.2003.00007.x.

Fortney, N.W., He, S., Converse, B.J., Beard, B.L., Johnson, C.M., Boyd, E.S., and Roden, E.E., 2016, Microbial Fe(III) oxide reduction potential in Chocolate Pots hot spring, Yellowstone National Park: Geobiology, v. 14, p. 255–275, doi:10.1111/gbi.12173.

Früh-Green, G.L., Kelley, D.S., Lilley, M.D., Cannat, M., Chavagnac, V., and Baross, J.A., 2022, Diversity of magmatism, hydrothermal processes and microbial interactions at mid-ocean ridges: Nature Reviews Earth & Environment, v. 3, p. 852–871, doi:10.1038/s43017-022-00364-y.

Gagnevin, D., Boyce, A.J., Barrie, C.D., Menuge, J.F., and Blakeman, R.J., 2012, Zn, Fe and S isotope fractionation in a large hydrothermal system: Geochimica et Cosmochimica Acta, v. 88, p. 183–198, doi:10.1016/j.gca.2012.04.031.

García-Ruiz, J.M., Hyde, S.T., Carnerup, A.M., Christy, A.G., Van Kranendonk, M.J., and Welham, N.J., 2003, Self-Assembled Silica-Carbonate Structures and Detection of Ancient Microfossils: Science, v. 302, p. 1194–1197, doi:10.1126/science.1090163.

Georgieva, M.N., Little, C.T.S., Maslennikov, V.V., Glover, A.G., Ayupova, N.R., and Herrington, R.J., 2021, The history of life at hydrothermal vents: Earth-Science Reviews, v. 217, p. 103602, doi:10.1016/j.earscirev.2021.103602.

Goodfellow, W.D., 1987, Anoxic stratified oceans as a source of sulphur in sediment-hosted stratiform ZnPb deposits (Selwyn Basin, Yukon, Canada): Chemical Geology: Isotope Geoscience section, v. 65, p. 359–382, doi:10.1016/0168-9622(87)90014-5.

Gorlas, A. et al., 2022, Precipitation of greigite and pyrite induced by Thermococcales: an advantage to live in Fe- and S-rich environments? Environmental Microbiology, p. 1462- 2920.15915, doi:10.1111/1462-2920.15915.

Guilbaud, R., Butler, I.B., and Ellam, R.M., 2011, Abiotic Pyrite Formation Produces a Large Fe Isotope Fractionation: Science, v. 332, p. 1548–1551, doi:10.1126/science.1202924.

Habicht, K.S., Gade, M., Thamdrup, B., Berg, P., and Canfield, D.E., 2002, Calibration of Sulfate Levels in the Archean Ocean: Science, v. 298, p. 2372–2374.

Hoefs, J., 2021, Stable Isotope Geochemistry: Cham, Springer International Publishing, Springer Textbooks in Earth Sciences, Geography and Environment, doi:10.1007/978-3-030-77692-3.

Hofmann, A., 2011, Archaean Hydrothermal Systems in the Barberton Greenstone Belt and Their Significance as a Habitat for Early Life, *in* Golding, S.D. and Glikson, M. eds., Earliest Life on Earth: Habitats, Environments and Methods of Detection, Dordrecht, Springer Netherlands, p. 51–78, doi:10.1007/978-90-481-8794-2_3.

Huston, D.L., Pehrsson, S., Eglington, B.M., and Zaw, K., 2010, The Geology and Metallogeny of Volcanic-Hosted Massive Sulfide Deposits: Variations through Geologic Time and with Tectonic Setting: Economic Geology, v. 105, p. 571–591, doi:10.2113/gsecongeo.105.3.571.

Johnson, C.M., Beard, B.L., and Roden, E.E., 2008, The Iron Isotope Fingerprints of Redox and Biogeochemical Cycling in Modern and Ancient Earth: Annual Review of Earth and Planetary Sciences, v. 36, p. 457–493, doi:10.1146/annurev.earth.36.031207.124139.

Johnson, C., Beard, B., and Weyer, S., 2020, Iron Geochemistry: An Isotopic Perspective: Cham, Springer International Publishing, Advances in Isotope Geochemistry, doi:10.1007/978-3-030-33828-2.

Johnston, D.T., 2005, Multiple sulfur isotope fractionations in biological systems: A case study with sulfate reducers and sulfur disproportionators: American Journal of Science, v. 305, p. 645–660, doi:10.2475/ajs.305.6-8.645.

Jørgensen, B.B., Böttcher, M.E., Lüschen, H., Neretin, L.N., and Volkov, I.I., 2004, Anaerobic methane oxidation and a deep H2S sink generate isotopically heavy sulfides in Black Sea sediments: Geochimica et Cosmochimica Acta, v. 68, p. 2095–2118, doi:10.1016/j.gca.2003.07.017.

Jørgensen, B.B., Isaksen, M.F., and Jannasch, H.W., 1992, Bacterial Sulfate Reduction Above 100°C in Deep-Sea Hydrothermal Vent Sediments: Science, v. 258, p. 1756–1757, doi:10.1126/science.258.5089.1756.

Kappler, A., Bryce, C., Mansor, M., Lueder, U., Byrne, J.M., and Swanner, E.D., 2021, An evolving view on biogeochemical cycling of iron: Nature Reviews Microbiology, v. 19, p. 360–374, doi:10.1038/s41579-020-00502-7.

Kashefi, K., and Lovley, D.R., 2003, Extending the Upper Temperature Limit for Life: Science, v. 301, p. 934–934, doi:10.1126/science.1086823.

Kelley, K.D., Leach, D.L., Johnson, C.A., Clark, J.L., Fayek, M., Slack, J.F., Anderson, V.M., Ayuso, R.A., and Ridley, W.I., 2004, Textural, Compositional, and Sulfur Isotope Variations of Sulfide Minerals in the Red Dog Zn-Pb-Ag Deposits, Brooks Range, Alaska: Implications for Ore Formation: Economic Geology, v. 99, p. 1509–1532.

Kiyosu, Y., and Krouse, H.R., 1990, The role of organic acid in the abiogenic reduction of sulfate and the sulfur isotope effect.: Geochemical Journal, v. 24, p. 21–27, doi:10.2343/geochemj.24.21.

Kohler, E., and Anhaeusser, C.R., 2002, Geology and geodynamic setting of Archaean silicic metavolcaniclastic rocks of the Bien Venue Formation, Fig Tree Group, northeast Barberton greenstone belt, South Africa: Precambrian Research, v. 116, p. 199–235, doi:10.1016/S0301-9268(02)00021-9.

Large, D., and Walcher, E., 1999, The Rammelsberg massive sulphide Cu-Zn-Pb-Ba-Deposit, Germany: an example of sediment-hosted, massive sulphide mineralisation: Mineralium Deposita, v. 34, p. 522–538, doi:10.1007/s001260050218.

Liang, C., Ji, S., Cao, Y., Liu, K., Wu, J., and Hao, F., 2024, Characteristics, origins, and significance of pyrites in deep-water shales: Science China Earth Sciences, v. 67, p. 313–342, doi:10.1007/s11430-022-1200-0.

Liu, K., Huang, F., Gao, S., Zhang, Z., Ren, Y., and An, B., 2022, Morphology of framboidal pyrite and its textural evolution: Evidence from the Logatchev area, Mid-Atlantic Ridge: Ore Geology Reviews, v. 141, p. 104630, doi:10.1016/j.oregeorev.2021.104630.

Lode, S., Piercey, S.J., Layne, G.D., Piercey, G., and Cloutier, J., 2017, Multiple sulphur and lead sources recorded in hydrothermal exhalites associated with the Lemarchant volcanogenic massive sulphide deposit, central Newfoundland, Canada: Mineralium Deposita, v. 52, p. 105–128, doi:10.1007/s00126-016-0652-1.

Luther, G.W., 1991, Pyrite synthesis via polysulfide compounds: Geochimica et Cosmochimica Acta, v. 55, p. 2839–2849, doi:10.1016/0016-7037(91)90449-F.

Lyons, T.W., Gellatly, A.M., McGoldrick, P.J., and Kah, L.C., 2006, Proterozoic sedimentary exhalative (SEDEX) deposits and links to evolving global ocean chemistry, *in* Evolution of Early Earth's Atmosphere, Hydrosphere, and Biosphere - Constraints from Ore Deposits, Geological Society of America, doi:10.1130/2006.1198(10).

Machel, H.G., 2001, Bacterial and thermochemical sulfate reduction in diagenetic settings Ð old and new insights: Sedimentary Geology,.

Machel, H.G., Krouse, H.R., and Sassen, R., 1995, Products and distinguishing criteria of bacterial and thermochemical sulfate reduction: Applied Geochemistry, v. 10, p. 373–389, doi:10.1016/0883-2927(95)00008-8.

Mansor, M., and Fantle, M.S., 2019, A novel framework for interpreting pyrite-based Fe isotope records of the past: Geochimica et Cosmochimica Acta, v. 253, p. 39–62, doi:10.1016/j.gca.2019.03.017.

Marin-Carbonne, J. et al., 2020, In Situ Fe and S isotope analyses in pyrite from the 3.2 Ga Mendon Formation (Barberton Greenstone Belt, South Africa): Evidence for early microbial iron reduction: Geobiology, v. 18, p. 306–325.

Marin-Carbonne, J., Rollion-Bard, C., Bekker, A., Rouxel, O., Agangi, A., Cavalazzi, B., Wohlgemuth-Ueberwasser, C.C., Hofmann, A., and McKeegan, K.D., 2014, Coupled Fe and S isotope variations in pyrite nodules from Archean shale: Earth and Planetary Science Letters, v. 392, p. 67–79, doi:10.1016/j.epsl.2014.02.009.

Marin-Carbonne, J., Rollion-Bard, C., and Luais, B., 2011, In-situ measurements of iron isotopes by SIMS: MC-ICP-MS intercalibration and application to a magnetite crystal from the Gunflint chert: Chemical Geology, v. 285, p. 50–61, doi:10.1016/j.chemgeo.2011.02.019.

Martin, A.J., Jamieson, J.W., De Ronde, C.E.J., Layne, G.D., Piercey, G., and Brandl, P.A., 2023, Constraining temporal variations in metal and sulfur sources using high-resolution mineral-scale analysis of pyrite: evidence from the Brothers volcano, Kermadec arc, New Zealand: Mineralium Deposita, v. 58, p. 1237–1262, doi:10.1007/s00126-023-01177-9.

McAnena, A., Severmann, S., Guilbaud, R., and Poulton, S.W., 2024, Iron isotope fractionation during sulfide-promoted reductive dissolution of iron (oxyhydr)oxide minerals: Geochimica et Cosmochimica Acta, v. 369, p. 17–34, doi:10.1016/j.gca.2024.01.032.

McMahon, S., 2019, Earth's earliest and deepest purported fossils may be iron-mineralized chemical gardens: Proceedings of the Royal Society B: Biological Sciences, v. 286, p. 20192410, doi:10.1098/rspb.2019.2410.

Meng, X., Jin, X., Li, X., Chu, F., Zhu, J., Wang, Y., and Zhou, P., 2022, Subseafloor mineralization related to the shallow seawater-hydrothermal circulation system in the Longqi hydrothermal field, Southwest Indian Ridge (49.6°E): Evidence from in situ trace element and sulfur isotope compositions of pyrite varieties: Ore Geology Reviews, v. 145, p. 104914, doi:10.1016/j.oregeorev.2022.104914.

Meshoulam, A. et al., 2016, Study of thermochemical sulfate reduction mechanism using compound specific sulfur isotope analysis: Geochimica et Cosmochimica Acta, v. 188, p. 73–92, doi:10.1016/j.gca.2016.05.026.

Mißbach, H., Duda, J.-P., van den Kerkhof, A.M., Lüders, V., Pack, A., Reitner, J., and Thiel, V., 2021, Ingredients for microbial life preserved in 3.5 billion-year-old fluid inclusions: Nature Communications, v. 12, p. 1101, doi:10.1038/s41467-021-21323-z.

Moreno, C., González, F., and Sáez, R., 2019, Basin Evolution and Massive Sulfide Deposition at Rammelsberg (Germany): Updating the Subsidence Analysis: Minerals, v. 9, p. 45, doi:10.3390/min9010045.

Moreras-Marti, A., Fox-Powell, M., Cousins, C.R., Macey, M.C., and Zerkle, A.L., 2022, Sulfur isotopes as biosignatures for Mars and Europa exploration: Journal of the Geological Society, v. 179, p. jgs2021-134, doi:10.1144/jgs2021-134.

Muchez, P., and Stassen, P., 2006, Multiple origin of the 'Kniest feeder zone' of the stratiform Zn–Pb–Cu ore deposit of Rammelsberg, Germany: Mineralium Deposita, v. 41, p. 46–51, doi:10.1007/s00126-005-0039-1.

Muller, É., Philippot, P., Rollion-Bard, C., Cartigny, P., Assayag, N., Marin-Carbonne, J., Mohan, M.R., and Sarma, D.S., 2017, Primary sulfur isotope signatures preserved in high-grade Archean barite deposits of the Sargur Group, Dharwar Craton, India: Precambrian Research, v. 295, p. 38–47, doi:10.1016/j.precamres.2017.04.029.

Murowchick, J.B., and Barnes, H.L., 1987, Effects of temperature and degree of supersaturation on pyrite morphology: American Mineralogist, v. 72, p. 1241–1250.

Nie, M., Li, X., Ding, Y., Pan, Y., Cai, Y., Liu, Y., and Liu, J., 2023, Effect of Stoichiometry on Nanomagnetite Sulfidation: Environmental Science & Technology, p. acs.est.2c08179, doi:10.1021/acs.est.2c08179.

Nielsen, H., 1985, Sulfur isotope ratios in stratabound mineralizations in Central Europe: Hannover, Geologisches Jahrbuch, Reihe D, v. 70, 225–262 p.

Nozaki, T., Nagase, T., Ushikubo, T., Shimizu, K., Ishibashi, J., and and the D/V Chikyu Expedition 909 Scientists, 2020, Microbial sulfate reduction plays an important role at the initial stage of subseafloor sulfide mineralization: Geology, v. 49, p. 222–227, doi:10.1130/G47943.1.

Nozaki, T., Nagase, T., Ushikubo, T., Shimizu, K., and Komuro, K., 2024, In situ sulfur isotope analysis of pyrite from the Ezuri Kuroko-type volcanogenic massive sulfide deposit, northeastern Japan: Contribution of microbial sulfate reduction to initial sulfide mineralization: Resource Geology, v. 74, p. e12328.

Oduro, H., Harms, B., Sintim, H.O., Kaufman, A.J., Cody, G., and Farquhar, J., 2011, Evidence of magnetic isotope effects during thermochemical sulfate reduction: Proceedings of the National Academy of Sciences, v. 108, p. 17635–17638, doi:10.1073/pnas.1108112108.

Ohmoto, H., and Lasaga, A.C., 1982, Kinetics of reaetions between aqueous sulfates and sulfides in hydrothermal systems: Geochimica et Cosmochimica Acta, v. 46, p. 1727–1745.

Ono, S., 2008, Multiple-Sulphur Isotope Biosignatures: Space Science Reviews, v. 135, p. 203–220, doi:10.1007/s11214-007-9267-2.

Otake, T., Yamada, R., Suzuki, R., Nakamura, S., Ito, A., Shin, K.-C., and Sato, T., 2021, Large Fe isotope fractionations in sulfide ores and ferruginous sedimentary rocks from the

Kuroko volcanogenic massive sulfide deposits in the Hokuroku district, northeast Japan: Geochimica et Cosmochimica Acta, v. 295, p. 49–64, doi:10.1016/j.gca.2020.12.009.

Paiste, K. et al., 2024, Sulfur isotopes from the Paleoproterozoic Francevillian Basin record multigenerational pyrite formation, not depositional conditions: Communications Earth & Environment, v. 5, p. 328, doi:10.1038/s43247-024-01498-1.

Paiste, K., Fike, D.A., Kirsimäe, K., Jones, C., and Lepland, A., 2022, Testing the global significance of the sulfur isotope record of the ca. 2.0 Ga Zaonega Formation: A micro-scale S isotope investigation: Geochimica et Cosmochimica Acta, v. 331, p. 86–104, doi:10.1016/j.gca.2022.05.021.

Pasquier, V., Rego, E.S., Dupeyron, J., Bouvier, A.-S., Bovay, T., Robyr, M., and Marin-Carbonne, J., 2024, SIMS Iron Isotope Measurements of the Balmat Pyrite Reference Material: A Non-Unique δ56Fe Signature: Geostandards and Geoanalytical Research, p. 12549, doi:https://doi.org/10.1111/ggr.12549.

Paul, D., 1975, Sedimentologische und geologische Untersuchungen zur Rekonstruktion des Ablagerungsraumes vor und nach Bildung der Rammelsberger Pb-Zn-Lager: Hannover, Geologisches Jahrbuch, Reihe D 12, 3–93 p.

Peiffer, S., Behrends, T., Hellige, K., Larese-Casanova, P., Wan, M., and Pollok, K., 2015, Pyrite formation and mineral transformation pathways upon sulfidation of ferric hydroxides depend on mineral type and sulfide concentration: Chemical Geology, v. 400, p. 44–55, doi:10.1016/j.chemgeo.2015.01.023.

Picard, A., Gartman, A., and Girguis, P.R., 2016, What Do We Really Know about the Role of Microorganisms in Iron Sulfide Mineral Formation? Frontiers in Earth Science, v. 4, doi:10.3389/feart.2016.00068.

Planavsky, N.J., Crowe, S.A., Fakhraee, M., Beaty, B., Reinhard, C.T., Mills, B.J.W., Holstege, C., and Konhauser, K.O., 2021, Evolution of the structure and impact of Earth's biosphere: Nature Reviews Earth & Environment, doi:10.1038/s43017-020-00116-w.

Pokrovski, G.S., Blanchard, M., Saunier, G., and Poitrasson, F., 2021, Mechanisms and rates of pyrite formation from hydrothermal fluid revealed by iron isotopes: Geochimica et Cosmochimica Acta, v. 304, p. 281–304, doi:10.1016/j.gca.2021.03.006.

Polyakov, V.B., Clayton, R.N., Horita, J., and Mineev, S.D., 2007, Equilibrium iron isotope fractionation factors of minerals: Reevaluation from the data of nuclear inelastic resonant X-ray scattering and Mössbauer spectroscopy: Geochimica et Cosmochimica Acta, v. 71, p. 3833–3846, doi:10.1016/j.gca.2007.05.019.

Poulton, S.W., Krom, M.D., and Raiswell, R., 2004, A revised scheme for the reactivity of iron (oxyhydr)oxide minerals towards dissolved sulfide: Geochimica et Cosmochimica Acta, v. 68, p. 3703–3715, doi:10.1016/j.gca.2004.03.012.

Present, T.M., Bergmann, K.D., Myers, C., Slotznick, S.P., Creveling, J.R., Zieg, J., Fischer, W.W., Knoll, A.H., and Grotzinger, J.P., 2017, Pyrite-walled tube structures in a Mesoproterozoic sediment-hosted metal sulfide deposit: Geological Society of America Bulletin, v. 130, p. 598–616.

Qian, G., Brugger, J., Skinner, W.M., Chen, G., and Pring, A., 2010, An experimental study of the mechanism of the replacement of magnetite by pyrite up to 300°C: Geochimica et Cosmochimica Acta, v. 74, p. 5610–5630, doi:10.1016/j.gca.2010.06.035.

Qian, G., Brugger, J., Testemale, D., Skinner, W., and Pring, A., 2013, Formation of As(II)-pyrite during experimental replacement of magnetite under hydrothermal conditions: Geochimica et Cosmochimica Acta, v. 100, p. 1–10, doi:10.1016/j.gca.2012.09.034.

Ramdohr, P., 1953, Mineralbestand, Strukturen und Genesis der Rammelsberg-Lagerstätte: Geologisches Jahrbuch, v. 67, p. 367–494.

Rasmussen, B., 2000, Filamentous microfossils in a 3,235-million-year-old volcanogenic massive sulphide deposit: Nature, v. 405, p. 676–679.

Reinhardt, M. et al., 2024, Aspects of the biological carbon cycle in a ca. 3.42-billion-year-old marine ecosystem: Precambrian Research, v. 402, p. 107289, doi:10.1016/j.precamres.2024.107289.

Rickard, D., 2019, How long does it take a pyrite framboid to form? Earth and Planetary Science Letters, v. 513, p. 64–68, doi:10.1016/j.epsl.2019.02.019.

Rickard, D.T., 1975, Kinetics and Mechanism of Pyrite Formation at Low Temperatures: American Journal of Science, v. 275, p. 636–652.

Rickard, D., 1997, Kinetics of pyrite formation by the H2S oxidation of iron (II) monosulfide in aqueous solutions between 25 and 125°C: The rate equation: Geochimica et Cosmochimica Acta, v. 61, p. 115–134, doi:10.1016/S0016-7037(96)00321-3.

Rickard, D., 1969, The microbiological formation of iron sulphides: Stockholm Contributions to Geology, v. 20, p. 49–66.

Rolison, J.M., Stirling, C.H., Middag, R., Gault-Ringold, M., George, E., and Rijkenberg, M.J.A., 2018, Iron isotope fractionation during pyrite formation in a sulfidic Precambrian ocean analogue: Earth and Planetary Science Letters, v. 488, p. 1–13, doi:10.1016/j.epsl.2018.02.006.

Rouxel, O., Dobbek, N., Ludden, J., and Fouquet, Y., 2003, Iron isotope fractionation during oceanic crust alteration: Chemical Geology, v. 202, p. 155–182, doi:10.1016/j.chemgeo.2003.08.011.

Rouxel, O., Fouquet, Y., and Ludden, J.N., 2004, Subsurface processes at the lucky strike hydrothermal field, Mid-Atlantic ridge: evidence from sulfur, selenium, and iron isotopes: Geochimica et Cosmochimica Acta, v. 68, p. 2295–2311, doi:10.1016/j.gca.2003.11.029.

Rouxel, O., Shanksiii, W., Bach, W., and Edwards, K., 2008, Integrated Fe- and S-isotope study of seafloor hydrothermal vents at East Pacific Rise 9–10°N: Chemical Geology, v. 252, p. 214–227, doi:10.1016/j.chemgeo.2008.03.009.

Roy, M., Rouxel, O., Martin, J.B., and Cable, J.E., 2012, Iron isotope fractionation in a sulfide-bearing subterranean estuary and its potential influence on oceanic Fe isotope flux: Chemical Geology, v. 300–301, p. 133–142, doi:10.1016/j.chemgeo.2012.01.022.

Runge, E., Mansor, M., Chiu, T.-H., Shuster, J., Fischer, S., Kappler, A., and Duda, J.-P., 2024, Hydrothermal sulfidation of biogenic magnetite produces framboid-like pyrite: Communications Earth & Environment, v. 5, p. 252.

Runge, E.A., Mansor, M., Kappler, A., and Duda, J.-P., 2023a, Microbial biosignatures in ancient hydrothermal sulfides: Geobiology, v. 21, p. 355–377.

Runge, E.A., Mansor, M., Shuster, J., Fischer, S., Liu, Y., Lunter, D.J., Kappler, A., and Duda, J.-P., 2023b, Sulfidation of nano-magnetite to pyrite: Implications for interpreting paleoenvironmental proxies and biosignature records in hydrothermal sulfide deposits: Earth and Planetary Science Letters, v. 617, p. 118261, doi:10.1016/j.epsl.2023.118261.

Sáez, R., Moreno, C., González, F., and Almodóvar, G.R., 2011, Black shales and massive sulfide deposits: causal or casual relationships? Insights from Rammelsberg, Tharsis, and Draa Sfar: Mineralium Deposita, v. 46, p. 585–614, doi:10.1007/s00126-010-0311-x.

Sansjofre, P., Cartigny, P., Trindade, R.I.F., Nogueira, A.C.R., Agrinier, P., and Ader, M., 2016, Multiple sulfur isotope evidence for massive oceanic sulfate depletion in the aftermath of Snowball Earth: Nature Communications, v. 7, p. 12192, doi:10.1038/ncomms12192.

Sawlowicz, Z., 1993, Pyrite framboids and their development: a new conceptual mechanism: Geologische Rundschau, v. 82, p. 148–156, doi:10.1007/BF00563277.

Schoonen, M.A.A., and Barnes, H.L., 1991, Mechanisms of pyrite and marcasite formation from solution: III. Hydrothermal processes: Geochimica et Cosmochimica Acta, v. 55, p. 3491–3504, doi:10.1016/0016-7037(91)90050-F.

Severmann, S., Johnson, C.M., Beard, B.L., German, C.R., Edmonds, H.N., Chiba, H., and Green, D.R.H., 2004, The effect of plume processes on the Fe isotope composition of hydrothermally derived Fe in the deep ocean as inferred from the Rainbow vent site, Mid-Atlantic Ridge, 36°14'N: Earth and Planetary Science Letters, v. 225, p. 63–76, doi:10.1016/j.epsl.2004.06.001.

Severmann, S., Johnson, C.M., Beard, B.L., and McManus, J., 2006, The effect of early diagenesis on the Fe isotope compositions of porewaters and authigenic minerals in continental margin sediments: Geochimica et Cosmochimica Acta, v. 70, p. 2006–2022, doi:10.1016/j.gca.2006.01.007.

Sim, M.S., Bosak, T., and Ono, S., 2011a, Large Sulfur Isotope Fractionation Does Not Require Disproportionation: Science, v. 333, p. 74–77, doi:10.1126/science.1205103.

Sim, M.S., Ono, S., Donovan, K., Templer, S.P., and Bosak, T., 2011b, Effect of electron donors on the fractionation of sulfur isotopes by a marine Desulfovibrio sp.: Geochimica et Cosmochimica Acta, v. 75, p. 4244–4259, doi:10.1016/j.gca.2011.05.021.

Sim, M.S., Woo, D.K., Kim, B., Jeong, H., Joo, Y.J., Hong, Y.W., and Choi, J.Y., 2023, What Controls the Sulfur Isotope Fractionation during Dissimilatory Sulfate Reduction? ACS Environmental Au, v. 3, p. 76–86, doi:10.1021/acsenvironau.2c00059.

Sivan, O., Adler, M., Pearson, A., Gelman, F., Bar-Or, I., John, S.G., and Eckert, W., 2011, Geochemical evidence for iron-mediated anaerobic oxidation of methane: Limnology and Oceanography, v. 56, p. 1536–1544.

Slack, J.F., Shanks, W.C., Ridley, W.I., Dusel-Bacon, C., DesOrmeau, J.W., Ramezani, J., and Fayek, M., 2019, Extreme sulfur isotope fractionation in the Late Devonian Dry Creek

volcanogenic massive sulfide deposit, central Alaska: Chemical Geology, v. 513, p. 226–238, doi:10.1016/j.chemgeo.2019.03.007.

Sperling, H., 1986, Das Neue Lager der Blei-Zink-Lagerstätte Rammelsberg: Hannover, Geologisches Jahrbuch, Reihe D 85, 5–177 p.

Strauss, H., 1997, The isotopic composition of sedimentary sulfur through time: Palaeogeography, Palaeoclimatology, Palaeoecology, v. 132, p. 97–118.

Syverson, D.D., Borrok, D.M., and Seyfried, W.E., 2013, Experimental determination of equilibrium Fe isotopic fractionation between pyrite and dissolved Fe under hydrothermal conditions: Geochimica et Cosmochimica Acta, v. 122, p. 170–183, doi:10.1016/j.gca.2013.08.027.

Taylor, B.E., 2004, Biogenic and thermogenic sulfate reduction in the Sullivan Pb–Zn–Ag deposit, British Columbia (Canada): Evidence from micro-isotopic analysis of carbonate and sulfide in bedded ores: Chemical Geology, v. 204, p. 215–236, doi:10.1016/j.chemgeo.2003.11.011.

Terabayashi, M., Masada, Y., and Ozawa, H., 2003, Archean ocean-floor metamorphism in the North Pole area, Pilbara Craton, Western Australia: Precambrian Research, v. 127, p. 167–180, doi:10.1016/S0301-9268(03)00186-4.

Thiel, J., Byrne, J.M., Kappler, A., Schink, B., and Pester, M., 2019, Pyrite formation from FeS and H2S is mediated through microbial redox activity: Proceedings of the National Academy of Sciences, v. 116, p. 6897–6902, doi:10.1073/pnas.1814412116.

Thomazo, C. et al., 2019, Multiple sulfur isotope signals associated with the late Smithian event and the Smithian/Spathian boundary: Earth-Science Reviews, v. 195, p. 96–113, doi:10.1016/j.earscirev.2018.06.019.

Tice, M.M., Bostick, B.C., and Lowe, D.R., 2004, Thermal history of the 3.5–3.2 Ga Onverwacht and Fig Tree Groups, Barberton greenstone belt, South Africa, inferred by Raman microspectroscopy of carbonaceous material: Geology, v. 32, p. 37, doi:10.1130/G19915.1.

Toner, B.M., Rouxel, O.J., Santelli, C.M., Bach, W., and Edwards, K.J., 2016, Iron Transformation Pathways and Redox Micro-Environments in Seafloor Sulfide-Mineral Deposits: Spatially Resolved Fe XAS and δ57/54Fe Observations: Frontiers in Microbiology, v. 7, doi:10.3389/fmicb.2016.00648.

Tornos, F., Peter, J.M., Allen, R., and Conde, C., 2015, Controls on the siting and style of volcanogenic massive sulphide deposits: Ore Geology Reviews, v. 68, p. 142–163, doi:10.1016/j.oregeorev.2015.01.003.

Truong, C., Bernard, S., Le Pape, P., Morin, G., Baya, C., Merrot, P., Gorlas, A., and Guyot, F., 2023, Production of carbon-containing pyrite spherules induced by hyperthermophilic Thermococcales: a biosignature? Frontiers in Microbiology, v. 14, p. 1145781, doi:10.3389/fmicb.2023.1145781.

Van Kranendonk, M., Philippot, P., Lepot, K., Bodorkos, S., and Pirajno, F., 2008, Geological setting of Earth's oldest fossils in the ca. 3.5 Ga Dresser Formation, Pilbara Craton, Western Australia: Precambrian Research, v. 167, p. 93–124, doi:10.1016/j.precamres.2008.07.003.

Vearncombe, S., Barley, M.E., Groves, D.I., McNaughton, N.J., Mikucki, E.J., and Vearncombe, J.R., 1995, 3.26 Ga black smoker-type mineralization in the Strelley Belt, Pilbara Craton, Western Australia: Journal of the Geological Society, v. 152, p. 587–590, doi:10.1144/gsjgs.152.4.0587.

Velasco-Acebes, J., Tornos, F., Kidane, A.T., Wiedenbeck, M., Velasco, F., and Delgado, A., 2019, Isotope geochemistry tracks the maturation of submarine massive sulfide mounds (Iberian Pyrite Belt): Mineralium Deposita, v. 54, p. 913–934, doi:10.1007/s00126-018-0853-x.

Walcher, E.H., 1986, Geologisch-lagerstättenkundliche Untersuchungen am Zeitäquivalent (Lagerhorizont) der Lagerstätte Rammelsberg [PhD thesis]: Technische Universität Clausthal, 84 p.

Wan, M., Schröder, C., and Peiffer, S., 2017, Fe(III):S(-II) concentration ratio controls the pathway and the kinetics of pyrite formation during sulfidation of ferric hydroxides: Geochimica et Cosmochimica Acta, v. 217, p. 334–348, doi:10.1016/j.gca.2017.08.036.

Wang, S., Li, C., Li, B., Dang, Y., Ye, J., Zhu, Z., Zhang, L., and Shi, X., 2022, Constraints on fluid evolution and growth processes of black smoker chimneys by pyrite geochemistry: A case study of the Tongguan hydrothermal field, South Mid-Atlantic Ridge: Ore Geology Reviews, v. 140, p. 104410, doi:10.1016/j.oregeorev.2021.104410.

Wang, Q., and Morse, J.W., 1996, Pyrite formation under conditions approximating those in anoxic sediments I. Pathway and morphology: Marine Chemistry, v. 52, p. 99–121, doi:10.1016/0304-4203(95)00082-8.

Wang, Q., Wang, J., Wang, X., Kumar, N., Pan, Z., Peiffer, S., and Wang, Z., 2023, Transformations of Ferrihydrite–Extracellular Polymeric Substance Coprecipitates Driven by Dissolved Sulfide: Interrelated Effects of Carbon and Sulfur Loadings: Environmental Science & Technology, p. acs.est.2c06921, doi:10.1021/acs.est.2c06921.

Watanabe, Y., Farquhar, J., and Ohmoto, H., 2009, Anomalous Fractionations of Sulfur Isotopes During Thermochemical Sulfate Reduction: Science, v. 324, p. 370–373, doi:10.1126/science.1169289.

Weimann, L. et al., 2024, Carbonaceous matter in ~ 3.5 Ga black bedded barite from the Dresser Formation (Pilbara Craton, Western Australia) – Insights into organic cycling on the juvenile Earth: Precambrian Research, v. 403, p. 107321, doi:10.1016/j.precamres.2024.107321.

Whitehouse, M.J., 2013, Multiple Sulfur Isotope Determination by SIMS : Evaluation of Reference Sulfides for Δ^{33}S with Observations and a Case Study on the Determination of Δ^{36}S: Geostandards and Geoanalytical Research, v. 37, p. 19–33, doi:10.1111/j.1751-908X.2012.00188.x.

Whitehouse, M.J., and Fedo, C.M., 2007, Microscale heterogeneity of Fe isotopes in >3.71 Ga banded iron formation from the Isua Greenstone Belt, southwest Greenland: Geology, v. 35, p. 719, doi:10.1130/G23582A.1.

Wilkinson, J.J., 2014, Sediment-Hosted Zinc–Lead Mineralization, *in* Treatise on Geochemistry, Elsevier, p. 219–249, doi:10.1016/B978-0-08-095975-7.01109-8.

Wu, N., Farquhar, J., and Strauss, H., 2014, δ34S and Δ33S records of Paleozoic seawater sulfate based on the analysis of carbonate associated sulfate: Earth and Planetary Science Letters, v. 399, p. 44–51, doi:10.1016/j.epsl.2014.05.004.

Zaback, D.A., Pratt, L.M., and Hayes, J.M., 1993, Transport and reduction of sulfate and immobilization of sulfide in marine black shales: Geology, v. 21, p. 141, doi:10.1130/0091-7613(1993)021<0141:TAROSA>2.3.CO;2.

Zerkle, A.L., Jones, D.S., Farquhar, J., and Macalady, J.L., 2016, Sulfur isotope values in the sulfidic Frasassi cave system, central Italy: A case study of a chemolithotrophic S-based ecosystem: Geochimica et Cosmochimica Acta, v. 173, p. 373–386, doi:10.1016/j.gca.2015.10.028.

5.10 SUPPLEMENTARY MATERIALS

Supplementary Table 1: Results of SIMS iron and sulfur isotope analyses of pyrite in the Rammelsberg sample. Analyses performed on the same spot are listed in the same line. Given errors (±) are propagated errors calculated from the internal reproducibility and the 2σ uncertainty of the instrumental mass fractionation.

ID (Fe)	δ^{56}Fe [‰]	±	ID (S)	δ^{34}S[‰]	±	Δ^{33}S [‰]	±	Morphology
5	-0.58	0.23	5	-15.13	0.18	0.167	0.188	Framboidal
12	0.12	0.25						Framboidal
13	1.44	0.23	12	11.70	0.20	0.140	0.231	Framboidal
14	0.32	0.27	13	15.35	0.21	0.162	0.252	Framboidal
16	0.95	0.24	17	15.27	0.24	0.115	0.287	Framboidal
20	1.01	0.24	15	15.03	0.20	0.036	0.232	Framboidal
29	-0.21	0.23						Framboidal
30	0.10	0.24						Framboidal
35	0.82	0.24						Framboidal
37	0.89	0.25						Framboidal
41	1.71	0.26						Framboidal
46	-0.37	0.24						Framboidal
66	0.46	0.22						Framboidal
32	1.35	0.22						Framboidal
47	1.73	0.29						Framboidal
10	-1.13	0.22	8	14.92	0.20	0.148	0.235	Framboidal
24	1.38	0.25	21	16.11	0.21	0.054	0.247	Framboidal
17	-0.65	0.25	16	15.74	0.18	0.084	0.184	Framboidal
23	-0.11	0.27	20	14.95	0.22	0.085	0.262	Framboidal
34	1.29	0.23						Framboidal
67	-0.12	0.24						Framboidal
62	0.32	0.26						Framboidal
72	0.96	0.26						Framboidal
73	0.04	0.26						Framboidal
15	1.11	0.24	18	17.01	0.18	0.096	0.181	Framboidal
19	0.60	0.25	19	16.63	0.19	0.055	0.212	Framboidal
28	-0.33	0.25						Framboidal
45	1.35	0.25						Framboidal
4	0.29	0.24	4	12.45	0.23	0.207	0.275	Framboidal
7	-1.15	0.24	10	13.39	0.22	-0.028	0.265	Framboidal
21	-0.64	0.26	23	6.83	0.18	0.028	0.182	Framboidal
36	-0.09	0.25						Framboidal
38	0.83	0.24						Framboidal
40	0.65	0.25						Framboidal
42	1.99	0.27						Framboidal
48	0.27	0.22						Framboidal
63	0.90	0.23						Subhedral

6	0.77	0.22						Subhedral
9	1.14	0.23	7	15.98	0.17	0.098	0.175	Subhedral
11	1.57	0.24	9	18.49	0.17	0.186	0.173	Subhedral
22	0.19	0.27	22	16.57	0.17	-0.043	0.177	Subhedral
25	1.19	0.25	24	14.86	0.17	-0.056	0.180	Subhedral
26	-0.39	0.23	25	9.29	0.18	0.135	0.190	Subhedral
27	0.42	0.22	26	12.38	0.17	-0.154	0.173	Subhedral
33	0.82	0.25						Subhedral
49	0.25	0.24						Subhedral
51	1.06	0.23						Subhedral
55	2.19	0.25						Subhedral
64	-0.73	0.28						Subhedral
65	1.11	0.25						Subhedral
1	-1.30	0.22	1	16.34	0.18	0.000	0.199	Euhedral
2	1.23	0.24	2	13.72	0.23	0.225	0.285	Euhedral
3	0.99	0.24	3	-0.30	0.18	0.242	0.182	Euhedral
8	0.66	0.24	6	5.72	0.18	0.124	0.199	Euhedral
74	1.22	0.23	29	17.25	0.17	-0.206	0.174	Euhedral
75	1.00	0.21						Euhedral
76	1.71	0.24	30	18.77	0.17	-0.176	0.173	Euhedral

CHAPTER 6 - CONCLUSIONS AND PERSPECTIVES

6.1 MAIN CONCLUSIONS

This thesis aimed to better understand the taphonomy of microbial biosignatures in ancient hydrothermal sulfide systems, which are considered critical environments for life's emergence and early evolution. It focused on biominerals known to form via microbial sulfur and iron cycling, key biogeochemical processes in hydrothermal environments from the distant past until today. However, the taphonomy of microbial sulfur and iron minerals (i.e., processes affecting their destruction or preservation) under sulfidic hydrothermal conditions has, so far, been largely unexplored. This limits our ability to disentangle microbial processes in ancient environments based on the rock record, possibly explaining the poor report of geobiological studies on Precambrian hydrothermal sulfide deposits (Runge et al., 2023, *Geobiology*). To tackle this problem, we used a geobiological approach combining experimental geomicrobiology with petrographic and stable isotope analysis of Phanerozoic hydrothermal sulfides. Aiming to unravel the mechanisms and products of microbial biomineral (trans)formation under sulfidic hydrothermal conditions, we addressed three specific research questions, each by a targeted work package.

Chapter 3 (WP I) (Runge et al., 2023, *Earth and Planetary Science Letters*) addressed *Q 1* (‘*What are the mechanisms and products of sulfur and iron mineral (trans)formation under sulfidic hydrothermal conditions?’*) using hydrothermal magnetite sulfidation as a case study. To understand the mechanisms and products of this process, incubation experiments with synthetic magnetite nanoparticles in anoxic artificial seawater were performed at varying pH (7 and 10), sulfide: iron ratios (4:1 and 1:4), temperatures (20, 40, 60, and 80°C), and in the presence or absence of S^0. Magnetite nanoparticles rapidly dissolved at excess sulfide conditions and temperatures above 20 °C, most likely driven by reductive dissolution. Iron and sulfide were initially reprecipitated as Fe(III)-containing mackinawite across all experimental setups. At pH 7, Fe(III)-containing mackinawite transformed into pyrite, a widespread mineral in hydrothermal sulfides of any geological age. Pyrite formed

faster in the presence of polysulfides, as evidenced by sequential iron extraction and UV-Vis spectroscopy, indicating that pyritization proceeds via the polysulfide pathway. Since magnetite-producing microorganisms (magnetotactic bacteria or dissimilatory Fe(III)-reducing prokaryotes) likely emerged in the Archean, the results of this study suggest magnetite sulfidation to pyrite is a critical taphonomic process in hydrothermal systems throughout life's history.

Chapter 4 (WP II) (Runge et al., 2024, *Communications Earth & Environment*) addressed *Q 2* (*'Does the hydrothermal alteration of microbial biominerals produce distinct taphonomic fingerprints?'*). Expanding on experiments of WP I, we incubated abiogenic (prepared synthetically) and biogenic magnetite nanoparticles (prepared using cultures of the Fe(III)-reducing bacterium *Geobacter sulfurreducens*) in anoxic artificial seawater (pH 7.5, sulfide/iron = 4, 80°C, with or without S^0). The experiments yielded pyrite with various distinct morphologies, including framboid-like spheroids, a commonly suggested biosignature of microbial sulfur cycling. We show that the variability in pyrite morphologies results from differing pyritization rates, most likely caused by interrelated effects between organic matter and S^0. Framboid-like pyrite was exclusively produced via the abiotic sulfidation of biogenic (i.e., organic matter-associated) magnetite. Thus, organic matter may be a more critical driver of framboid-like pyrite formation than microbial sulfide. This implies that framboid-like pyrite may be a taphonomic fingerprint of biogenic magnetite or other organic matter-associated iron minerals in ancient hydrothermal sulfides. Framboid-like pyrite may, therefore, record ancient microbial iron cycling in hydrothermal systems.

Chapter 5 (WP III) (in revision for *Chemical Geology*) addressed *Q 3* (*'Can biosignatures of microbial sulfur and iron cycling be preserved in hydrothermal sulfide systems?'*), targeting the metamorphic ~390 Ma Rammelsberg sediment-hosted massive sulfide deposit. We analyzed the textures and triple sulfur ($\delta^{34}S$, $\Delta^{33}S$) as well as iron ($\delta^{56}Fe$) isotope composition of pyrite by SEM-EDS and Secondary Ion Mass Spectrometry (SIMS) to explore the preservation potential of stable isotope biosignatures for microbial sulfur and iron cycling in hydrothermal sulfide systems. The study revealed a complex pyrite formation sequence, most likely involving early

diagenetic microbial sulfur and iron cycling, hydrothermal alteration, and secondary high-temperature pyrite formation. Except for one likely microbially derived grain ($\delta^{34}S$ = -15.13‰), most pyrite $\delta^{34}S$ values were best explained by secondary hydrothermal processes. In contrast, $\delta^{56}Fe$ values dominantly preserved primary signals of early diagenetic iron cycling, implying a better preservation potential of iron isotope compositions. The results highlight that in-situ stable isotope signatures of microbial sulfur and iron cycling can be preserved in sediment-hosted massive sulfides despite extensive hydrothermal alteration of the precursor sediment and greenschist metamorphism later in the rock's history.

Together, these studies substantially advance our understanding of microbial biosignature preservation in hydrothermal sulfide systems. The experimental studies (*Chapters 3 and 4*) show that the mechanisms of hydrothermal magnetite sulfidation and its products' characteristics (i.e., mineral identity and morphology) strongly depend on environmental conditions. These conditions include temperature, E_h, pH, sulfide/iron ratio, intermediate sulfur species (i.e., S^0, polysulfides), and organic matter. Framboid-like pyrite, commonly attributed to microbial sulfur cycling, emerged as a novel taphonomic fingerprint of biogenic iron mineral transformation in hydrothermal sulfide systems. These results highlight the critical role of taphonomic processes in detecting microbial biosignatures in hydrothermal sulfides. On the one hand, biosignatures encoded in minerals can easily be altered or erased, particularly under hydrothermal conditions. On the other hand, secondary minerals in ancient rocks can still encode textural evidence for their precursors. Therefore, a detailed assessment of relevant diagenetic and metamorphic processes over the rock's history is crucial when interpreting ancient deposits. Moreover, the complex interplay of abiotic and biotic parameters influencing pyrite morphology inferred from these experiments demands additional evidence for detecting biosignatures. The presence of $\delta^{34}S$, $\Delta^{33}S$, and $\delta^{56}Fe$ signatures of microbial sulfur and iron cycling in the greenschist facies Rammelsberg deposit demonstrates that in-situ sulfur and iron isotope analyses of pyrite can provide such evidence (*Chapter 5*). Notably, this metamorphic grade is comparable to Paleoarchean hydrothermal sulfides from the

Pilbara Craton and Barberton Greenstone Belt, extending the applicability of this proxy to some of Earth's oldest rocks. In concert, the results of this thesis demonstrate that the combined analysis of pyrite morphology and in-situ sulfur and iron isotope composition is a powerful approach for detecting microbial biominerals and their transformation products in hydrothermal sulfides throughout the geological record. This, in turn, is crucial for identifying microbial biosignatures in deep time, enabling a better understanding of life's emergence and early evolution.

6.2 FURTHER IMPLICATIONS

6.2.1 Assessing the impact of microbial activity on ore formation

Minerals in hydrothermal deposits are usually considered abiotic products from mixing metal-rich hot fluids with cool seawater (Pirajno, 2010). However, the additional role of microbial processes in mineral (trans)formation is becoming increasingly apparent in various hydrothermal environments (Heppenheimer et al., 1995; McGoldrick, 1999; Taylor, 2004; Southam and Saunders, 2005; Schroll and Rantitsch, 2005; Kucha et al., 2005; Tornos et al., 2014, 2019; Nozaki et al., 2020, 2024). *Chapter 5* (Runge et al., under review) adds to this idea and, by extension, implies a critical role of geobiological feedback to geodynamic processes in forming sediment-hosted massive sulfides. Throughout Earth's history, these deposits appear particularly abundant during major orogenic events (e.g., Tornos et al., 1998; Sáez et al., 2011; Wilkinson, 2014). The Devonian Rammelsberg deposit formed in the Goslar trough, a fault-bound basin associated with the Variscan orogen, which received substantial continental sediment input and experienced vigorous hydrothermal fluid circulation (Large and Walcher, 1999; Kroner and Romer, 2013; Moreno et al., 2019). The link with orogenic events is of geobiological significance because the weathering of fresh crustal rocks deriving from arc volcanism likely supplied nutrients such as phosphate (cf. Filippelli, 2002), while hydrothermal fluid circulation recycled bioavailable nitrogen from associated shales (cf. Stüeken et al., 2021; Martin et al., 2024). Hence, these processes provided two of the most limiting nutrients in modern oceans (i.e., phosphorous and nitrogen), likely increasing primary productivity and organic matter fluxes to the sediment in the Goslar Trough.

Aerobic respiration rapidly consumes O_2 in surface layers of sediments, creating anoxic conditions immediately below, particularly in semi-restricted basins (Lyons et al., 2006). In these anoxic environments, the microbial reduction of Fe(III) and sulfate drives pyrite formation (*Chapter 5*, Runge et al., under review), which is then shielded from oxidative weathering due to the O_2 consumption in surface sediments (Sáez et al., 2011). The increased precipitation of early diagenetic (microbial) pyrite, possibly serving as nuclei for further sulfide mineralization, and the establishment of favorable conditions for sulfide mineral preservation may have promoted the formation of the Rammelsberg deposit. Hence, the association of sediment-hosted massive sulfides with major orogenic events can plausibly be explained by the convergence of geodynamic processes with hydrothermal activity and intense biogeochemical cycling.

6.2.2 A framework for biosignature detection in ancient hydrothermal sulfides

The results of this study call for a novel framework for understanding the taphonomy of microbial biosignatures in ancient hydrothermal sulfides (Fig. 6.1). Advances in biomineral taphonomy presented herein concern mechanisms that operate on various scales. This includes multiple scales in space, such as the hydrothermal fluid circulation system affecting hydrothermal systems over kilometers (Fig. 6.1A) versus the microbially mediated formation of nanometer-scale minerals (Fig. 6.1B). Therefore, the analysis of ancient hydrothermal sulfides must start with a detailed description at the outcrop scale (e.g., geological context, rock fabrics, macrotextures). However, only in-situ work that zooms into the micro- or nanoscale (e.g., microtextures, mineralogy, geochemistry) of rocks, minerals, and experimental products will provide the complete picture of potential microbial biosignatures.

Taphonomic processes also operate on various scales in time. For instance, ancient rocks commonly experienced one or more metamorphic events driven by hundred-million- to billion-year orogenic cycles (Fig. 6.1C). Conversely, mineral (trans)formation in the environments operates on scales of years to seconds (Fig. 6.1D-E). Thus, taphonomic processes affecting biominerals can broadly be categorized into geologically controlled (long-term) and biogeochemically controlled

(short-term) mechanisms. In retrospect, these processes can only be understood by integrated studies of ancient rocks, recent and Phanerozoic analogs, and experimental work. Analyses of ancient rocks need to involve a reconstruction of paleoenvironmental, diagenetic, and metamorphic conditions to inform the search for suitable analogs and the design of experiments. Studies on recent analogs and experimental systems can test interpretations of features in ancient rocks on humanly observable timescales and under better-constrained environmental conditions and microbial community compositions. In turn, analog and experimental studies can reveal potential features to search for in ancient rocks, such as framboid-like pyrite as a taphonomic fingerprint of a biogenic magnetite precursor (*Chapter 4*, Runge et al., 2024). Thus, the life detection process is not linear but circular (Fig. 6.1C-E). The multiscale approach of this thesis can serve as a blueprint for future studies that iteratively lead to a better understanding of the taphonomy of microbial biosignatures in deep time. This, in turn, is fundamental for their detection in ancient hydrothermal sulfides and other geological materials.

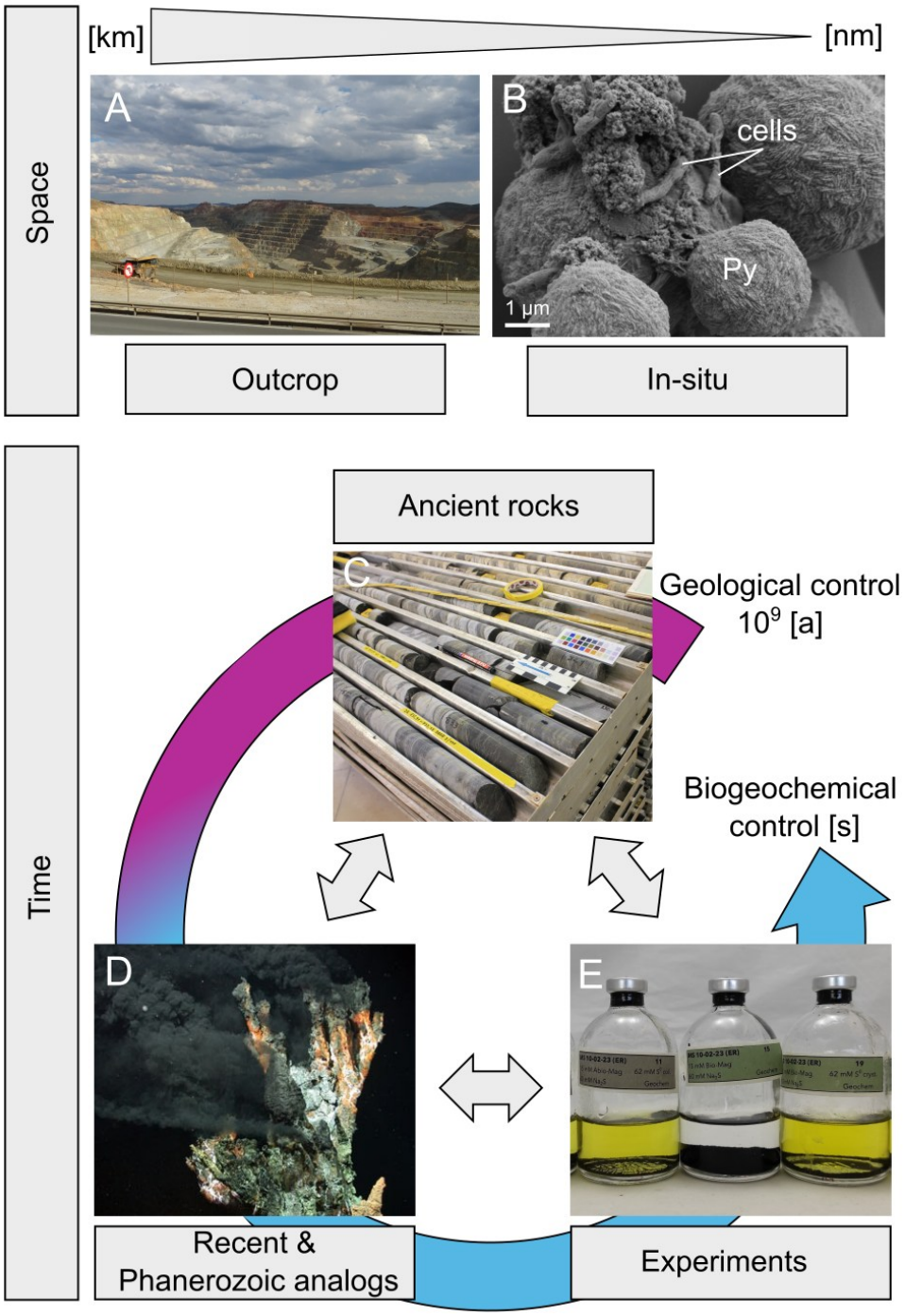

Figure 6.1: Framework for geobiological studies in deep time. A: Massive sulfides of the Iberian Pyrite Belt, exposed in the Rio Tinto mining district, as the product of km-scale hydrothermal fluid circulation. B: Spherical pyrite (Py) and cells of the sulfur disproportionating microorganism *Desulfocapsa spp.* in a culturing experiment (image: Jeremiah Shuster). C: Drillcores of early Archean rocks from the Barberton Greenstone Belt, South Africa (Image: Jan-Peter Duda). D: Black smoker at the Logatchev hydrothermal field (Mid-Atlantic Ridge) as a recent analog for ancient hydrothermal sulfide systems (image: MARUM, University of Bremen). E: Hydrothermal sulfidation experiments with magnetite nanoparticles, simulating their taphonomy under early Earth conditions.

6.3 OPEN QUESTIONS AND FUTURE WORK

Next to the advances synthesized above, this thesis has also uncovered several open questions. The following section critically discusses limitations in interpreting the presented data and suggests future studies to address them. This future work should adopt the multiscale approach outlined in Figure 6.1. Thus, it can be categorized into (i) petrographic and geochemical work on Precambrian hydrothermal sulfides, (ii) studies on recent analogs for ancient environments, and (iii) additional or refined experimental work.

6.3.1 Precambrian hydrothermal sulfides

The next step in applying the insights from this study is the combined textural in-situ stable isotope analysis of hydrothermal sulfides from the Precambrian rock record (Fig. 6.1C). Potential localities are the 3.2 Ga Bien Venue Deposit (Barberton Greenstone Belt, South Africa), the 3.2 Ga Sulphur Springs Group (Pilbara Craton, Western Australia), and the 3.5 Ga Dresser Formation (Pilbara Craton, Western Australia), which represent the most ancient sulfidic hydrothermal systems on Earth (Van Kranendonk et al., 2008; Hofmann, 2011; Huston et al., 2019). Notably, all of these localities have experienced greenschist facies metamorphism or less (Buick et al., 2002; Kohler and Anheusser, 2002; Terabayashi et al., 2003; Tice et al., 2004), which can permit the preservation of sulfur and iron isotope compositions in pyrite (Taylor, 2004; Marin-Carbonne et al., 2020; *Chapter 5,* Runge et al., under review). Indeed, previous bulk and in-situ sulfur isotope analyses revealed signals of microbial sulfur cycling in the Dresser Formation (Shen et al., 2001; Shen and Buick, 2004; Philippot et al., 2007; Ueno et al., 2008; Wacey et al., 2015; Baumgartner et al., 2020; Liu et al., 2021). However, in-situ sulfur and iron isotope analyses have not been done in the abovementioned localities. Following the results of this study, coupled SEM and SIMS analyses of pyrite from these units have a high potential for novel insights into microbial sulfur and iron cycling in hydrothermal systems on early Earth.

6.3.2 Recent analogs

Studies of recent analog systems are crucial to complement the experimental, petrographic, and geochemical analyses presented in this thesis (Fig. 6.1D). Submarine brine pools are commonly suggested as possible analogs for sediment-hosted hydrothermal sulfide systems (e.g., Sangster, 2002; Tornos, 2006; Wilkinson, 2014). Examples of such brine pools exist in the Red Sea, where rift-related volcanism drives the discharge of sulfidic hydrothermal fluids into submarine subbasins, forming anoxic and hypersaline subaquatic ponds (Schardt, 2016). Notably, the mixing of hydrothermal fluids with cooler brines or seawater causes metal sulfide and oxide (e.g., Cu, Fe, Zn) precipitation, including pyrite, forming stratiform deposits (Zierenberg and Shanks, 1988). This is analogous to depositional models of the Rammelsberg deposit (Large and Walcher, 1999; Sáez et al., 2011). Thus, submarine brine pools offer a unique opportunity to better constrain the role of microbial sulfur and iron cycling in forming sediment-hosted massive sulfides.

Enrichment cultures and phylogenetic analysis revealed the presence of diverse sulfate-reducing microorganisms at the brine-seawater interfaces of several Red Sea brine pools (e.g., Trüper, 1969; Bougouffa et al., 2013; Guan et al., 2015). Previous studies conducted bulk sulfur isotope analysis on brine pool sediments, indicating a variable role of hydrothermal and microbial sulfide (Shanks and Bischoff, 1980; Zierenberg and Shanks, 1988). However, in-situ sulfur isotope data from recent submarine brine pool sediments are currently unavailable, and the intragrain and intergenerational variability of pyrite isotope compositions cannot be resolved. This is crucial for understanding the isotopic evolution of pyrite in systems where microbial and hydrothermal sulfide formation may co-occur (Eldridge et al., 1988; Nozaki et al., 2020, 2024; Meng et al., 2022; Martin et al., 2023; this study). Thus, combined SIMS stable isotope analyses ($\delta^{34}S$, $\delta^{56}Fe$) of pyrite from brine pool sediments could further illuminate the role of microbial sulfur and iron cycling in forming sediment-hosted hydrothermal sulfides.

Studies on modern environments could also better constrain the significance of sulfidation reactions for the taphonomy of biogenic magnetite to pyrite in natural

hydrothermal systems. Fe(III)-reducing microorganisms, commonly involved in magnetite formation, occur in various deep-sea hydrothermal sulfide systems (Kashefi and Lovley, 2003; Roh et al., 2006; Reysenbach et al., 2006; Sylvan et al., 2012). Niches for mesophilic and (hyper)thermophilic Fe(III)-reducers in hydrothermal environments likely exist along mixing gradients between oxic seawater (~4°C) and hydrothermal fluids (≤400°C) across chimney walls or in reduced sediments. Here, biogenic magnetite could interact with sulfidic fluids during or after its formation, potentially driving its sulfidation (Poulton et al., 2004; Qian et al., 2010, 2013; Runge et al., 2023a, 2023b, 2024; Nie et al., 2023). However, the role of biogenic magnetite sulfidation in recent seafloor hydrothermal systems has not been investigated directly on environmental samples. Detailed analysis of pyrite and/or its potential precursors in fluid-affected sediments and sulfide chimney samples by SEM, Raman spectroscopy, (Nano)SIMS, and synchrotron-based scanning transmission X-ray microscopy (STXM) could reveal spatial associations of pyrite morphotypes, including framboid-like spheroids, with organic matter and its stable isotope composition. These parameters would be critical tracers of magnetite sulfidation in hydrothermal systems.

6.3.3 Experimental work

Finally, additional experimental work is necessary to delineate the effects of abiotic and biotic parameters in biosignature taphonomy (Fig. 6.1E). Results from *Chapters 3 and 4* (Runge et al., 2023b, 2024) highlight the significance of pH for reaction mechanisms and products in pyrite-forming magnetite sulfidation experiments (pH 7.0 in *Chapter 3* vs. 7.5 in *Chapter 4*). The sulfidation of abiogenic magnetite in the presence of S^0 yielded dendritic pyrite at pH 7 and cubic pyrite at pH 7.5. This suggests that the pH-dependent difference in pyritization rate is a major controlling factor for morphology. Moreover, pyritization rates were slower at pH 7.5. The surface-associated globules present at pH 7, suggesting crystal growth via particle attachment, were not observed in any experiment at pH 7.5. This suggests that pH may also control crystal growth mechanisms. Therefore, future experiments should investigate magnetite sulfidation over a broader pH spectrum. Specifically, the

experimental setups producing framboid-like pyrite should be conducted at neutral to slightly acidic conditions, which are more representative of microbial niches closer to the endmember fluid source (pH 2-4; Früh-Green et al., 2022). This would help evaluate the environmental relevance of these experiments for natural hydrothermal systems.

Moreover, the pyrite-yielding experiments (i.e., at pH 7) were only conducted at 80°C. However, microbial habitats in hydrothermal systems span 4°C to more than 100°C (Reysenbach and Cady, 2001). Magnetite sulfidation to pyrite widely occurs in low-temperature environments, which has been observed by microscopic, mineralogical, and geochemical analyses of marine sediments (Karlin and Levi, 1983; Canfield and Berner, 1987; Karlin, 1990). Notably, a substantial fraction of marine dissolved iron precipitates as highly reactive biogenic magnetite (Amor et al., 2020), while nanoparticulate magnetite is rapidly dissolved by sulfide even at 20°C (Poulton et al., 2004; Runge et al., 2023b, 2024). This suggests that biogenic magnetite is a crucial precursor to pyrite in low-temperature niches of hydrothermal systems and other marine sediments. However, magnetite sulfidation experiments at circumneutral pH and ambient temperature have, thus far, not detected pyrite (Nie et al., 2023). This is most likely due to the kinetic inhibition of pyrite formation under strongly reducing and circumneutral conditions (Benning et al., 2000) and highlights that future experiments should be tuned to yield insights into the mechanisms of magnetite sulfidation to pyrite at low temperatures.

One potential parameter to better represent natural conditions is the presence of dissolved or solid oxidants, such as Fe(III), Mn(IV), organic matter, and S^0. Sulfide oxidation to polysulfides mediated by these species was essential for pyrite formation in the experiments at 80°C presented in *Chapters 3* and *4*. While previous studies at ambient temperature also observed Fe(III)-mediated sulfide oxidation, polysulfide formation seemed insufficient for producing pyrite (Nie et al., 2023). However, in natural environments, other oxidants are likely to enhance this process. Mn(IV) is an even more effective driver for polysulfide formation than Fe(III) or S^0 (Avetisyan et al., 2021). The combined effect of Fe(III), Mn(IV), S^0, and microbial

organic matter could sufficiently drive polysulfide formation for the rapid sulfidation of magnetite to pyrite, even at 20°C (Fig. 6.2). Therefore, future experiments in the co-presence of these species could illuminate the mechanisms of magnetite sulfidation to pyrite at low temperatures, providing insights into its role in various marine sediments and global biogeochemical cycles.

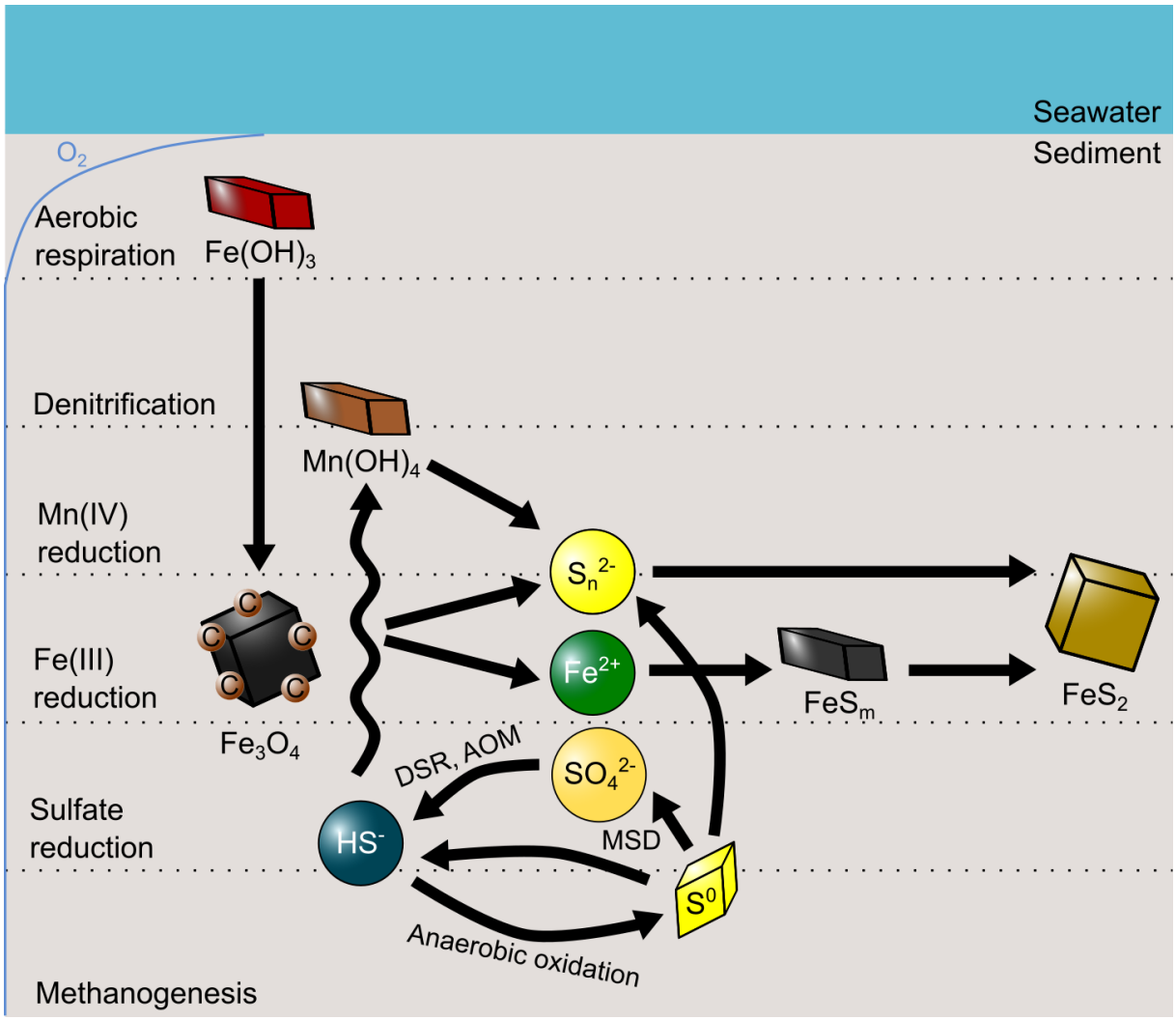

Figure 6.2: Schematic model of biogenic magnetite sulfidation to pyrite in low-temperature niches of hydrothermal systems and other marine sediments. Magnetite is produced in the Fe(III) reduction zone via dissimilatory reduction of iron (oxyhydr)oxides (here: $Fe(OH)_3$). Upward sulfide (here: HS^-) diffusion and burial into the sulfate reduction zone expose magnetite to sulfide from microbial sulfur cycling (bottom). Fe(III), Mn(IV) (here: $Mn(OH)_4$), S^0, and organic matter mediate polysulfide formation at circumneutral pH, enhancing pyrite formation via the polysulfide pathway. DSR: dissimilatory sulfate reduction; AOM: anaerobic oxidation of methane; MSD: microbial sulfur disproportionation; FeS_m: mackinawite.

6.4 REFERENCES

Amor, M., Tharaud, M., Gélabert, A., and Komeili, A., 2020, Single-cell determination of iron content in magnetotactic bacteria: implications for the iron biogeochemical cycle: Environmental Microbiology, v. 22, p. 823–831, doi:10.1111/1462-2920.14708.

Avetisyan, K., Zweig, I., Luther, G.W., and Kamyshny, A., 2021, Kinetics and mechanism of polysulfides and elemental sulfur formation by a reaction between hydrogen sulfide and δ-MnO2: Geochimica et Cosmochimica Acta, v. 313, p. 21–37, doi:10.1016/j.gca.2021.08.022.

Baumgartner, R.J., Caruso, S., Fiorentini, M.L., Van Kranendonk, M.J., Martin, L., Jeon, H., Pagès, A., and Wacey, D., 2020, Sulfidization of 3.48 billion-year-old stromatolites of the Dresser Formation, Pilbara Craton: Constraints from in-situ sulfur isotope analysis of pyrite: Chemical Geology, v. 538, p. 119488, doi:10.1016/j.chemgeo.2020.119488.

Benning, L.G., Wilkin, R.T., and Barnes, H.L., 2000, Reaction pathways in the Fe–S system below 100°C: Chemical Geology, v. 167, p. 25–51, doi:10.1016/S0009-2541(99)00198-9.

Bougouffa, S., Yang, J.K., Lee, O.O., Wang, Y., Batang, Z., Al-Suwailem, A., and Qian, P.Y., 2013, Distinctive Microbial Community Structure in Highly Stratified Deep-Sea Brine Water Columns: Applied and Environmental Microbiology, v. 79, p. 3425–3437, doi:10.1128/AEM.00254-13.

Buick, R. et al., 2002, Geochronology and stratigraphic relationships of the Sulphur Springs Group and Strelley Granite: a temporally distinct igneous province in the Archaean Pilbara Craton, Australia: Precambrian Research, v. 114, p. 87–120, doi:10.1016/S0301-9268(01)00221-2.

Canfield, D.E., and Berner, R.A., 1987, Dissolution and pyritization of magnetite in anoxic marine sediments: Geochimica et Cosmochimica Acta, v. 51, p. 645–659, doi:10.1016/0198-0254(87)90182-8.

Eldridge, C.S., Compston, W., Williams, I.S., Both, R.A., Walshe, J.L., and Ohmoto, H., 1988, Sulfur isotope variability in sediment-hosted massive sulfide deposits as determined using the ion microprobe SHRIMP; I, An example from the Rammelsberg orebody: Economic Geology, v. 83, p. 443–449, doi:10.2113/gsecongeo.83.2.443.

Filippelli, G.M., 2002, The Global Phosphorus Cycle: Reviews in Mineralogy and Geochemistry, v. 48, p. 391–425, doi:10.2138/rmg.2002.48.10.

Früh-Green, G.L., Kelley, D.S., Lilley, M.D., Cannat, M., Chavagnac, V., and Baross, J.A., 2022, Diversity of magmatism, hydrothermal processes and microbial interactions at mid-ocean ridges: Nature Reviews Earth & Environment, v. 3, p. 852–871, doi:10.1038/s43017-022-00364-y.

Guan, Y., Hikmawan, T., Antunes, A., Ngugi, D., and Stingl, U., 2015, Diversity of methanogens and sulfate-reducing bacteria in the interfaces of five deep-sea anoxic brines of the Red Sea: Research in Microbiology, v. 166, p. 688–699, doi:10.1016/j.resmic.2015.07.002.

Heppenheimer, H., Hagemann, H.W., and Püttmann, W., 1995, A comparative study of the influence of organic matter on metal accumulation processes in the Kupferschiefer from the Hessian Depression and the North Sudetic Syncline: Ore Geology Reviews, v. 9, p. 391–409, doi:10.1016/0169-1368(94)00021-F.

Hofmann, A., 2011, Archaean Hydrothermal Systems in the Barberton Greenstone Belt and Their Significance as a Habitat for Early Life, *in* Golding, S.D. and Glikson, M. eds., Earliest Life on Earth: Habitats, Environments and Methods of Detection, Dordrecht, Springer Netherlands, p. 51–78, doi:10.1007/978-90-481-8794-2_3.

Huston, D.L., Pirajno, F., Morant, P., Cummins, B., Baker, D., and Mernagh, T.P., 2019, Paleoarchean Mineral Deposits of the Pilbara Craton: Genesis, Tectonic Environment, and Comparisons With Younger Deposits, *in* Earth's Oldest Rocks, Elsevier, p. 519–551.

Karlin, R., 1990, Magnetite diagenesis in marine sediments from the Oregon continental margin: Journal of Geophysical Research, v. 95, p. 4405, doi:10.1029/JB095iB04p04405.

Karlin, R., and Levi, S., 1983, Diagenesis of magnetic minerals in Recent haemipelagic sediments: Nature, v. 303, p. 327–330.

Kashefi, K., and Lovley, D.R., 2003, Extending the Upper Temperature Limit for Life: Science, v. 301, p. 934–934, doi:10.1126/science.1086823.

Kohler, E.A., and Anheusser, C.R., 2002, Geology and geodynamic setting of Archaean silicic metavolcaniclastic rocks of the Bien Venue Formation, Fig Tree Group, northeast Barberton greenstone belt, South Africa: Precambrian Research, v. 116, p. 199–235, doi:10.1016/S0301-9268(02)00021-9.

Kroner, U., and Romer, R.L., 2013, Two plates — Many subduction zones: The Variscan orogeny reconsidered: Gondwana Research, v. 24, p. 298–329, doi:10.1016/j.gr.2013.03.001.

Kucha, H., Schroll, E., and Stumpfl, E.F., 2005, Fossil sulphate-reducing bacteria in the Bleiberg lead-zinc deposit, Austria: Mineralium Deposita, v. 40, p. 123–126, doi:10.1007/s00126-005-0473-0.

Large, D., and Walcher, E., 1999, The Rammelsberg massive sulphide Cu-Zn-Pb-Ba-Deposit, Germany: an example of sediment-hosted, massive sulphide mineralisation: Mineralium Deposita, v. 34, p. 522–538, doi:10.1007/s001260050218.

Liu, L., Ireland, T.R., and Holden, P., 2021, SHRIMP 4-S isotope systematics of two pyrite generations in the 3.49 Ga Dresser Formation: Geochemical Perspectives Letters, p. 5.

Lyons, T.W., Gellatly, A.M., McGoldrick, P.J., and Kah, L.C., 2006, Proterozoic sedimentary exhalative (SEDEX) deposits and links to evolving global ocean chemistry, *in* Evolution of Early Earth's Atmosphere, Hydrosphere, and Biosphere - Constraints from Ore Deposits, Geological Society of America, doi:10.1130/2006.1198(10).

Marin-Carbonne, J. et al., 2020, In Situ Fe and S isotope analyses in pyrite from the 3.2 Ga Mendon Formation (Barberton Greenstone Belt, South Africa): Evidence for early microbial iron reduction: Geobiology, v. 18, p. 306–325.

Martin, A.J., Jamieson, J.W., De Ronde, C.E.J., Layne, G.D., Piercey, G., and Brandl, P.A., 2023, Constraining temporal variations in metal and sulfur sources using high-resolution mineral-scale analysis of pyrite: evidence from the Brothers volcano, Kermadec arc, New Zealand: Mineralium Deposita, v. 58, p. 1237–1262, doi:10.1007/s00126-023-01177-9.

Martin, A.N., Stüeken, E.E., Michaud, J.A.-S., Münker, C., Weyer, S., Van Hees, E.H.P., and Gehringer, M.M., 2024, Mechanisms of nitrogen isotope fractionation at an ancient black smoker in the 2.7 Ga Abitibi greenstone belt, Canada: Geology, v. 52, p. 181–186, doi:10.1130/G51689.1.

McGoldrick, P., 1999, Northern Australian "Sedex" Zn-Pb deposits: microbial oases in Proterozoic seas, *in* Stanley, C.J. ed., Mineral Deposits: Processes to Processing, Rotterdam, Brookfield, A.A. Balkema, v. Volume 1.

Meng, X., Jin, X., Li, X., Chu, F., Zhu, J., Wang, Y., and Zhou, P., 2022, Subseafloor mineralization related to the shallow seawater-hydrothermal circulation system in the Longqi hydrothermal field, Southwest Indian Ridge (49.6°E): Evidence from in situ trace element and sulfur isotope compositions of pyrite varieties: Ore Geology Reviews, v. 145, p. 104914, doi:10.1016/j.oregeorev.2022.104914.

Moreno, C., González, F., and Sáez, R., 2019, Basin Evolution and Massive Sulfide Deposition at Rammelsberg (Germany): Updating the Subsidence Analysis: Minerals, v. 9, p. 45, doi:10.3390/min9010045.

Nie, M., Li, X., Ding, Y., Pan, Y., Cai, Y., Liu, Y., and Liu, J., 2023, Effect of Stoichiometry on Nanomagnetite Sulfidation: Environmental Science & Technology, p. acs.est.2c08179, doi:10.1021/acs.est.2c08179.

Nozaki, T., Nagase, T., Ushikubo, T., Shimizu, K., Ishibashi, J., and and the D/V Chikyu Expedition 909 Scientists, 2020, Microbial sulfate reduction plays an important role at the initial stage of subseafloor sulfide mineralization: Geology, v. 49, p. 222–227, doi:10.1130/G47943.1.

Nozaki, T., Nagase, T., Ushikubo, T., Shimizu, K., and Komuro, K., 2024, In situ sulfur isotope analysis of pyrite from the Ezuri Kuroko-type volcanogenic massive sulfide deposit, northeastern Japan: Contribution of microbial sulfate reduction to initial sulfide mineralization: Resource Geology, v. 74, p. e12328.

Philippot, P., Van Zuilen, M., Lepot, K., Thomazo, C., Farquhar, J., and Van Kranendonk, M.J., 2007, Early Archaean Microorganisms Preferred Elemental Sulfur, Not Sulfate: Science, v. 317, p. 1534–1537, doi:10.1126/science.1145861.

Pirajno, F., 2010, Hydrothermal processes and mineral systems: Dordrecht, Springer, 1250 p.

Poulton, S.W., Krom, M.D., and Raiswell, R., 2004, A revised scheme for the reactivity of iron (oxyhydr)oxide minerals towards dissolved sulfide: Geochimica et Cosmochimica Acta, v. 68, p. 3703–3715, doi:10.1016/j.gca.2004.03.012.

Qian, G., Brugger, J., Skinner, W.M., Chen, G., and Pring, A., 2010, An experimental study of the mechanism of the replacement of magnetite by pyrite up to 300°C: Geochimica et Cosmochimica Acta, v. 74, p. 5610–5630, doi:10.1016/j.gca.2010.06.035.

Qian, G., Brugger, J., Testemale, D., Skinner, W., and Pring, A., 2013, Formation of As(II)-pyrite during experimental replacement of magnetite under hydrothermal conditions: Geochimica et Cosmochimica Acta, v. 100, p. 1–10, doi:10.1016/j.gca.2012.09.034.

Reysenbach, A.-L., and Cady, S.L., 2001, Microbiology of ancient and modern hydrothermal systems: Trends in Microbiology, v. 9, p. 79–86, doi:10.1016/S0966-842X(00)01921-1.

Reysenbach, A.-L., Liu, Y., Banta, A.B., Beveridge, T.J., Kirshtein, J.D., Schouten, S., Tivey, M.K., Von Damm, K.L., and Voytek, M.A., 2006, A ubiquitous thermoacidophilic archaeon from deep-sea hydrothermal vents: Nature, v. 442, p. 444–447, doi:10.1038/nature04921.

Roh, Y. et al., 2006, Metal Reduction and Iron Biomineralization by a Psychrotolerant Fe(III)-Reducing Bacterium, *Shewanella* sp. Strain PV-4: Applied and Environmental Microbiology, v. 72, p. 3236–3244, doi:10.1128/AEM.72.5.3236-3244.2006.

Runge, E., Mansor, M., Chiu, T.-H., Shuster, J., Fischer, S., Kappler, A., and Duda, J.-P., 2024, Hydrothermal sulfidation of biogenic magnetite produces framboid-like pyrite: Communications Earth & Environment, v. 5, p. 252.

Runge, E.A., Mansor, M., Kappler, A., and Duda, J.-P., 2023a, Microbial biosignatures in ancient hydrothermal sulfides: Geobiology, v. 21, p. 355–377.

Runge, E.A., Mansor, M., Shuster, J., Fischer, S., Liu, Y., Lunter, D.J., Kappler, A., and Duda, J.-P., 2023b, Sulfidation of nano-magnetite to pyrite: Implications for interpreting paleoenvironmental proxies and biosignature records in hydrothermal sulfide deposits: Earth and Planetary Science Letters, v. 617, p. 118261, doi:10.1016/j.epsl.2023.118261.

Sáez, R., Moreno, C., González, F., and Almodóvar, G.R., 2011, Black shales and massive sulfide deposits: causal or casual relationships? Insights from Rammelsberg, Tharsis, and Draa Sfar: Mineralium Deposita, v. 46, p. 585–614, doi:10.1007/s00126-010-0311-x.

Sangster, D.F., 2002, The role of dense brines in the formation of vent-distal sedimentary-exhalative (SEDEX) lead–zinc deposits: field and laboratory evidence: Mineralium Deposita, v. 37, p. 149–157, doi:10.1007/s00126-001-0216-9.

Schardt, C., 2016, Hydrothermal fluid migration and brine pool formation in the Red Sea: the Atlantis II Deep: Mineralium Deposita, v. 51, p. 89–111, doi:10.1007/s00126-015-0583-2.

Schroll, E., and Rantitsch, G., 2005, Sulphur isotope patterns from the Bleiberg deposit (Eastern Alps) and their implications for genetically affiliated lead-zinc deposits: Mineralogy and Petrology, v. 84, p. 1–18, doi:10.1007/s00710-004-0071-3.

Shanks, W.C., and Bischoff, J.L., 1980, Geochemistry, sulfur isotope composition, and accumulation rates of Red Sea geothermal deposits: Economic Geology, v. 75, p. 445–459.

Shen, Y., and Buick, R., 2004, The antiquity of microbial sulfate reduction: Earth-Science Reviews, v. 64, p. 243–272, doi:10.1016/S0012-8252(03)00054-0.

Shen, Y., Buick, R., and Canfield, D.E., 2001, Isotopic evidence for microbial sulphate reduction in the early Archaean era: Nature, v. 410, p. 77–81, doi:10.1038/35065071.

Southam, G., and Saunders, J.A., 2005, The Geomicrobiology of Ore Deposits: Economic Geology, v. 100, p. 1067–1084.

Stüeken, E.E., Boocock, T.J., Robinson, A., Mikhail, S., and Johnson, B.W., 2021, Hydrothermal recycling of sedimentary ammonium into oceanic crust and the Archean ocean at 3.24 Ga: Geology, v. 49, p. 822–826, doi:10.1130/G48844.1.

Sylvan, J.B., Toner, B.M., and Edwards, K.J., 2012, Life and Death of Deep-Sea Vents: Bacterial Diversity and Ecosystem Succession on Inactive Hydrothermal Sulfides: mBio, v. 3, p. e00279-11, doi:10.1128/mBio.00279-11.

Taylor, B.E., 2004, Biogenic and thermogenic sulfate reduction in the Sullivan Pb–Zn–Ag deposit, British Columbia (Canada): Evidence from micro-isotopic analysis of carbonate and sulfide in bedded ores: Chemical Geology, v. 204, p. 215–236, doi:10.1016/j.chemgeo.2003.11.011.

Terabayashi, M., Masada, Y., and Ozawa, H., 2003, Archean ocean-floor metamorphism in the North Pole area, Pilbara Craton, Western Australia: Precambrian Research, v. 127, p. 167–180, doi:10.1016/S0301-9268(03)00186-4.

Tice, M.M., Bostick, B.C., and Lowe, D.R., 2004, Thermal history of the 3.5–3.2 Ga Onverwacht and Fig Tree Groups, Barberton greenstone belt, South Africa, inferred by Raman microspectroscopy of carbonaceous material: Geology, v. 32, p. 37, doi:10.1130/G19915.1.

Tornos, F. et al., 2019, Do microbes control the formation of giant copper deposits? Geology, v. 47, p. 143–146, doi:10.1130/G45573.1.

Tornos, F., 2006, Environment of formation and styles of volcanogenic massive sulfides: The Iberian Pyrite Belt: Ore Geology Reviews, v. 28, p. 259–307, doi:10.1016/j.oregeorev.2004.12.005.

Tornos, F., Clavijo, E.G., and Spiro, B., 1998, The Filon Norte orebody (Tharsis, Iberian Pyrite Belt): a proximal low-temperature shale-hosted massive sulphide in a thin-skinned tectonic belt: Mineralium Deposita, v. 33, p. 150–169, doi:10.1007/s001260050138.

Tornos, F., Velasco, F., Menor-Salván, C., Delgado, A., Slack, J.F., and Escobar, J.M., 2014, Formation of recent Pb-Ag-Au mineralization by potential sub-surface microbial activity: Nature Communications, v. 5, p. 4600, doi:10.1038/ncomms5600.

Trüper, H.G., 1969, Bacterial Sulfate Reduction in the Red Sea Hot Brines, *in* Degens, E.T. and Ross, A. eds., Hot brines and recent heavy metal deposits in the Red Sea - a geochemical and geophysical account, New York, Springer, p. 263–271.

Ueno, Y., Ono, S., Rumble, D., and Maruyama, S., 2008, Quadruple sulfur isotope analysis of ca. 3.5Ga Dresser Formation: New evidence for microbial sulfate reduction in the early Archean: Geochimica et Cosmochimica Acta, v. 72, p. 5675–5691, doi:10.1016/j.gca.2008.08.026.

Van Kranendonk, M., Philippot, P., Lepot, K., Bodorkos, S., and Pirajno, F., 2008, Geological setting of Earth's oldest fossils in the ca. 3.5 Ga Dresser Formation, Pilbara Craton, Western Australia: Precambrian Research, v. 167, p. 93–124, doi:10.1016/j.precamres.2008.07.003.

Wacey, D., Noffke, N., Cliff, J., Barley, M.E., and Farquhar, J., 2015, Micro-scale quadruple sulfur isotope analysis of pyrite from the ~3480Ma Dresser Formation: New insights into sulfur cycling on the early Earth: Precambrian Research, v. 258, p. 24–35, doi:10.1016/j.precamres.2014.12.012.

Wilkinson, J.J., 2014, Sediment-Hosted Zinc–Lead Mineralization, *in* Treatise on Geochemistry, Elsevier, p. 219–249, doi:10.1016/B978-0-08-095975-7.01109-8.

Zierenberg, R.A., and Shanks, W.C., 1988, Isotopic studies of epigenetic features in metalliferous sediment, Atlantis II Deep, Red Sea: Canadian Mineralogist, v. 26, p. 737–753.